

Uptake, translocation and transformation of three pharmaceuticals in green pea plants

Aleš Klement^{1*}, Radka Kodešová¹, Oksana Golovko², Miroslav Fér¹, Antonín Nikodem¹,
Martin Kočárek¹, Roman Grabic²

¹ Czech University of Life Sciences Prague, Faculty of Agrobiolgy, Food and Natural Resources, Dept. of Soil Science and Soil Protection, Kamýcká 129, 16500 Prague 6, Czech Republic.

² University of South Bohemia in České Budějovice, Faculty of Fisheries and Protection of Waters, South Bohemian Research Center of Aquaculture and Biodiversity of Hydrocenoses, Zátíší 728/II, 38925 Vodňany, Czech Republic.

* Corresponding author. Tel: +420224382757. Fax: +420234381836. E-mail: klement@af.czu.cz

Abstract: Treated water from wastewater treatment plants that is increasingly used for irrigation may contain pharmaceuticals and, thus, contaminate soils. Therefore, this study focused on the impact of soil conditions on the root uptake of selected pharmaceuticals and their transformation in a chosen soil–plant system. Green pea plants were planted in 3 soils. Plants were initially irrigated with tap water. Next, they were irrigated for 20 days with a solution of either atenolol (ATE), sulfamethoxazole (SUL), carbamazepine (CAR), or all of these three compounds. The concentrations of pharmaceuticals and their metabolites [atenolol acid (AAC), N1-acetyl sulfamethoxazole (N1AS), N4-acetyl sulfamethoxazole (N4AS), carbamazepine 10,11-epoxide (EPC), 10,11-dihydrocarbamazepine (DHC), trans-10,11-dihydro-10,11-dihydroxy carbamazepine (RTC), and oxcarbazepine (OXC)] in soils and plant tissues were evaluated after harvest. The study confirmed high (CAR), moderate (ATE, AAC, SUL), and minor (N4AC) root uptake of the studied compounds by the green pea plants, nonrestricted transfer of the CAR species into the different plant tissues, and a very high efficiency in metabolizing CAR in the stems and leaves. The results showed neither a synergic nor competitive influence of the application of all compounds in the solution on their uptake by plants. The statistical analysis proved the negative relationships between the CAR sorption coefficients and the concentrations of CAR, EPC, and OXC in the roots ($R = -0.916$, -0.932 , and -0.925 , respectively) and stems ($R = -0.837$, -0.844 , and -0.847 , respectively).

Keywords: Atenolol; Carbamazepine; Sulfamethoxazole; Irrigation with contaminated water; Sorption in soils; Metabolites.

INTRODUCTION

It has been recognized that human pharmaceuticals are not entirely removed from wastewater in wastewater treatment plants (e.g., Golovko et al., 2014a, b; Loos et al., 2013). As a result, pharmaceuticals contaminate surface and ground waters (Loos et al., 2010). They may also pollute soils if contaminated water is used for irrigation or if sewage sludge is used as soil amendment (e.g., Thiele-Bruhn, 2003; Verlicchi and Zambello, 2015). The water environment and soils can be also polluted by veterinary pharmaceuticals from animal urine or farm waste (e.g., Charnaud et al., 2019). Pharmaceuticals present in soils can be taken up by plants (e.g., Ahmed et al., 2015; Al-Farsi et al., 2017; Christou et al., 2019; Goldstein et al., 2014; Kodešová et al., 2019a, b; Li et al., 2018, 2019a, b; Malchi et al., 2014; Montemurro et al., 2017; Mordechay et al., 2018; Shenker et al., 2011; Winker et al., 2010; Wu et al., 2013). Some of the studies (e.g., Kodešová et al., 2019b; Malchi et al., 2014; Paltiel et al., 2016) indicated a potential human health treat, if contaminated plant tissues (mainly roots and leaves) are consumed. Contaminations of plant fruits and associated risks have rarely been studied (e.g., Paltiel et al., 2016).

The mobility of a pharmaceutically active compound in soil-water and the potential availability for plants are largely controlled by the pharmaceutical's sorption into soil constituents and persistence in this environment. Sorption of pharmaceuticals in soils is driven by different mechanisms, which depend

on the form of their molecules (e.g., Klement et al., 2018; Kodešová et al., 2015; Schaffer and Licha, 2015). A simultaneous sorption of differently charged compounds can be competitive (i.e., a decreased sorption of some compounds due to a competition for the same sorption sites) as well as synergistic (i.e., an increased sorption of some compounds due to their synergistic behavior) (e.g., Fér et al., 2018; Kočárek et al., 2016). There are just few studies that have focused on the soil impact on the uptake of pharmaceuticals from soils or the impact of simultaneously applied compounds to soils. The studies by Malchi et al. (2014), Goldstein et al. (2014), and Mordechay et al. (2018) indicated that the uptake of some compounds increased with decreasing organic carbon or clay content, but these trends were not proven statistically. A study by Kodešová et al. (2019a), which focused on the plant uptake of 3 pharmaceuticals (atenolol – ATE, sulfamethoxazole – SUL, and carbamazepine – CAR) from 3 different soil types, proved the statistically significant, negative relationships between the CAR sorption coefficients and CAR concentrations in roots of radishes, spinach and lamb's lettuce (no arugula), and leaves of radishes. No statistically significant relationships were found for ATE and SUL. Kodešová et al. (2019b), who studied pharmaceutical uptake from sewage sludge applied to 7 soils through spinach plants, documented close relationships between bioaccumulation factors (BAFs) and soil properties positively affecting sorption of some of analyzed compounds. They proved negative relationships between cation exchange capacity (or organic

carbon content) and BAF for CAR in leaves and roots, and negative relationships between cation exchange capacity and BAF for tramadol, citalopram, or telmisartan in roots. Distinct behaviors in two different soil groups were observed for sertraline, which was largely taken up from soils with a large base cation saturation. The sorption of organic compounds onto soil constituents reduces their amounts dissolved in pore water and thus reduces their uptake into plants (Li et al., 2019a, b). However, actual root-uptake of water and dissolved compounds is also controlled by soil water conditions (Brunetti et al., 2019). Uptake of water and available dissolved substances decreases at negative pressure heads close to zero and pressure heads above zero corresponding to soil saturation and pressure heads below the limit of decreased availability of water for plants or even below the wilting point (Feddes et al., 1978). Root-uptake can also be reduced by soil solution salinity (van Genuchten, 1987), which may also reduce plant growth and take up behavior of compounds in plant bodies (Kodešová et al., 2019b).

The study by Winker et al. (2010) documented lower concentrations of carbamazepine in ryegrass tissues when applied in a mixture with ibuprofen than when applied as a single compound solution. Christou et al. (2019) showed that while the SUL concentration in tomato fruits was reduced when applied together with trimethoprim or diclofenac, trimethoprim followed the opposite trend. On the other hand, Kodešová et al. (2019a) did not find statistical differences between the uptake of ATE, SUL, and CAR applied in single compound solutions or their mixture.

Studies by Goldstein et al. (2014), Malchi et al. (2014), Kodešová et al. (2019a, b), Montemurro et al. (2017), Mordechay et al. (2018), and Riemenschneider et al. (2017) documented that CAR can be metabolized mainly in plant leaves, and the CAR uptake and its transformation strongly depend on particular plant physiologies. Kodešová et al. (2019a) statistically proved that the metabolic efficiencies of radish and arugula (both family Brassicaceae) were very low, contrary to the high and moderate efficiencies of lamb's lettuce and spinach, respectively. The very low efficiency in metabolizing CAR (as well as some other compounds) in the roots and leaves of radish was also proven by Li et al. (2018). They documented that CAR was mostly unmetabolized in radish tissue enzyme extracts, contrary, for instance, to the intensive SUL metabolism in these extracts (the SUL recoveries in root and leaf enzyme extracts after 96 hours were 34% and 72%, respectively). Similarly, Wu et al. (2016) documented an even faster metabolism of SUL and a very low metabolism of CAR and ATE in carrot cell cultures. In addition, Kodešová et al. (2019a) found statistically significant, negative relationships between the CAR sorption coefficients and CAR two metabolite concentrations (carbamazepine 10,11-epoxide, oxcarbazepine) in the roots and leaves of radishes. Similar statistically significant relationships were not found for spinach and lamb's lettuce, which contributed to the larger metabolism of all CAR species in these plants.

In the study by Kodešová et al. (2019a), the uptake, transfer, and transformation of ATE, SUL, and CAR was studied in the roots and leaves of 3 leaf vegetables and radishes. Thus, an impact of soil conditions on the compounds' concentrations in stems and fruits could not be evaluated. The current study, therefore, focused on the evaluation of the distributions of these 3 compounds and their metabolites in tissues of green pea plants, i.e., in roots, stems, leaves, and pea pods. Our previous study also showed that the statistically significant negative correlations between sorption of compounds in soils and their concentrations in plant tissues were mostly observed for roots

and not so often for leaves, which could be likely due to metabolism of accumulated compounds in leaves. Therefore the main goal was to test a hypothesis that compound concentrations in stems (and pea pods) should be less impacted by compounds' metabolism than in leaves; thus, concentrations of the compounds in stems (and pea pods) can be negatively related to their sorption coefficients in soils. In addition, a hypothesis that uptake of ATE, SUL, and CAR applied in single compound solutions and in solution of their mixture should not concededly differ, was tested.

MATERIAL AND METHODS

Experimental setup

The same soils and pharmaceuticals (Table 1 and 2) were used in this study, and the same procedures were followed as described by Kodešová et al. (2019a). Briefly, soil samples were taken from topsoils of the Haplic Chernozem developed on loess (HCh), Haplic Cambisol on paragneiss (HCa), and Arenosol Epieutric on sand (AE). Soil samples were air-dried to a soil-water content of 0.1 g/g and homogenized. These soils had very diverse soil properties (Table 1) and represented different soil environments that should affect behavior of selected compounds in soils in different ways. All 3 selected compounds ATE, SUL and CAR frequently occur in wastewater in the Czech Republic (Golovko et al., 2014a, b). ATE (Beta blocker used to treat hypertension) according to its pKa value (Table 2) should occur in tested soils (according soil pH in Table 1) in cationic form and its sorption affinity to soils is high (Table 2). SUL (antibiotic that is usually applied together with an antibiotic trimethoprim, used to treat a variety of bacterial infections) should prevail mostly in anionic form in soil of higher pH, and partly in anionic and neutral form, respectively, in soils of low pH. SUL sorption in soils is low (Table 2). Degradation half-lives (DT_{50}) of both compounds (ATE and SUL) in soils are relatively low (Table 2). CAR (anticonvulsant used primarily in the treatment of epilepsy, to control seizures and to treat pain resulting from trigeminal neuralgia and diabetic neuropathy) occurs in soils in neutral form, moderately sorbs in soils (Table 2) and is very stable in the soil environment (Table 2).

Experiments were carried out in June under greenhouse conditions (natural light, air humidity of 30%–40%, and air temperature of 20–24°C). A single plant of green peas (*Pisum sativum* L. var. *Axiphium*) was planted in a small pot (volume of 340 cm³) in five replicates for each soil and treatment. Each plant was initially given 8 days of irrigation with tap water, followed by a period of 20 days of irrigation with solution of a single pharmaceutical (ATE, SUL, or CAR), a solution of all 3 pharmaceuticals (Table 3), or tap water. It should be mentioned that the concentrations (Table 3) were five hundred to one thousand times over environmentally relevant concentrations, e.g., in wastewater presented by Golovko et al. (2014a, b) or Loos et al. (2013). Such concentrations were used to enhance the detection and quantification of all compounds and their metabolites in all matrices. Similar concentrations were also used in our previous study (Kodešová et al., 2019a) and some other studies. For more details, see Kodešová et al. (2019a). After treatment, plants were carefully removed from soils and washed. Plant tissues (i.e., roots, stems, leaves, and pods) were separated. Since the same procedure as applied by Kodešová et al. (2019a) was followed, plant and soil samples from 5 replicates were pooled, freeze-dried, and weighed. The reason for this approach was to collect enough amount of dry plant materials for chemical analyses (i.e., at least 0.1 g of dry plant tissues, see below). As we found (Figure 1), in the case of the

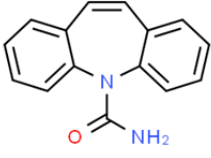
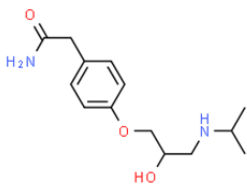
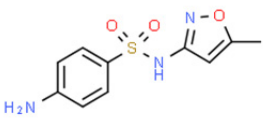
green pea plant, this problem was not as acute as in our previous study for 3 leaf vegetables and radish (Kodešová et al., 2019a). However, just few pods of different early stages of their development were collected, which would likely result in a high variability of measured concentrations (i.e., different time of exposure) and in some cases data would not be available for all plants. Next, all samples were ground, and concentrations of

compounds (ATE, SUL, and CAR) and their metabolites [atenolol acid (AAC), N1-acetyl sulfamethoxazole (N1AS), N4-acetyl sulfamethoxazole (N4AS), carbamazepine 10,11-epoxide (EPC), 10,11-dihydrocarbamazepine (DHC), trans-10,11-dihydro-10,11-dihydroxy carbamazepine (RTC), and oxcarbazepine (OXC)] in plant tissues and soils were measured using the methods described below.

Table 1. Selected soils and their properties: organic carbon content (Cox), CaCO₃ content, pH_{H2O}, pH_{KCl}, content of nitrogen (N) phosphorus (P) and potassium (K), cation exchange capacity (CEC), soil hydrolytic acidity (HA), basic cation saturation (BCS), sorption complex saturation (SCS), salinity, and clay, silt and sand contents (Kodešová et al. 2019a).

Soil Type		Haplic Chernozem - HCh	Haplic Cambisol - HCa	Arenosol Epieutric - AE
Soil substrate		Loess	Paragneiss	Sand
Cox	(%)	1.74	1.57	0.46
CaCO ₃	(%)	4.17	0.19	0.05
pH _{H2O}	–	8.2	6.0	5.6
pH _{KCl}	–	7.2	4.7	4.3
N	(mg/kg)	18.6	25.5	4.03
P	(mg/kg)	135	92.7	220
K	(mg/kg)	340	194	85.8
CEC	(mmol ⁺ /kg)	234.9	188.1	47.0
HA	(mmol ⁺ /kg)	4.5	49.9	25.5
BCS	(mmol ⁺ /kg)	230.4	138.2	21.5
SCS	(%)	98	74	46
Salinity	(μS/cm)	126.9	53.0	25.3
Clay	(%)	25.8	25.4	5.0
Silt	(%)	60.3	30.1	4.5
Sand	(%)	13.9	44.5	90.5

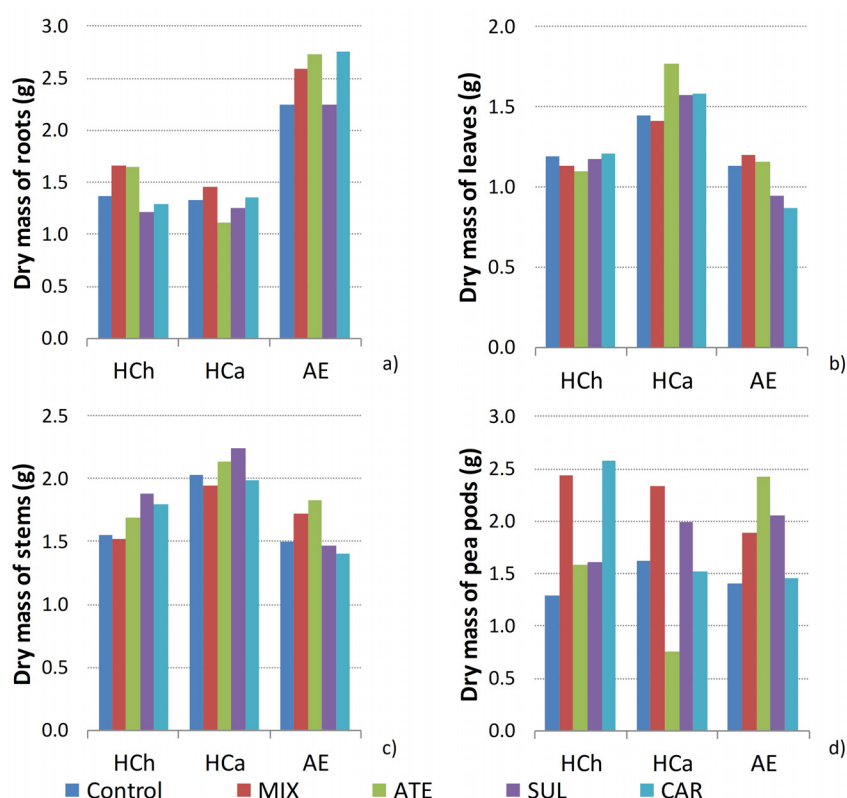
Table 2. Selected pharmaceuticals, their properties and the parameters K_F and n of the Freundlich sorption isotherms ($s = K_F c^{1/n}$, where s is the concentration sorbed onto the soil particles and c is the concentration in soil water) and dissipation half-lives DT₅₀: HCh – Haplic Chernozem, HCa – Haplic Cambisol, AE – Arenosol Epieutric (Kodešová et al., 2019a).

Pharmaceutical	Carbamazepine			Atenolol			Sulfamethoxazole		
CAS	298-46-4			29122-68-7			723-46-6		
Molecular structure ^a									
pKa	pKa ₁ = 1.0 (basic) pKa ₂ = 13.9 (acidic)			9.6 (basic)			pKa ₁ = 1.7 (basic) pKa ₂ = 5.6 (acidic)		
Log Kow	2.25			0.16			0.89		
H-bonds Donors, Acceptors	1 1			3 4			2 6		
MW (g/mol)	236.27			266.34			253.28		
Soil	HCh	HCa	AE	HCh	HCa	AE	HCh	HCa	AE
K_F (cm ^{3/n} /μg ^{1-1/n} /g)	3.86	2.97	0.71	16.24	5.36	2.11	0.88	4.01	1.39
n	1.13			1.17			1.65		
DT ₅₀ (days)	>1 000	>1 000	>1 000	3.7	9.0	7.7	5.0	15.0	8.0

^a blue – basic, red – acidic

Table 3. Irrigation doses and concentrations of pharmaceuticals: ATE – atenolol, SUL – sulfamethoxazole, CAR – carbamazepine, S – single-solute solution, M – tri-solute solution.

Day	Irrigation (mL)	Concentrations (mg/L)					
		ATE-S	SUL-S	CAR-S	ATE-M	SUL-M	CAR-M
8	150	1.7	0.96	1	0.72	0.64	0.49
10	150	1.7	0.96	1	0.72	0.64	0.49
11	200	1.7	0.96	1	0.72	0.64	0.49
14	150	1.3	1	0.65	0.8	0.77	0.53
16	150	1.3	1	0.65	0.8	0.77	0.53
18	200	1.1	1	0.68	0.89	0.85	0.58
21	150	1.1	1	0.68	0.89	0.85	0.58
23	150	1.2	0.78	0.64	0.87	0.88	0.58
25	150	1.2	0.78	0.64	0.87	0.88	0.58
26	100	1.2	0.78	0.64	0.87	0.88	0.58
28	Harvest	1.1	1.1	0.66	0.88	0.74	0.48

**Fig. 1.** Dry masses of plant parts (sums of all 5 replicates) measured for different treatments: a) roots, b) leaves, c) stems, d) pea pods, Control – irrigation with tap water, MIX – irrigation with the solution of all compounds, and ATE, SUL and CAR – irrigation with the solution of atenolol, sulfamethoxazole and carbamazepine, respectively, HCh – Haplic Chernozem, HCa – Haplic Cambisol, AE – Arenosol Epietric.

Chemical analyses

The method for extraction of compounds (CAR, ATE, and SUL) and their metabolites (EPC, OXC, RTC, DHC, AAC, N1AS, and N4AS) from plant tissues followed a procedure previously validated for these compounds by Kodešová et al. (2019a, b). Briefly, the freeze-dried plant samples were extracted as follows: 0.1 g of sample was placed in an Eppendorf tube with a safe lock, 5 ng of internal standard, and a stainless steel ball, and 1 mL of extraction mixture 1 (acetonitrile/water, 1/1, 0.1% of formic acid) was added. Samples were consequently extracted by shaking at 1800 min^{-1} for 5 min (TissueLyser II, Qiagen, Germany). The samples were then centrifuged at $10,000 \text{ min}^{-1}$ for 5 min (Mini spin centrifuge, Eppendorf), and the supernatant was filtered through a syringe filter (0.45 μm regenerated cellulose filters) to clean Eppendorf tube. Aliquots

of 100 μl were taken and placed in an autosampler vial for LC-MS analysis.

An ultrasound-based extraction approach with two solvent mixtures was applied for the analysis of the selected compounds and their metabolites in the soil matrix (Golovko et al., 2016; Koba et al., 2016, 2017). This method was validated for 63 compounds and their metabolites in 13 soils (including compounds and soils used in this study). Briefly, 2 g of each freeze-dried soil sample was placed in a 10-mL autosampler vial, and 20 ng of internal standard was added. The samples were then extracted with 4 mL of extraction mixture 1 (acetonitrile/water 1/1, v/v acidified with 0.1% of formic acid) followed with 4 mL of mixture 2 (acetonitrile/2-propanol/H₂O, 3/3/4, v/v/v, acidified with 0.1% of formic acid) in an ultrasonic bath (DT 255, Bandelin electronic, Sonorex).

The liquid chromatography-tandem mass spectrometry (LC-MS/MS) and either isotope dilution or an internal standard (IS) method with using matrix matching standard was used to determine concentrations of pharmaceuticals in irrigation doses and concentrations of pharmaceuticals and their metabolites in supernatants from plant tissues and soils. A triple-stage quadrupole mass spectrometer, Quantiva (Thermo Fisher Scientific, San Jose, CA, USA), coupled with an Accela 1250 LC pump (Thermo Fisher Scientific) and HTS XT-CTC autosampler (CTC Analytics AG, Zwingen, Switzerland), were used for the analysis of irrigation water (Koba et al., 2016). A hybrid quadrupole-orbital trap mass spectrometer, Q Exactive (Thermo Fisher Scientific, San Jose, CA, USA), operated in high-resolution product scan mode (HRPS), was used instead of a triple quadrupole for more complex soil and plant extracts. A Hypersil Gold aQ column (50 mm × 2.1 mm i.d., 5 µm particle size, from Thermo Fisher Scientific San Jose, CA, USA) was used for the chromatographic separation of the target compounds. The matrix effects were corrected using a matrix matching standard if deviation from calibration curve response factor was greater than 30%. Detail descriptions of the instrument settings can be found in article of Grabicova et al. (2018). For other details about the methods (procedures, validation of the methods etc.) please see Kodešová et al. (2019a), Golovko et al. (2016) and Koba et al. (2016, 2017). The average limits of quantification (LOQs) are shown in Table 4. Estimated uncertainty of the methods is 30%. However, both sulfamethoxazole metabolites had lower response in ESI-HRPS, which resulted in high LOQs.

Resulting concentrations of chemicals in soils and plant tissues were expressed in ng/g (dry weight) (Figure 2a, c) and also in nmol/g (dry weight). To calculate these values, the molecular weight (MW) values in Table 2 were used for the parent compounds, and the MW values of 267.33 (AAC), 295.31 (N4AS), 252.27 (EPC), 238.28 (DHC), 270.29 (RTC), and 252.27 (OXC) g/mol were used for the metabolites.

Table 4. Average limits of quantification, LOQs (ng/g), calculated from real samples analyzed in different sequences and time: ATE – atenolol, AAC – atenolol acid, N1AS – N1-acetyl sulfamethoxazole, N4AS – N4-acetyl sulfamethoxazole, SUL – sulfamethoxazole, CAR – carbamazepine, EPC – carbamazepine 10,11-epoxide, DHC – 10,11-dihydrocarbamazepine, RTC – trans-10,11-dihydro-10,11-dihydroxy carbamazepine, and OXC – oxcarbazepine.

Compound	Roots	Stems	Leaves	Pods	Soils
ATE	0.41	0.41	0.43	0.24	6.03
AAC	1.10	1.73	2.05	1.10	4.67
SUL	9.77	13.6	22.2	11.5	2.97
N1AS	24.0	28.5	50.4	23.2	1.19
N4AS	34.2	36.2	70.9	37.3	2.15
CAR	0.99	2.80	1.38	1.17	1.41
EPX	0.65	1.50	0.76	0.93	0.91
OXC	4.13	3.58	4.69	3.33	0.62
RTC	6.65	5.48	6.23	5.40	4.41
DHC	2.07	1.31	1.35	1.11	1.48

Data evaluation

The data expressed in nmol/g were next used to calculate molar fractions of the measured parent compounds and their metabolites relative to the total of all measured compounds (Figure 2b, d) or in a sum of measured parent compound and its metabolites (Figure 3). It should be noted that the studied com-

pounds could be transformed also into other metabolites and transformation products. However, Koba et al. (2016, 2017) showed that concentrations of other metabolites of CAR, SUL and ATE in our soils can be very low and even negligible. Similarly, previous studies (e.g., Riemenschneider et al., 2017) dealing with the uptake of CAR, SUL and ATE did not suggest considerable fractions of other metabolites in tested plant materials.

The data expressed in nmol/g were also used to evaluate bioaccumulation of the compounds in plant tissues. Since exposure of plants to soil contamination was not constant (i.e., concentrations of repeatedly applied solutions differed (Table 3) and in-between applications compounds transformed in soils) standard bioaccumulation factors could be evaluated. Therefore, the parent compound load normalized concentrations (CLNC, 1/g) were calculated as, the concentrations in plant tissues divided by the parent compound load as follows (Kodešová et al., 2019b):

$$CLNC = \frac{C_p}{\sum_{i=1}^N V_i C_{sol,i}} \quad (1)$$

where C_p (nmol/g) is the solute concentration in plant tissue, V_i (cm³) is the volume of the irrigation dose, $C_{sol,i}$ (nmol/cm³) is the solute concentration of the parent compound in the irrigation dose, and N is the number of irrigation doses (Table 3). The CLNC values were next analyzed using STATGRAPHICS Centurion XV Version 15.2.06. Kruskal–Wallis tests were used to compare the CLNC values for the different tissues and treatments (Figure 4): 1. A data set for a particular chemical and plant tissue included the CLNC values from all soils and both treatments (i.e., application of chemical in solution of a single compound or their mixture); 2. A data set for a particular chemical and plant tissue included the CLNC values from all soils and one treatment. Simple correlations between the Freundlich sorption coefficients (K_F values in Table 1) and the CLNC values for the corresponding pharmaceutical or its metabolites were assessed using the Pearson product-moment correlation coefficient. The statistical significance was assessed according to the p-value.

RESULTS AND DISCUSSION

Plant growth

As found by Kodešová et al. (2019a), the dry masses of plant tissues and the total masses of plants (Figure 1) irrigated with solutions of a single compound or all three compounds did not differ from those irrigated with tap water. However, plant growth was largely impacted by soil type. While the masses of roots (Figure 1a) from AE were considerably larger than those from HCh and HCa (likely due to decreased availability of water in sandy soil), the masses of leaves (Figure 1b) and stems (Figure 1c) from HCa were larger than those from HCh and AE probably due to the optimal water and air conditions in HCa. Nevertheless, the masses of pods (Figure 1d) were similar for all scenarios.

Bioaccumulation of pharmaceuticals and their metabolites - Neutral molecules of CAR

The low concentrations of the CAR metabolites (Figures 2a and 2b) indicated that CAR was not considerably transformed in the soils by microbial activity or other chemical processes

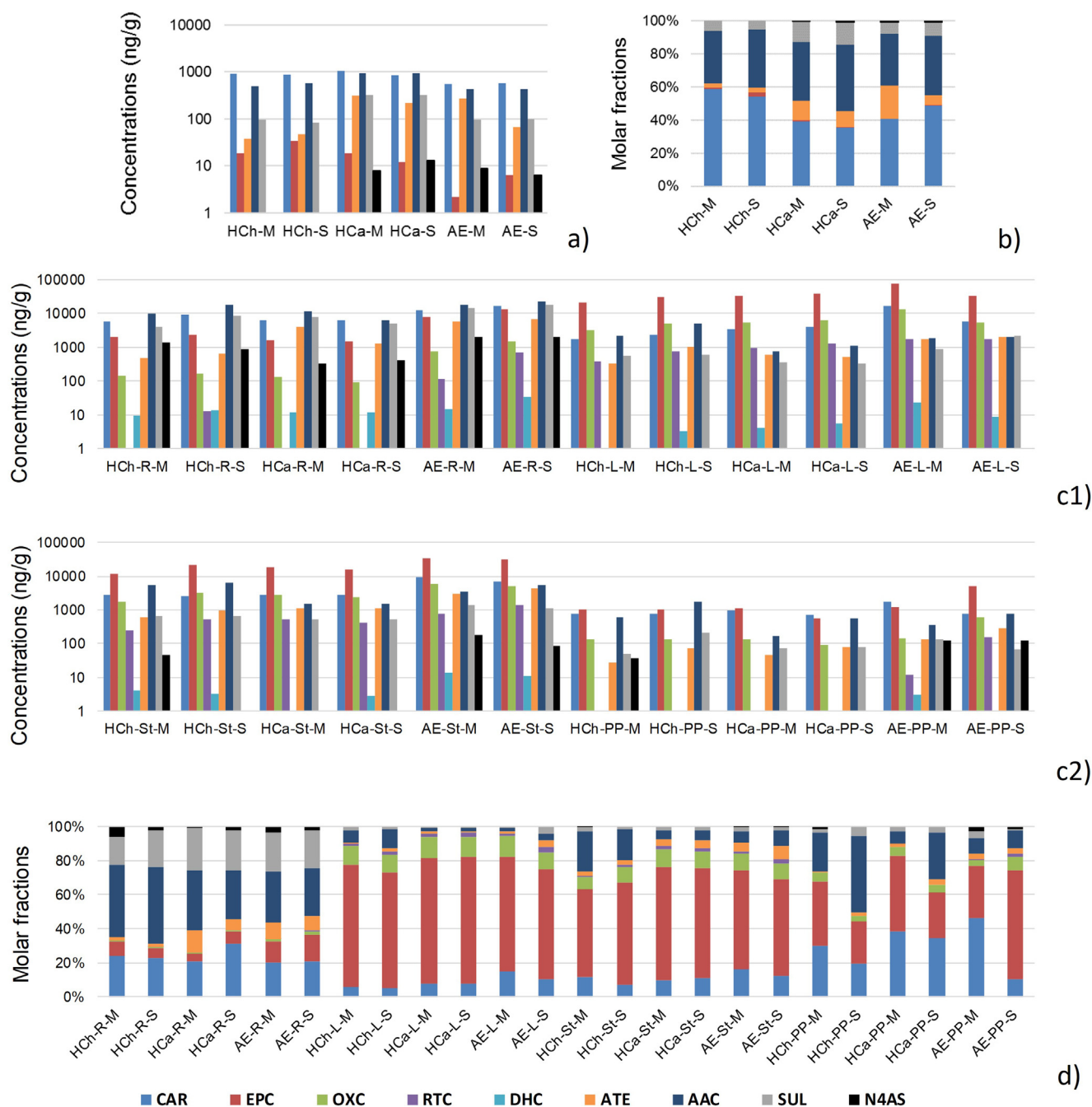


Fig. 2. Concentrations of pharmaceuticals (CAR, ATE, and SUL) and their metabolites (EPC, OXC, RTC, DHC, AAC, and N4AS) in soils HCh, HCa and AE (a), and plant tissues: (c), i.e., roots (R), stems (St), leaves (L) and pea pods (PP). Fractions of each compound in the sums of molar concentrations of all parent compounds and their metabolites quantified in soils (b) and plant tissues (d): S – single-solute solution, M – tri-solute solution, HCh – Haplic Chernozem, HCa – Haplic Cambisol, AE – Arenosol Epieutric, ATE – atenolol, SUL – sulfamethoxazole, CAR – carbamazepine, AAC – atenolol acid, N4AS – N4-acetyl sulfamethoxazole, EPC – carbamazepine 10,11-epoxide, DHC – 10,11-dihydrocarbamazepine, RTC – trans-10,11-dihydro-10,11-dihydroxy carbamazepine, and OXC – oxcarbazepine.

taking place in a soil environment (Koba et al., 2016; Kodešová et al., 2016). On the other hand, CAR was greatly metabolized in plant bodies (Figures 2c and 2d). It is widely assumed that CAR transformation in plant tissues is affected by plant cytochrome P450 enzymes (e.g., Goldstein et al., 2014; Gunnarsson et al., 2012; Malchi et al., 2014; Montemurro et al., 2017). The fractions of CAR from the sum of CAR and its metabolite molar concentrations (Figure 3a) in the roots varied between 80% and 60%, by 15% in the leaves and stems, and the fractions in the pea pods varied by 40%. The EPC fractions were dominant in the stems and leaves (70%). The relatively large

fractions of OXC (15%–10%) were also measured in the stems, leaves, and pods.

Significant differences between the accumulations of different CAR species in different plant tissues were also proven by analyzing the CLNC values using Kruskal–Wallis tests and box-and-whisker plots (Figure 4a). The highest sums of concentrations of CAR and its metabolites (Figure 2) were obtained in the leaves, followed by stems, roots, pods, and soils. Our findings are consistent with the results of Riemenschneider et al. (2017), who found the largest concentrations in leaves followed by concentrations in the stems, roots, and fruits of

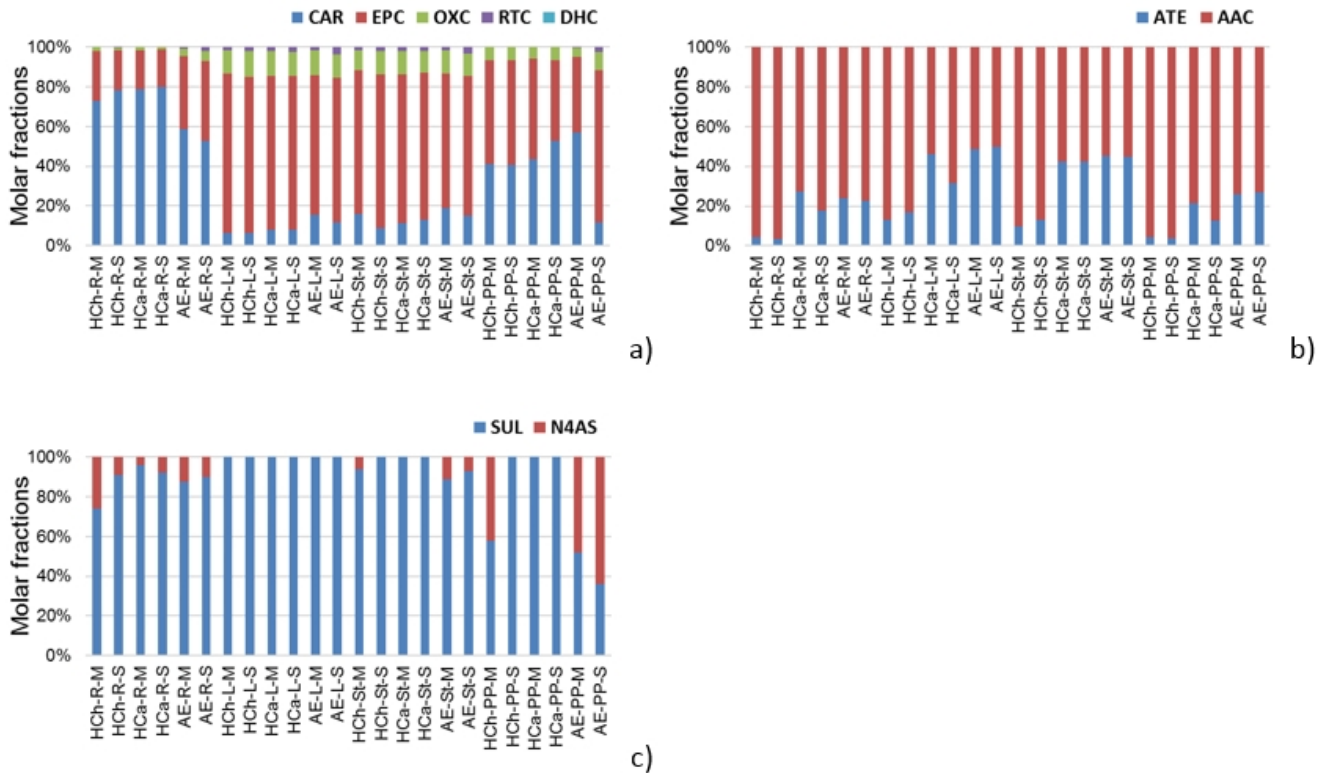


Fig. 3. Fractions of each compound in the sums of molar concentrations of the parent compound and its metabolites, i.e., sum of CAR, EPC, OXC, RTC and DHC (a), sum of ATE and AAC (b), and sum of SUL and N4AS (c) in plant tissues: R – roots, L – leaves, St – stems, PP – pea pods, S – single-solute solution, M – tri-solute solution, HCh – Haplic Chernozem, HCa – Haplic Cambisol, AE – Arenosol Epieutric ATE – atenolol, SUL – sulfamethoxazole, CAR – carbamazepine, AAC – atenolol acid, N4AS – N4-acetyl sulfamethoxazole, EPC – carbamazepine 10,11-epoxide, DHC – 10,11-dihydrocarbamazepine, RTC – trans-10,11-dihydro-10,11-dihydroxy carbamazepine, and OXC – oxcarbazepine.

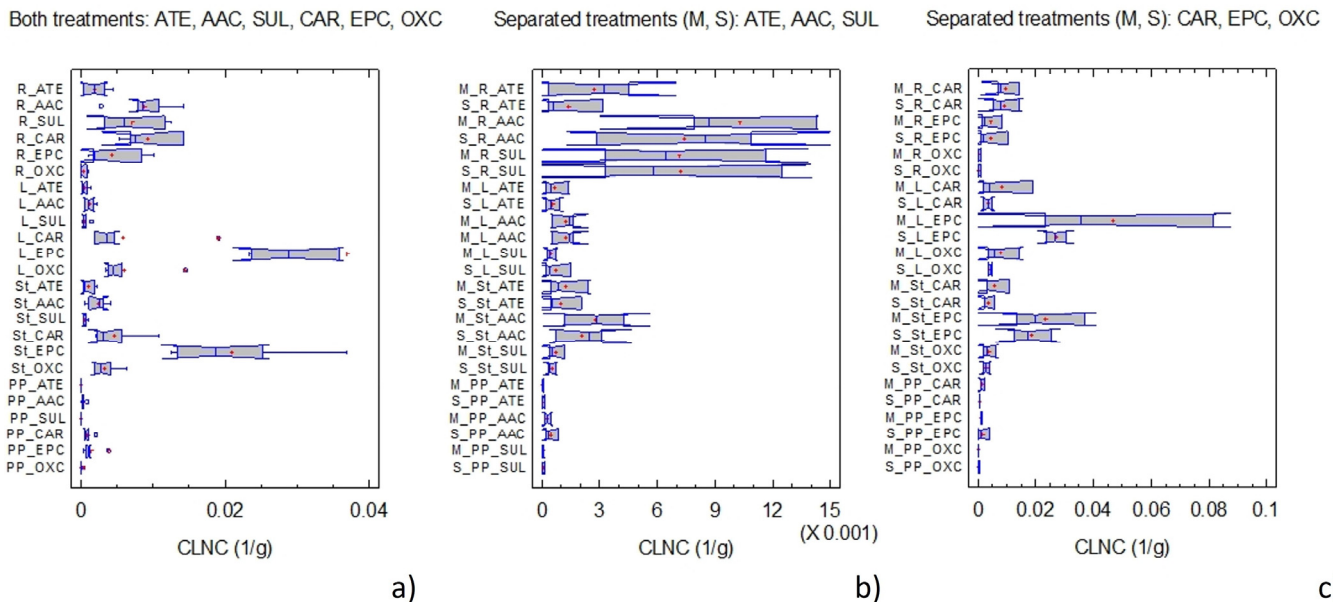


Fig. 4. (a) The CLNC values for the main compounds quantified in plant tissues (ATE – atenolol, AAC – atenolol acid, SUL – sulfamethoxazole, CAR – carbamazepine, EPC – carbamazepine 10,11-epoxide, and OXC – oxcarbazepine) from all soils and both treatments (a data set for a particular chemical and plant tissue included the CLNC values from all soils and both treatments, i.e., application of chemical in solution of a single compound or their mixture) (L_EPC data include an outlier value of 0.0815 1/g), and (b) and (c) the CLNC values for the main compounds measured in plant tissues from all soils and different treatments (a data set for a particular chemical and plant tissue included the CLNC values from all soils and one treatment either S – single-solute solution, or M – tri-solute solution): R – roots, L – leaves, St – stems, and PP – pea pods.

tomato plants. Similarly Shenker et al. (2011) found the largest concentrations in the leaves followed by the concentrations in the roots, stems, and fruits of cucumber plants. The high accumulation in the leaves of green pea plants is associated with the transpiration stream and not the restricted transfer of neutral molecules of low MW, lipophilicity, and number of H-bonds (Kumar and Gupta, 2016) through the plant bodies (e.g., Goldstein et al., 2014; Hurtado et al., 2016; Kodešová et al., 2019a, b; Malchi et al., 2014; Montemurro et al., 2017; Mordechay et al., 2018; Shenker et al., 2011, Winker et al., 2010; Wu et al., 2013) due to a passive diffusion through lipid bilayer membranes (Chuang et al., 2019). The lower accumulation in the pods is explained by the significantly shorter exposure to the contamination and a lower transpiration of pods in comparison to that in the leaves. Compared to the study by Kodešová et al. (2019a), the metabolism of CAR in green pea leaves was as efficient as in lamb's lettuce leaves.

Bioaccumulation of pharmaceuticals and their metabolites - ionic molecules of ATE and SUL

The bioaccumulations of both ionic compounds were considerably lower than the bioaccumulation of CAR. Compared to that of CAR, the roots also contained relatively large amounts of ATE (positively charged) and its metabolite AAC (Figures 2c and 2d). The $CLNC_{AAC}$ values were significantly higher than the $CLNC_{ATE}$ values and similar to the $CLNC_{CAR}$ values (Figure 4a). The fractions of ATE and AAC from the sum of their molar concentrations were 20% and 80%, respectively (Figure 3b). These findings can be explained by ATE's rapid transformation in soils (Figures 2a and 2b, and Kodešová et al., 2016), a moderately larger persistence of the AAC metabolite in soils (Koba et al., 2016), and its subsequent root uptake (Kodešová et al., 2019a). Significantly lower concentrations of ATE were found in the other plant tissues (Figures 2c and 4a). This is explained by the positive charge of the ATE molecules and their sorption onto the negatively charged cell membranes (and, thus, restricted transfer in plant bodies), which is consistent with the findings of Kodešová et al. (2019a) but is in contrast to the results of Wu et al. (2013), who found similar ATE concentrations in the leaves and roots of all plants. The fractions of ATE and AAC in the pods were similar to those in the roots (Figure 3c). The molar fractions of ATE and AAC in the leaves and stems were 40% and 60%, respectively.

Similar to ATE, considerably larger concentrations of SUL (molecules were mostly negatively charged) were measured in the roots than in the other tissues (Figures 2c, 4a), which is consistent with studies by Ahmed et al. (2015), Kodešová et al. (2019a), Malchi et al. (2014), and Wu et al. (2013). The sulfamethoxazole metabolite N1AS was not found in any matrices. Low concentrations of N4AS were quantified in all roots and some stems and pea pods. These findings differ from the results of the study by Kodešová et al. (2019a), in which neither of these two metabolites were observed in the roots and leaves of spinach, lamb's lettuce, arugula, and radishes. On the other hand, this metabolite was also found in lettuce and carrot plants by Mullen et al. (2017). The significantly lower concentrations in the above surface plant tissues, compared to that in the roots, can be explained by the negative charge of the SUL molecules and, thus, their repulsion from the cell membranes (i.e., restricted transfer in the plant bodies). Very low concentrations, or absence, of the SUL metabolites in the plants and soils can be explained by their very rapid dissipation from the soils (Figures 2a and 2b, and Koba et al., 2017). In addition, as shown by Li et al. (2018) and Wu et al. (2016), SUL (and likely also its

metabolites) can be very efficiently metabolized in plant bodies (particularly in roots). The bioaccumulation of SUL in the roots (Figure 4a) was significantly larger than ATE's bioaccumulation and comparable with AAC's bioaccumulation, respectively. This finding is in contrast with the findings of Wu et al. (2013), who documented considerably lower concentrations of SUL than ATE, and to the results of Kodešová et al. (2019a), who observed similar SUL and ATE bioaccumulations. It should be noted that, contrary to SUL, the metabolism of ATE could be quite low (Wu et al., 2016). Thus, the difference between the actual uptakes of SUL and ATE (indicating the larger uptake of SUL compared to that of ATE) could be even greater.

Influence of treatment on the compound's uptake and distribution in plant tissues

No trends between the concentrations measured in the plant tissues from the different treatments (i.e., the single compound application or application of the mixture of 3 pharmaceuticals) were found (Figure 2c). Except EPC in leaves, the Kruskal-Wallis tests and the box-and-whisker plots (Fig. 4b and 4c) did not show significant differences between the CLNC values of a certain compound (i.e., CAR, EPC, OXC, ATE, AAC, and SUL) in specific plant tissues for all soils obtained under the different treatments, which is consistent with the findings by Kodešová et al. (2019a). However, it should be noted that plant tissues for an individual soil and treatment were pooled and thus difference between the CLNC values resulted from different treatments for a specific soil could not be assessed statistically. Therefore, a new study with a greater amount of plants planted in a certain soil, which would allow pooling plant tissues at least in 3 groups (i.e., replicates), is needed to prove or disprove this hypothesis.

Influence of soil on the compound's uptake and distribution in plant tissues

The correlation coefficients (Table 5) between the parent compound K_F coefficients (Table 1) and the CLNC values of the parent compound or its metabolite (merged sets of values obtained from both treatments) consistently displayed a negative influence of the sorption of the parent compound in soils on its uptake and transfer in the plant bodies.

However, statistically significant relationships were found only for the CAR concentrations in roots and stems. In these plant tissues, statistically significant, negative relationships were found also between the $K_{F,CAR}$ and CLNC values of the CAR metabolites (EPC and OXC). Similar to the study by Kodešová et al. (2016), positive relationships (but not significant) were observed between the $K_{F,ATE}$ and $CLNC_{AAC}$ values. This can be explained by the negative charge of the AAC molecule and, thus, an opposite sorption affinity to soils compared to ATE, i.e., the sorption of ATE and AAC increases and decreases, respectively, with an increasing number of negatively charged sorption sites of soil constituents (Kodešová et al., 2016).

Potential human health risks

As mentioned above applied concentrations were five hundred to one thousand times over environmentally relevant concentrations. Therefore concentrations of some compounds in leaves were very high. In the case of pods, the concentrations of CAR, ATE, SUL and their metabolites (excluding N4AS from AE scenarios) were at least 10 time lower than those in leaves.

Table 5. The correlation coefficients between the parent compound load normalized concentrations (CLNC) of particular pharmaceutical or its metabolite and the Freundlich sorption coefficient (K_F) of parent compound: CAR – carbamazepine, EPC – carbamazepine 10,11-epoxide, OXC – oxcarbazepine, ATE – atenolol, AAC – atenolol acid, and SUL – sulfamethoxazole.

Plant	CLNC	K_F , CAR	K_F , ATE	K_F , SUL
Roots	CAR	-0.916*		
	EPC	-0.932**		
	OXC	-0.928**		
	ATE		-0.805	
	AAC		-0.306	
	SUL			-0.155
Stems	CAR	-0.837*		
	EPC	-0.844*		
	OXC	-0.847*		
	ATE		-0.750	
	AAC		0.596	
	SUL			-0.304
Leaves	CAR	-0.716		
	EPC	-0.627		
	OXC	-0.629		
	ATE		-0.630	
	AAC		0.724	
	SUL			-0.315
Pea pods	CAR	-0.501		
	EPC	-0.682		
	OXC	-0.661		
	ATE		-0.724	
	AAC		0.752	
	SUL			-0.402

* $p < 0.05$, ** $p < 0.01$.

In general larger concentrations were measured in plants planted in AE. Thus a greatest health risk when consuming green pea pods can be expected in case of plants planted in sandy soils.

Exposure and potential health risk associated with consumption of the pharmaceuticals and their metabolites in crops can be examined relative to acceptable daily intake (ADI) values for each substance (e.g., Kodešová et al., 2019b). Because information about long term exposure of pharmaceuticals to human health is often not available (Williams and Brooks, 2012), the ADI values can be calculated from minimal therapeutic doses (1.43 (CAR), 0.71 (ATE) and 1.43 (SUL) mg/kg of person) divided by an uncertainty factor (UF). In case they are not CMR or EDC type chemicals (Bruce et al., 2010; Bull et al., 2011; Semerjian et al., 2018), UF of 3000 can be applied. The worst case scenario can be assumed in the case of the metabolites (i.e., metabolites can have a similar impact on human health as a parent compound) and the ADI values for metabolites can be calculated assuming the ADI values for the parent compound and molar masses (Kodešová et al., 2019b). Daily consumption (DC) of fresh green pea pods by a child (25 kg) and an adult (70 kg) to reach ADI can be calculated using the measured concentrations and the mean percentage of pod dry mass of 18% (calculated from fresh and dry masses of pods obtained from different scenarios). Assuming this approach and concentrations in pea pods (Figure 2c), the DC values for children ranges from 0.12 to 0.30 kg for CAR, 0.05–0.42 kg for EPC 0.37–2.3 kg for OXC, 0.37–3.8 kg for ATE, 0.06–0.63 kg for AAC, 1.0–4.4 kg for SUL, and 1.8 kg for N4AS and AE. Some of these values are close to a possibly consumable amount of pods. In the case of adults the DC values would be

2.8 time higher. However, it can be expected that in the case of the environmentally relevant concentrations, the DC values should be more than 2 orders of magnitude higher and thus a potential health risk is likely very low. Nevertheless, it should be mentioned that pods were harvested in an early stage of their development. Concentrations could be higher after longer-time exposure. Additional studies should be carried out with environmentally relevant concentrations of various compounds to elucidate a potential health treat related to these compounds uptake to fruits.

CONCLUSION

This study confirmed high (CAR), moderate (ATE, AAC, SUL), and minor (N4AC) root uptake of the studied compounds by green pea plants, the unrestricted transfer of the CAR species into the different plant tissues and the very high efficiency in metabolizing CAR in the stems and leaves of green pea plants. As anticipated, the results showed neither competitive nor synergic effects of the simultaneous application of the compounds on their uptake by these plants. However, this phenomenon should be further studied using a larger number of plants planted in an individual soil, which would allow a statistical assessment for a certain soil environment. The results indicated the negative impact of the parent compounds' sorption affinity on their uptake by the plants, which was statistically proven for CAR, EPC, and OXC in the roots and stems. Thus, our results partly confirmed our main hypothesis, that the concentrations of some compounds in the roots and stems (but not in the pea pods) can be negatively dependent on their sorption affinities to soils.

Acknowledgement. Authors acknowledge the financial support of the Czech Science Foundation project No. 17-08937S, Behavior of pharmaceuticals in soil-water-plant system, and partly also our previous project No. 13-12477S, Transport of pharmaceuticals in soils. Pharmaceutical concentrations were measured using devices financially supported by the Ministry of Education, Youth and Sports of the Czech Republic, projects CENAKVA (No. CZ.1.05/2.1.00/01.0024), CENAKVA Center Development (No. CZ.1.05/2.1.00/19.0380) and CENAKVA II (No. LO1205 under the NPU I program). The work was also supported from European Regional Development Fund, project Centre for the investigation of synthesis and transformation of nutritional substances in the food chain in interaction with potentially harmful substances of anthropogenic origin: comprehensive assessment of soil contamination risks for the quality of agricultural products (No. CZ.02.1.01/0.0/0.0/16_019/0000845).

REFERENCES

- Ahmed, M.B.M., Rajapaksha, A.U., Lim, J.E., Vu, N.T., Kim, I.S., Kang, H.M., Lee, S.S., Ok, Y.S., 2015. Distribution and accumulative pattern of tetracyclines and sulfonamides in edible vegetables of cucumber, tomato, and lettuce. *J. Agric. Food Chem.*, 63, 2, 398–405. <https://doi.org/10.1021/jf5034637>.
- Al-Farsi, R.S., Ahmed, M., Al-Busaidi, A., Choudri, B.S., 2017. Translocation of pharmaceuticals and personal care products (PPCPs) into plant tissues: A review. *Emerg. Contam.* 3, 132–137. <https://doi.org/10.1016/j.emcon.2018.02.001>.
- Bruce, G.M., Pleus, R.C., Snyder, S.A., 2010. Toxicological relevance of pharmaceuticals in drinking water. *Environ. Sci. Technol.*, 44, 5619–5626. <https://doi.org/10.1021/es1004895>.
- Brunetti, G., Kodešová, R., Šimůnek, J., 2019. Modeling the

- translocation and transformation of chemicals in the soil-plant continuum: A dynamic plant uptake module for the HYDRUS model. *Water Resour. Res.*, 55, 8967–8989. <https://doi.org/10.1029/2019WR025432>.
- Bull, R.J., Crook, J., Whittaker, M., Cotruvo, J.A., 2011. Therapeutic dose as the point of departure in assessing potential health hazards from drugs in drinking water and recycled municipal wastewater. *Regul. Toxicol. Pharmacol.*, 60, 1–19. <https://doi.org/10.1016/j.yrtph.2009.12.010>.
- Charuaud, L., Jardem E., Jaffrezic, A., Thomas, M.F., Le Bot, B., 2019. Veterinary pharmaceutical residues from natural water to tap water: Sales, occurrence and fate. *J. Hazard. Mater.*, 361, 169–186. <https://doi.org/10.1016/j.jhazmat.2018.08.075>.
- Christou, A., Kyriacou, M.C., Georgiadou, E.C., Papamarkou, R., Hapeshi, E., Karaolia, P., Michael, C., Fotopoulos, V., Fatta-Kassinos, D., 2019. Uptake and bioaccumulation of three widely prescribed pharmaceutically active compounds in tomato fruits and mediated effects on fruit quality attributes. *Sci. Total Environ.*, 647, 1169–1178. <https://doi.org/10.1016/j.scitotenv.2018.08.053>.
- Chuang, Y.-H., Liu, C.-H., Sallach, J.B., Hammerschmidt, R., Zhang, W., Boyd, S.A., Li, H., 2019. Mechanistic study on uptake and transport of pharmaceuticals in lettuce from water. *Environ. Int.*, 131, 104976. <https://doi.org/10.1016/j.envint.2019.104976>.
- Feddes, R.A., Kowalik, P.J., Zaradny, H., 1978. Simulation of field water use and crop yield. PUDOC (Centre for agricultural publishing and documentation), Wageningen.
- Fér, M., Kodešová, R., Golovko, O., Schmidtová, Z., Klement, A., Kočárek, M., Grabic, R., 2018. Sorption of atenolol, sulfamethoxazole and carbamazepine onto soil aggregates from the illuvial horizon of the Haplic Luvisol on loess. *Soil Water. Res.*, 13, 3, 177–183. <https://doi.org/10.17221/82/2018-SWR>.
- Goldstein, G., Shenker, M., Chefetz, B., 2014. Insights into the uptake processes of wastewater-borne pharmaceuticals by vegetables. *Environ. Sci. Technol.*, 48, 10, 5593–5600. <https://doi.org/10.1021/es5008615>.
- Golovko, O., Kumar, V., Fedorova, G., Randak, T., Grabic, R., 2014a. Removal and seasonal variability of selected analgesics/anti-inflammatory, anti-hypertensive/cardiovascular pharmaceuticals and UV filters in wastewater treatment plant. *Environ. Sci. Pollut. Res.*, 21, 7578–7585. <https://doi.org/10.1016/j.chemosphere.2014.03.132>.
- Golovko, O., Kumar, V., Fedorova, G., Randak, T., Grabic, R., 2014b. Seasonal changes in antibiotics, antidepressants/psychiatric drugs, antihistamines and lipid regulators in a wastewater treatment plant. *Chemosphere*, 111, 418–426. <https://doi.org/10.1016/j.chemosphere.2014.03.132>.
- Golovko, O., Koba, O., Kodešová, R., Fedorova, G., Kumar, V., Grabic, R., 2016. Development of fast and robust multi-residual LC-MS/MS method for determination of pharmaceuticals in soils. *Environ. Sci. Pollut. Res.*, 23, 14, 14068–14077. <https://doi.org/10.1007/s11356-016-6487-6>.
- Grabicova, K., Stanova, A.V., Ucin, O.K., Borik, A., Randak, T., Grabic, R., 2018. Development of a robust extraction procedure for the HPLC-ESI-HRPS determination of multi-residual pharmaceuticals in biota samples. *Anal. Chim. Acta*, 1022, 53–60. <https://doi.org/10.1016/j.aca.2018.04.011>.
- Gunnarsson, L., Kristiansson, E., Larsson, D.G.J., 2012. Environmental comparative pharmacology: theory and application. In: Brooks, B.W., Huggett, D.B. (Eds.): *Human Pharmaceuticals in the Environment: Current and Future Perspectives*. Springer, New York, pp. 85–108.
- Hurtado, C., Domínguez, C., Pérez-Babace, L., Cañameras, N., Comas, J., Bayon, J.M., 2016. Estimate of uptake and translocation of emerging organic contaminants from irrigation water concentration in lettuce grown under controlled conditions. *J. Hazard. Mater.*, 305, 139–148. <https://doi.org/10.1016/j.jhazmat.2015.11.039>.
- Klement, A., Kodešová, R., Bauerová, M., Golovko, O., Kočárek, M., Fér, M., Koba, O., Nikodem, A., Grabic, R., 2018. Sorption of citalopram, irbesartan and fexofenadine in soils: Estimation of sorption coefficients from soil properties. *Chemosphere*, 195, 615–623. <https://doi.org/10.1016/j.chemosphere.2017.12.098>.
- Koba, O., Golovko, O., Kodešová, R., Klement, A., Grabic, R., 2016. Transformation of atenolol, metoprolol, and carbamazepine in soils: The identification, quantification, and stability of the transformation products and further implications for the environment. *Environ. Pollut.*, 218, 574–585. <https://doi.org/10.1016/j.envpol.2016.07.041>.
- Koba, O., Golovko, O., Kodešová, R., Fér, M., Grabic, R., 2017. Antibiotics degradation in soil: A case of clindamycin, trimethoprim, sulfamethoxazole and their transformation products. *Environ. Pollut.*, 220, 1251–1263. <https://doi.org/10.1016/j.envpol.2016.11.007>.
- Kočárek, M., Kodešová R., Vondráčková, L., Golovko, O., Fér, M., Klement, A., Nikodem, A., Jakšík, O., Grabic, R., 2016. Simultaneous sorption of four ionizable pharmaceuticals in different horizons of three soil types. *Environ. Pollut.*, 218, 563–573. <https://doi.org/10.1016/j.envpol.2016.07.039>.
- Kodešová, R., Grabic, R., Kočárek, M., Klement, A., Golovko, O., Fér, M., Nikodem, A., Jakšík, O., 2015. Pharmaceuticals' sorptions relative to properties of thirteen different soils. *Sci. Total Environ.*, 511, 435–443. <https://doi.org/10.1016/j.scitotenv.2014.12.088>.
- Kodešová, R., Kočárek, M., Klement, A., Golovko, O., Koba, O., Fér, M., Nikodem, A., Vondráčková, L., Jakšík, O., Grabic R., 2016. An analysis of the dissipation of pharmaceuticals under thirteen different soil conditions. *Sci. Total Environ.*, 544, 369–381. <https://doi.org/10.1016/j.scitotenv.2015.11.085>.
- Kodešová, R., Klement, A., Golovko, O., Fér, M., Nikodem, A., Kočárek, M., Grabic, R., 2019a. Root uptake of atenolol, sulfamethoxazole and carbamazepine, and their transformation in three soils and four plants. *Environ. Sci. Pollut. Res.*, 26, 10, 9876–9891. <https://doi.org/10.1007/s11356-019-04333-9>.
- Kodešová, R., Klement, A., Golovko, O., Fér, M., Kočárek, M., Nikodem, A., Grabic, R., 2019b. Soil influences on uptake and transfer of pharmaceuticals from sewage sludge amended soils to spinach. *J. Environ. Manage.*, 250, 109407. <https://doi.org/10.1016/j.jenvman.2019.109407>.
- Kumar, K., Gupta, S.C., 2016. A Framework to predict uptake of trace organic compounds by plants. *J. Environ. Qual.*, 45, 2, 555–564. <https://doi.org/10.2134/jeq2015.06.0261>.
- Li, Y., Chuang, Y.H., Sallach, J.B., Zhang, W., Boyd, S.A., Li, H., 2018. Potential metabolism of pharmaceuticals in radish: Comparison of in vivo and in vitro exposure. *Environ. Pollut.*, 242, 962–969. <https://doi.org/10.1016/j.envpol.2018.07.060>.
- Li, Y., Chiou, C.T., Li, H., Schnoor, J.L., 2019a. Improved prediction of the bioconcentration factors of organic contaminants from soils into plant/crop roots by related physico-chemical parameters. *Environ. Int.*, 126, 46–53. <https://doi.org/10.1016/j.envint.2019.02.020>.
- Li, Y., Sallach, J.B., Zhang, W., Boyd, S.A., Li, H., 2019b. Insight into the distribution of pharmaceuticals in soil-water-plant systems. *Water Res.*, 152, 38–46. <https://doi.org/10.1016/j.watres.2018.12.039>.

- Loos, R., Locoro, G., Comero, S., Contini, S., Schwesig, D., Werres, F., Balsaa, P., Gans, O., Weiss, S., Blaha, L., Bolchi, M., Gawlik, B.M., 2010. Pan-European survey on the occurrence of selected polar organic persistent pollutants in ground water. *Water Res.*, 44, 4115–4126. <https://doi.org/10.1016/j.watres.2010.05.032>.
- Loos, R., Carvalho, R., António, D.C., Comero, S., Locoro, G., Tavazzi, S., Paracchini, B., Ghiani, M., Lettieri, T., Blaha, L., Jarosova, B., Voorspoels, S., Servaes, K., Haglund, P., Fick, J., Lindberg, R.H., Schwesig, D., Gawlik, B.M., 2013. EU-wide monitoring survey on emerging polar organic contaminants in wastewater treatment plant effluents. *Water Res.*, 47, 6475–6487. <https://doi.org/10.1016/j.watres.2013.08.024>.
- Malchi, T., Maor, Y., Tadmor, G., Shenker, M., Chefetz, B., 2014. Irrigation of root vegetables with treated wastewater: Evaluating uptake of pharmaceuticals and the associated human health risks. *Environ. Sci. Technol.*, 48, 16, 9325–9333. <https://doi.org/10.1021/es5017894>.
- Montemurro, N., Postigo, C., Lonigro, A., Perez, S., Barceló, D., 2017. Development and validation of an analytical method based on liquid chromatography–tandem mass spectrometry detection for the simultaneous determination of 13 relevant wastewater-derived contaminants in lettuce. *Anal. Bioanal. Chem.*, 409, 5375–5387. <https://doi.org/10.1007/s00216-017-0363-1>.
- Mordechay, E.B., Tarchitzky, J., Chen, Y., Shenker, M., Chefetz, B., 2018. Composted biosolids and treated wastewater as sources of pharmaceuticals and personal care products for plant uptake: A case study with carbamazepine. *Environ. Pollut.*, 232, 164–172. <https://doi.org/10.1016/j.envpol.2017.09.029>.
- Mullen, R.A., Wigginton, K.R., Noe-Hays, A., Nace, K., Love, N.G., Bott, C.B., Aga, D.S., 2017. Optimizing extraction and analysis of pharmaceuticals in human urine, struvite, food crops, soil, and lysimeter water by liquid chromatography–tandem mass spectrometry. *Anal. Methods*, 9, 5952–5962. <https://doi.org/10.1039/C7AY01801K>.
- Paltiel, O., Fedorova, G., Tadmor, G., Kleinstern, G., Maor, Y., Chefetz, B., 2016. Human exposure to wastewater-derived pharmaceuticals in fresh produce: A randomized controlled trial focusing on carbamazepine. *Environ. Sci. Technol.*, 50, 4476–4482. <https://doi.org/10.1021/acs.est.5b06256>.
- Riemenschneider, C., Seiwert, B., Moeder, M., Schwarz, D., Reemtsma, T., 2017. Extensive transformation of the pharmaceutical carbamazepine following uptake into intact tomato plants. *Environ. Sci. Technol.*, 51, 11, 6100–6109. <https://doi.org/10.1021/acs.est.6b06485>.
- Schaffer, M., Licha, T., 2015. A framework for assessing the retardation of organic molecules in groundwater: implications of the species distribution for the sorption influenced transport. *Sci. Total Environ.*, 524–525, 187–194. <https://doi.org/10.1016/j.scitotenv.2015.04.006>.
- Semerjian, L., Shanableh, A., Semreenc, M.H., Samarai, M., 2018. Human health risk assessment of pharmaceuticals in treated wastewater reused for non-potable applications in Sharjah, United Arab Emirates. *Environ. Int.*, 121, 325–331. <https://doi.org/10.1016/j.envint.2018.08.048>.
- Shenker, M., Harush, D., Ben-Ari, J., Chefetz, B., 2011. Uptake of carbamazepine by cucumber plants – A case study related to irrigation with reclaimed wastewater. *Chemosphere*, 82, 905–910. <https://doi.org/10.1016/j.chemosphere.2010.10.052>.
- Thiele-Bruhn, S., 2003. Pharmaceutical antibiotic compounds, in soils - a review. *J. Plant Nutr. Soil Sci.*, 166, 145–167. <https://doi.org/10.1002/jpln.200390023>.
- van Genchten, M.Th., 1987. A numerical model for water and solute movement in and below the root zone. Research Report No 121, U.S. Salinity laboratory, USDA, ARS, Riverside, California.
- Verlicchi, P., Zambello, E., 2015. Pharmaceuticals and personal care products in untreated and treated sewage sludge: occurrence and environmental risk in the case of application on soil - A critical review. *Sci. Total Environ.*, 538, 750–767. <https://doi.org/10.1016/j.scitotenv.2015.08.108>.
- Williams, E.S., Brooks, B.W., 2012. Human health risk assessment of pharmaceuticals in the environment: existing practice, uncertainty, and future directions. In: Brooks, B.W., Huggett, D.B. (Eds.): *Human Pharmaceuticals in the Environment: Current and Future Perspectives*. Springer, New York, pp. 167–224.
- Winker, M., Clements, J., Reich, M., Gulyas, H., Otterpohl, R., 2010. Ryegrass uptake of carbamazepine and ibuprofen applied by urine fertilization. *Sci. Total Environ.*, 408, 1902–1908. <https://doi.org/10.1016/j.scitotenv.2010.01.028>.
- Wu, X., Ernst, F., Conkle, J.L., Gan, J., 2013. Comparative uptake and translocation of pharmaceutical and personal care products (PPCPs) by common vegetables. *Environ. Int.*, 60, 15–22. <https://doi.org/10.1016/j.envint.2013.07.015>.
- Wu, X., Fu, Q., Gan, J., 2016. Metabolism of pharmaceutical and personal care products by carrot cell cultures. *Environ. Pollut.*, 211, 141–147. <https://doi.org/10.1016/j.envpol.2015.12.050>.

Received 19 August 2019
Accepted 10 January 2020

Impact of secondary succession in abandoned fields on some properties of acidic sandy soils

Ľubomír Lichner^{1*}, Massimo Iovino², Peter Šurda¹, Viliam Nagy¹, Anton Zvala¹, Jozef Kollár³, Jozef Pecho⁴, Vladimír Píš⁵, Nasrollah Sepehrnia⁶, Renáta Sándor⁷

¹ Institute of Hydrology, Slovak Academy of Sciences, Dúbravská cesta 9, 84104 Bratislava, Slovakia.

² Dipartimento di Scienze Agrarie, Alimentari e Forestali, Università degli Studi di Palermo, Viale delle Scienze, Ed. 4 Ingr. E, 90128 Palermo, Italy.

³ Institute of Landscape Ecology, Slovak Academy of Sciences, Štefánikova 3, 81499 Bratislava, Slovakia.

⁴ Slovak Hydrometeorological Institute, Jeséniova 17, 833 15 Bratislava, Slovakia.

⁵ Soil Science and Conservation Research Institute, Trenčianska 55, 82109 Bratislava, Slovakia.

⁶ Institute of Soil Science, Leibniz Universität Hannover, Herrenhäuser Str. 2, D-30419 Hannover, Germany.

⁷ Agricultural Institute, Centre for Agricultural Research, Brunszvik u.2, 2462 Martonvásár, Hungary.

* Corresponding author. E-mail: lichner@uh.savba.sk

Abstract: Abandonment of agricultural lands in recent decades is occurring mainly in Europe, North America and Oceania, and changing the fate of landscapes as the ecosystem recovers during fallow stage. The objective of this study was to find the impact of secondary succession in abandoned fields on some parameters of acidic sandy soils in the Borská nížina lowland (southwestern Slovakia). We investigated soil chemical (pH and soil organic carbon content), hydrophysical (water sorptivity, and hydraulic conductivity), and water repellency (water drop penetration time, water repellency cessation time, repellency index, and modified repellency index) parameters, as well as the ethanol sorptivity of the studied soils. Both the hydrophysical and chemical parameters decreased significantly during abandonment of the three investigated agricultural fields. On the other hand, the water repellency parameters increased significantly, but the ethanol sorptivity did not change during abandonment. As the ethanol sorptivity depends mainly on soil pore size, the last finding could mean that the pore size of acidic sandy soils did not change during succession.

Keywords: Water repellency; Acidic sandy soil; Land abandonment; Secondary succession; Soil properties.

INTRODUCTION

Farmland abandonment in recent decades (with about 210 million ha abandoned in 1990 (cf. Fig. 1 in Cramer et al., 2008)) is occurring mainly in Europe, North America and Oceania, with the most drastic decrease in agricultural lands (by about a third) seen in Europe (cf. Panel 1a in Queiroz et al., 2014). Land abandonment is a type of land use transformation that potentially causes the recovery of ecosystems (Cerdà et al., 2018). Passive revegetation in permanently abandoned arable land (called secondary succession) is characterized by the replacement of arable plant species by vegetation that disperse from surrounding habitats and will be subsequently established (Cseceserits et al., 2011). Such secondary succession initially starts with annual or biannual plants, is then followed by perennial forbs, grasses and shrubs, and finally under usual Central European conditions ending up in a forest (climax stage).

Farmland abandonment represents a significant land use change from cropping to a complex of plant successions. Throughout most of Europe, vegetation on abandoned farmland has evolved into dense forest or shrub. The expansion of vegetation explains, in part, the perceived decline in water resources, reductions in soil loss and sediment delivery, and the progressive improvement of soil characteristics (García-Ruiz and Lana-Renault, 2011).

Vegetation change can also induce soil water repellency (SWR), which parameters are influenced by soil temperature (Novák et al., 2009), moisture (Leelamanie and Nishiwaki, 2019; Oostindie et al., 2017), texture (Benito et al., 2019), pH (Diehl et al., 2010), soil organic carbon (SOC) and clay (mainly

kaolinite) content (Lichner et al., 2002). SWR may affect soil properties with depth (Orfánus et al., 2016; Sepehrnia et al., 2017) and time (Orfánus et al., 2014; Moret-Fernandez et al., 2019), and has positive effects on the stability of soil aggregates (Fér et al., 2016). Soil compaction may reduce SWR mainly as a consequence of decreased surface roughness (Bryant et al., 2007), but the hydrophobic conditions are readily restored a few days after removal of compaction load. Soil water repellency can be alleviated by addition of lime (Roper, 2005), kaolinite clay (Lichner et al., 2002; McKissock et al., 2000), and wax degrading bacteria (Roper, 2006). Naveed et al. (2019) found that the large impact of plant exudates and mucilages on water retention characteristics could be explained by differences in surface tension, contact angle and viscosity between exudates and mucilages of different origin. These properties may be driven by the relative amounts of organic acids and sugars (free and polysaccharide derived) in the exudates and mucilages. Guo et al. (2016) and Nik et al. (2015) also found the chemical composition of SOC changes during vegetation evolution.

Primary succession was found to increase SWR parameters and SOC content in acidic sandy soils in the Borská nížina lowland, Slovakia (Lichner et al., 2018), however there is a lack of knowledge in terms of secondary succession. The objective of this research was thus to estimate the effects of secondary succession during 28 years lasting abandonment of agricultural fields on chemical (pH and SOC content), hydrophysical (water sorptivity and hydraulic conductivity), and water repellency parameters (water drop penetration time, water repellency cessation time, repellency index, and modified repellency index),

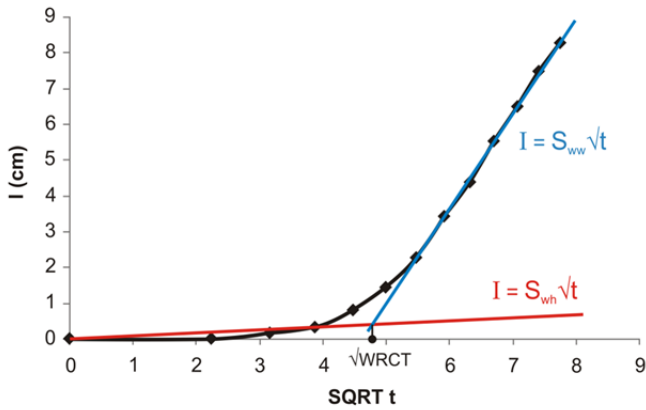


Fig. 1. The hockey-stick-like relationship of the cumulative infiltration of water (I) against the square root of time (SQRT t) for a sandy soil. The water sorptivity S_{wr} (–2 cm) for water-repellent state of soil and the water sorptivity S_{wv} (–2 cm) for nearly wettable state of soil were estimated, respectively, from the two different slopes of the relationship. The water repellency cessation time (WRCT) was estimated from the point of intersection of two straight lines, representing the $I = f(\text{SQRT } t)$ relationships for water-repellent and nearly wettable states of the soil.

as well as ethanol sorptivity of the top layer of three acidic sandy soils in the Borská nížina lowland, Slovakia. We hypothesize that the soil chemical and hydrophysical parameters will decrease, while the soil water repellency parameters will increase with the duration of abandonment.

MATERIAL AND METHODS

Study sites

The experimental sites S1, S2 are located at Sekule village (48°36'58.2'' N, 16°59'39.0'' E), while the experimental site S3 is placed at Studienka village (48°31'49.3'' N, 17°08'34.5'' E) in the Borská nížina lowland (southwestern Slovakia). The closest distance between the sites in Sekule and Studienka is about 12 km. According to the Köppen-Geiger climate classification, the region has temperate climate without dry season, warm summer (Cfb) (Kottek et al., 2006). Mean annual precipitation is about 550 mm, which is mainly summer-dominant. Elevation is 158 m a.s.l. at Sekule and 299 m a.s.l. at Studienka. Site S1 was a cultivated agricultural area planted with barley (*Hordeum vulgare* L.) in 2017. Site S2, abandoned for 12 years, is an early succession stage dominated by psammophilous grass *Corynephorus canescens* (L.) P. Beauv. with an admixture of other psammophytes and sand-tolerant weeds, such as *Bromus tectorum* L., *Cerastium semidecandrum* L., *Acetosella vulgaris* Fourr., *Anthemis ruthenica* M. Bieb., *Conyza canadensis* (L.) Cronquist, *Filago arvensis* L., *Myosotis stricta* Link ex Roem. et Schult., *Setaria pumila* (Poir.) Roem. et Schult., *Spergula morisonii* Boreau, *Trifolium arvense* L., *Veronica dillenii* Crantz, *Chondrilla juncea* L., and *Crepis* sp. Site S3 is a former arable land abandoned for 28 years. It is covered by synanthropized grassland dominated by *Festuca rupicola* Heuff. and *Chondrilla juncea* L., which are accompanied by admixture of psammophilous species (e.g. *Corynephorus canescens* (L.) P. Beauv., *Jasione montana* L., *Acetosella vulgaris* Fourr.) and sand-tolerant weeds (e. g. *Calamagrostis epigejos* (L.) Roth, *Setaria pumila* (Poir.) Roem. et Schult., *Conyza canadensis* (L.) Cronquist). The soils of the Sekule and Studienka sites are classified as Arenosol (WRB, 2014) and have sandy texture (Soil Survey Division Staff, 1993).

Methods

Laboratory methods

Basic soil properties were determined on disturbed samples with two replicates in the ISO Certified Laboratory of the Soil Science and Protection Research Institute in Bratislava. Particle size distribution was determined by sieving and sedimentation according to ISO 11277 (2009), pH(KCl) and pH(H₂O) were measured according to ISO 10390 (2005), SOC content was determined by oxidation with K₂Cr₂O₇-H₂SO₄ and titration of non-reduced dichromate according to ISO 10694 (1995), and carbonate content was determined from the volume of CO₂, produced during the decomposition of carbonates with about 10% hydrochloric acid, according to ISO 10693 (1995). The disturbed soil samples were taken randomly within an area of 25 m² in the surface (0–5 cm) layer at S1 site on 2 August 2018, at S2 site on 30–31 July 2018, and at S3 site on 9 October 2018.

Field methods

All the measurements of soil hydrophysical and SWR parameters were carried out on the surface of the studied soils during the hot and dry spell and the number of their replicates is presented in Table 2. The above-mentioned parameters were measured and the disturbed soil samples for laboratory determination of physical and chemical properties were taken from the top (0–5 cm) layer on 2 August 2018 (Site S1), 30–31 July 2018 (Site S2), and 9 October 2018 (Site S3). The places for the infiltration runs were chosen in the neighbourhood of each vegetal species and the surface to put the infiltrometers was flattened.

The volumetric water content, w (% vol), of the superficial (0–5 cm) soil layer was measured with a moisture meter type HH2 and soil moisture sensor SM200 (Delta-T Devices Ltd, Cambridge, UK).

Field water and ethanol infiltration measurements were performed with a minidisk infiltrometer (MDI) (Decagon, 2012) under a negative tension $h_0 = -2$ cm (Alagna et al. 2017, 2019). The cumulative infiltration I was calculated based on the Philip infiltration equation:

$$I = C_1 t^{1/2} + C_2 t + C_3 t^{3/2} + \dots + C_m t^{m/2} + \dots \quad (1)$$

where C_1, C_2, C_3, \dots , and C_m are coefficients, and t is time.

The sorptivity, S (–2 cm), was estimated from the first term of the Philip infiltration equation ($I = C_1 t^{1/2}$) during early-time infiltration of water and ethanol (Clothier et al., 2000):

$$S(-2 \text{ cm}) = I / t^{0.5} \quad (2)$$

Duration of early-time infiltration is 60–180 s for a wettable (WDPT = 0–5 s) and slightly repellent (WDPT = 5–60 s) soil (Hallett, 2008), or it is equal to the time of passing the first five bubbles (with the total volume of about 1 mL) through MDI (Time to First Five Bubbles, TFFB, in Beatty and Smith, 2014) for strongly (WDPT = 60–600 s), severely (WDPT = 600–3600 s), and extremely (WDPT > 3600 s) water repellent soils. During this time the process is dominated by the capillarity and the other terms of the Philip infiltration equation can be neglected.

Equation (2) was used to calculate both the water sorptivity (S_w (–2 cm)) and ethanol sorptivity (S_e (–2 cm)) from the cumulative infiltration vs. time relationships taken from the MDI measurements. It was found that S_w is not function of water source tension, but is function of initial soil water content. The highest value of S_w corresponded to the lowest soil water con-

tent, remaining practically constant in a large range of soil water content, and abruptly decreasing near saturation toward zero (Villarreal et al., 2019). It should be mentioned that the water sorptivity depends on SWR and soil pore size, and ethanol sorptivity depends mainly on soil pore size.

The repellency index RI (Decagon, 2012; Hallett and Young, 1999; Lichner et al., 2007)

$$RI = 1.95 S_e(-2 \text{ cm}) / S_w(-2 \text{ cm}) \quad (3)$$

was estimated from the combination of all the ethanol and water sorptivities, i.e., $m \times n$ values of RI were calculated from m values of $S_w(-2 \text{ cm})$ and n values of $S_e(-2 \text{ cm})$ (Pekárová et al., 2015). The RI values correlated closely with water drop penetration time (WDPT), which was used to develop a classification of RI by Iovino et al. (2018).

In the second method of estimating the RI, the water sorptivity $S_{wh}(-2 \text{ cm})$ for water-repellent state of soil and the water sorptivity $S_{wr}(-2 \text{ cm})$ for nearly wettable state of soil were estimated, respectively, from the slopes of the initial and subsequent stages of hockey-stick-like relationship (Fig. 1), and used to calculate a modified repellency index RI_m (Sepehrnia et al., 2016):

$$RI_m = S_{wr}(-2 \text{ cm}) / S_{wh}(-2 \text{ cm}) \quad (4)$$

The persistence of SWR was assessed by both the WDPT and water repellency cessation time, WRCT (Lichner et al., 2013). The WDPT test involves placing a $50 \pm 5 \mu\text{L}$ water drop from a standard medicine dropper or pipette on the soil surface and recording the time of its complete penetration. A standard droplet release height of approximately 10 mm above the soil surface was used to minimize the cratering effect on the soil surface (Doerr, 1998; Tinebra et al., 2019). The following classes of the persistence of SWR were distinguished: wettable or non-water-repellent soil (WDPT < 5 s), slightly (WDPT = 5–60 s), strongly (WDPT = 60–600 s), severely (WDPT = 600–3600 s), and extremely (WDPT > 3600 s) water repellent soil (Bisdorn et al., 1993). The values of WRCT were estimated from the intersection of two straight lines, representing the two stages of infiltration (Fig. 1).

Field water infiltration measurements with the MDI under a negative tension $h_0 = -2 \text{ cm}$ were used to estimate the hydraulic conductivity $k(-2 \text{ cm})$. Zhang (1997) proposed to use the first two terms of the Philip infiltration equation to fit the cumulative infiltration vs. time relationship and estimate the hydraulic conductivity $k(-2 \text{ cm})$ from equation:

$$k(-2 \text{ cm}) = C_2 / A \quad (5)$$

where A is a dimensionless coefficient. Fitting of the two terms infiltration equation to cumulative infiltration data was performed through the linearization technique suggested by the Minidisk Infiltrometer User's Manual (Decagon, 2012). A value of $A = 1.73$, corresponding to sandy soil and suction $h_0 = -2 \text{ cm}$, was used to calculate the hydraulic conductivity $k(-2 \text{ cm})$. Given capillarity can be ignored at long times, estimation of k is expected to be more accurate as t increases (Zhang, 1997). The MDI experiments were therefore conducted until apparent steady state conditions were observed.

Statistical treatment

The statistical analysis to find differences between the parameters estimated in different sites was performed with NCSS 12 Statistical Software (2018), using single factor ANOVA and

Tukey's Honestly Significant Difference (HSD) post-hoc test ($p < 0.05$). The Tukey-Kramer method (also known as Tukey's HSD (Honest Significant Difference) method) uses the Studentized Range distribution to compute the adjustment to c_α . The Tukey-Kramer method achieves the exact alpha level (and simultaneous confidence level $(1 - \alpha)$) if the group sample sizes are equal and is conservative if the sample sizes are unequal. The Tukey-Kramer test is one of the most powerful all-pairs testing procedures and is widely used.

The Tukey-Kramer adjusted critical value for tests and simultaneous confidence intervals is

$$c_\alpha = \frac{q_{1-\alpha, k, v}}{\sqrt{2}} \quad (6)$$

where $q_{1-\alpha, k, v}$ is the $1 - \alpha$ quantile of the studentized range distribution.

RESULTS AND DISCUSSION

Basic soil-physical and chemical properties are presented in Table 1. A decrease in pH value of the studied soils from 6.55 to 4.50 was registered after 28-year lasting abandonment of agricultural fields in southwestern Slovakia. The great decrease in pH value in the studied abandoned fields is consistent with the findings of Zhao et al. (2014) during progressive succession of vegetation (grassland, shrubland, forest) occurring in karst sites in southwestern China, as well as Bautista-Cruz and del Castillo (2005) during the development of second-growth forest after abandonment of agricultural fields in tropical montane cloud forest areas in southern Mexico.

The significant decrease in pH value during abandonment was accompanied with the significant decrease in SOC content (Table 1) and significant increase in SWR parameters (Table 2), indicating that the composition of organic matter and its overall effectiveness to influence the wetting properties of soil particles is more important than the total amount of soil organic carbon (Ellerbrock et al., 2005). It should be mentioned that the SOC content in the top layer of acidic sandy soil under grass cover in Studienka is about 2-times less than the SOC content in the top layer of acidic silt loam soil under grass cover in Hněvčevy, the Czech Republic (0.80% vs. 1.74%) (Kodešová et al., 2011). Substantially higher clay and silt content in the top layer of Hněvčevy soil in comparison with that of Studienka soil (87.72% vs. 3.52%) resulted in better ability to accumulate organic matter.

Statistical characteristics of soil hydrophysical parameters ($k(-2 \text{ cm})$ and $S_w(-2 \text{ cm})$), ethanol sorptivity, $S_e(-2 \text{ cm})$, and soil water repellency parameters (WDPT, WRCT, RI, and RI_m) of the top layer of acidic sandy soils from the sites S1, S2 (Sekule, Slovakia), and S3 (Studienka, Slovakia) are presented in Table 2. As to the hydrophysical and chemical parameters, the mean value of $S_w(-2 \text{ cm})$ decreased about 2.8 times, $k(-2 \text{ cm})$ about 15.6 times, and SOC content about 2.3 times, while $S_e(-2 \text{ cm})$ did not change significantly after 28 years lasting abandonment of agricultural field with acidic sandy soil in the Borská nížina lowland, Slovakia. As the ethanol sorptivity depends mainly on soil pore size, the last finding could mean that the soil pore size of acidic sandy soil did not change during succession. Soil structure is poorly developed in sandy soils whereas soil compaction due to human activity was negligible, thus pore size distribution is mainly determined by particle size distribution that is a relatively stable soil property at this time scale (Table 1). The results of $S_w(-2 \text{ cm})$ ($0.679 \pm 0.469 \text{ mm s}^{-1/2}$) and $k(-2 \text{ cm})$ ($9.1 \pm 7.5 \mu\text{m s}^{-1}$) estimated in acidic

sandy soil at the 28 years abandoned agricultural field covered with grass created by secondary succession at Studienka are not significantly different from the results of $S_w(-2\text{ cm})$ ($1.14 \pm 0.677\text{ mm s}^{-1/2}$) and $k(-2\text{ cm})$ ($48.0 \pm 35.0\text{ }\mu\text{m s}^{-1}$) estimated in an acidic sandy soil under grass created by primary succession at Sekule (Šurda et al., 2015). It could mean that the values of hydraulic conductivity and water sorptivity of acidic sandy soil under grass do not depend on the type (primary or secondary) of succession resulting in the grass cover.

As to the soil water repellency parameters, the mean value of WDPT increased about 747 times, WRCT about 229 times, RI about 14 times, and RI_m about 2.5 times after 28 years lasting abandonment of agricultural field with acidic sandy soil in the Borská nížina lowland, Slovakia. The increase in WDPT is consistent with the findings of Hewelke (2019) who registered an increase in WDPT after excluding albic Podzols from agricultural production. The results of WDPT ($949 \pm 568\text{ s}$) and RI (35.0 ± 58.7) estimated in acidic sandy soil at the 28 years abandoned agricultural field covered with grass created by secondary succession at Studienka are, respectively, smaller

and higher than the results of WDPT ($1723 \pm 1610\text{ s}$) and RI (4.27 ± 2.05) estimated in acidic sandy soil under grass created by primary succession at Sekule (Šurda et al., 2015).

Dependence of soil parameters on the duration of field abandonment for the southwestern Slovakia sites is presented on Fig. 2. It can be seen that pH, $S_w(-2\text{ cm})$, and $k(-2\text{ cm})$ decreased continuously, WDPT, WRCT, RI, and RI_m increased continuously, while $S_e(-2\text{ cm})$ did not change significantly with the duration of field abandonment. A similar course of soil parameters was observed during the primary succession in acidic sandy soils in Sekule and Mehlinger Heide, Germany (Lichner et al., 2018). Rather than the continuous increase or decrease in soil parameters with duration of field abandonment, a “zigzag” pattern of all but one ($S_e(-2\text{ cm})$) soil parameter relationships was registered during the 44 years lasting abandonment of agricultural field with alkaline sandy soils in Csólyospálos, Hungary (Lichner et al., 2018). This can be explained by the different vegetation cover and the resulting changes in the vegetation uptake of fertilizers and production of root exudates (cf. Naveed et al., 2019) and thatch.

Table 1. Physical and chemical properties of the top (0–5 cm) soils taken from the experimental sites S1, S2, and S3. The results are presented in the form: arithmetic mean \pm standard deviation. (SOC – soil organic carbon).

Attribute	S1	S2	S3
Clay (%)	3.663 ± 0.936	2.126 ± 0.202	2.750 ± 0.607
Silt 1–10 μm (%)	5.232 ± 0.483	1.886 ± 0.226	0.100 ± 0.017
Silt 10–50 μm (%)	6.641 ± 0.934	1.605 ± 0.424	0.673 ± 0.085
Sand 50–250 μm (%)	25.952 ± 4.121	20.608 ± 3.511	26.607 ± 2.052
Sand 0.25–2 mm (%)	58.516 ± 6.479	73.775 ± 4.364	69.870 ± 2.761
CaCO ₃ (%)	<0.05	0.10 ± 0.03	<0.05
SOC (%)	$1.80^a \pm 0.11$	$1.06^b \pm 0.04$	$0.80^b \pm 0.06$
pH (H ₂ O)	$6.55^a \pm 0.06$	$5.60^b \pm 0.03$	$4.50^c \pm 0.03$
pH (KCl)	$6.25^a \pm 0.03$	$4.20^b \pm 0.03$	$4.16^b \pm 0.01$

Properties denoted with different letters are significantly different on significance level 0.05.

Table 2. Statistical characteristics of soil hydrophysical parameters (namely the hydraulic conductivity, $k(-2\text{ cm})$, water sorptivity, $S_w(-2\text{ cm})$, and ethanol sorptivity, $S_e(-2\text{ cm})$) and soil water repellency parameters (namely the water drop penetration time, WDPT, water repellency cessation time, WRCT, repellency index, RI, and modified repellency index, RI_m) of the top layer of acidic soils from the sites S1, S2, and S3.

Site	Attribute	Minimum	Maximum	Median	Mean	Standard deviation	Number of replicates
S1	w (% vol)	<0.1	<0.1	<0.1	<0.1	<0.1	10
	$k(-2\text{ cm})$ ($\mu\text{m s}^{-1}$)	6.6	228	158	142^a	66	10
	$S_w(-2\text{ cm})$ ($\text{mm s}^{-1/2}$)	1.31	2.42	1.94	1.89^a	0.35	10
	$S_e(-2\text{ cm})$ ($\text{mm s}^{-1/2}$)	2.10	2.63	2.29	2.33^a	0.25	4
	WDPT (s)	1	2	1	1.27^a	0.47	11
	WRCT (s)	5.10	8.77	6.45	6.68^a	1.45	10
	RI (–)	1.69	3.91	2.32	2.49^a	0.57	40
	RI_m (–)	2.54	5.91	5.19	4.59^a	1.27	10
S2	w (% vol)	<0.1	<0.1	<0.1	<0.1	<0.1	10
	$k(-2\text{ cm})$ ($\mu\text{m s}^{-1}$)	12.7	69.4	46.6	42.3^b	24.4	10
	$S_w(-2\text{ cm})$ ($\text{mm s}^{-1/2}$)	0.42	1.48	1.08	1.03^b	0.38	10
	$S_e(-2\text{ cm})$ ($\text{mm s}^{-1/2}$)	1.49	2.39	2.09	2.01^a	0.40	4
	WDPT (s)	2	1520	20	179^a	448	11
	WRCT (s)	8.8	99.6	33.4	36.5^a	25.5	10
	RI (–)	2.0	11.1	3.64	4.59^a	2.54	40
	RI_m (–)	3.5	13.4	4.82	$5.62^{a,b}$	2.96	10
S3	w (% vol)	<0.1	3.0	0.45	0.79	1.06	10
	$k(-2\text{ cm})$ ($\mu\text{m s}^{-1}$)	0	19.7	9.0	9.1^b	7.5	10
	$S_w(-2\text{ cm})$ ($\text{mm s}^{-1/2}$)	0.02	1.21	0.83	0.68^b	0.47	10
	$S_e(-2\text{ cm})$ ($\text{mm s}^{-1/2}$)	1.93	2.39	2.01	2.08^a	0.21	4
	WDPT (s)	20	1960	980	949^b	568	15
	WRCT (s)	61.9	4172	1065	1572^b	1463	9
	RI (–)	3.1	221	5.1	35.0^b	58.7	40
	RI_m (–)	3.6	30.8	6.6	11.4^b	9.5	9

Properties denoted with different letters are significantly different on significance level 0.05.

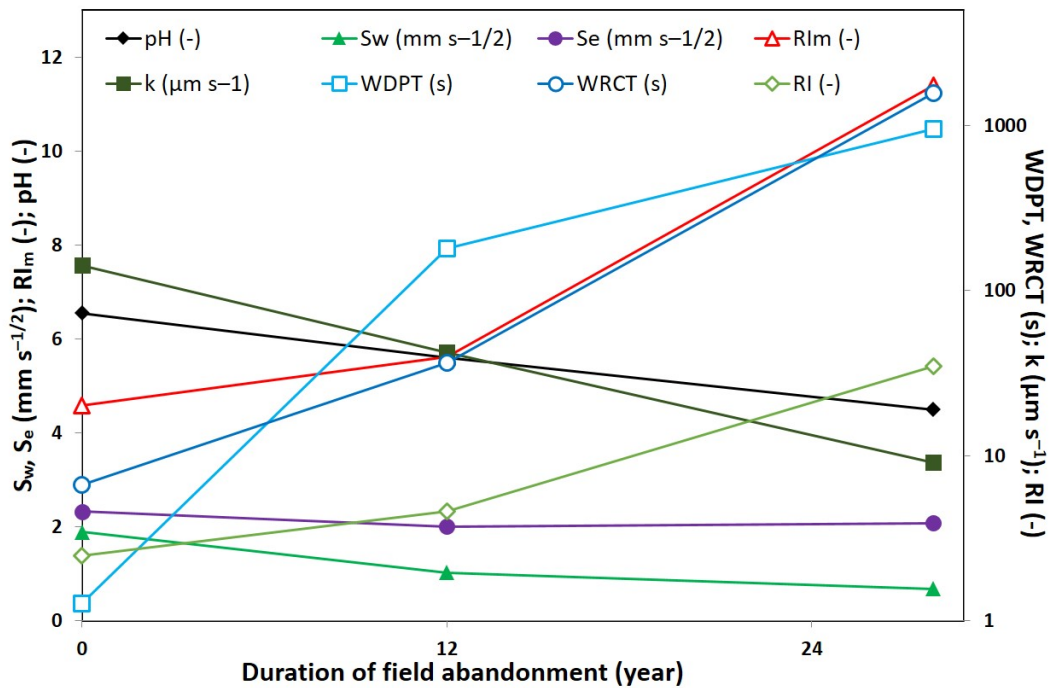


Fig. 2. Soil water repellency parameters (water drop penetration time, WDPT, water repellency cessation time, WRCT, repellency index, RI, and modified repellency index, RI_m) and soil hydrophysical parameters (hydraulic conductivity, $k(-2\text{ cm})$, water sorptivity, $S_w(-2\text{ cm})$, and ethanol sorptivity, $S_e(-2\text{ cm})$) of the top layer of acidic soils vs. duration of field abandonment relationships for the southwestern Slovakia sites.

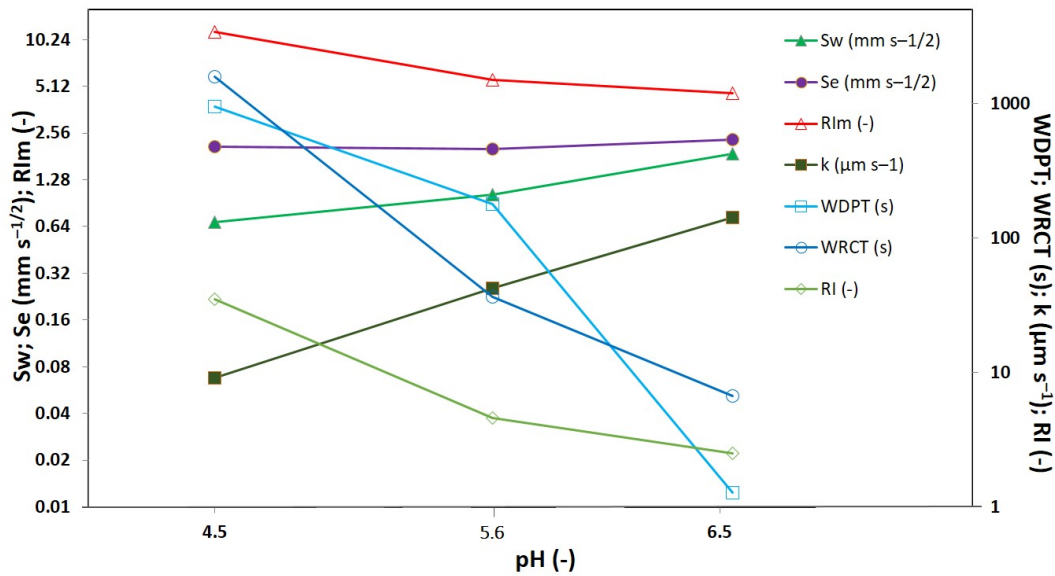


Fig. 3. Soil water repellency parameters (water drop penetration time, WDPT, water repellency cessation time, WRCT, repellency index, RI, and modified repellency index, RI_m) and soil hydrophysical parameters (hydraulic conductivity, $k(-2\text{ cm})$, water sorptivity, $S_w(-2\text{ cm})$, and ethanol sorptivity, $S_e(-2\text{ cm})$) of the top layer of acidic soils vs. pH relationships for the southwestern Slovakia sites.

Dependence of soil parameters on pH for the southwestern Slovakia sites is presented on Fig. 3. It can be seen that $S_w(-2\text{ cm})$, and $k(-2\text{ cm})$ increased continuously, WDPT, WRCT, RI, and RI_m decreased continuously, while $S_e(-2\text{ cm})$ did not change significantly with pH. The decrease in WDPT with an increase in pH value in the studied abandoned fields is consistent with the findings of Diehl et al. (2010).

CONCLUSION

Abandonment of agricultural fields with acidic sandy soil in the Borská nížina lowland, Slovakia, results in a significant decrease in the hydrophysical (water sorptivity and hydraulic conductivity) and chemical (pH and soil organic carbon content) parameters, significant increase in the water repellency

(water drop penetration time, water repellency cessation time, repellency index, and modified repellency index) parameters, but insignificant change in the ethanol sorptivity. As the ethanol sorptivity depends mainly on soil pore size, the last finding could mean that the soil pore size of acidic sandy soil did not change during succession.

Acknowledgements. The authors thank Prof. Kodešová and two anonymous reviewers for their wise comments and suggestions, which helped to improve the paper. This work was supported by the Slovak Scientific Grant Agency VEGA Project 2/0189/17, the Slovak Research and Development Agency Project APVV-15-0160, and the János Bolyai Research Scholarship of the Hungarian Academy of Sciences.

REFERENCES

- Alagna, V., Iovino, M., Bagarello, V., Mataix-Solera, J., Lichner, E., 2017. Application of minidisk infiltrometer to estimate water repellency in Mediterranean pine forest soils. *Journal of Hydrology and Hydromechanics*, 65, 254–263.
- Alagna, V., Iovino, M., Bagarello, V., Mataix-Solera, J., Lichner, L., 2019. Alternative analysis of transient infiltration experiment to estimate soil water repellency. *Hydrological Processes*, 33, 661–674.
- Bautista-Cruz, A., del Castillo, R.F., 2005. Soil changes during secondary succession in a tropical montane cloud forest area. *Soil Science Society of America Journal*, 69, 906–914.
- Beatty, S.M., Smith, J.E., 2014. Infiltration of water and ethanol solutions in water repellent post wildfire soils. *Journal of Hydrology*, 514, 233–248.
- Benito, E., Varela, E., Rodríguez-Alleres, M., 2019. Persistence of water repellency in coarse-textured soils under various types of forests in NW Spain. *Journal of Hydrology and Hydromechanics*, 67, 129–134.
- Bisdorn, E.B.A., Dekker, L.W., Schoute, J.F.T., 1993. Water repellency of sieve fractions from sandy soils and relationships with organic material and soil structure. *Geoderma*, 56, 105–118.
- Bryant, R., Doerr, S.H., Hunt, G., Conan, S., 2007. Effects of compaction on soil surface water repellency. *Soil Use and Management*, 23, 238–244.
- Cerdà, A., Rodrigo-Comino, J., Novara, A., Brevik, E.C., Vaezi, A.R., Pulido, M., Giménez-Morera, A., Keesstra, S.D., 2018. Long-term impact of rainfed agricultural land abandonment on soil erosion in the Western Mediterranean basin. *Progress in Physical Geography: Earth and Environment*, 42, 202–219.
- Clothier, B.E., Vogeler, I., Magesan, G.N., 2000. The breakdown of water repellency and solute transport through a hydrophobic soil. *Journal of Hydrology*, 231–232, 255–264.
- Cramer, V.A., Hobbs, R.J., Standish, R.J., 2008. What's new about old fields? Land abandonment and ecosystem assembly. *Trends in Ecology and Evolution*, 23, 104–112.
- Csecserits, A., Czucz, B., Halassy, M., Kröel-Dulay, G., Rédei, T., Szabó, R., Szitár, K., Török, K., 2011. Regeneration of sandy old-fields in the forest steppe region of Hungary. *Plant Biosystems*, 145, 715–729.
- Decagon, 2012. Mini Disk Infiltrometer – User's Manual. Version 10. Decagon Devices, Inc., Pullman.
- Diehl, D., Bayer, J.V., Woche, S.K., Bryant, R., Doerr, S.H., Schaumann, G.E., 2010. Reaction of soil water repellency to artificially induced changes in soil pH. *Geoderma*, 158, 375–384.
- Doerr, S.H., 1998. On standardizing the "Water Drop Penetration Time" and the "Molarity of an Ethanol Droplet" techniques to classify soil hydrophobicity: a case study using medium textured soils. *Earth Surface Processes and Landforms*, 23, 663–668.
- Ellerbrock, R.H., Gerke, H.H., Bachmann, J., Goebel, M.-O., 2005. Composition of organic matter fractions for explaining wettability of three forest soils. *Soil Science Society of America Journal*, 69, 57–66.
- Fér, M., Leue, M., Kodešová, R., Gerke, H.H., Ellerbrock, R.H., 2016. Droplet infiltration dynamics and soil wettability related to soil organic matter of soil aggregate coatings. *Journal of Hydrology and Hydromechanics*, 64, 111–120.
- García-Ruiz, J.M., Lana-Renault, N., 2011. Hydrological and erosive consequences of farmland abandonment in Europe, with special reference to the Mediterranean region – A review. *Agriculture, Ecosystems and Environment*, 140, 317–338.
- Guo, X.P., Meng, M.J., Zhang, J.C., Chen, H.Y.H., 2016. Vegetation change impacts on soil organic carbon chemical composition in subtropical forests. *Scientific Reports*, 6, 29607. DOI: 10.1038/srep29607.
- Hallett, P.D., 2008. A brief overview of the causes, impacts and amelioration of soil water repellency – a review. *Soil & Water Res.*, 3, Special Issue 1, S21–S29.
- Hallett, P.D., Young, I.M., 1999. Changes to water repellence of soil aggregates caused by substrate-induced microbial activity. *European Journal of Soil Science*, 50, 35–40.
- Hewelke, E., 2019. Influence of abandoning agricultural land use on hydrophysical properties of sandy soil. *Water*, 11, 525. DOI:10.3390/w11030525.
- Iovino, M., Pekárová, P., Hallett, P.D., Pekár, J., Lichner, E., Mataix-Solera, J., Alagna, V., Walsh, R., Raffan, A., Schacht, K., Rodný, M., 2018. Extent and persistence of soil water repellency induced by pines in different geographic regions. *Journal of Hydrology and Hydromechanics*, 66, 360–368.
- ISO 10390, 2005. Soil quality. Determination of pH. International Organization of Standardization, Geneva. (<https://www.iso.org/standard/40879.html>)
- ISO 10693, 1995. Soil quality. Determination of carbonate content. Volumetric method. International Organization of Standardization, Geneva. (<https://www.iso.org/standard/18781.html>)
- ISO 10694, 1995. Soil quality. Determination of organic and total carbon after dry combustion (elementary analysis). International Organization of Standardization, Geneva. (<https://www.iso.org/standard/18782.html>)
- ISO 11277, 2009. Soil quality. Determination of particle size distribution in mineral soil material. Method by sieving and sedimentation. International Organization of Standardization, Geneva. (<https://www.iso.org/standard/54151.html>)
- Kodešová, R., Jirků, V., Kodeš, V., Mühlhanslová, M., Nikodem, A., Žigová, A., 2011. Soil structure and soil hydraulic properties of Haplic Luvisol used as arable land and grassland. *Soil & Tillage Research*, 111, 154–161.
- Kottek, M., Grieser, J., Beck, C., Rudolf, B., Rubel, F., 2006. World map of the Köppen-Geiger climate classification updated. *Meteorologische Zeitschrift*, 15, 259–263.
- Leelamanie, D.A.L., Nishiwaki, J., 2019. Water repellency in Japanese coniferous forest soils as affected by drying temperature and moisture. *Biologia*, 74, 127–137.
- Lichner, L., Babejová, N., Dekker, L.W., 2002. Effects of kaolinite and drying temperature on the persistence of soil water repellency induced by humic acids. *Rostlinná Výroba*, 48, 203–207.

- Lichner, L., Hallett, P.D., Feeney, D., Ďugová, O., Šír, M., Tesář, M., 2007. Field measurement of the impact of hydrophobicity on soil water transport under different vegetation over time. *Biologia*, 62, 537–541.
- Lichner, L., Hallett, P.D., Drongová, Z., Czachor, H., Kovacik, L., Mataix-Solera, J., Homolák, M., 2013. Algae influence hydrophysical parameters of a sandy soil. *Catena*, 108, 58–68.
- Lichner, L., Felde, V.J.M.N.L., Büdel, B., Leue, M., Gerke, H.H., Ehlerbrock, R.H., Kollár, J., Rodný, M., Šurda, P., Fodor, N., Sándor, R., 2018. Effect of vegetation and its succession on water repellency in sandy soils. *Ecohydrology*, 11, Article Number: UNSP e1991.
- McKissock, I., Walker, E.L., Gilkes, R.J., Carter, D.J., 2000. The influence of clay type on reduction of water repellency by applied clays: a review of some West Australian work. *Journal of Hydrology*, 231–232, 323–332.
- Moret-Fernandez, D., Latorre, B., Giner, M.L., Ramos, J., Alados, C.L., Castellano, C., Lopez, M.V., Jimenez, J.J., Pueyo, Y., 2019. Estimation of the soil hydraulic properties from the transient infiltration curve measured on soils affected by water repellency. *Catena*, 178, 298–306.
- Naveed, M., Ahmed, M.A., Benard, P., Brown, L.K., George, T.S., Bengough, A.G., Roose, T., Koebnick, N., Hallett, P.D., 2019. Surface tension, rheology and hydrophobicity of rhizodeposits and seed mucilage influence soil water retention and hysteresis. *Plant and Soil*, 437, 65–81.
- NCSS 12 Statistical Software, 2018. NCSS, LLC. Kaysville, Utah, USA. ncss.com/software/ncss
- Nik, K.S., Nael, M., Assadian, G., Sinegani, A.A.S., Kha, S.J., 2015. Soil organic carbon fractions as influenced by vegetation type and land management: A case study in semiarid rangelands of Hamedan, Iran. *Eurasian Journal of Soil Science*, 4, 2, 76–81.
- Novák, V., Lichner, L., Zhang, B., Kňava, K., 2009. The impact of heating on the hydraulic properties of soils sampled under different plant cover. *Biologia*, 64, 483–486.
- Oostindie, K., Dekker, L.W., Wesseling, J.G., Geissen, V., Ritsema, C.J., 2017. Impacts of grass removal on wetting and actual water repellency in a sandy soil. *Journal of Hydrology and Hydromechanics*, 65, 88–98.
- Orfánus, T., Dlapa, P., Fodor, N., Rajkai, K., Sándor, R., Nováková, K., 2014. How severe and subcritical water repellency determines the seasonal infiltration in natural and cultivated sandy soils. *Soil and Tillage Research*, 135, 49–59.
- Orfánus, T., Stojkovicová, D., Rajkai, K., Czachor, H., Sándor, R., 2016. Spatial patterns of wetting characteristics in grassland sandy soil. *Journal of Hydrology and Hydromechanics*, 64, 167–175.
- Queiroz, C., Beilin, R., Folke, C., Lindborg, R., 2014. Farmland abandonment: threat or opportunity for biodiversity conservation? A global review. *Frontiers in Ecology and the Environment*, 12, 288–296.
- Pekárová, P., Pekár, J., Lichner, L., 2015. A new method for estimating soil water repellency index. *Biologia*, 70, 1450–1455.
- Roper, M.M., 2005. Managing soils to enhance the potential for bioremediation of water repellency. *Australian Journal of Soil Research*, 43, 803–810.
- Roper, M.M., 2006. Potential for remediation of water repellent soils by inoculation with wax-degrading bacteria in south-western Australia. *Biologia*, 61, S358–S362.
- Sepehrnia, N., Hajabbasi, M.A., Afyuni, M., Lichner, L., 2016. Extent and persistence of water repellency in two Iranian soils. *Biologia*, 71, 1137–1143.
- Sepehrnia, N., Hajabbasi, M.A., Afyuni, M., Lichner, L., 2017. Soil water repellency changes with depth and relationship to physical properties within wettable and repellent soil profiles. *Journal of Hydrology and Hydromechanics*, 65, 99–104.
- Soil Survey Division Staff, 1993. *Soil Survey Manual*. Soil Conservation Service. U.S. Department of Agriculture Handbook, 18 p.
- Šurda, P., Lichner, L., Nagy, V., Kollár, J., Iovino, M., Horel, Á., 2015. Effects of vegetation at different succession stages on soil properties and water flow in sandy soil. *Biologia*, 70, 1474–1479.
- Tinebra, I., Alagna, V., Iovino, M., Bagarello, V., 2019. Comparing different application procedures of the water drop penetration time test to assess soil water repellency in a fire affected Sicilian area. *Catena*, 177, 41–48.
- Villarreal, R., Lozano, L.A., Melani, E.M., Salazar, M.P., Otero, M.F., Soracco, C.G., 2019. Diffusivity and sorptivity determination at different soil water contents from horizontal infiltration. *Geoderma*, 338, 88–96.
- WRB, 2014. *World Reference Base for Soil Resources 2014*. World Soil Resources Reports No. 106. Rome, 192 p.
- Zhang, R., 1997. Determination of soil sorptivity and hydraulic conductivity from the disk infiltrometer. *Soil Science Society of America Journal*, 61, 1024–1030.
- Zhao, J., Li, S.P., He, X.Y., Liu, L., Wang, K.L., 2014. The soil biota composition along a progressive succession of secondary vegetation in a karst area. *PLoS ONE*, 9, 11, e112436.

Received 6 September 2019

Accepted 6 December 2019

Are coastal deserts necessarily dew deserts? An example from the Tabernas Desert

Giora J. Kidron^{1*}, Roberto Lázaro²

¹ Institute of Earth Sciences, The Hebrew University of Jerusalem, Givat Ram Campus, Jerusalem 91904, Israel.

² Estación Experimental de Zonas Áridas (CSIC), Carretera Sacramento, W/n, La Cañada de San Urbano, 04120 Almería, Spain.

* Corresponding author. Tel.: + 972-544-967-271. Fax: +972-2-566-2581. E-mail: kidron@mail.huji.ac.il

Abstract: Vapor condensation, whether due to dew or fog, may add a stable and important source of water to deserts. This was also extensively assessed in the Negev, regarded as a dew desert. Dew deserts necessitate a large reservoir of vapor, and are therefore confined to near oceans or seas. Yet, examples of such deserts are scarce. Here we try to assess whether the Tabernas Desert in SE Spain can be regarded as a dew desert, and may therefore facilitate the growth of certain organisms that otherwise would not survive the dry season. We analyze some of the abiotic conditions of four relatively dry months (June, July, August, September) in the Tabernas and Negev deserts (with the Negev taken as an example of a dew desert) during 2003–2012. The analysis showed substantially lower values of relative humidity (by 10–13%) in the Tabernas in comparison to the Negev, with RH $\geq 95\%$ being on average only 0.9–1.1 days a month in the Tabernas in comparison to 9.7–13.9 days in the Negev. Our findings imply that the Tabernas Desert cannot be regarded as a dew desert, suggesting that rain will be the main factor responsible for the food web chain in the Tabernas.

Keywords: Fog; Negev Desert; Relative humidity; Vapor condensation; Wind speed.

INTRODUCTION

In comparison to fog deserts, there are much less references in the literature to dew deserts, with the Negev being probably the most known dew desert (Kidron, 2019a). Yet, in a similar way to fog deserts (Büdel et al., 2009; Rundel et al., 1991; Schieferstein and Loris, 1992), dew deserts may have unique characteristics stemming from the additional contribution of a stable source of water.

Dew deserts like fog deserts may provide a stable source of water to different organisms during the dry season and may therefore enable the survival of variable organisms that otherwise would not have survived, or would have experienced substantially lower biomass in this harsh arid environment. Yet, no clear definition exists. Not having sufficient knowledge regarding the contribution of dew to variable organisms or having a reference organism which may attest to the contribution of dew leads us to seek an indirect definition. Here, we regard a desert as being a dew desert once it receives on average at least 8–12 dew events per month during the dry season and the annual dew amount is at least 10% of the total annual rain amount. Our definition does not include distillation, i.e., vapor condensation that stems from the wet ground and therefore, from a hydrological point of view, is not regarded as an additional source of water (Monteith, 1957). Here we assume that sufficient water supply by dew for 8–12 mornings per month, may facilitate the survival of certain organisms that otherwise would not survive under the dry and rainless months.

Our estimates are based on detailed photosynthetic measurements of the lichen *Ramalina maciformis* that were undertaken in the Negev during one year of measurements (1971/1972) by Kappen et al. (1979). According to these authors, the dewy dry season (July–October) is characterized by high RH fluctuation, which may also result in dewless days or a negative carbon (C) balance during a dewy day. Dewless days characterized ~20–25% of the days (~8 days per month). How-

ever, out of the dew events, approximately 30% of the days (~6 days per month) yielded a negative balance during which C loss following nocturnal respiration was higher than C gain during the day. Negative balance, which may result in organism starvation and death (Barker et al., 2005; Proctor et al., 2007) may stem from early evaporation of the dew (usually by pre-dawn winds), but also as a result of low amounts of dew that do not remain long enough during the daytime hours to compensate for the C loss during nocturnal respiration. Taking the Negev conditions as our model, it implies that at least eight days of dew per month which will result in positive C balance will be needed to compensate for the C loss during days with a negative C balance.

The calculations presented above reflect common RH fluctuations. Nevertheless, occasional heat spells may also occur. However, under such conditions, both daytime and nighttime RH is very low, too low to induce respiration. If we exclude these weather conditions (during which the lichens are likely not active), it is suggested that on average, at least 8–12 days of dew events per month are apparently required in order to guarantee a positive C balance. This amount of dew along with the prerequisite that the annual dew amount should reach at least 10% of the total amount of the annual rain is proposed herein as a requirement to meet the definition of a dew desert.

Extensive research on the dew regime and its contribution to the different organisms was carried out in the Negev. Similarly to fog deserts where high-biomass communities of lichens inhabit the fog-impacted zones of the desert (Büdel et al., 2009; Kidron, 2019b; Lange et al., 1994, 2006), dew in the Negev is seen responsible for a lush cover of lithic lichens (mainly crustose, which are closely attached to the substratum, but also foliose, which are loosely attached to the substratum) on most rock surfaces and of almost all cobbles (Danin and Garty, 1983; Kidron et al., 2011), and for the growth of fruticose (shrub-like) lichens (Kappen et al., 1979, 1980; Lange, 1969). Among all lichen types, biomass of the crustose lichens was the highest,

with the fruticose lichen, *R. maciformis*, being especially abundant on the north-facing slope, attributed to the overwhelming effect of dew (Kappen et al., 1980).

Dew however is not formed at the south- and east-facing bedrocks of the Negev, explained by the higher nocturnal temperatures that impede vapor condensation. These surfaces support lithic cyanobacteria (Kidron et al., 2014, 2016). This however is not the case at the north- and west-facing bedrocks and in all cobbles. With the addition of dew water on these surfaces, a much more developed community of lithobionts, mainly crustose lichens, exists. With lichens supporting snails and isopods, the entire food web is positively impacted (Jones and Shachak, 1990; Shachak et al., 1987). Dew has also an important contribution to plants in the Negev, providing water (Hill et al., 2015) and nutrients (Kidron and Starinsky, 2012). According to Hill et al. (2015), dew even serves as the main source of water for some of the Negev plants.

Whether a fog or a dew desert, both types of deserts are located near large water reservoirs, usually up to tens of kilometers away. Fog deserts are located along oceans and include regions in the Namib, the Atacama and the Sonoran deserts (Baja California). Fog and dew deserts may however extend to over 100 km from the coast (Kidron, 1999). Once reaching the colder land during the night, and especially when forced to rise due to topography, vapor may condense at the air mass, resulting in fog. Once condensation takes place only at the substrates-air interface, dew is formed (Beysens, 1995; Monteith, 1957). In addition to the Negev, dew also forms regularly in Western Sahara (Clus et al., 2013; Lekouch et al., 2012), which benefits from vapor stemming from the Atlantic Ocean and may also be termed a dew desert. Certain locations along the coast of Western Australia may be also potentially regarded as a dew desert. Another possible candidate for a dew desert is the Iberian southeast, which includes the Tabernas Desert.

Located 20–60 km from the Mediterranean Sea and having an average annual precipitation of 200–240 mm, dew was thought to play an important role in the water budget of the Tabernas Desert. It was reported to have a positive effect on the water budget of many organisms including plants (Uclés et al., 2016), and to provide water to fruticose (del Prado and Sancho, 2007), and crustose (Pintado et al., 2010) lichens. These reports, along with the proximity of the desert to the Mediterranean, led to the current research. Our goal is to compare the relevant meteorological variables of the Tabernas to that of the Negev, in order to evaluate the possibility that the Tabernas, like the Negev, is a dew desert, and subsequently, dew may potentially be responsible for the survival and growth of variable organisms during the dry season.

METHODOLOGY

The Research sites: Tabernas and Negev

The Tabernas Desert is located in SE Spain, in the Almeria province, about 20 km north and 60 km west from the Mediterranean (Fig. 1a). It is located in the Rioja-Tabernas basin, surrounded by several mountain ranges: Gador in the southwest, Nevada in the west and northwest, Filabres in the north, and Alhamilla in the east and southeast. Except for the Alhamilla range (up to 1387 m above msl), all mountain ranges are higher than 2000 m above msl. All mountain ranges are higher than the Rioja-Tabernas basin, which extend between 150 and 800 m above msl. These mountain ranges intercept most rainfall fronts, which come from the west during the winter, or vapor that mainly comes from the east during the summer months (Lázaro et al., 2001). Average precipitation is between 200 and

240 mm, falling during 40–50 days a year, mainly during the fall, winter and spring. Average annual temperature is 18°C; average daily maximum during the hottest and coldest months is 34.5°C and 17.5°C, respectively, whereas the average daily minimum is 4°C and 19.5°C in the coldest and the hottest months, respectively (Lázaro et al., 2001, 2004).

The Tabernas Desert is mostly a badlands area due to a dense drainage net, including multiple catchments of several orders on deeply dissected Toronian mudstone of marine origin. The parent material mainly consists of silt-size (>60%) gypsum-calcareous and siliceous particles, 20–35% of fine sand, and 5–10% of clay (Cantón et al., 2003). Semi-flat areas may exist corresponding to old residual hanging pediments (Alexander et al., 2008). Vegetation shows a clear pattern. While south- and west-facing slopes are normally bare and eroded, north- and east-facing slopes are covered by grass, dwarf shrubs, annuals, and biocrusts (biological soil crusts). While eroded landforms occupy a third of the territory, vascular vegetation with biocrusts in the interspaces cover another third, and the rest is covered by biocrusts (Fig. 1b; Lázaro et al., 2000). Crustose chlorolichens (lichens with green algae as photobiont, such as *Psora decipiens*, *Squamarina lentigera* and *Diploschistes diacapsis*) predominate in the Tabernas (Lázaro et al., 2008; Miralles et al., 2012).

In comparison to the Tabernas, the Negev is substantially more xeric. It lies in the southern part of Israel (Fig. 1c), and has a low cover of soil lichens (Fig. 1d; Kappen et al., 1980). Long-term annual precipitation is 95 mm, with precipitation mainly falling between November and April (Rosenan and Gilad, 1985). Yet, it benefits from ~200 days of dew, providing ~33 mm of water per year (Evenari et al., 1971), with the late summer and fall being the most dewy months. These conditions, which can be found in many regions in the globe (such as in the UK; Monteith, 1957, South Africa; Baier, 1966 or North America; Tuller and Chilton, 1973), stem from the sea breeze that provide vapor to the inland desert and from the relatively long nights, which facilitate long time of vapor condensation (Zangvil, 1996). In Sede Boqer (500–550 m above msl), an average amount of 0.2 mm per dewy night was recorded, using the cloth-plate method (CPM). This represented an average yield between the 0.1 mm that were concomitantly recorded at Nizzana, at the western edge of the Negev Highlands (250 mm above msl) and 0.3 mm recorded at the higher altitudes of the Negev Highlands, at Har Harif, ~1000 m above msl (Kidron, 1999).

For a comparison of the abiotic conditions of the Tabernas and the Negev, 9 years of meteorological data were analyzed. For the Tabernas, the meteorological station at the northeast corner of the Tabernas Desert was taken as representative of the meteorological variables. It lies at ~500 m a.s.l., approximately 8 km northeast of the town of Tabernas (02°18'W, 37°05'N). For the Negev, the meteorological station of Sede Boqer, at the heart of the Negev Highlands (~500 m a.s.l.; 34°46'E, 30°56'N) was taken to represent the Negev Highlands (hereafter the Negev). Both stations have automatic recordings at a resolution of 10 (Negev) and 30 (Tabernas) minutes.

Data from the 9 years (2003–2012) were analyzed. It includes all the relatively dry season of both deserts: the late spring and early summer (June), the core of the summer (July, August) and the late summer and early fall (September). During these months, rain precipitation is low or minimal. In fact, while very rare in the Negev, it is relatively low at Tabernas during June, rare in July and August, but unpredictable and sometimes moderate during September. By choosing relatively rainless months, high relative humidity which may stem from rain or



Fig. 1. (a) Map of the Tabernas Desert (marked by dashed lines); (b) lush cover of crustose lichens inhabiting the ground in the Tabernas; (c) map of the Negev Desert (marked by dashed lines); and (d) a photograph of the rock and soil surfaces in the Negev. While the rock surfaces are covered by lithic lichens, only small patches of crustose lichens cover the soil, almost solely confined to the feet of the rocks. Arrows indicate the predominating wind direction (summer-fall).

distillation, i.e., rain-induced wet ground was avoided (Monteith, 1957). Indeed, even small amounts of rain tend to abruptly increase the relative humidity (RH) as recorded in the Tabernas (for instance, on 23.9.2006 during which 2.6 mm of rain increased the RH from 74 to 90% within one hour). Therefore, although rain-induced vapor could also produce dew, the analysis did not include rainy nights or nights during which >4 mm of rain fell during the preceding day to avoid possible confusion between dew and distillation.

Relative humidity, air temperature, and wind may largely dictate dew formation (Beysens, 2018). High nocturnal temperatures may impede condensation, as it may not drop below the dew point temperature (T_d). Wind will also affect vapor condensation. While a minimum velocity of 0.5 m s^{-1} is required to guarantee vapor supply (Monteith, 1957), high nocturnal wind velocity of $>4.5 \text{ m s}^{-1}$ may on the other hand impede inversion and subsequently condensation (Beysens et al., 2006; Leuning and Cremer, 1988; Oke, 1978). Relatively windy morning may also negatively affect dew by triggering evaporation (Kidron, 2000a). On the other hand, high-speed winds during the afternoon may enhance substrate cooling, minimizing the time lag until T_d is reached (Kidron et al., 2016).

As for the RH, hours during which RH exceeds 90% and 95% during the night and the early morning are analyzed, assuming that:

(a) RH of 90% is sufficiently high to facilitate low net photosynthesis for chlorolichens (25% of maximum; Lange, 1969). As for RH of 95%, since the RH of the meteorological station is based on temperature sensors which are shielded (to avoid direct radiation), RH of 95% at the meteorological station is likely to facilitate near surface condensation as verified in the Negev (Kidron unpub. data and see also below).

(b) The longer the nighttime duration with high RH, the higher the dew amount obtained during dawn (Zangvil, 1996). Higher dew amounts facilitate longer daylight dew duration allowing in turn for long hours of photosynthesis (Kappen et al., 1980; Kidron et al., 2000, 2011).

Since dew duration directly affects lichen biomass (Kappen et al., 1980; Kidron et al., 2011), we believe that the information will serve to evaluate the possible role of dew as a water source for the lichens in both ecosystems.

RESULTS

Average number of light rains (<1 mm) and ≥ 1 mm rains in the Tabernas was 49.6 and 36.1 days, respectively. It was substantially lower in the Negev, 12.7 and 11.6 days, respectively.

Figure 2 shows the average monthly precipitation for the research periods in both deserts. July and August were almost completely dry in the Tabernas, while June and especially September received occasional rains. June and September were also not completely rainless in the Negev, although it was reflected in only one year (2009) during which 12.9 mm fell in June and 0.6 mm fell in September. Average precipitation in the Tabernas for June was 8.3 mm, with September receiving on average a fairly high amount of rain, 35.8 mm, approximately twice as high as the long-term average (1967–1997) of 18.0 mm (Lázaro et al., 2001). All together, aiming to avoid confusion between dew and distillation, one day was discarded in the

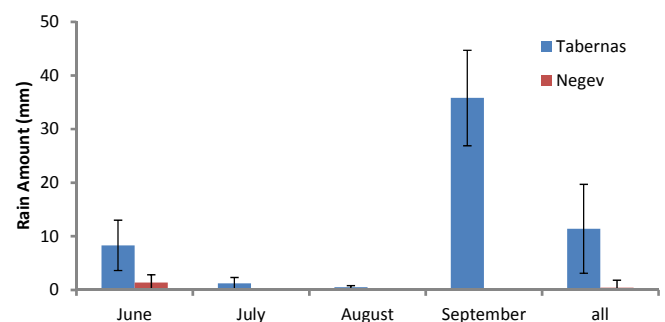


Fig. 2. Average monthly precipitation during 2003–2012 in the Tabernas and the Negev deserts. Bars indicate one SE.

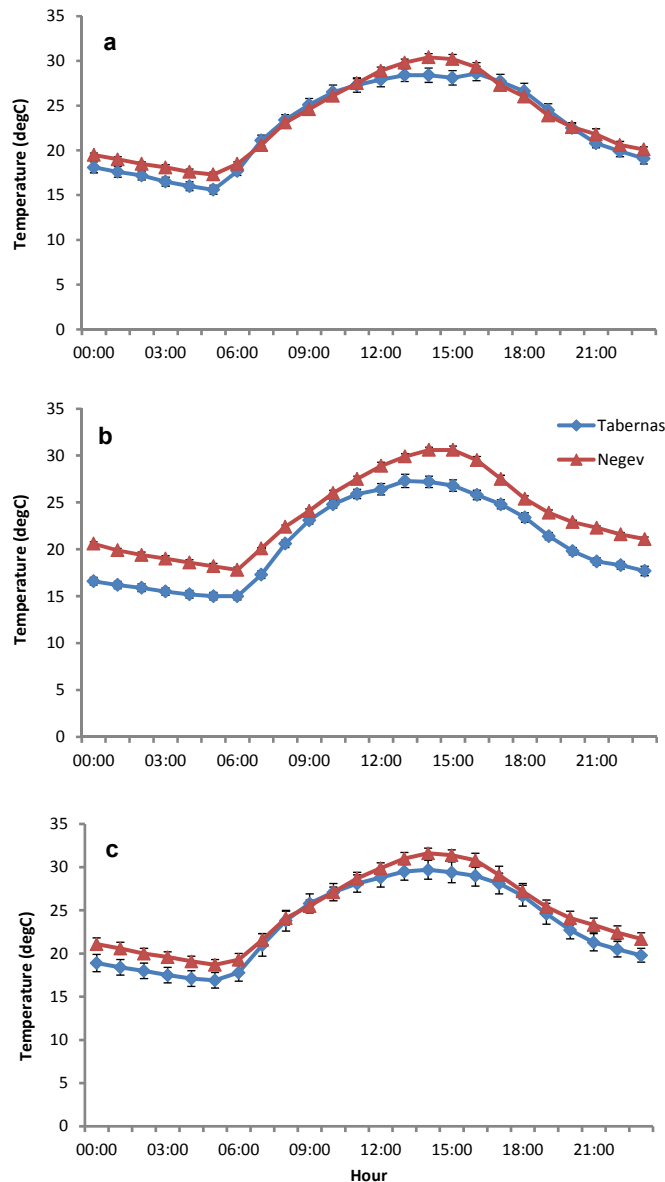


Fig. 3. The average hourly temperatures during June (a), September (b) and the average values for the months of June, July, August and September (c) of 2003–2012 as calculated for the middle (14th to 16th) of each month. Bars indicate one SE.

Negev (following the 12.9 mm rain event), while a total of 28 days were discarded in the Tabernas, i.e., approximately 3 days per year.

For space limitation, and due to the fact that the patterns of all months were similar, the average hourly values of temperature, wind speed, and relative humidity will be presented for the months of June and September, along with the average value of all four months (June, July, August, September).

Average hourly air temperatures for June, September, and for all research months are shown in Figure 3, and the average hourly wind speed are shown in Figure 4. While cooler temperatures characterize the Tabernas, both sites show an afternoon increase in the wind speeds. Yet the afternoon wind speeds were substantially higher for the Negev (2.8–5.4 m s⁻¹) in comparison to the Tabernas (2.4–3.7 m s⁻¹). At both deserts, the threshold nocturnal velocities of <0.5 and >4.5 m s⁻¹ were not reached, excluding therefore a possible lack of vapor on the one hand and impediment of the inversion conditions on the other hand in both deserts.

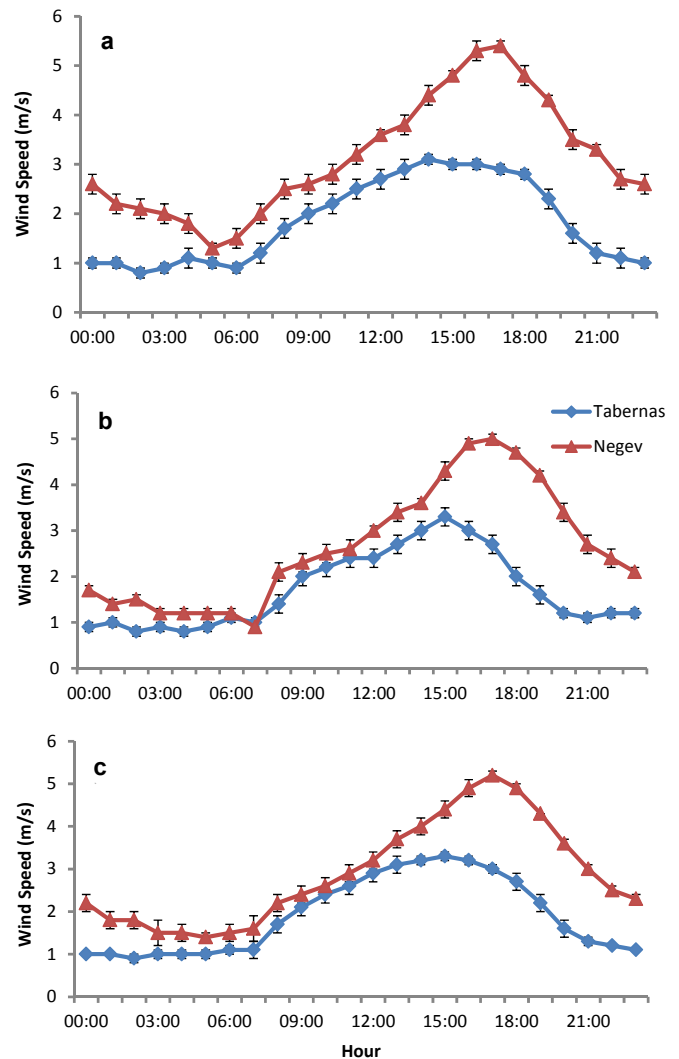


Fig. 4. Average hourly wind speed during June (a), September (b) and the average values for the months of June, July, August and September (c) of 2003–2012 as calculated for the middle (14th to 16th) of each month. Bars indicate one SE.

Average hourly RH for June (Fig. 5a), September (Fig. 5b), and for all four months (Fig. 5c) show substantially higher RH in the Negev. Only during a short period during the afternoon (12:00–17:00), RH at the Negev was below that of the Tabernas. As for the nocturnal RH, average monthly RH was by 10–20% higher in the Negev. While being carried by northwesterly winds in the Negev (Kidron et al., 2000), it is mainly carried by easterly winds in the Tabernas. This was verified when an analysis of the days during which RH $\geq 90\%$ took place in the Tabernas. Nocturnal winds having a prominent eastern vector characterize 77.3% of all nights with prolonged (>6 h) high RH ($\geq 90\%$).

Average hourly maximum RH for the night and early morning of all months was substantially higher for the Negev (Fig. 6a). While ranging between 86.0% and 91.0% in the Negev (averaging 88.8%), it only ranged between 76.1% and 79.5% in the Tabernas (averaging 77.0%). At the same time, average hourly minimum temperatures at the Tabernas were slightly lower, between 16.0° and 18.7° (with an average of 17.4°) in comparison to 17.5° and 19.7° (with an average of 18.7°) for the Negev (Fig. 6b). As far as *T_d* is concerned, lower nocturnal air temperatures may imply lower substrate temperatures and a higher likelihood of vapor condensation, but yet, despite the lower nocturnal temperatures, lower values of RH characterize the Tabernas.

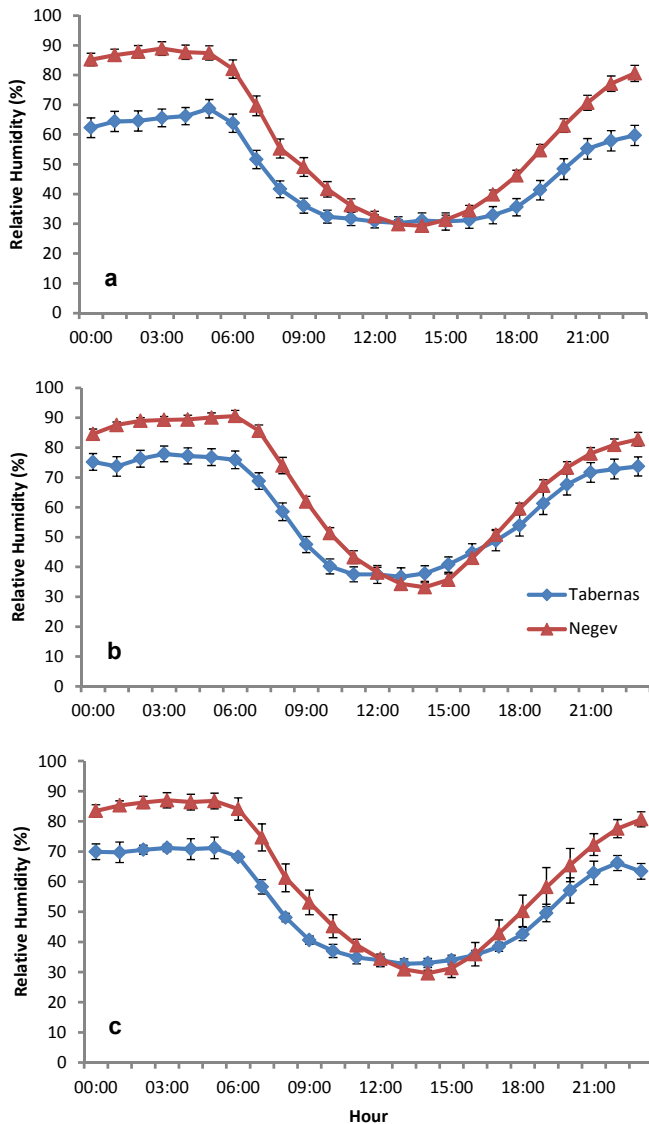


Fig. 5. The average hourly relative humidity during June (a), September (b) and the average values for the months of June, July, August and September (c) of 2003–2012 as calculated for the middle (14th to 16th) of each month. Bars indicate one SE.

The average nighttime duration during which $RH \geq 90\%$ and $RH \geq 95\%$ per night are shown in Figure 7a and Figure 7b, respectively. Time duration during which $RH \geq 90\%$ took place was only 3.1 h in the Tabernas, while being 5.2 h in the Negev. As for the amount of hours during which $RH \geq 95\%$ took place during a dewy night, it was identical during September (2.9 h), but exhibited high differences in the remaining months. It ranged between 1.5–2.2 h during June, July and August in the Tabernas and between 2.9–3.3 h in the Negev.

However, a much more pronounced difference was found for the number of the dewy days. A large difference characterized the amount of days during which $RH \geq 90\%$ and $RH \geq 95\%$ occurred. While the average monthly amount of days during which $RH \geq 90\%$ ranged between 5.1 and 9.4 days in the Tabernas (averaging 7.1), it ranged between 17.9 and 23.8 days (averaging 21.4 days) in the Negev (Fig. 7c). The differences were much more pronounced for days during which $RH \geq 95\%$ was reached. In comparison to an average of 0.9–1.1 days per month in the Tabernas, it was 9.7–13.9 days per month in the Negev (Fig. 7d).

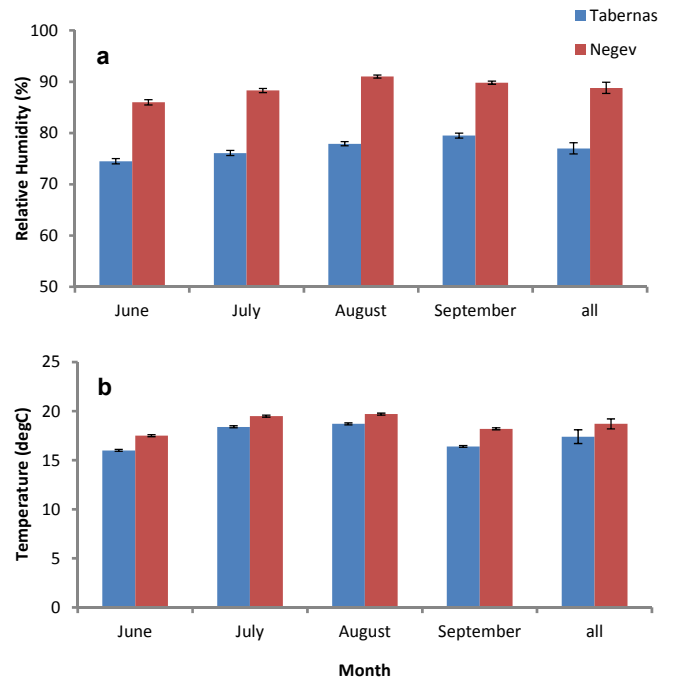


Fig. 6. Average maximum relative humidity (a) and average minimum temperatures (b) during 2003–2012 in the Tabernas and the Negev deserts. Bars indicate one SE. Significant differences ($P < 0.05$) characterize the values of the Tabernas and the Negev for each month.

DISCUSSION

By providing an additional source of water during the dry months, dew may act to alleviate the harsh conditions of high radiation, high evaporation and prolonged dryness that characterize deserts. While dew may take place in different climatic regions (Csintalan et al., 2000; Fischer et al., 2012; Tuba et al., 1996) and in variable deserts (Jia et al., 2014), it is especially important to those deserts where it provides a stable source of water during the dry season, and may therefore facilitate the growth and/or survival of different organisms that otherwise would not be able to thrive in the desert. Under such conditions it may be regarded as a dew desert.

While no attempts were made before to categorize the Tabernas desert, previous publications tended to emphasize the possible role of dew for the Tabernas ecosystem. According to del Prado and Sancho (2007), the fruticose lichen *Teloschistes lacunosus* use dew for photosynthesis. According to Pintado et al. (2010) also the crustose soil lichen *Diploschistes diacapsis* utilizes dew. Uclés et al. (2013, 2015) regard dew as an important source of water for the Tabernas based on measurements of atmospheric water that was conducted with microlysimeters (MLs), while Moro et al. (2007) regard the Tabernas as dewy based on eddy covariance calculations. Based on these data, Maestre et al. (2011) concluded that dew occurs in the Tabernas during ~12% of the year, which seems a prudent estimation. While we cannot rule out the ecological importance of dew to the Tabernas Desert, at least in some microhabitats or periods, our data show that it may have lower importance than supposed and much lower in comparison to the Negev. Perhaps due to that, *Teloschistes lacunosus* is the only fruticose lichen in the area (and, though frequent, its cover is quite low), while *Ramalina* spp. are absent, but nevertheless inhabit the coastal locations of the Iberian semiarid southeast. As will be expanded

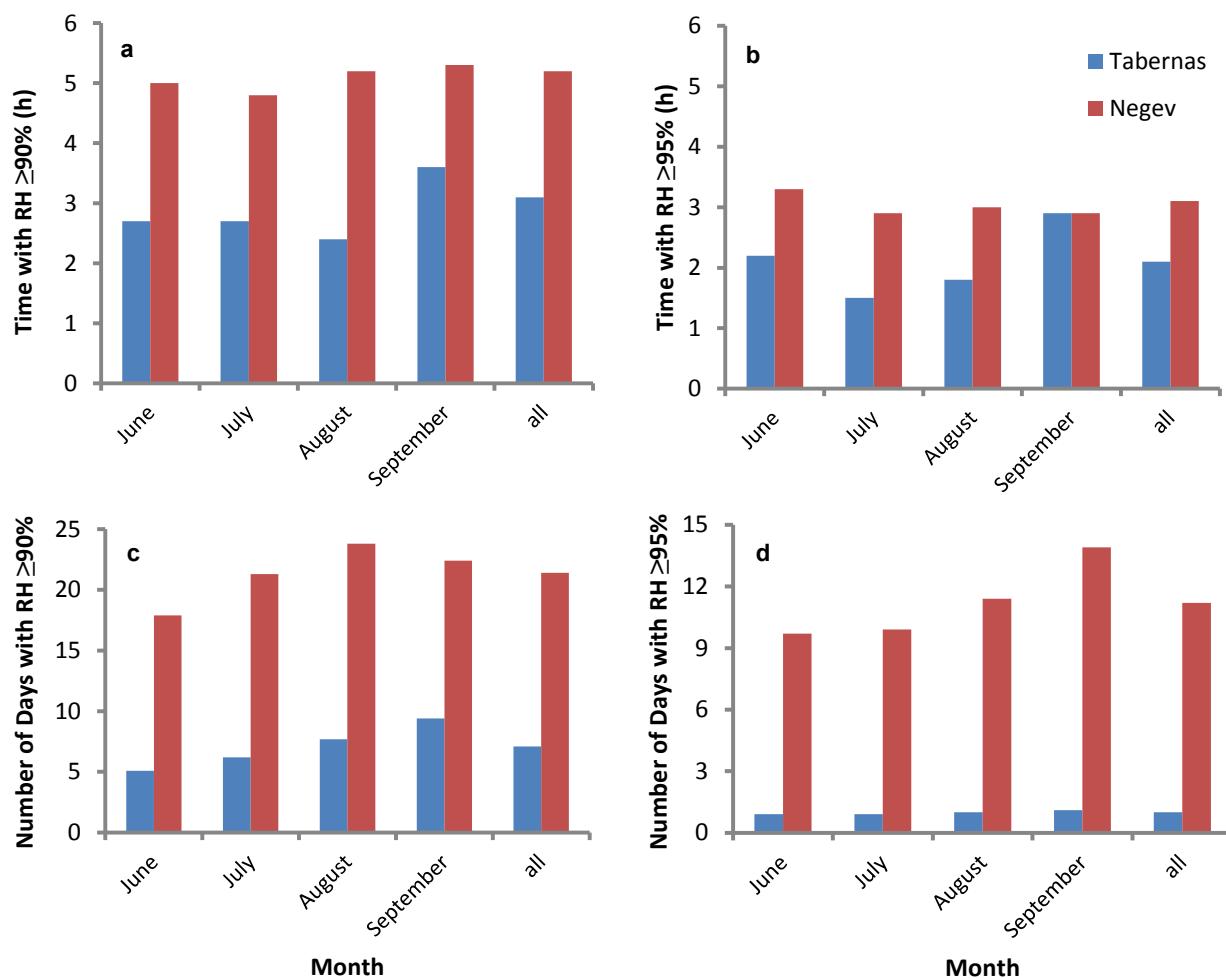


Fig. 7. The average duration of hours per dew days with $RH > 90\%$ (a) and $RH > 95\%$ (b) and the average amounts of days per month with $RH > 90\%$ (c) and $RH > 95\%$ (d). Bars indicate one SE. Significant differences ($P < 0.05$) characterize the values of the Tabernas and the Negev for each month.

below and in agreement with previous publications (Lázaro, 2004; Lázaro et al., 2001), the abundance of biocrusts at Tabernas is mainly attributed to the rain regime, i.e., the high proportion of small events (57%) and high number of rainy days per year (85.7 days) as found for our study period (2003–2012).

The limited role played by dew is also supported by the measurements conducted during 2006 and 2007 by Pintado et al. (2010). No photosynthesis was recorded by the crustose soil lichen *Diploschistes diacapsis* during July and August, 2006 and during June and July, 2007, which were also the only rainless months. Photosynthesis was however recorded during all other months, which also benefited from rain. Photosynthesis during rainy months was also reported by Moro et al. (2007). This however may point to the possible occurrence of distillation. On the other hand, measurements of dew that were carried out by Uclés et al. (2013, 2015) during the rainless months reported relatively high amounts of dew. Yet, they were performed by MLs.

The use of MLs may lead to overestimation of the actual values. Not only that the ML register vapor (a problem which the authors partially solved), but as shown by Kidron and Kronenfeld (2017), the ML experienced fast cooling rates due to a preferential heat flux through its walls. The air gap in between the inner and outer walls (essential to create a totally disconnected body which allows the measurement of its weight) is claimed to react like a loose stone that facilitates high vapor condensation due to efficient nocturnal cooling. Termed as the

'loose stone effect' (LSE), loose stones (Kidron, 2000b) as well as MLs (Kidron and Kronenfeld, 2017) will preferentially condense vapor, resulting in overestimation of the actual amounts that are condensed on the intact soil. As a result, the high values of 0.24 mm reported by Uclés et al. (2013) for the bare soil of the Tabernas may not genuinely reflect the real amounts which are condensed on the intact soil.

In light of the possible overestimated values that are obtained by the ML (Kidron and Kronenfeld, 2017), and lack of reported manual measurements from the Tabernas, our current analysis is therefore based on a comparison of the abiotic conditions of the Tabernas and the Negev. Our comparison points to fundamental differences in the RH, as well differences in the wind regime and the air temperatures.

Wind speeds and air temperatures were found to be lower in the Tabernas. Despite the lower temperatures, lower RH characterizes the Tabernas. Monthly RH is by 10–13% lower in the Tabernas, with an average RH being below 80% in the Tabernas in comparison to ~90% in the Negev. Furthermore, while $RH \geq 90\%$ occurred on average 5–9 times per month during the summer months in the Tabernas, it occurred between 18–24 times per month during the summer months in the Negev.

This may be explained by the topography. While ascending air is responsible for the increase in RH during the late afternoon and the nighttime hours in the Negev, lower RH characterize the descending air in the Tabernas. Although the southern

boundaries of the Tabernas are very close to the sea (about 20 km), southern winds (as well as northern winds) are rare, and most winds flow from the east. Yet, although only ~60 km away from the Mediterranean, these winds are intercepted by the Cabrera and Alhamilla Mountains. However, vapor can also be delivered from Atlantic Ocean western winds. Yet, these winds are also partly intercepted by high mountain ranges (Sierra Nevada and surrounding mountain ranges, Sierra Contraviesa - Gador, Baza-Filabres). This may explain the lower occurrence of nights with $RH \geq 90\%$.

Nevertheless, for dew formation, near-surface RH should reach 100%. However, the RH, as reported by us, was measured at the meteorological station. Due to its structure (with RH being recorded within a screen in the Negev or by a protected solid-state capacitive sensor in the Tabernas), the meteorological station tends to underestimate the actual RH obtained in the open air near soil surface. This can be easily seen by a comparison of the temperatures. An analysis of temperatures measured within a meteorological station and in the open, at 10 cm-height next to the station by the Israeli Meteorological Service in the Negev (Beer Sheva) has shown that the minimum temperatures at the open are ~1°C lower than those at the station (Kidron, unpub.). It implies, that the lower the height over the soil, the larger the difference in temperature (and RH) with regard to those measured in the meteorological station. Moreover, according to Lawrence (2005), 1°C lower temperature near the ground implies a higher RH value of ~5%. Therefore, RH of 90% at the meteorological station will imply $RH \approx 95\%$ in the open air, while RH of 95% in the meteorological station will imply $RH \approx 100\%$, i.e., vapor condensation (dew). Obviously, condensation may take at lower RH once the substrate is much cooler.

According to our proposed definition, a dew desert should be regarded as a desert in which annual dew equals at least 10% of the total annual rain precipitation, and during which dew occurs for an average for at least 8–12 mornings during each month of the dry season. As for the Negev, as previously found, the annual amount of dew is >10% of the total annual rain precipitation (Evenari et al., 1971; Kappen et al., 1979). This was also verified during the current analysis based on the monthly number of dewy days during the dry season. While this threshold is met for the Negev (with 10–14 events per month), it is not met for the Tabernas (having only 0.9–1.1 days per month during the dry season). We therefore conclude that apparently, the Tabernas cannot be regarded as a dew desert. We suggest that the xeric conditions of the Tabernas stem from its location at the shadow of the vapor-carrying winds. This may explain the relatively low RH of the Tabernas and also the relatively low precipitation there, similarly to other rain-shadow deserts such as the Judean Desert (which is formed at the shadow of the Judean Mountains; Danin, 1989), and the Washington Desert (formed at the shadow of the Cascade Mountains; Siler et al., 2013).

This conclusion is also supported by the lithic community. While covering >90% of all rock (and cobble) surfaces in the Negev, lithic lichens do not cover extensive surfaces in loci with rock outcrops in Tabernas, albeit the ~2.5-fold higher precipitation received in the Tabernas. On the other hand, while cyanobacterial soil crusts abound in the Negev (Lange et al., 1992), soil lichens cover only limited areas in the Negev Highlands (Kappen et al., 1980). Being aware of the fact that the different rock and soil types may also determine the abundance of lithobionts or biocrusts in both deserts, we nevertheless suggest that at least partially, the abundance of lithic lichens in the Negev can be attributed to dew, while their scarcity in the

Tabernas may be attributed to insufficient dew. Likewise, we are also inclined to suggest that the lush cover of soil lichens in the Tabernas is at least partially linked to the higher amounts and frequent occurrence of rain events and subsequently to the possible use of rainwater by these soil lichens (Lázaro, 2004). On the other hand, the low cover of soil lichens in the Negev cannot be linked to the frequent occurrence of dew but rather to the low amounts of rain (Kidron and Starinsky, 2019). This may explain the confinement of lichens to the feet of rock outcrops where they benefit from extra water by runoff (Fig. 1d).

In agreement with our conclusions, the research by Palmer and Friedmann (1990) is of special interest. Analyzing the structure and respiration of two fruticose lichens in the Negev, *Ramalina maciformis* that inhabit rocks and *Teloschistes lacunosus* that inhabit soil, the authors concluded that out of both lichens, *R. maciformis* is primarily adapted to utilize high RH. This may also explain the absence of *Ramalina* spp. from the Tabernas, while present in the more humid and dewy coastal regions of southeast Spain.

As far as the food web is concerned, both deserts may therefore experience different paths. While rain would be mainly responsible for the food web chain in the Tabernas, dew and rain will be concomitantly responsible for the food web chain in the Negev. Subsequently, both deserts may also be differently affected by global warming. While a decrease in rain, as predicted by some models (Berg et al., 2016; Dai, 2013) will affect both deserts, nighttime warming, as predicted by some of the models (Peng et al., 2004; Price et al., 1999), may principally affect the Negev.

Acknowledgements. This study was completed thanks to the Research Project 'Biocrust Dynamics' (DINCOS, CGL2016-78075-P) funded by the Spanish State Plan for Scientific and Technical Research and Innovation.

REFERENCES

- Alexander, R.W., Calvo-Cases, A., Arnau-Rosalén, E., Mather, A.E., Lázaro-Suau, R., 2008. Erosion and stabilization sequences in relation to base level changes in the El Cautivo badlands, SE Spain. *Geomorphology*, 100, 83–90.
- Baier, W., 1966. Studies on dew formation under semi-arid conditions. *Agric. Forest Meteorol.*, 3, 103–112.
- Barker, D.H., Stark, L.R., Zimpfer, J.F., McLetchie, N.D., Smith, S.D., 2005. Evidence of drought-induced stress on biotic crust moss in the Mojave Desert. *Plant, Cell, Environ.* 28, 939–947.
- Berg, A., Findell, K., Lintner, B., Giannini, A., Seneviratne S, van den Hurk, B, Lorenz, R., Pitman, A., Hagemann, S, Meier, A., Cheruy, F., Ducharme, A., Mslyshev, S., Milly, P.C.D., 2016. Land-atmosphere feedbacks amplify aridity increase over land under global warming. *Nature Climate Change*, 6, 869–874.
- Beysens, D., 1995. The formation of dew. *Atmos. Res.*, 39, 215–237.
- Beysens, D., 2018. *Dew Water*. River Publishers, Gistrup, Denmark. 305p.
- Beysens, D., Milimouk, I., Nikolayev, V.S., Berkowicz, S., Muselli, M., Heusinkveld, B., Jacobs, A.F.G., 2006. Comment on "the moisture from the air as water resource in arid region: Hope, doubt and facts" by Kogan and Trahtman. *J. Arid Environ.*, 67, 343–352.
- Büdel, B., Darienko, T., Deuschewitz, K., Dojani, S., Friedl, T., Mohr, K., Salisch, M., Reisser, W., Weber, B., 2009. Southern African biological soil crusts are ubiquitous and

- highly diverse in drylands, being restricted by rainfall frequency. *Microb. Ecol.*, 57, 229–247.
- Cantón, Y., Solé-Benet, A., Lázaro, R., 2003. Soil-geomorphology relations in gypsiferous materials of the Tabernas Desert (Almería, SE Spain). *Geoderma*, 115, 193–222.
- Clus, O., Lekouch, I., Muselli, M., Milimouk-Melnychouk, I., Beysens, D., 2013. Dew, fog and rain water collectors in a village of S-Morocco (Idouassksou). *Desalination Water Treatment*, 51, 4235–4238.
- Csintalan, Z., Takács, Z., Proctor, M.C.F., Nagy, Z., Tuba, Z., 2000. Early morning photosynthesis of the moss *Tortula ruralis* following summer dew fall in a Hungarian temperate dry sandy grassland. *Plant Ecology*, 151, 51–54.
- Dai, A., 2013. Increasing drought under global warming in observations and models. *Nature Climate Change*, 3, 52–58.
- Danin, A., 1989. The impact of prevailing winter winds on the distribution of vegetation in the Judean Desert, Israel. *J. Arid Environ.*, 17, 301–305.
- Danin, A., Garty, J., 1983. Distribution of cyanobacteria and lichens on hillsides of the Negev Highlands and their impact on biogenic weathering. *Z. Geomorph.*, 27, 423–444.
- del Prado, R., Sancho, L.G., 2007. Dew as a key factor for the distribution pattern of the lichen species *Teloschistes lacunosus* in the Tabernas Desert (Spain). *Flora*, 202, 417–428.
- Evenari, M., Shanan, L., Tadmor, N., 1971. *The Negev, The Challenge of a Desert*. Harvard Univ. Press, Cambridge, Massachusetts, 345 p.
- Fischer, T., Veste, M., Bens, O., Hüttl, R.F., 2012. Dew formation on the surface of biological soil crusts in central European sand ecosystems. *Biogeosciences*, 9, 4621–4628.
- Hill, A., Dawson, T.E., Shelef, O., Rachmilevitch, S., 2015. The role of dew in Negev Desert plants. *Oecologia*, 178, 317–327.
- Jia, R.L., Li, X.R., Liu, L.C., Pan, Y.X., Gao, Y.H., Wei, Y.P., 2014. Effects of sand burial on dew deposition on moss soil crust in a revegetated area of the Tengger Desert, Northern China. *J. Hydrol.*, 519, 2341–2349.
- Jones, C.G., Shachak, M., 1990. Fertilization of the desert soil by rock-eating snails. *Nature*, 346, 839–841.
- Kappen, L., Lange, O.L., Schulze, E.-D., Evenari, M., Buschbom, V., 1979. Ecophysiological investigations on lichens of the Negev Desert, IV: Annual course of the photosynthetic production of *Ramalina maciformis* (Del.) Bory. *Flora*, 168, 85–105.
- Kappen, L., Lange, O.L., Schulze, E.-D., Buschbom, U., Evenari, M., 1980. Ecophysiological investigations on lichens in the Negev Desert, VII: The influence of the habitat exposure on dew imbibition and photosynthetic productivity. *Flora*, 169, 216–229.
- Kidron, G.J., 1999. Altitude dependent dew and fog in the Negev desert, Israel. *Agrig. Forest Meteorol.*, 96, 1–8.
- Kidron, G.J., 2000a. Analysis of dew precipitation in three habitats within a small arid drainage basin, Negev Highlands, Israel. *Atmos. Res.*, 55, 257–270.
- Kidron, G.J., 2000b. Dew moisture regime of endolithic and epilithic lichens inhabiting calcareous cobbles and rock outcrops, Negev Desert, Israel. *Flora*, 195, 146–153.
- Kidron, G.J., 2015. Dune crests serve as preferential habitats for perennial plants during frequent drought years. *Journal of Hydrology*, 522, 295–304.
- Kidron, G.J., 2019a. *Dew Deserts*. Encyclopedia of Water. John Wiley.
- Kidron, G.J., 2019b. The enigmatic absence of cyanobacterial biocrusts from the Namib fog belt: do dew and fog hold the key? *Flora*, 257, 151416.
- Kidron, G.J., Kronenfeld, R., 2017. Assessing the effect of micro-lysimeters on NRWI: Do micro-lysimeters adequately represent the water input of natural soil? *J. Hydrol.*, 548, 382–390.
- Kidron, G.J., Starinsky, A., 2012. Chemical composition of dew and rain in an extreme desert (Negev): Cobbles serve as sink for nutrients. *J. Hydrol.*, 420–421, 284–291.
- Kidron, G.J., Starinsky, A., 2019. Measurements and ecological implications of non-rainfall water in desert ecosystems – a review. *Ecohydrology*, 2019; e2121.
- Kidron, G.J. Yair, A., Danin, A., 2000. Dew variability within a small arid drainage basin in the Negev highlands, Israel. *Quart. J. Royal Meteorol. Soc.*, 126, 63–80.
- Kidron, G.J., Temina, M., Starinsky, A., 2011. An investigation of the role of water (rain and dew) in controlling the growth form of lichens on cobbles in the Negev Desert. *Geomicrobiol. J.*, 28, 335–346.
- Kidron, G.J., Starinsky, A., Yaalon, D.H., 2014. Dewless habitat within a dew desert: Implications for weathering and terrestrial evolution. *J. Hydrol.*, 519, 3606–3614.
- Kidron, G.J., Kronenfeld, R., Starinsky, A., 2016. Wind as a cooling agent: Substrate temperatures are responsible for variable lithobiont-induced weathering patterns at the west- and east-facing limestone bedrocks of the Negev. *Earth Surf. Process. Landf.*, 41, 2078–2084.
- Lange, O.L., 1969. Ecophysiological investigations on lichens of the Negev Desert. I. CO₂ gas exchange of *Ramalina maciformis* (Del.) Bory under controlled conditions in the laboratory. *Flora*, 158, 324–359.
- Lange, O.L., Meyer, A., Zellner, H., Heber, U., 1994. Photosynthesis and water relations of lichen soil crusts: field measurements in the coastal fog zone of the Namib Desert. *Func. Ecol.*, 8, 253–264.
- Lange, O.L., Green, T.G.A., Melzer, B., Meyer, A., Zellner, H., 2006. Water relations and CO₂ exchange of the terrestrial lichen *Teloschistes capensis* in the Namib fog Desert: Measurements during two seasons in the field and under controlled conditions. *Flora*, 201, 268–280.
- Lange, O.L., Kidron, G.J., Büdel, B., Meyer, A., Kilian, E., Abeliovitch, A., 1992. Taxonomic composition and photosynthetic characteristics of the biological soil crusts covering sand dunes in the Western Negev Desert. *Func. Ecol.*, 6, 519–527.
- Lawrence, M.G., 2005. The relationship between relative humidity and the dewpoint temperature in moist air. *Bull. Am. Meteorol. Soc.*, 86, 225–233.
- Lázaro, R., 2004. Implications of precipitation on vegetation of water-limited lands. In: Pandalai, S.G. (Ed.): *Recent Research Development in Environmental Biology*, Vol. I. Research Signpost. Kerala (India), pp. 553–591.
- Lázaro, R., Alexander, R.W., Puigdefabregas, J., 2000. Cover distribution patterns of lichens, annuals and shrubs in the Tabernas Desert, Almería, Spain. In: Alexander, R.W., Millington, A.C. (Eds.): *Vegetation Mapping: From Patch to Planet*. Wiley, Chichester, pp. 19–40.
- Lázaro, R., Rodríguez-Tamayo, M.L., Ordiales, R., 2004. El Clima. In: Pandalai, S.G., Mota, J., Cerrillo, M.I., Rodríguez Tamayo, M.L. (Eds.): *Subdesiertos de Almería: Naturaleza de Cine*. Consejería de Medi, pp. 63–79.
- Lázaro, R., Rodrigo, F.S., Gutiérrez, L., Domingo, F., Puigdefabregas, J., 2001. Analysis of a thirty-year rainfall record (1967–1997) from semi-arid SE Spain for implications on vegetation. *J. Arid Environ.*, 48, 373–395.
- Lázaro, R., Cantón, Y., Solé-Benet, A., Bevan, J., Alexander, R., Sancho, L.G., Puigdefabregas, J., 2008. The influence of

- competition between lichen colonization and erosion on the evolution of soil surfaces in the Tabernas badlands (SE Spain) and its landscape effects. *Geomorphology*, 102, 252–266.
- Lekouch, I., Lekouch, K., Muselli, M., Mongruel, A., Kabbachi, B., Beysens, D., 2012. Rooftop dew, fog and rain collection in southwest Morocco and predictive dew modeling using neural networks. *J. Hydrol.*, 448–449, 60–72.
- Leuning, R., Cremer, K.W., 1988. Leaf temperatures during radiation frost part I. Observations. *Agric. Forest Meteorol.*, 42, 121–133.
- Maestre, F.T., Bowker, M.A., Cantón, Y., Castillo-Monroy, A.P., Cortina, J., Escolar, C., Escudero, A., Lázaro, R., Martínez, I., 2011. Ecology and functional roles of biological soil crusts in semi-arid ecosystems of Spain. *J. Arid Environ.*, 75, 1282–1291.
- Miralles, I., Domingo, F., Cantón, Y., Trasar-Cepeda, C., Leirós, M.C., Gil-Sotres, F., 2012. Hydrolase enzyme activities in a successional gradient of biological soil crusts in arid and semi-arid zones. *Soil Biol. Biochem.*, 53, 124–132.
- Monteith, J.L., 1957. Dew. *Quart. J. Royal Meteorol. Soc.*, 83, 322–341.
- Moro, M.J., Were, A., Villagarcía, L., Cantón, Y., Domingo, F., 2007. Dew measurements by Eddy covariance and wetness sensor in a semiarid ecosystem of SE Spain. *J. Hydrol.*, 335, 295–302.
- Oke, T.R., 1978. *Boundary Layer Climates*. John Wiley and Sons, New York, 372 p.
- Palmer, R.J., Friedmann, E.I., 1990. Water relations, thallus structure and photosynthesis of Negev Desert lichens. *New Phytol.*, 116, 597–603.
- Peng, S., Huang, J., Sheehy, J.E., Laza, R.C., Vesperas, R.M., Zhong, X., Centeno, G.S., Khush, G.S., Gassman, K.G., 2004. Rice yields decline with higher night temperature from global warming. *PNAS (USA)*, 101, 9971–9975.
- Pintado, A., Sancho, L.G., Blanquer, J.M., Green, T.G.A., Lázaro, R., 2010. Microclimatic factors and photosynthetic activity of crustose lichens from the semiarid southeast of Spain: long-term measurements for *Diploschistes diacapsis*. *Bibliotheca Lichenologica*, 105, 211–224.
- Price, C., Michaelides, S., Pashiardis, S., Alpert, P., 1999. Long term changes in diurnal temperature range in Cyprus. *Atmos. Res.*, 51, 85–98.
- Rosenan, N., Gilad, M., 1985. Atlas of Israel, Meteorological data, sheet IV/2. Carta, Jerusalem.
- Proctor, M.C.F., Oliver, M.J., Wood, A.J., Alpert, P., Stark, L.R., Cleavitt, N.L., Mishler, B.D., 2007. Desiccation-tolerance in bryophytes: a review. *Bryologist* 110, 595–621.
- Rundel, P.W., Dillon, M.O., Palma, B., Mooney, H.A., Gulmon, S.L., Ehleringer, J.R., 1991. The phytogeography and ecology of the coastal Atacama and Peruvian deserts. *Aliso*, 13, 1–49.
- Schieferstein, B., Loris, K., 1992. Ecological investigations on lichen fields of the Central Namib, I. Distribution patterns and habitat conditions. *Vegetatio*, 98, 113–128.
- Shachak, M., Jones, C.G., Granot, Y., 1987. Herbivory in rocks and a weathering of a desert. *Science*, 236, 1098–1099.
- Siler, N., Roe, G., Durran, D., 2013. On the dynamical causes of variability in the rain-shadow effect: A case study of the Washington Cascades. *J. Hydrometeorol.*, 14, 122–139.
- Tuba, Z., Csintalan, Z., Proctor, M.C.F., 1996. Photosynthetic responses of a moss, *Tortula ruralis*, ssp. *ruralis*, and the lichens *Cladonia convoluta* and *C. furcata* to water deficit and short periods of desiccation, and their ecophysiological significance: a baseline study at present-day CO₂ concentration. *New Phytol.*, 133, 353–361.
- Tuller, S.T., Chilton, R., 1973. The role of dew in the seasonal moisture balance of a summer-dry climate. *Agric. Forest Meteorol.*, 11, 135–142.
- Uclés, O., Villagarcía, L., Cantón, Y., Domingo, F., 2013. Microlysimeter station for long term non-rainfall water input and evaporation studies. *Agric. Forest Meteorol.*, 182–183, 13–20.
- Uclés, O., Villagarcía, L., Cantón, Y., Lázaro, R., Domingo, F., 2015. Non-rainfall water inputs are controlled by aspect in a semiarid ecosystem. *J. Arid Environ.*, 113, 43–50.
- Uclés, O., Villagarcía, L., Cantón, Y., Domingo, F., 2016. Partitioning of non rainfall water input regulated by soil cover type. *Catena*, 139, 265–270.
- Zangvil, A., 1996. Six years of dew observation in the Negev Desert, Israel. *J. Arid Environ.*, 32, 361–372.

Received 25 November 2019

Accepted 14 January 2020

Ski piste snow ablation versus potential infiltration (Veporic Unit, Western Carpathians)

Michal Mikloš¹, Dušan Igaz², Karol Šinka³, Jana Škvareninová⁴, Martin Jančo^{1,5}, Ilja Vyskot⁶, Jaroslav Škvarenina^{1*}

¹ Department of Natural Environment, Faculty of Forestry, Technical University in Zvolen, Ul. T. G. Masaryka 24, 960 53 Zvolen, Slovakia. E-mail: miklosmiso@gmail.com

² Department of Biometeorology and Hydrology, Faculty of Horticulture and Landscape Engineering, Slovak University of Agriculture in Nitra, Hospodárska 7, 949 76 Nitra, Slovakia. E-mail: dusan.igaz@uniag.sk

³ Department of Landscape Planning and Land Consolidation, Faculty of Horticulture and Landscape Engineering, Slovak University of Agriculture in Nitra, Hospodárska 7, 949 76 Nitra, Slovakia. E-mail: sinka.karol@gmail.com

⁴ Department of Applied Ecology, Faculty of Ecology and Environmental Sciences, Technical University in Zvolen, Ul. T. G. Masaryka 24, 960 53 Zvolen, Slovakia.

⁵ Faculty of Ecology and Environmental Sciences, Technical University in Zvolen, Ul. T. G. Masaryka 24, 960 53 Zvolen, Slovakia.

⁶ Department of Environmentalistics and Natural Resources (FRDIS), Faculty of Regional Development and International Studies, Mendel University in Brno, Tř. Generála Píky 2005/7, 613 00 Brno, Czech Republic. E-mail: vyskot@mendelu.cz

* Corresponding author. Tel.: +421455206209. E-mail: skvarenina@tuzvo.sk

Abstract: Snow production results in high volume of snow that is remaining on the low-elevation ski pistes after snow-melt of natural snow on the off-piste sites. The aim of this study was to identify snow/ice depth, snow density, and snow water equivalent of remaining ski piste snowpack to calculate and to compare snow ablation water volume with potential infiltration on the ski piste area at South-Central Slovak ski center Košútka (Inner Western Carpathians; temperate zone). Snow ablation water volume was calculated from manual snow depth and density measurements, which were performed at the end of five winter seasons 2010–2011 to 2015–2016, except for season 2013–2014. The laser diffraction analyzes were carried out to identify soil grain size and subsequently the hydraulic conductivity of soil to calculate the infiltration. The average rate of water movement through soil was seven times as high as five seasons' average ablation rate of ski piste snowpack; nevertheless, the ski piste area was potentially able to infiltrate only 47% of snow ablation water volume on average. Limitation for infiltration was frozen soil and ice layers below the ski piste snowpack and low snow-free area at the beginning of the studied ablation period.

Keywords: Snow water equivalent; Snow density; Artificial snow; Snow ablation; Soil temperature; Hydraulic conductivity.

INTRODUCTION

Snow ablation water plays important role in the hydrological cycle of the snow-dominated basins, where it fundamentally affects seasonal patterns of stream flow (Barnett et al., 2005; Bartík et al., 2014; Hribík et al., 2012). Because of climate change, the less accumulated snow and earlier snow ablation were observed in North America (Cayan et al., 2001; Mote et al., 2005) and Central Europe (Steiger, 2010; Wipf and Rixen, 2010), especially in lower altitudes (Mikloš et al., 2018a). Earlier snow ablation timing of natural snowpack in combination with the warmer climate results in earlier peak runoff, earlier increase in soil moisture, and earlier start of the vegetation period in the season (Babálová et al., 2018; Barnett et al., 2005; Igaz et al., 2008). The shift of snow ablation water available for evapotranspiration to earlier dates can fundamentally change climatic water balance on the local and regional scale (Hrvol' et al., 2009; Ohmura and Wild, 2002). Studies focused on the precipitation variability in the Central Europe show tendency of drought occurrence in the early spring (Beniston, 2007). Prolonged ablation period of ski piste snowpack probably significantly influences availability of snow ablation water for evapotranspiration longer period than on the off-piste site.

A number of European studies identified shift in snowfall pattern (Laternser and Schneebeli, 2003; Rixen et al., 2012;

Wipf et al., 2009) and increase in the mean air temperature (Kammer, 2002). Shift of liquid winter precipitation to lower elevations of Central European mountains was recorded by numerous studies (Mikloš et al., 2018a; Škvarenina et al., 2009; Steger et al., 2013; Vido et al., 2015; Wipf et al., 2009). Winter tourism that is vulnerable to the snow reliability had to adapt in the last decades. To stay operable, ski centers have had to produce artificial snow (since the middle of the 1980s), which decreased their dependency on the natural snow (Bark et al., 2010; Gilaberte-Búrdalo et al., 2014). Nevertheless, snowmaking has economic and physical boundaries, mainly for lower elevation and small-sized ski centers (Mikloš et al., 2018a; Steiger, 2010; Steiger and Mayer, 2008), because of high water and energy consumption (Damm et al., 2014) and temperature/humidity limitations. Artificial snow has different physical and chemical properties than natural snow (Mind'áš and Škvarenina, 1995; Rixen et al., 2003). Nutrient-rich rounded particles of artificial snow, instead of nutrient-poor dendritic snowflakes, create homogenous snowpack with occurrence of ice layers (Rixen et al., 2003, 2008). Generally, snow production increases snow depth and snow density as well (Keller et al., 2004; Mossner et al., 2013). Compared with off-piste sites with natural snow, melting of ski piste snowpack is significantly prolonged because of the higher snow water equivalent (SWE), density, and snow/ice layers (Melanie and Rixen,

2014). Rixen et al. (2004) identified that snowmelt water volume from Swiss snowed piste with artificial snow is twice as high as that from the piste with natural snow. Snow ablation water from ski piste snowpack has significant impact on the local water cycle when it strongly influences the runoff (De Jong and Barth, 2008; Szolgay et al., 2016) and soil moisture over several weeks after natural snowmelt (Freppaz et al., 2012; Tárnik and Igaz, 2015). Volume of infiltrated water from ski piste snowpack has not yet been studied, and determining it is the aim of this current article. Volume of infiltrated water depends on the thermal and physical properties of soil (infiltrability) at the time of snowmelt (Gray et al., 1986) and structure of vegetation cover. Physical properties of soil and plant communities are degraded on the majority of ski pistes because of machine grading (Pintaldi et al., 2017; Ristić et al., 2012). Generally, the disturbed and compacted soil profile with removed or changed vegetation cover can hold less water, causing soil erosion or flood events (Freppaz et al., 2012; Muchová et al., 2015; Nagy et al., 2018). Vegetation and soil cover are being disturbed even during the winter season by the snow-grooming machines (Kňazovičová et al., 2018; Melanie and Rixen, 2014; Roux-Fouillet et al., 2011). Groomed snowpack has reduced insulation capacity because of lower air content and subsequently higher density (Newesely, 1997). Thus, the top soil layers on the pistes can suffer from long-lasting soil frost (Rixen et al., 2004). There are three soil classes, which were determined by Gray et al. (2001), according to their surface entry for meltwater if the soil is frozen during the snow ablation period: unlimited (high infiltration), restricted (low infiltration), and limited (defined by soil physical properties).

Our previous study (Mikloš et al., 2018a) showed that operability of low-elevation ski slopes in South-Central Slovakia is possible only with high snow production. Intensive snowmaking results in ski piste snowpack that is melting even a few weeks after disappearance of natural snow on the off-piste sites. The ski piste snowpack of South-Central Slovakian ski center Košútka was analyzed five seasons after snowmelt of natural snow on the off-piste sites to achieve the following objectives:

(1) to identify snow depth, snow density, and SWE during snow ablation period; to assess correlation between snow depth and snow density; and to identify occurrence of basal ice layer in snowpack and its relationship with snow depth;

(2) to identify and to compare soil temperature on the snow-free and snow-covered ski piste sites as limitation for infiltration; and

(3) to calculate potential infiltration on the ski piste and to compare calculated infiltration with modeled snow ablation water volume based on manual snow depth and density measurements.

MATERIALS AND METHODS

Study site

The study was conducted at the ski center Košútka (Figure 1) localized in the Slovenské Rudohorie Mts., Veporic Unit (Inner Western Carpathians; temperate zone). The ski center was established and equipped with the snowmaking technology in 2007. The stream “Slanec” flowing at the foot of the ski slope is used as the water source for snowmaking. Sole, 950-m-long ski piste with an elevation difference of 220 m (500–720 m above sea level [a.s.l.]), western-to-northern aspect and slope from 7° to 25°, was based on the partly forested slope. Smooth ski piste was built with use of machine grading; obstacles such as rocks and trees were removed, and soil surface was leveled. Disturbed parts of ground surface were visible even after 5 years (Figure 1). The original soil type Modal Cambisol, formed from andesite tuffs and granodiorites (Gömörýová et al., 2013), was degraded when its horizons were mixed or covered by soil during grading. Areas on the ski piste with bare soil were fertilized and revegetated after creation with original plant communities. Nevertheless, the high occurrence of ruderal plant species (*Sambucus ebulus*, *Calamagrostis epigejos*, *Cirsium arvense*, *Solidago canadensis*, *Tanacetum vulgare*, etc.), pioneer tree species (*Betula pendula*, *Salix caprea*, *Populus tremula*), and bare soil was identified on the piste by Mikloš et al. (2018b). According to the data from 1961 to 1990 and the Czechoslovak climate classification modified in Landscape Atlas of the Slovak Republic (2002), the climate is moderately warm with cool to cold winters, mean annual temperature and precipitation of 5.5°C and 850 mm, mean January temperature and precipitation of –5°C and 45 mm, respectively (Šťastný et al., 2002; Faško and Šťastný, 2002), and duration of 36.7-cm-thick mean snow depth of 90 days on average (Faško et al., 2002; Štáala et al., 2017).

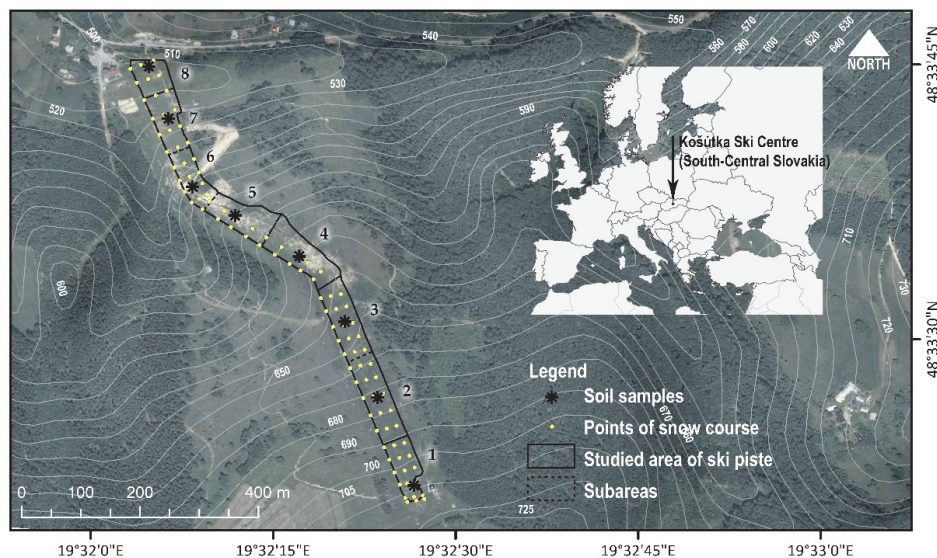


Fig. 1. Ski slope of Košútka ski center (Central Europe; South-Central Slovakia) with defined boundaries of ski piste area and eight subareas. Positions where the soil samples were taken and where the snow depth was measured (snow course) are displayed. Orthophotomap is from 2012.

Soil temperature and characteristics of ski piste snowpack

Soil temperature was logging continuously during the studied ablation period of season 2015 and 2016 in the hourly intervals on the snow-covered and snow-free part of ski piste. Data loggers Minikin Tie with built-in sensor and 20-mm diameter measured soil temperature 3 to 5 cm under the ground surface with $\pm 0.15^\circ\text{C}$ accuracy. Data loggers were placed into the relatively homogenous soil with similar environmental conditions. Data logger on the snow-covered part of ski piste was situated close to the snowmaking lance where the ski piste snowpack with addition of artificial snow has the longest duration and highest snow depth (Mikloš et al., 2018b). Natural snow absented at the time of measuring. Air temperature was recorded by its own meteorological station, which was localized at the base of ski slope of ski center Košútka. Online meteorological data of this station can be accessed from www.emsbrno.cz.

Snow depth and snow density of groomed snowpack with additional artificial snow were measured on the studied ski piste area of 4.1 ha at the end of five winter seasons from 2010–2011 to 2015–2016, except for season 2013–2014 (ski center was out of service). The first survey in each of five seasons was carried out after disappearance of natural snow on the off-piste sites at all elevations and then subsequently until the end of melting in the irregular time intervals. Ski piste (4.1 ha) represented the marked area of ski slope under the winter management (grooming, snowmaking). Snow depth was measured at 96 points, whereas snow density was at least 5 points of snow course (Figure 1). Snow water equivalent was calculated for each of the 96 points of snow course from snow depth and mean snow density identified in the particular survey. Technique of measuring the snow depth and density is described in more detail by Mikloš et al. (2018a) and in general by, for example, López-Moreno et al. (2013). In the first survey of the first three seasons, the depth of basal or bare ice layer was measured at 96 points of snow course. Basal ice could have occurred on the bottom of snowpack, whereas bare ice could have occurred instead of snow.

Snow ablation water volume and potential infiltration

The ski piste area under the winter management (grooming, snowmaking) was divided into eight continuous subareas because of different soil properties, slope, and aspect. For each subarea and survey, the snow water volume and the snow-free ski piste area were calculated from the model of interpolated SWE. An SWE model with raster value of $1\text{ m} \times 1\text{ m}$ was created in ArcGIS 10.3.1 by the interpolation technique spline from 96 points of manual snow depth measurements, which were multiplied by the mean snow density. Mean density instead of interpolated density was used because of the small number of density measurements (time-consuming measurement), which were performed on at least five points of the snow course. Area of positive values of the SWE model represented the snow-covered area, whereas area of negative and zero values of the SWE model represented the snow-free area. Snow water volume stored in snowpack (in millimeters) was calculated from the SWE model as sum of positive raster values divided by the snow-covered area. If the time interval between the two surveys was longer than 8 days, the additional intermediate SWE model was created between these two surveys. The intermediate SWE model was created from the SWE of 96 points that were modeled by the linear relationship between two neighboring surveys. The difference of two subsequent snow water volumes represented the snow ablation water volume.

Ablation rate was calculated by dividing the snow ablation water volume by the number of days between particular snow water volumes (Boon, 2009). The ablation period in the presented study means the period from the disappearance of natural snow on the off-piste sites until the melt of ski piste snowpack on the studied area. The ski piste snowpack was considered melted when less than 5% of the observed area (4.1 ha) was covered by snow, and similarly, the natural snowpack on the off-piste sites was considered melted when less than 5% of the adjacent off-piste area was covered by snow in all elevations and aspects.

Potential infiltration on the studied area is limited by the frozen soil below the snowpack; therefore, potential infiltration of snow ablation water was calculated only for the snow-free part of each subarea. For this purpose, snow ablation water volume had to be calculated from the SWE model in cubic meters instead of millimeters. To identify the potential infiltration of snow ablation water volume, the ablated water volume (in cubic meters) was compared with maximum volume of water (V_i) that was able to infiltrate between the two surveys on the snow-free subarea. If ablated water volume was higher than V_i , the difference represented noninfiltrated volume of water. Potentially infiltrated volume of water in eight subareas was summed together and transferred to millimeters (divided by the snow-free area) for better interpretation of the results.

The maximal volume of water (V_i) was calculated as follows:

$$V_i = (K_{\text{SAT}} S t) - V \quad (1)$$

where K_{SAT} is saturated hydraulic conductivity of soil on subarea, S is snow-free area identified at the first of two measurement dates, t is sum of hours when average hourly air temperature was higher than 0°C , and V is total rainfall volume fallen on the snow-free subarea (S).

One soil sample from a depth of 0 to 20 cm was taken from the middle of each subarea, to determine grain size fraction distribution. Preparation of soil samples for laser diffraction analysis was described in detail by Šinkovičová et al. (2017). The analyses were performed with use of an analyzer ANALYSETTE 22 MicroTec plus (Fritsch GmbH, Idar-Oberstein, Germany). Each soil sample was analyzed three times, and subsequently average value was calculated. If the soil was fully saturated by the meltwater, the saturated hydraulic conductivity expressed the rate of water movement through soil (Schoeneberger et al., 2002). Soil type and percentage of clay/silt/sand in the soil samples are specified in Table 1.

Table 1. Percentages of clay, silt and sand in the eight samples. The percentages are used for determination of soil type (according to USDA soil texture triangle).

Subarea No.	Clay % (<0.002 mm)	Silt % (0.002–0.05 mm)	Sand % (0.05–2 mm)	Soil type (USDA classification)
1	4.9	90.04	4.7	Silt
2	3.5	83.6	12.9	Silt
3	3.6	80	16.4	Silt loam
4	5.1	87.8	7.1	Silt
5	4.3	89.6	6.1	Silt
6	3.6	78.2	18.2	Silt loam
7	3.8	87.2	9	Silt
8	3.8	83.3	12.9	Silt

Saturated hydraulic conductivity (K_{SAT} in m/s) was determined from the results of grain size analyses, according to the following equation (Špaček, 1987):

$$K_{SAT} = 20.577d_{10}^{1.013} \left(\frac{0.5}{d_{60} - d_{10}} \right)^{0.059} \quad (2)$$

where d_{10}/d_{60} represents size in millimeters, such that 10%/60% of particles are finer than this size.

RESULTS

Characteristics of the ski piste snowpack

Five seasons' mean snow density of ski piste snowpack was $621.6 \pm 107.3 \text{ kg/m}^3$ (Figure 2). Mean snow density during the ablation period had a decreasing trend in seasons 2011, 2015, and 2016 and increasing trend in seasons 2012 and 2013 (Figure 2a). The lowest minimal density (137 kg/m^3) was measured in season 2013. Ski piste snowpack ablation period started at the latest in season 2013, with the lowest surveyed mean snow density. In each of the five seasons, density greater than 800 kg/m^3 was measured, which is the density close to the density of ice. The highest maximal and mean snow density was identified in the first survey in season 2015. Between mean snow density and corresponding depth average, the mean snow depth of the first survey in the seasons was identified to have a strong positive correlation ($r = 0.93$; Figure 2b). Moreover, with the earlier date of the first survey, the mean snow depth ($r = 0.47$) and mean snow density ($r = 0.63$) of the first survey in the season were higher.

In the scale of the ablation period, negative correlation was found between snow depth and depth average snow density, in all of five seasons (Figure 3a). The snow density increased with decreasing snow depth by approximately 1 kg/m^3 per 1 cm if the data of all five seasons were analyzed. The depth average snow density increased with decreasing snow depth also because of the basal ice layer formation from the melted ski piste

snowpack. During the three seasons, when the basal/bare ice layer occurrence was observed in the first survey in the season, the depth of the basal/bare ice layer increased from 0.04 to 0.12 cm per each 1 cm of decreasing snow depth (Figure 3b). Calculation of these trends taken into the account even measurements where only snow or bare ice was identified. Probability of basal ice layer occurrence in the bottom of snow profile was 57% (calculated from 176 measurements), while probability of bare ice layer occurrence instead of snow was 18% (calculated from 215 measurements).

In the each of the five studied seasons, the snow depth and the SWE of ski piste snowpack were highly variable after snowmelt of natural snow on the off-piste sites (Figure 4). While some parts of the studied ski piste area were covered by thick snowpack, the other parts were completely melted (Figures 4, 5). The maximum snow depth and SWE in the first survey in each of the five seasons were always higher than 100 cm and 800 mm , respectively (Figure 4). The highest maximum snow depth and SWE (225 cm and 1229 mm , respectively) were identified in season 2013, whereas the highest mean snow depth (57 cm and 349 mm , respectively) was identified in season 2012. The five seasons' average mean snow depth and mean SWE from the first surveys were 45 cm and 280 mm , respectively (mean snow depth on the studied area of ski piste). The decrease in mean snow depth during the studied ablation periods varied from 0.6 cm/d in season 2016 to 2.1 cm/d in season 2011 (five seasons' average, 1.5 cm/d). The mean SWE decreased on the studied area of ski piste in a different trend from snow depth because of the changing snow density over the studied ablation period. The decrease in SWE during the ablation periods varied from 4 mm/d in season 2016 to 12.7 mm/d in season 2011 (five seasons' average, 9.5 mm/d). The authors note that the mean snow depth was calculated from 96 points of snow course including zero values.

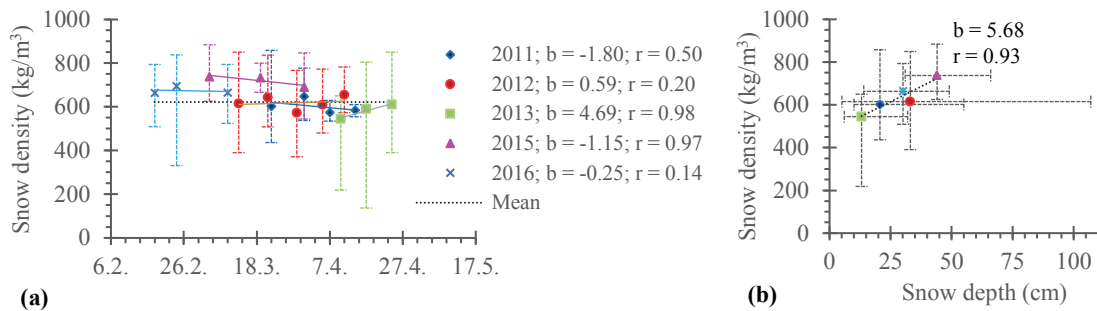


Fig. 2. (a) Trend of mean snow density over the ablation period of ski piste snowpack in five seasons; (b) Correlation between mean snow depth and mean snow density at first survey in the season. Signs indicate mean density. Bars indicate the maximum and minimum values measured in each survey. Horizontal dot line indicates mean density calculated from all surveys.

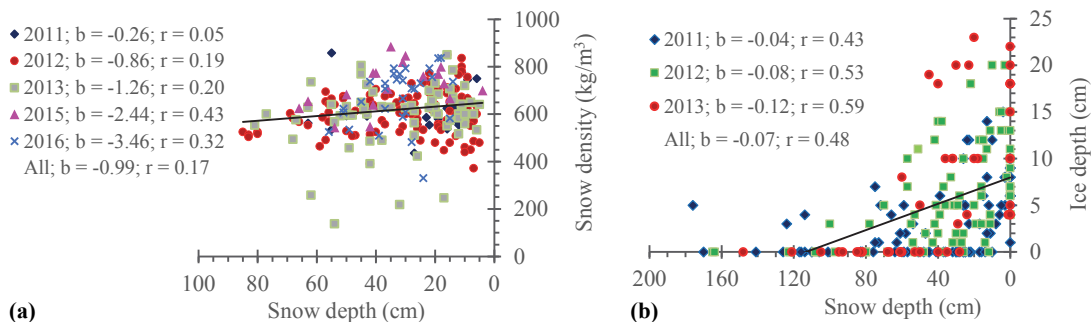


Fig. 3. (a) Correlation between snow depth and snow density at the individual seasons; (b) Correlation between snow depth and depth of basal or bare ice layer. Signs indicate individual measurements while solid lines indicate trend calculated from all displayed measurements.

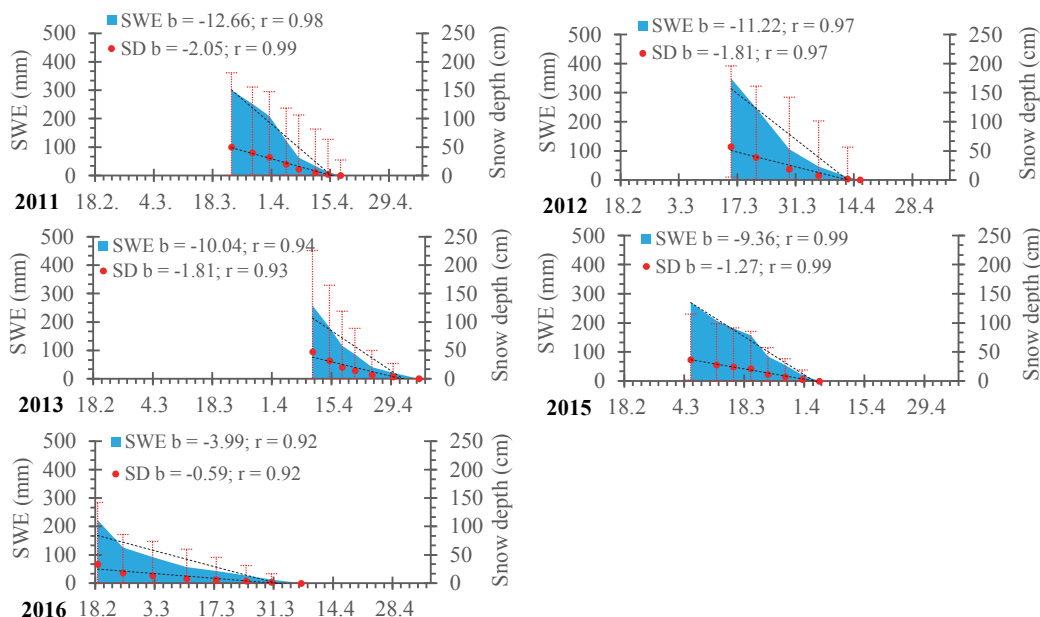


Fig. 4. Decrease of mean snow water equivalent (SWE) and mean snow depth (SD) on the ski piste during ablation period in the five seasons after snowmelt of natural snow on the off-piste sites. Bars indicate the maximum and minimum snow depth measured in each survey. Dash lines indicates trends.

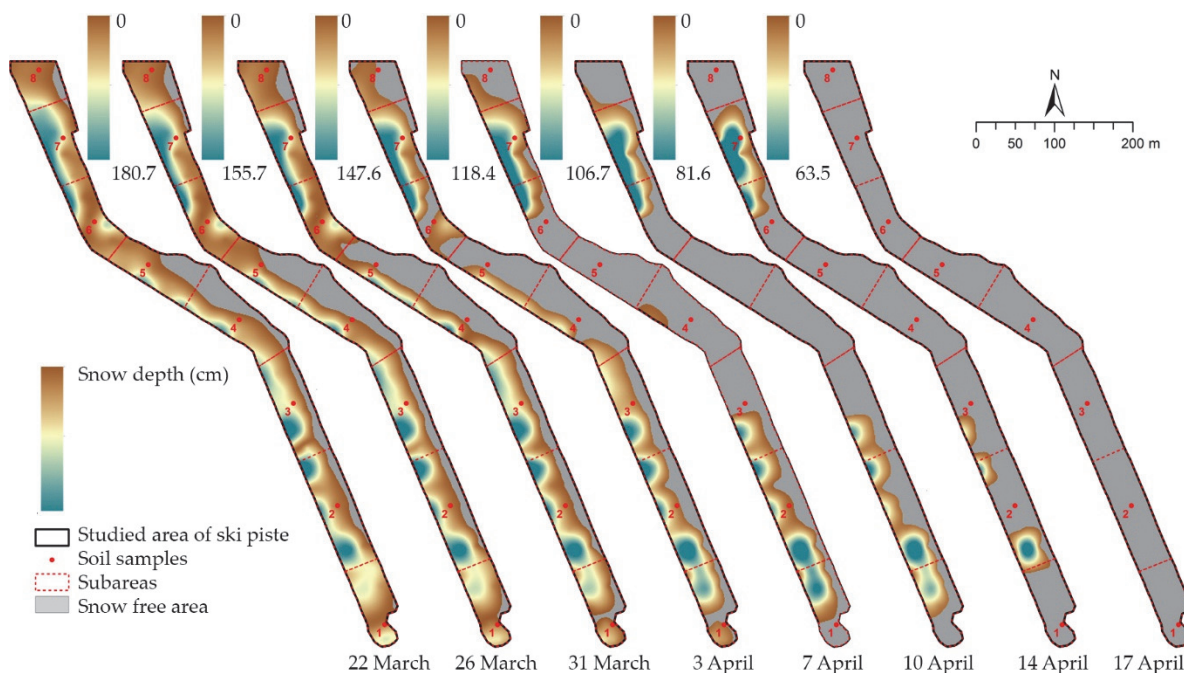


Fig. 5. Development of snowpack and snow-free area on the ski piste during ablation period of winter season 2010–2011.

Soil temperature

During the observed period, the top soil layer on the snow-covered part of ski piste with snowpack occurrence was constantly frozen, even when hourly air temperature reached its maximum of 15°C in season 2015 (Table 2). Mean hourly soil temperature under the snowpack varied maximally 1°C around zero. At the same period, the mean top soil hourly temperature on the snow-free part of ski piste was 3°C in season 2015 and 4°C in season 2016. The maximal hourly soil temperatures on the snow-free part were 12°C and 11°C, respectively. Because of the frozen top soil layer under the ski piste snowpack, the infiltration below the snowpack was limited.

Table 2. Mean, minimal and maximal hourly soil and air temperature (in °C; mean ± standard deviation) during observed period (seasons 2015 and 2016). Soil temperature was logged on the snow-covered part and on the snow-free part of ski piste.

	Soil temperature (Snow) (°C)		Soil temperature (Snow-free) (°C)		Air temperature (°C)	
	2015	2016	2015	2016	2015	2016
Mean	-0.1 ± 0.0	-0.2 ± 0.2	2.9 ± 2.4	3.6 ± 2.1	4.6 ± 4.5	3.5 ± 3.3
Min	-0.2	-1.0	-0.6	0.1	-4.2	-3.8
Max	0.0	0.9	11.9	11.4	15.1	12.0

Ski piste snowpack snow ablation water volume versus potential infiltration

The rate of water movement through soil (saturated hydraulic conductivity) on the ski piste was identified as 89.8 ± 9.5 mm of water per day on average (Table 3). The highest saturated hydraulic conductivity (K_{SAT}) was identified on subarea number 2 (97.5 ± 1.4 mm/d). The average K_{SAT} (89.8 mm/d) could be ranked according to Schoeneberger et al. (2002) as moderately high K_{SAT} class, whose boundaries are 86.4 to less than 864.0 mm/d. The average rate of water movement through soil was 6.8 times as high as the five seasons' average ablation rate of ski piste snowpack (89.9 vs. 13.3 ± 6.1 mm/d). The ablation rate was highly variable during the ablation period and also between the seasons (Figure 6). In season 2011, the highest average ablation rate of 17 ± 7 mm/d and the steepest increasing seasonal trend of 5 mm/d were identified; thus, the ablation period in this season was the second shortest (26 days) from the five studied seasons. On the contrary, because of the lowest average ablation rate of 9 ± 5 mm/d and decreasing seasonal trend of 2 mm/d in season 2016, the ablation period of ski piste snowpack in this season was the longest (47 days).

Because of frozen soil below the snowpack, the infiltration on the studied area was limited to the snow-free part. At the beginning of each ablation period (first survey), the snow ablation water volume to the snow-free area was the highest because of the lowest snow-free area that represented 12% of

Table 3. d_{10}/d_{60} represents a size of particles on the subareas, such that 10%/60% of particles are finer than this size (mean \pm standard deviation). On each subarea, the mean value \pm standard deviation (SD) of saturated hydraulic conductivity (K_{SAT}) was calculated from three soil samples (mean \pm SD).

Subarea No.	Subarea (m ²)	d_{10} (μ m)	d_{60} (μ m)	K_{SAT} (mm/day)
1	4131	3.2 ± 0.1	14.0 ± 0.0	76.3 ± 1.4
2	6833	4.2 ± 0.1	17.0 ± 0.0	97.5 ± 1.4
3	6122	4.1 ± 0.0	17.2 ± 0.8	95.8 ± 0.3
4	6653	3.1 ± 0.0	10.7 ± 0.1	74.3 ± 0.1
5	5443	3.7 ± 0.1	10.9 ± 0.1	87.9 ± 2.8
6	3950	4.1 ± 0.1	11.4 ± 0.0	97.4 ± 1.4
7	4537	3.9 ± 0.1	11.1 ± 0.1	93.5 ± 2.5
8	3329	4.0 ± 0.0	11.2 ± 0.2	95.9 ± 0.1
Sum/Mean \pm SD	≈ 40999	3.8 ± 0.4	12.9 ± 2.8	89.8 ± 9.5

studied area on average (Figure 6). In the first survey in the season, the five seasons' average snow ablation water volume to the five seasons' average snow-free area was 137 ± 70 mm/m² and potentially infiltrated 43 ± 7 mm/m² (31%) (Figure 6a). At the beginning of season 2012, the highest snow ablation water volume to the snow-free area (247 mm/m²) was identified, but potentially infiltrated only 53 mm/m² (21%) because of the low snow-free area that represented 4% of the studied area. The snow-free area expanded over the five studied ablation periods in the comparable trends (Figure 6). The five seasons'

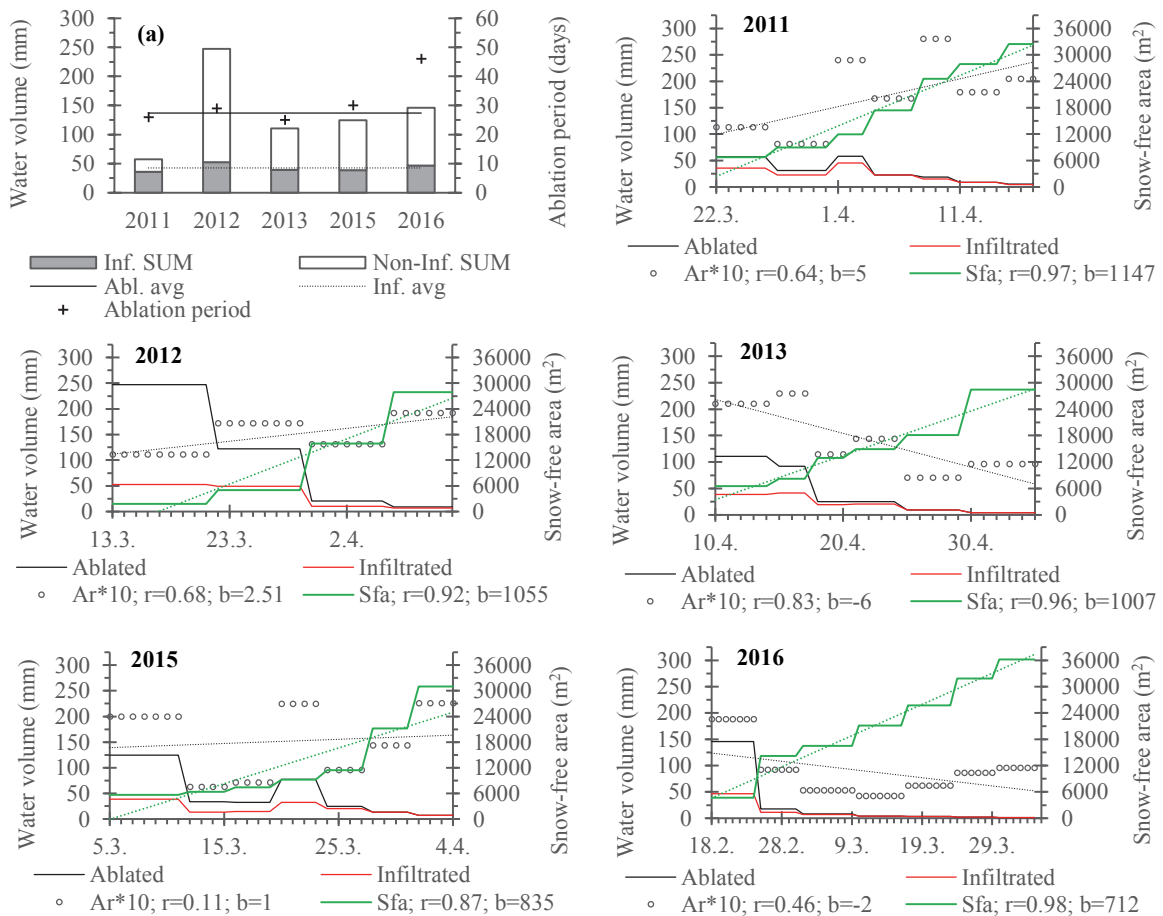


Fig. 6. (a) Infiltrated and non-infiltrated snow ablation water volume (abl.) to the snow-free area of ski piste, in the first survey in each season. Horizontal lines indicate averages (avg.) from displayed ablated and infiltrated water volumes while crosses indicate duration of ablation periods; (2011–2016) Modeled daily course of ablated and infiltrated water volume to the snow-free area of ski piste, modeled development of snow-free area (Sfa) during ablation period and modeled ablation rate of ski piste snowpack (Ar; multiplied by ten for visualization). Black dot line indicates trend of ablation rate while green dot line indicates trend of snow-free area over the ablation period.

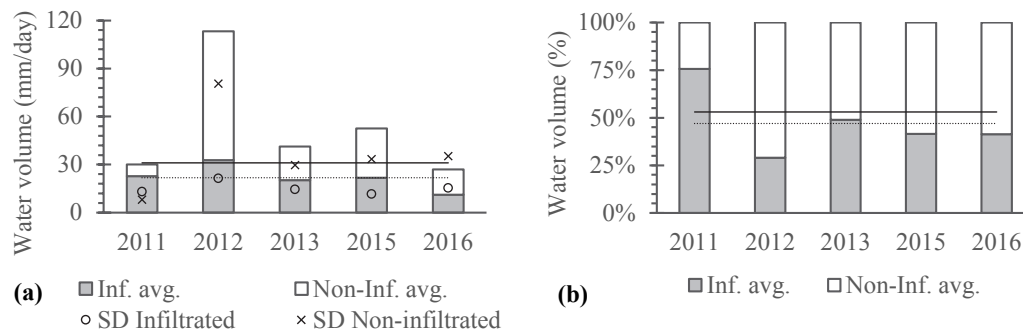


Fig. 7. (a) Average and (b) percentage of infiltrated and non-infiltrated (sum = ablation) snow ablation water volume during ablation period to the snow-free ski piste area. Signs indicate standard deviation (SD) of average values. Horizontal lines indicate mean from displayed values (solid line = non-infiltrated volume; dot line = infiltrated volume).

average slope of trend of snow-free area was $951 \pm 175 \text{ m}^2/\text{d}$. Decrease in snow ablation water volume to the snow-free area and simultaneous expansion of the snow-free area from the first survey resulted to an increase in potentially infiltrated water volume on the snow-free square meter over the ablation periods. At the end of each ablation period, except season 2012, all the ablated water volume was potentially able to infiltrate the snow-free area. Increase in the ablated water volume over the ablation period was identified only one time in season 2011 and 2015, when comparable conditions occurred. The snow-free areas at this time were 11,968 and 9213 m^2 , whereas ablation rates were 23 and 22 mm/d , respectively.

In the five seasons' average, the water volume of $22 \pm 8 \text{ mm}/\text{d}$ potentially infiltrated during 31 ± 9 -day-long ablation period on the snow-free ski piste area (Figure 7a). This water volume represented 47% ($53 \pm 35 \text{ mm}$) of the ablated water volume per day on average on the snow-free 1 m^2 of ski piste area (Figure 7b). In each of the five seasons, except season 2011, the average potential infiltration on the snow-free ski piste area represented less than 50% of ablated water. In season 2011, the potential infiltration represented 76% of ablated water on average because of the low ablation rate and high snow-free area at the first surveys compared with other seasons. On the contrary, the lowest percentage of ablated water potentially infiltrated in season 2012 (29%). It was because season 2012 started and continued with high ablated water volumes that were not able to potentially infiltrate because of the low snow-free ski piste area in the first two surveys.

DISCUSSION

Characteristics of the ski piste snowpack and soil temperature

This study confirms the results of Rixen et al. (2003), Keller et al. (2004), and Mossner et al. (2013), which found high-density snowpack on the ski pistes of European Alps. They reported that mean density on the groomed ski pistes with artificial snow varied between 500 and 600 kg/m^3 on average. Our study from Košútka ski center (Central Europe, Western Carpathians) showed the higher mean snow density of 622 kg/m^3 probably due to intensive snowmaking in this ski center (Mikloš et al., 2018a) and late datum of measuring (end of winter season). The impact of wind packing that enhances snow density (Vihma, 2011) was negligible because of the low wind speed in the studied locality (Mikloš et al., 2018a). In contrast to the mentioned studies, the presented study was focused on the ablation period of ski piste snowpack, at the end of the winter season. Thus, the high maximal density of snow greater than

800 kg/m^3 and ice layer occurrence in the base of snowpack or ice instead of snowpack were found at the end of the season on the studied ski piste. Keller et al. (2004) also found increasing compaction of ski piste snowpack over the time while it becomes a mixture of ice and hard snow with a maximum density of 700 kg/m^3 . Because of the high density and depth of the studied ski piste snowpack, the prolongation of the ablation period to about 29 days was identified (Mikloš et al., 2018a). Snow density increases over the time because of dry and wet metamorphism of snow (Domine, 2011); however, the increasing tendency of snow density was not identified in all of the five studied seasons. It is probably due to the late datum of measuring and subsequently high above-zero daily temperatures in the studied locality when snow ablation water did not refreeze in the snowpack but instead drained or sublimated. In the presented study, negative correlation was identified between snow depth and snow density, probably due to the observed basal ice layers in the ski piste snowpack. These findings are supported by Rixen et al. (2003; 2004) and Fauve et al. (2002), which attribute the occurrence of ice layers to snow compaction by the heavy machinery and warm conditions during the snow production. Both compaction and higher temperatures during snowmaking were identified in our previous study carried out in the same low-elevation Košútka ski center (Mikloš et al., 2018a). Ice occurrence instead of snowpack in the late winter was not described by other authors. This phenomenon can be explained by the occurrence of hot days and cold nights during winter time (Mikloš et al., 2018a) and the isothermal conditions that render the artificial snow more prone to melting and re-freezing during daytime (Vihma, 2011).

High density of the studied ski piste snowpack resulted in the high SWE at the end of winter season. Hříbik et al. (2012), who studied natural snowpack 10 km away from Košútka ski center in the comparable elevation, identified maximum above-average mean SWE of 170 mm in March 2005 and February 2006 (studied seasons from 2004 to 2009). For comparison, the maximum mean SWE of the studied ski piste snowpack was 349 mm in March 2013, whereas after snowmelt of natural snow on the adjacent off-piste sites, the mean SWE of ski piste snowpack was 280 mm. The studied ski piste snowpack showed high snow depth maxima due to the essential high production of artificial snow (Mikloš et al., 2018a). The maximum snow depth of studied ski piste snowpack was 225 cm in April 2013, whereas the maximum snow depth of natural snow identified by Hříbik et al. (2012) was 70 cm in winter 2005 and 2006 (whole season average is 30 cm). Rixen et al. (2004) compared snow depth and SWE of the groomed/snowed ski piste snowpack with natural undisturbed snowpack in the Swiss ski cen-

ters greater than 1000 m a.s.l. at the turn of February and March 2000. They found comparable differences (approximately 40 cm and 300 mm) with the presented research from Košútka ski center (45 cm and 280 mm) where measurements for this comparison were performed directly after disappearance of natural snowpack from the off-piste sites.

The presented study confirms long-lasting soil frost beneath the snowed and groomed ski piste snowpack as reported by Rixen et al. (2003; 2004) on the Swiss pistes. Kammer (2002) and Rixen et al. (2008) proved long-lasting soil frost with high depth and density of ski piste snowpack, which extends the snow ablation period. The presented study confirms their findings and shows high difference in top soil temperature between snow-covered and snow-free sites on the piste, even at 12°C. The occurrence of basal ice layers and frozen top soil layer below the studied snowpack results in restricted infiltration of snow ablation water on the snow-covered area. Similarly, Gray et al. (2001) pointed out that soil infiltrability is restricted by impervious surface as the basal ice lens found on the pistes by Rixen et al. (2004).

Snow ablation water volume and potential infiltration

There is a negligible number of studies that describe snow ablation processes on the ski pistes and subsequently quantify their balance (infiltration, sublimation, evaporation, surface runoff). The presented study shows that the mean seasonal ablation rate on the ski piste ranged between 9 and 17 mm/d at the end of winter season. Ablation rate is difficult to compare between studies because of the specific characteristics of ski piste snowpack and microclimatic conditions (energy balance) of research localities. For example, the ablation rate of natural snowpack in Fraser Lake (700 m a.s.l., 53.72° N, 124.92° W) is lower than that in Košútka ski center (610 m a.s.l., 48.56° N, 19.54° E) varying between 11 and 14 mm/d. It is probably due to the northern latitude (approximately 5° N) and different climatic conditions of locality (North America). However, Mosimann (1998) and Rixen et al. (2004) declare that the snow ablation rate of ski piste snowpack is lower than the natural undisturbed snowpack because of the increased snow mass (snowmaking), ice layers in snow profile, spherical shape of ice crystals, and long-lasting soil frost below the ski piste snowpack. These findings confirm the presented study because of the prolonged ablation period of ski piste snowpack of approximately 1 month, while increased snow mass, ice layers, and soil frost on the ski piste were observed.

Infiltration of water into soil is dependent on the rate of water movement through soil (saturated hydraulic conductivity [K_{sat}]), which was identified as moderately high (90 mm/d) for the modal cambisol of the studied ski piste. This K_{sat} was low compared with the study on Californian ski pistes in Tahoe Basin (2000 m a.s.l., approximately 39° N, 120° W), where mean K_{sat} was 7968 mm/d on granitic soil and 5952 mm/d on the volcanic soil (Grismer and Hogan, 2005). High K_{sat} is the result of large average particle sizes; however, the larger particle sizes suggest larger erosion events that were seen in Tahoe Basin (Grismer and Hogan, 2005). The presented study assumes with bare soil surface the calculation of infiltration; however, some parts of ski piste were covered by meadow vegetation, which can decrease the infiltration rate (Dunne et al., 1991; Lichner et al., 2018). Anyway, less disturbed soil surface and vegetation cover of ski pistes mean more water to be held in soil (Pintar et al., 2009). Infiltration of snow ablation water on the area of ski piste was limited to snow-free areas; therefore, not all ablation water could infiltrate. The part of the

discussion about the volume of infiltrated snow ablation water to the soil profile of ski piste is omitted because of lack of studies dealing with this issue. The presented study showed that ski piste snowpack properties and duration of the ablation period in low-elevation ski center are comparable with the findings of other studies, even from higher elevations greater than 1000 m a.s.l. Therefore, the methods used for calculation of the ablation and infiltration can be used in these regions, while it can be assumed that the results will differ, depending on the snowpack and soil properties and the meteorological conditions of the study sites.

CONCLUSIONS

This study shows that after snowmelt of natural snow on the off-piste sites the high volume of water is still stored in the groomed ski piste snowpack with additional artificial snow. The density of such snowpack is highly variable, while it can reach the density of ice. With lower snow depth, higher snow density and higher thickness of basal ice layer or bare ice (ice instead of snow) can be expected. The depth and SWE of such snowpack are even highly heterogeneous over the piste (marked, groomed, and snow-covered part of ski slope). Whereas some parts of the ski piste are completely melted, the others could be covered by 200-cm-thick snowpack with SWE higher than 1000 mm. The SWE of the remaining snowpack decreases 9.5 mm/d during 1-month-long ablation period on average. The ablation rate of ski piste snowpack is lower than water movement through soil. However, not all snow ablation water is potentially able to infiltrate the ski piste because of the frozen top soil layer below the snowpack and the low snow-free area. As the snow-free area increases during the ablation period over the ski piste, the higher water volume is potentially able to infiltrate the piste. Nearly 50% of snow ablation water is potentially able to infiltrate the area of ski piste on average.

Acknowledgements. This work was accomplished as a part of VEGA projects nos. 1/0500/19, 1/0111/18, and 1/0064/19 of the Ministry of Education, Science, Research, and Sport of the Slovak Republic and the Slovak Academy of Science and the projects of the Slovak Research and Development Agency nos. APVV-15-0425, APVV-18-0347, APVV-15-0160, and APVV-15-0497. The authors thank the agencies for their support.

REFERENCES

- Babálová, D., Škvareninová, J., Fazekaš, J., Vyskot, I., 2018. The dynamics of the phenological development of four woody species in South-West and Central Slovakia. *Sustainability*, 10, 1497.
- Bark, R.H., Colby, B.G., Dominguez, F., 2010. Snow days? Snowmaking adaptation and the future of low latitude, high elevation skiing in Arizona, USA. *Clim. Change*, 102, 467–491.
- Barnett, T.P., Adam, J.C., Lettenmaier, D.P., 2005. Potential impacts of a warming climate on water availability in snow-dominated regions. *Nature*, 438, 303.
- Bartík, M., Sitko, R., Oreňák, M., Slovík, J., Škvarenina, J., 2014. Snow accumulation and ablation in disturbed mountain spruce forest in West Tatra Mts. *Biologia*, 69, 1492–1501.
- Beniston, M., 2007. Entering into the ‘greenhouse century’: recent record temperatures in Switzerland are comparable to the upper temperature quantiles in a greenhouse climate. *Geophys. Res. Lett.*, 34, 16710.

- Boon, S., 2009. Snow ablation energy balance in a dead forest stand. *Hydrol. Process.*, 23, 2600–2610.
- Cayan, D.R., Kammerdiener, S.A., Dettinger, M.D., Caprio, J.M., Peterson, D.H., 2001. Changes in the onset of Spring in the Western United States. *Bull. Am. Met. Soc.*, 82, 399–415.
- Damm, A., Köberl, J., Pretenthaler, F., 2014. Does artificial snow production pay under future climate conditions? – A case study for a vulnerable ski area in Austria. *Tourism Manage.*, 43, 8–21.
- De Jong, C., Barth, T., 2008. Challenges in hydrology of mountain ski resorts under changing climatic and human pressures. In: *ESA Proceedings Surface Water Storage and Runoff: Modeling, In-Situ data and Remote Sensing*. Geneva.
- Domine, F., 2011. Physical properties of snow. In: Singh, V.P., Singh, P., Haritashya, U.K. (Eds.): *Encyclopedia of Snow, Ice and Glaciers*. London: Springer, pp. 66–75.
- Dunne, T., Zhang, W., Aubry, B.F., 1991. Effects of rainfall, vegetation, and microtopography on infiltration and runoff. *Water Resour. Res.*, 27, 2271–2285.
- EMS Brno. Available online: <http://www.emsbrno.cz/p.axd/sk/Lokality.TUZVO.html> (accessed on 2 October 2019).
- Faško, P., Šťastný, P., 2002. Mean annual precipitation totals, Mean January precipitation totals. In: Miklós, L., Hrnčiarová, T., (Eds.): *Landscape atlas of the Slovak Republic. Revised 1st printing*. Slovak Environmental Agency, Bratislava, p. 99.
- Faško, P., Handžák, S., Šrámková, M., 2002. Number of days with snow cover and the mean height of snow cover. In: Miklós, L., Hrnčiarová, T. (Eds.): *Landscape Atlas of the Slovak Republic. Revised 1st printing*. Slovak Environmental Agency, Bratislava, p. 99.
- Fauve, M., Rhyner, H., Schneebeli, M., 2002. *Pistenpräparation und Pistenpflege – Das Handbuch für den Praktiker*. Eidgenössisches Institut für Schnee- und Lawinenforschung, Davos.
- Freppaz, M., Filippa, G., Corti, G., Cocco, S., Williams, M.W., Zenini, E., 2012. Soil properties on ski runs. In: Rixen, C., Rolando, A. (Eds.): *The Impact of Skiing on Mountain Environments. Revised 1st printing*. Bentham Science Publishers, Bussum, pp. 45–64.
- Gilaberte-Búrdalo, M., López-Martín, F., Pino-Otín, M.R., López-Moreno, J.I., 2014. Impact of climate change on ski industry. *Environ. Sci. Policy*, 44, 51–61.
- Gray, D.M., Granger, R.J., Landine, P.G., 1986. Modelling snowmelt infiltration and runoff in a Prairie environment. In: Kane, D.L. (Eds.): *Proceedings of the Cold Regions Hydrology Symposium*. University of Alaska-Fairbanks, Fairbanks, Alaska. American Water Resources Association, Bethesda, Maryland, pp. 427–438.
- Gray, D.M., Toth, B., Zhao, L., Pomeroy, J.W., Granger, R.J., 2001. Estimating a real snowmelt infiltration into frozen soils. *Hydrol. Process.*, 15, 3095–3111.
- Grismer, M. E., Hogan, M. P., 2005. Simulated rainfall evaluation of revegetation/mulch erosion control in the Lake Tahoe basin: 2. Bare soil assessment. *Land. Degrad. Dev.*, 16, 397–404.
- Gömöryová, E., Šťelcová, K., Škvarenina, J., Gömöry, D., 2013. Responses of soil microorganisms and water content in forest floor horizons to environmental factors. *Eur. J. Soil Biol.*, 55, 71–76.
- Hříbik, M., Vida, T., Škvarenina, J., Škvareninová, J., Ivan L., 2012. Hydrological effects of Norway spruce and European beech on snow cover in a mid-mountain region of the Polana Mts. *J. Hydrol. Hydromech.*, 60, 319–332.
- Hrvol', J., Horecká, V., Škvarenina, J., Šťelcová, K., Škvareninová, J., 2009. Long-term results of evaporation rate in xerothermic Oak altitudinal vegetation stage in Southern Slovakia. *Biologia.*, 64, 605–609.
- Igaz, D., Bárek, V., Halaj, P., Takáč, J., Čimo., 2008. A comparison of measured soil moisture with simulated results obtained by selected models for Danubian lowland. *Cereal Research Communications*, 36, 1619–1622.
- Kammer, P.M., 2002. Floristic changes in subalpine grasslands after 22 years of artificial snowing. *J. Nat. Conserv.*, 10, 109–123.
- Keller, T., Pielmeier, C., Rixen, C., Gadiant, F., Gustoffson, D., Stahli, M., 2004. Impact of artificial snow and ski-slope grooming on snowpack properties and soil thermal regime in a sub-alpine ski area. *Ann. Glac.*, 38, 314–318.
- Kňazovičová, L., Chasníková, S., Novák, J., Barančok, P., 2018. Impacts of ski pistes preparation and ski tourism on vegetation. *Ekol. Bratislava*, 37, 152–163.
- Laternser, M., Schneebeli, M., 2003. Long-term snow climate trends of the Swiss Alps (1931–99). *Int. J. Climatol.*, 23, 733–750.
- Lichner, L., Felde, V.J.M.N.L., Büdel, B., Leue, M., Gerke, H.H., Ellerbrock, R.H., Kollár, J., Rodný, M., Šurda, P., Fodor, N., Sándor, R., 2018. Effect of vegetation and its succession on water repellency in sandy soils. *Ecohydrology*, 11, 6, Article Number: UNSPe1991.
- López-Moreno, J.I., Fassnacht, S.R., Heath, J.T., Musselman, K.N., Revuelto, J., Latron, J., Morán-Tejada, E., Jonas, T., 2013. Small scale spatial variability of snow density and depth over complex alpine terrain: Implications for estimating snow water equivalent. *Adv. Water. Resour.*, 55, 40–52.
- Melanie, P., Rixen, C., 2014. Management, winter climate and plant-soil feedbacks on ski slopes: a synthesis. *Ecol. Res.*, 29, 583–592.
- Mikloš, M., Jančo, M., Koristeková, K., Škvareninová, J., Škvarenina, J., 2018a. The suitability of snow and meteorological conditions of South-Central Slovakia for ski slope operation at low elevation – A case study of the Košútka Ski Centre. *Water*, 10, 907.
- Mikloš, M., Koristeková, K., Jančo, M., Váľková, M., 2018b. Vegetation of the selected Slovakian ski pistes. In: *Proceedings of International PhD Students Conference MendelNet*. Mendel University in Brno, Brno, pp. 201–204.
- Miklós, L., Hrnčiarová, T. (Eds.), 2002. *Landscape Atlas of the Slovak Republic. Revised 1st printing*. Slovak Environmental Agency, Bratislava, 344 p.
- Mind'áš, J., Škvarenina, J., 1995. Chemical composition of fog cloud and rain snow water in Biosphere Reserve Poľana. *Ekol. Bratislava.*, 14, Supplement 2, 125–137.
- Mosimann, T., 1998. *Beschneigungsanlagen in der Schweiz. Weitere Entwicklung Umweltverträglichkeit Folgerungen für die Prüfung und Bewilligung von Beschneigungsanlagen*. Schweiz. Verband der Seilbahnunternehmungen, Bubendorf and Hannover, 42 p.
- Mossner, M., Innerhofer, G., Schindelwig, K., Kaps, P., Schretter, H., Nachbauer, W., 2013. Measurement of mechanical properties of snow for simulation of skiing. *J. Glaciol.*, 59, 1170–1178.
- Mote, P.W., Hamlet, A.F., Clark, M.P., Lettenmaier, D.P., 2005. Declining mountain snow pack in western North America. *Bull. Am. Met. Soc.*, 86, 39–49.
- Muchová, Z., Tárniková, M., Petrovič, F., 2015. A more detailed approach to the assessment of the water erosion threat for a territory. In: *SGEM 2015. STEP92 Technology*, Sofia, pp. 3–10.

- Nagy, V., Šurda, P., Lichner, L., Kovács, A. J., Milics, G., 2018. Impact of soil compaction on water content in sandy loam soil under sunflower. *J. Hydrol. Hydromech.*, 66, 416–420.
- Newesely, C., 1997. Auswirkungen der künstlichen Beschneigung von Schipisten auf Aufbau, Struktur und Gasdurchlässigkeit der Schneedecke, sowie auf den Verlauf der Bodentemperatur und das Auftreten von Bodenfrost. Dissertation, Naturwissenschaftliche Fakultät, Leopold Franzens Universität, Innsbruck.
- Ohmura, A., Wild, M., 2002. Is the hydrological cycle accelerating? *Science*, 298, 1345–1346.
- Pintaldi, E., Hudek, C., Stanchi, S., Spiegelberg, T., Rivella, E., Freppaz, M., 2017. Sustainable soil management in ski areas: threats and challenges. *Sustainability*, 9, 2150.
- Pintar, M., Mali, B., Kraigher, H., 2009. The impact of ski slopes management on Krvavec ski resort (Slovenia) on hydrological functions of soils. *Biologia*, 64, 639–642.
- Ristić, R., Kašanin-Grubin, M., Radić, B., Nikić, Z., Vasiljević, N., 2012. Land degradation at the Stara Planina ski resort. *Environ. Manage.*, 49, 580–592.
- Rixen, C., Stoeckli, V., Ammann, W., 2003. Does artificial snow production affect soil and vegetation of ski pistes? A review. *Perspect. Plant. Ecol.*, 5, 219–230.
- Rixen, C., Haerberli, W., Stoeckli, V., 2004. Ground temperatures under ski pistes with artificial and natural snow. *Arct. Antarct. Alp. Res.*, 36, 419–427.
- Rixen, C., Freppaz, M., Stoeckli, V., Huovinen, C., Huovinen, K., Wipf, S., 2008. Altered snow density and chemistry change soil nitrogen mineralization and plant growth. *Arct. Antarct. Alp. Res.*, 40, 568–575.
- Rixen, C., Dawes, M.A., Wipf, S., Hagedorn, F., 2012. Evidence of enhanced freezing damage in treeline plants during six years of CO₂ enrichment and soil warming. *Oikos*, 121, 1532–1543.
- Roux-Fouillet, P., Wipf, S., Rixen, C., 2011. Long-term impacts of ski piste management on alpine vegetation and soils. *J. Appl. Ecol.*, 48, 906–915.
- Schoeneberger, P.J., Wysocki, D.A., Benham, E.C., Broderick, W.D., 2002. Field Book for Describing and Sampling Soils: Version 2.0. National Soil Survey Center and Natural Resources Conservation Service, Lincoln, 228 p.
- Steger, C., Kotlarski, S., Jonas, T., Schär, C., 2013. Alpine snow cover in a changing climate: a regional climate model perspective. *Clim. Dynam.*, 41, 735–754.
- Steger, R., Mayer, M., 2008. Snowmaking and climate change future options for snow production in Tyrolean ski resorts. *Mt. Res. Dev.*, 28, 292–298.
- Steger, R., 2010. The impact of climate change on ski season length and snowmaking requirements in Tyrol, Austria. *Clim. Res.*, 43, 251–262.
- Szolgay, J., Gaál, L., Bacigál, T., Kohnová, S., Hlaváčová, K., Výleta, R., Parajka, J., Blöschl, G., 2016. A regional comparative analysis of empirical and theoretical flood peak-volume relationships. *J. Hydrol. Hydromech.*, 64, 367–381.
- Šatala, T., Tesař, M., Hanzelová, M., Bartík, M., Šípek, V., Škvarenina, J., Mindáš, J., Waldhauserová, P. D., 2017. Influence of beech and spruce sub-montane forests on snow cover in Poľana Biosphere Reserve. *Biologia*, 72, 854–861.
- Šinkovičová, M., Igaz, D., Kondrlová, E., Jarošová, M., 2017. Soil Particle Size Analysis by Laser Diffractometry: Result Comparison with Pipette Method. In: *IOP Conf. Series: Materials Science and Engineering*, 245, DOI: 10.1088/1757-899X/245/7/072025.
- Škvarenina, J., Tomlain, J., Hrvol', J., Škvareninová, J., 2009. Occurrence of dry and wet periods in altitudinal vegetation stages of West Carpathians in Slovakia: Time-Series Analysis 1951–2005. In: Střelcová, K., Matyas, C., Kleidon, A., Lapin, M., Matejka, F., Blazenec, M., Škvarenina, J., Holec, J. (Eds.): *Bioclimatology and Natural Hazards*. Revised 1st printing. Springer, Netherlands, pp. 97–106.
- Špaček, J., 1987. Stanovení koeficientu filtrace z totálních křivek zrnitosti. *Meliorace*, 1, 1–13.
- Šťastný, P., Nieplová, E., Melo, M., 2002. Mean annual air temperature, Mean January air temperature. In: Miklós, L., Hrnčiarová, T. (Eds.): *Landscape Atlas of the Slovak Republic*. Revised 1st printing. Slovak Environmental Agency, Bratislava, p. 98.
- Tárnik, A., Igaz, D., 2015. Quantification of soil water storage available to plants in the Nitra river basin. *Acta Scientiarum Polonorum*, 14, 209–216.
- Vido, J., Tadesse, T., Šustek, Z., Kandrik, R., Hanzelová, M., Škvarenina, J., Škvareninová, J., Hayes, M., 2015. Drought occurrence in Central European mountainous region (Tatra National Park, Slovakia) within the period 1961–2010. *Adv. Meteorol.*, 2015, 248728.
- Vihma, T., 2011. Atmosphere-snow/ice interactions. In: Singh, V.P., Singh, P., Haritashya, U.K. (Eds.): *Encyclopedia of Snow, Ice and Glaciers*. London: Springer, pp. 66–75.
- Wipf, S., Stoeckli, V., Bebi, P., 2009. Winter climate change in alpine tundra: plant responses to changes in snow depth and snowmelt timing. *Clim. Change*, 94, 105–121.
- Wipf, S., Rixen, C., 2010. A review of snow manipulation experiments in Arctic and alpine tundra ecosystems. *Polar Res.*, 29, 95–109.

Received 19 February 2019

Accepted 23 October 2019

The variability of ice phenomena on the rivers of the Baltic coastal zone in the Northern Poland

Jan Tadeusz Łukaszewicz^{*}, Renata Graf

Department of Hydrology and Water Management, Institute of Physical Geography and Environmental Planning, Faculty Geographical and Geological Sciences, Adam Mickiewicz University in Poznań, 61-680 Poznań, Poland.

^{*}Corresponding author. Tel.: (+48) 693 627 497. E-mail: janluk@amu.edu.pl

Abstract: The main purpose of the research was to determine the conditions affecting ice phenomena, including the three-phase cycle of ice: expansion, retention and decay of the ice cover on selected rivers of the Baltic coastal zone in the Northern Poland (Przymorze region). The analysis has been elaborated for the years 1951–2010 against the backdrop of currently occurring climatic changes, with particular emphasis on the development and phase variability of the NAO. The article presents the impact of the variability in atmospheric circulation which has manifested in an increase in air temperature, over the last 20 years, on thermal conditions during winter periods in the South Baltic Coastal Strip. The increase in air temperature has contributed to an increase in the temperature of river waters, thus leading to a shortening of the duration of ice phenomena on rivers in the Przymorze region. The article also brings to light an increased occurrence of winter seasons classified as cool, and a disruption in the occurrence of periods classified as normal over the last 30 observed years. The research has demonstrated a significant dependence between the seasonal change in air temperature and the variability of thermal conditions of water, which has a direct impact on the variability of the icing cycle of rivers in the Przymorze region. The authors also show that the variability in forms of ice phenomena for individual river sections is determined by the local factors, i.e. anthropogenic activity, impact of urbanized areas or inflow of pollutants.

Keywords: Ice phenomena; Rivers; Coastal zone; Air temperature; NAO; Water temperature.

INTRODUCTION

Ice phenomena are an inseparable element of river regime in temperate climate zones (Kreft, 2013; Prowse and Beltaos, 2002). They also play a key role in shaping this regime by modifying river flow (Klavins et al., 2009; Majewski, 2009). The intensity and frequency of occurrence for ice phenomena depends, in particular, on the predominant climatic conditions for a given area (Agafonova and Frolova, 2007; Frolova and Alekseevskiy, 2010). The primary factor determining the form and duration of ice phenomena on rivers is air temperature (Łukaszewicz, 2017b), the variability of which depends on atmospheric circulation (Girjatowicz et al., 2002; Graf and Tomczyk 2018; Kozuchowski and Degirmendžic, 2002; Łukaszewicz, 2017a; Marsz and Styszyńska, 2001; Niedźwiedz, 2002; Przybylak et al., 2003). Air temperature fluctuations determine the variability in thermal conditions for waters in a given catchment area (Graf, 2015; Jurgelėnaitė et al., 2012; Klavins et al., 2009; Łukaszewicz, 2017c; Webb and Nobilis, 2007), and consequently have a direct impact on the formation of various ice forms on rivers and water reservoirs (Ptak et al., 2016).

Significant influence on the occurrence and development of ice phenomena on rivers is also exerted by local environmental factors, such as the structure of the river bed, the river gradient, its autochthonous or allochthonous characteristics (Hester and Doyle, 2011; Kreft, 2013; Łukaszewicz, 2017b), and the percentage of underground water supplying the rivers (Graf, 2015). The conditions in which ice phenomena form on rivers are also significantly affected by anthropogenic factors, for example the channeling and regulation of rivers and the erection of dams and hydropower plants. The channeling of a section of a river helps clear the flow of ice floats and limits the formation of embacles and ice covers (Majewski, 2009), thus eliminating the

serious risk of flooding caused by embacles that may arise when broken ice accumulates. Research has shown that for more than 60% of the rivers in the Northern Hemisphere, seasonal effects on the occurrence of ice phenomena can be observed. It is assumed that extreme hydrological phenomena, such as floods and low river waters in winter, are mainly the result of the occurrence and disappearance of ice phenomena (Majewski, 2009). Ice phenomena significantly influence the functioning of the fluvial system and the water ecosystem, but also on the life cycles of water organisms (Allan, 1998).

The broad scope of the impact ice phenomena has on river regimes and living organisms has become the topic of a great number of studies. Some of the research focuses on the effect of weather anomalies (Bednorz and Kossowski, 2004; Filipiak, 2004; Kozuchowski, 2000), particularly the recently registered rise in air temperature (Graf, 2018; Graf and Tomczyk, 2018; IPCC, 2007; Russak, 2009; Tylkowski, 2013), on changes in thermal conditions of waters and the development and duration of icing on rivers. One of the most important aspects of the macroscale changes in climatic conditions is the impact of the North Atlantic Oscillation's (NAO) influence on changes in individual elements of river regimes, not only because individual catchments can be compared on a regional basis, but also because this type of research captures the problem in relation to a series of long-term measurements. The influence of the variability of the NAO on hydrological phenomena, including river regime, changes in the flow rate and the thermal and ice regime of rivers and lakes, has been described, among others, by Yoo and D'Odorico (2002) and Klavins et al. (2009). Due to the strong climatic factors that determine the formation of ice phenomena on rivers, the phenomena can be used as a significant indicator of climatic changes.

Records from the last two centuries regarding the dates for the disappearance of ice cover on rivers of the Northern Hemi-

sphere provide consistent evidence indicating their subsequent freezing and earlier disappearance of ice phenomena (Magnuson et al., 2000). The results of reports and studies carried out over the last 40 years on European rivers show a decrease in the frequency and appearance of ice phenomena, especially ice sheets (EEA Report No. 12/2012). This is a result of the impact of climate change, especially the increase in the incidence of warmer winters. The observed tendency is also confirmed by studies on changes in river thermo-waves, which have been determined to have increased by about 1–3°C over the last century. Analyses of long-term trends in changes in river congestion have shown that the surface water ice regime in Northern Europe is linked to changes in the NAO, having features that confirm long-term climate change (Klavins et al., 2009; Kuusisto and Elo, 1998; Yoo and D'Odorico, 2002). Changes in the ice melting regime are also observed in the Baltic region, where the direct impact of the sea is the factor influencing the structure and duration of ice phenomena. It is pointed out that the duration for the ice cover on the rivers of the Baltic region during the last decades, even centuries, has shortened. Periods of interruption in the observation of ice phenomena in particular years and periodic changes in the intensity of ice formation have been increasingly observed. These tendencies are confirmed by the observed trend of air temperature increase of coastal areas during the winter season (Hagen and Feistel, 2005), which translates into an increase in the temperature of river waters and a hinderance in the occurrence of ice phenomena (Klavins et al., 2002, 2009; Lizuma et al., 2007).

The main purpose of the research was to determine the conditions affecting ice phenomena, including the three-phase cycle of ice (the phases of expansion, retention and decay of the ice cover) on selected rivers of the Przymorze area in Northern Poland for the years 1951–2010. These rivers flow into the Baltic Sea, which directly impacts their hydrologic and thermic conditions. The analysis has been elaborated against the backdrop of currently occurring climatic changes, with particular emphasis on the winter periods, which are dependent on the development and phase variability of the NAO. The work also takes into consideration changes in thermal conditions of river waters and local environmental factors impacting catchments, including the level of anthropogenic impact.

The research has been undertaken to answer the following questions:

- what has been the frequency and duration of the ice phenomena on rivers in the Baltic Coastal Zone over a multi-year period?
- how have the trends in air temperature changes affected water thermal conditions in rivers and characteristics of the ice phenomena, i.e. duration of ice and individual forms of the ice phenomena?
- how does the historical data base influence the future data base and how does it facilitate forecasting?

The results will be useful in monitoring the temporal and spatial changes of ice on rivers in the temperate zone, especially in areas that are impacted by the Baltic Sea.

TEST AREA

According to the physico-geographical division of Poland (Kondracki, 2009), the Przymorze region is located in the Southern Baltic Coastal macro-region, which is characterized by considerable variability in weather conditions (Fig. 1). The region is located in the temperate climate zone and is affected by Atlantic Ocean climate factors, the Baltic Sea – with which it is in direct contact - and certain elements of the Eastern Eu-

ropean continental climate. The North Atlantic is considered as the main climate forming zone of Poland (Marsz and Styszyńska, 2001), and therefore it also plays a significant role in shaping the thermal conditions of the Southern Baltic Coastal Strip.

Near the sea, winters are less frosty than in other regions of the country (Woś, 2010). To a large extent, the Baltic Sea determines the annual range of air temperature, particularly through the reduction of daily values, annual amplitudes and fluctuations in temperature distribution primarily during the winter periods (Woś, 2010). The thermal impact of the Baltic Sea also lengthens and shifts the duration of transient seasons (Niedźwiedz, 2002).

Changes in air temperature in the Baltic coastal zone are also impacted by anemometric factors and cloud cover. Westerly winds influence the occurrence of positive thermic anomalies in the winter season. Winds from the northern sector bring warmer air, whereas easterly winds bring cooler weather. Cloud cover is also of considerable importance in relation to air temperature changes in Pomerania. Increased cloud cover is related to a decrease in the value of temperature amplitude and an increase in extreme temperatures (Filipiak, 2004).

The test area covers the catchment area of 5 rivers in the Przymorze hydrographical region – Rega, Parsęta, Wieprza, Słupia and Łupawa – which flow into the Baltic Sea (Fig. 1). The analyzed rivers are classified as small rivers, i.e. not exceeding 200 km in length and having a drainage area of no more than 10,000 km² (Table 1).

Table 1. The selected morphometric parameters of selected rivers from the Przymorze region.

River	Length of the river [km]	Catchment area [km ²]
Słupia	138.6	1310.0
Łupawa	98.7	924.5
Łeba	117.0	1801.2
Wieprza	140.3	2172.7
Rega	167.8	2723.3
Sum	662.4	8931.7

In hydrological terms, the rivers located east of the Parsęta River (Fig. 1) are characterized by a weakly developed nival regime and their average flow in a spring month does not exceed 130% of the average annual flow. In the annual cycle, rivers with such a regime are distinguished by the most even flows and the greatest share of subterranean outflow from the total outflow. The Parsęta River and rivers located west of it (Fig. 1) are characterized by a moderately developed nival regime typical of rivers with an average flow during spring months totaling between 130–180% of the average annual flow. Rivers in northern Poland and in the Wieprza River catchment area are characterized by a high share of subterranean supply (60–80%), which is 40–60% for the other rivers with this type of regime. Temperature stability of subterranean waters may have a considerable influence on the development of the icing cycle of rivers (Graf, 2015; Łukaszewicz, 2017a, b).

The selected rivers are typified by a diverse level of anthropogenic impact. Some of their sections are located in urbanised municipal areas (e.g. the section in Słupsk) (Fig. 1), while others flow through land that has retained its natural character, or through areas that have experienced only a slight degree of anthropogenic impact (Łukaszewicz, 2017b). This is particularly visible in the case of the Łupawa River (Fig. 1), for which the headwaters flow through the Słowiński National Park.

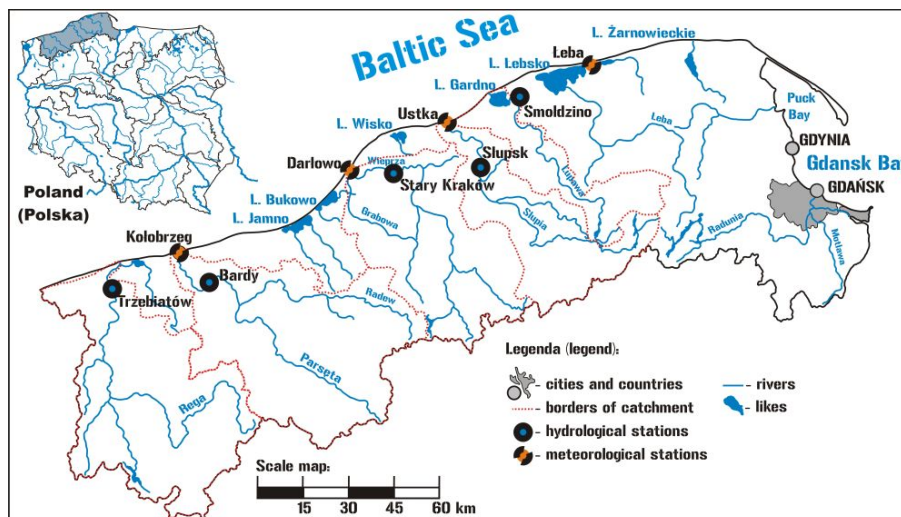


Fig. 1. Location of the test area and arrangement of measuring stations for the Institute of Meteorology and Water Management – National Research Institute (IMGW-PIB) in the Przymorze hydrographical region.

Table 2. Thermic classification criteria according H. Lorenc (1998).

Class No.	Year evaluation	Values interval calculated according $T_{mpt. year}$
1	Extremely warm	$T_{mat. year} > T_{mpt. multiyear} + 2.5 SD$
2	Anomalously warm	$T_{mpt. multiyear} + 2.0 SD < T_{mat. year} \leq T_{mpt. multiyear} + 2.5 SD$
3	Very warm	$T_{mpt. multiyear} + 1.5 SD \leq T_{mat. year} \leq T_{mpt. multiyear} + 2.0 SD$
4	Warm	$T_{mpt. multiyear} + 1.0 SD < T_{mat. year} \leq T_{mpt. multiyear} + 1.5 SD$
5	Slightly warm	$T_{mpt. multiyear} + 0.5 SD < T_{mat. year} \leq T_{mpt. multiyear} + 1.0 SD$
6	Normal	$T_{mpt. multiyear} - 0.5 SD \leq T_{mat. year} \leq T_{mpt. multiyear} + 0.5 SD$
7	Slightly cold	$T_{mpt. multiyear} - 1.0 SD \leq T_{mat. year} < T_{mpt. multiyear} - 0.5 SD$
8	Cold	$T_{mpt. multiyear} - 1.5 SD \leq T_{mat. year} < T_{mpt. multiyear} - 1.0 SD$
9	Very cold	$T_{mpt. multiyear} - 2.0 SD \leq T_{mat. year} < T_{mpt. multiyear} - 1.5 SD$
10	Anomalously cold	$T_{mpt. multiyear} - 2.5 SD \leq T_{mat. year} < T_{mpt. multiyear} - 2.0 SD$
11	Extremely cold	$T_{mat. year} < T_{mpt. multiyear} - 2.5SD$

Explanations: ($T_{mpt. multiyear}$ – average multi-year temperature; $T_{mat. year}$ – average annual, monthly or seasonal temperature; SD – standard deviation). Classes of winter seasons. distinguished on the basis of data from analyzed meteorological stations. have been marked in bold.

Some of the analyzed rivers, for example the Słupia River, have been significantly transformed in their upper and middle reaches through the modification of the river beds, the erection of numerous dams and a network of hydropower plants (Łukaszewicz, 2016).

SOURCE MATERIALS

The analysis was performed using data from 5 measuring stations which are in the standard observation network of the Institute of Meteorology and Water Management – National Research Institute (IMGW – PIB, Warsaw – Poland): 1) Trzebiatów – the Rega River; 2) Bardy – the Parsęta River; 3) Stary Kraków – the Wieprza River; 4) Słupsk – the Słupia River; and 5) Smoldzino – the Łupawa River (Fig.1). The database contains daily information about the occurrence or non-occurrence of ice phenomena on the rivers studied during the period of 1951-2010. The analyses take into consideration:

- the division of ice phenomena into individual forms: frazil ice; stranded ice; ice cover; ice floe; ice jam; and frazil ice jam.
- the number of days when some of the abovementioned forms occurred simultaneously, e.g. stranded ice and frazil ice, stranded ice and ice floe.
- in addition, daily water temperature values were analyzed for each of the rivers.

The authors have also utilized meteorological data concerning average daily air temperature values from the meteorologi-

cal stations (IMGW-PIB) in Kolobrzeg, Darłowo, Ustka and Łeba, which are located in close proximity to water-level indicator points for the analyzed rivers of the Przymorze region (Fig. 1). The frequency of occurrence and the course of individual phases of the NAO were determined using the database of the National Weather Service (<https://www.weather.gov/>). The Jones' Index, which is calculated as the difference in atmospheric pressure between Gibraltar and southwest Iceland, was also used (Niedźwiedz, 2002).

METHODS

The frequency and phasality of ice phenomena on rivers in the Baltic coastal zone was analyzed for the period of 1951–2010. The frequency was defined as the sum total of days with the observed ice phenomenon in the cool half-year period of the hydrological year (November – April), with reference to average air and water temperature values for individual years. In order to evaluate the connection between air temperature and the course of atmospheric circulation, the phase variation of the NAO was also considered. Using the Jones' index helped to determine the percentage of variation in the occurrence of individual NAO phases. A thermic classification (Lorenc, 1998) – (Table 2), on the basis of which distinguished out of the 11 classes of winter seasons, was used to determine the thermic variability of winter periods and distinguish anomalies during the 60-year period under study. This research was conducted

utilizing data from selected IMGW-PIB (Institute of Meteorology and Water Management – National Research Institute in Warsaw) meteorological stations located in the Baltic coastal zone (Fig. 1).

The influence of anthropogenic factors on the development of ice phenomena has been determined by comparing the number of days, in which ice forms occurred along selected river sections, taking into consideration any hydrotechnical infrastructure that could modify the nature of a river's icing cycle.

The LOESS (Local regrESSion, i.e. locally weighted scatterplot smoothing) method was utilized for analyzing dependence between individual parameters. The method is also known as locally weighted regression or weighted locally polynomial regression (Cleveland and Devlin, 1988; Shumway and Stoffer, 2010) LOESS regression involves the evaluation of separate regression equations for each point (h) in a time series in which observations located closest to the point are of greatest importance, while those that are more distant exert a lesser impact on the result obtained (Cleveland and Devlin, 1988). The equation for LOESS is:

$$h(T) = \alpha_0 + \alpha_{01}(T_i - T) + \mathcal{E}(T) \quad (1)$$

where: coefficients α_0 and α_{01} are calculated separately for each requested T , using the method of locally weighted lesser squares with weights w , while the model itself takes the following form:

$$\sum_{i=1}^n w = \left(\frac{(T_i - T)^2}{n} \right) e_i^2 = \sum_{i=1}^n w = \left(\frac{(T_i - T)^2}{n} \right) (H_i - \alpha_0 - \alpha_1(T_i - T))^2 = \min \quad (2)$$

where: H – point magnitude of cloud smoothness (T_i and H_i), α_0 , α_{01} – regression coefficients used to determine $H(T_i) = \alpha_0$, w – weight function, T – values, for example, of air temperature.

The approximate strength of the trend in changes for the analyzed thermal characteristics and ice phenomena on rivers (assuming linearity) was determined using the modified Mann-Kendall trend test, also referred to as the Yue-Pillon method (Yue et al., 2002). This made it possible to approximate the average monthly change and changes within the entire period. In addition, on the basis of Kendall's non-parametric correlation τ_b , it allowed to quantify the strength of the changes. This is useful due to the interpretation of the τ_b coefficient being purely probabilistic. It determines how much greater/smaller the probability is, for a random selection of observed pairs, of drawing a pair concordant with the observed trend (i.e. for a positive trend, a pair where $\tau_{n+k} \geq \tau_n$). Furthermore, it is possible to determine the level of significance for the τ_b coefficient, which allows us to reliably separate trends that may be merely accidental.

The trend analysis was supplemented with a KPSS test (Kwiatkowski et al., 1992) and an analysis of the time series structure based on the classical ARIMA model (Box and Jenkins, 1983), which has made it possible to answer the question of how historical values determine future values and to what extent this makes forecasting possible. ARIMA model comprises three fundamental elements: the autoregressive process AR (autoregressive), the degree of integration (integrated), and the moving average MA (moving averages). The order determines how many earlier values impact the current value. For the AR (2) and AR (3) processes, the following equations are used, respectively:

$$y_t = \varphi_1 y_{t-1} + \varphi_2 y_{t-2} + \varepsilon_t \quad (3)$$

$$y_t = \varphi_1 y_{t-1} + \varphi_2 y_{t-2} + \varphi_3 y_{t-3} + \varepsilon_t \quad (4)$$

where: y_t – value of the series at moment t , y_{t-1} – value of the series at moment $t-1$, etc., ε_t – random component, disturbance at moment t , t – successive 24-hour periods/days, φ – a parameter determining the strength of the impact of the previous process value (or successive, older values) on the current value.

In the adopted model, the selection of the degree for individual ARIMA components is made in such a way as to ensure that it minimizes the model's AIC (Akaike Information Criterion). The statistical model may contain various AIC measures, but the one clearly having the lowest measure is preferred (Akaike, 1969). The authors also made use of the SARIMA model, which is the ARIMA model modified into half-year periods.

Additionally, the time series was reconstructed using the GAM (General Additive Model) forecasting model, thus allowing to determine periods with clear trend changes (Taylor and Letham, 2017). This allowed us to more precisely model the trend as a linear function, however with a directional coefficient that may be variable over time. GAM constitutes one of the most universal procedures for non-parametric regression models and has the form of:

$$E(Y_i | x_{i1}, x_{i2}, \dots, x_{iP}) = \alpha + f_1(x_{i1}) + f_2(x_{i2}) + \dots + f_P(x_{iP}) \quad (5)$$

where: Y – explained variable, x – explaining variables, α – constant, f_j – the additive function, where $j = 1, 2, \dots, P$ – unknown functions of j explaining variable, estimated through unknown functions determined by means a multiple fitting algorithm, $E(Y|X)$ – the average of explained variable Y conditioned by explaining variables.

In the GAM model, the unknown functions (P) are estimated through local polynomial regression, regimented, for example, by the LOESS (stats) function, which fits locally smoothed polynomials to the second degree. Estimation of the f_j functions takes place jointly for $j = 1, 2, \dots$, and for P using the iterative backfitting algorithm procedure, known as the Multiple Fitting Algorithm (Koronacki and Cwik, 2005).

The dispersion (diversity) of the annual distributions of ice phenomena has been expressed by means of Shannon's entropy index (Shannon and Weaver, 1949). Usage of the index was necessary when analyzing data having considerable diversity of distribution (the duration of phenomena differs significantly among the various phenomena, in both individual years and months) and a non-stationary nature for the time series. This allowed to compare and determine the impact of the variability of individual parameters, for example, water temperature, on the variability of the trend throughout the duration of ice phenomena.

The analysis was supplemented with the basic descriptive statistics of the distributions of air and river water temperatures for various time-resolution levels. Due to the large quantity of data, the normality of distributions in individual periods was assessed based on histograms and quantile charts. Using the selected statistical methods, it was possible to distinguish the longest periods of occurrence of ice phenomena on individual river sections and the tendencies appearing in the change in occurrence and duration of these phenomena.

The analyses and calculations were performed in the R calculation environment, version 3.4.0 (2017–04–21). R Suite is both a programming language and a programming environment and is available as "Free Software Foundation's GNU – General Public License", functioning in the UNIX/Linux, Windows and MacOS systems. The results of the applied statistical signifi-

cance tests were assessed with reference to the adopted level of $\alpha = 0.05$.

RESULTS

In the first three observed decades, there was recorded an increased number of days with ice phenomena on rivers and a greater differentiation of ice forms – irrespective of the river section along which research was conducted (Fig. 2) In the last two decades, frazil ice and border ice were the predominant ice forms observed in the first phase of the freezing over of rivers. The exception is the Parsęta River, for which, in recently observed years, the occurrence of ice cover was recorded, however the number of days with this form decreased by

nearly one half in comparison to preceding years, i.e. the period 1951–1980.

Due to the shortening of the duration of ice phenomena over the last decade, practically no ice forms characteristic of the final, third phase of the river freezing cycle, i.e. ice floe and frazil ice, have been observed other than on river sections with only slight traces of anthropogenic impact, i.e. places where the river bed was not regulated by the erection of damming systems or the shortening of river course (the Rega and Parsęta Rivers). The frequency of occurrence of forms characteristic of the second and third phase of the icing cycle is decidedly greater along sections of rivers typified by a moderately developed rival regime and located in the western part of the test area (Figs. 2–3).

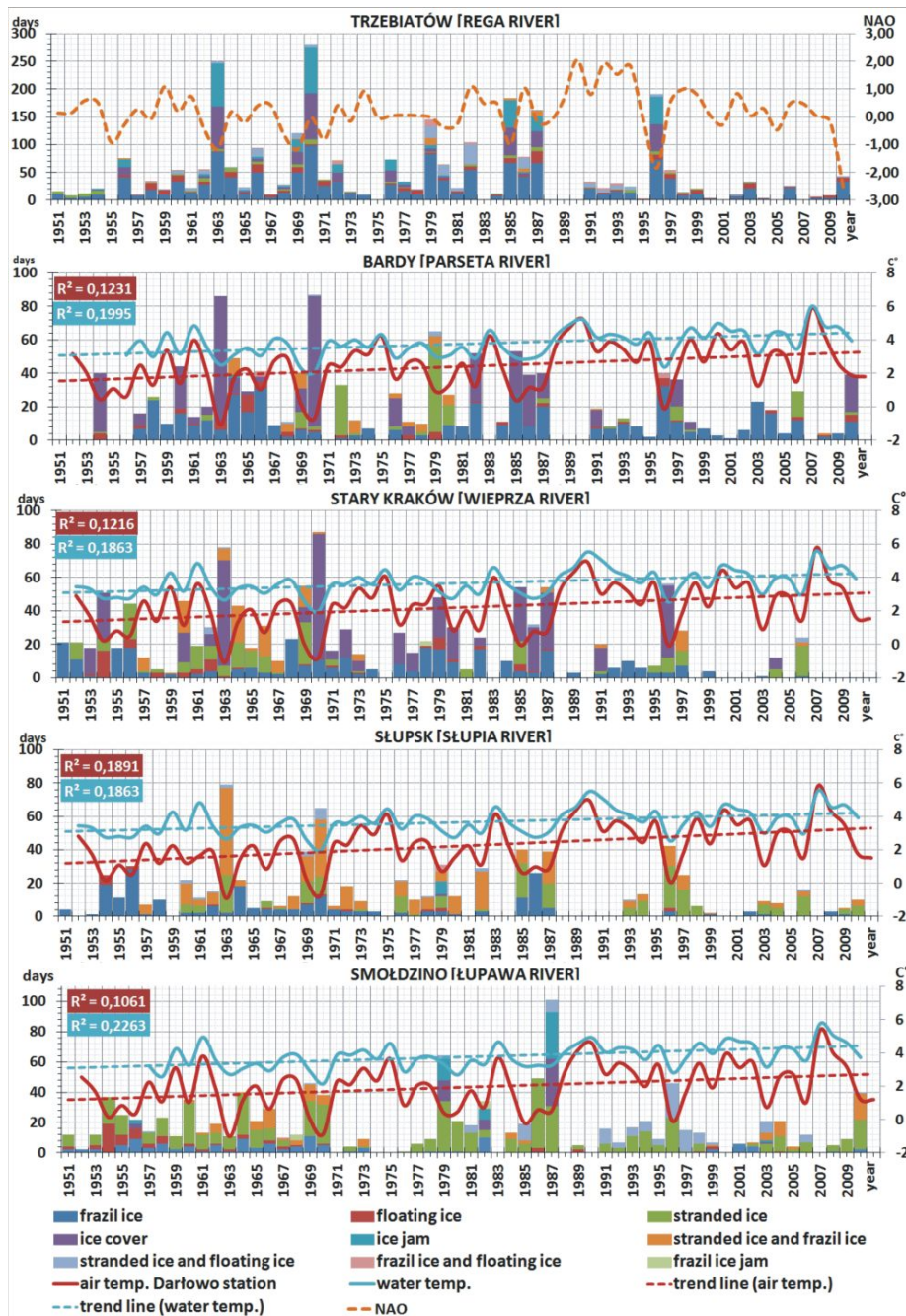


Fig. 2. Frequency of ice phenomena occurrence on Przymorze region rivers during the years 1951–2010, taking into consideration the individual types, the variability of the NAO and the variability of air and water temperature.

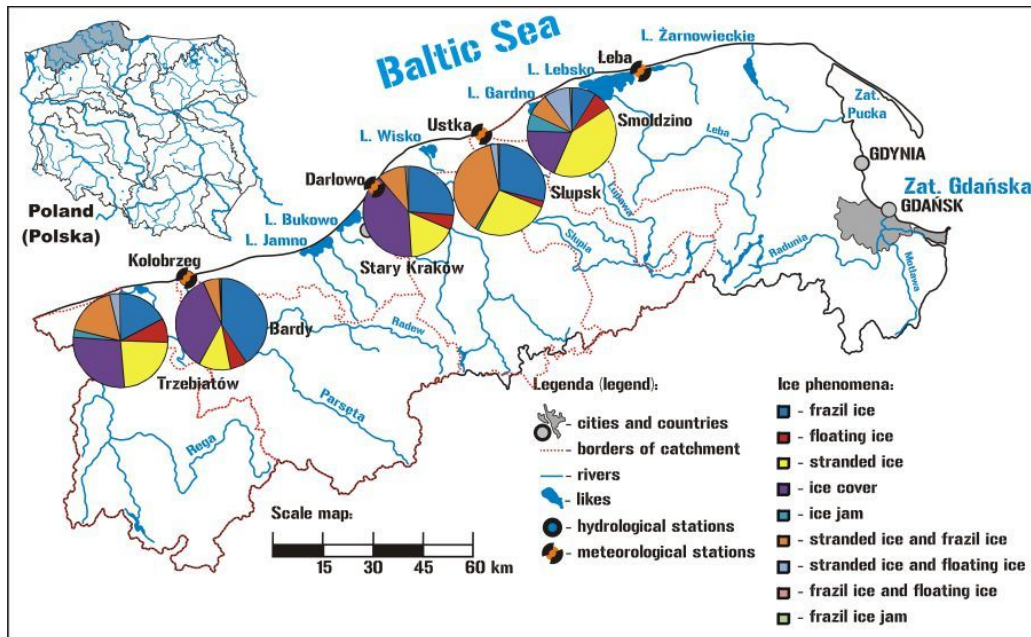


Fig. 3. Frequency (%) of occurrence of individual types of ice phenomena on rivers of the Przymorze region in the years 1951–2010.

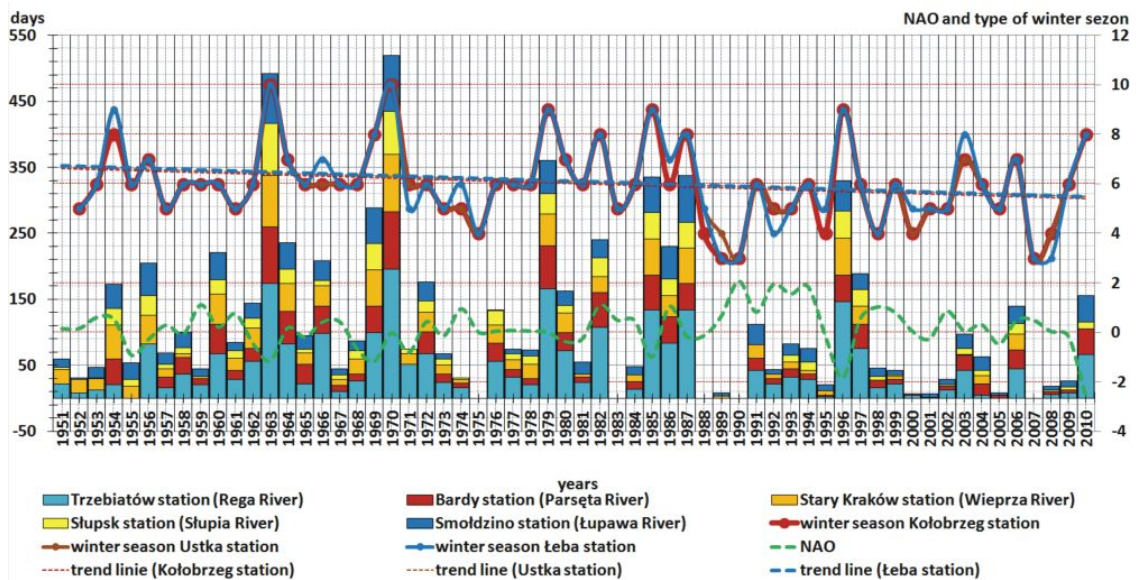


Fig. 4. Number of days with ice phenomena on rivers of the Przymorze region in relation to the variability of thermal conditions in winter periods and the North Atlantic Oscillation (NAO) index. Explanations – classification of winter seasons: 1 – extremely warm; 2 – anomalously warm; 3 – very warm; 4 – warm; 5 – slightly warm; 6 – normal; 7 – slightly cool; 8 – cool; 9 – very cool; 10 – anomalously cool; 11 – extremely cool.

In the first half of the researched period, 1951–1980, the greatest number of days with ice phenomena, as well as the greatest diversity of their forms, on rivers of the Przymorze region was observed, (Figs. 2 and 4). Since 1987, there has been a clear and on-going reduction in the number of days with a single recorded ice phenomenon. This is linked to the increase in Jones' index during the positive phase of the NAO, as shown in the present work. The increase in the index coincides with an increase in average air temperature during winter periods, which in turn impacts the thermal conditions of river waters. Changes in thermal conditions of waters impact the variable frequency of occurrence of ice phenomena and icing forms observed on rivers. The coefficient of correlation between air and water temperature is statistically significant and assumes values within the range of 0.74 to 0.83 at individual stations.

Research demonstrated the considerable impact of the variability of the North Atlantic Oscillation index phases on the increase in air temperature, particularly in the cool half-year period of the hydrological year. This translates directly into an increase in the temperature of waters and the disappearance of ice phenomena in the analyzed region. In the years 1951–2010, the positive phase of the NAO occurred more frequently (57.6%) than the negative phase (42.4%) in the winter season (hydrological year). Taking the winter months into consideration, we may state that the positive phase occurred most frequently in January (64.4%), followed by February (61.0%), while the negative phase was most frequent in December (50.8%). However, the percentage difference between the phases in December was decidedly smaller than in the remaining months of the winter period (Fig. 5).

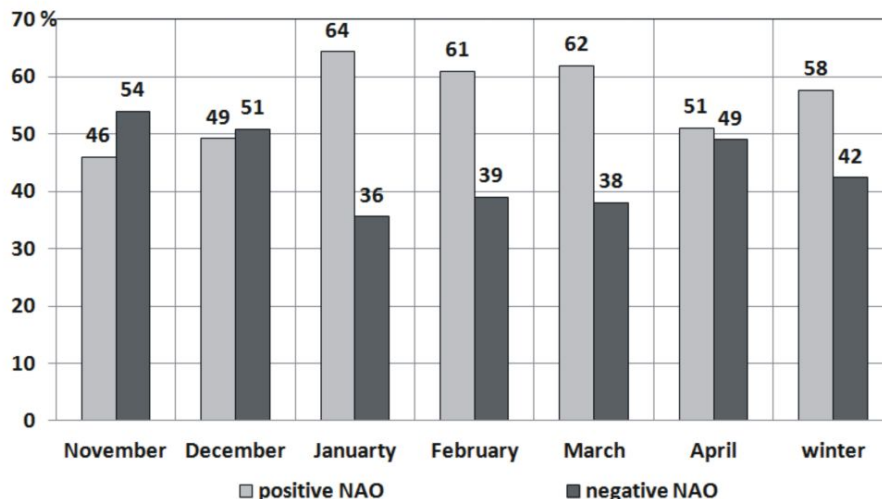


Fig. 5. Frequency [%] of occurrence of the positive and the negative phases of the North Atlantic Oscillation (NAO) in the winter season of the hydrological year (November – April) in the Baltic coastal zone during the years 1951–2010.

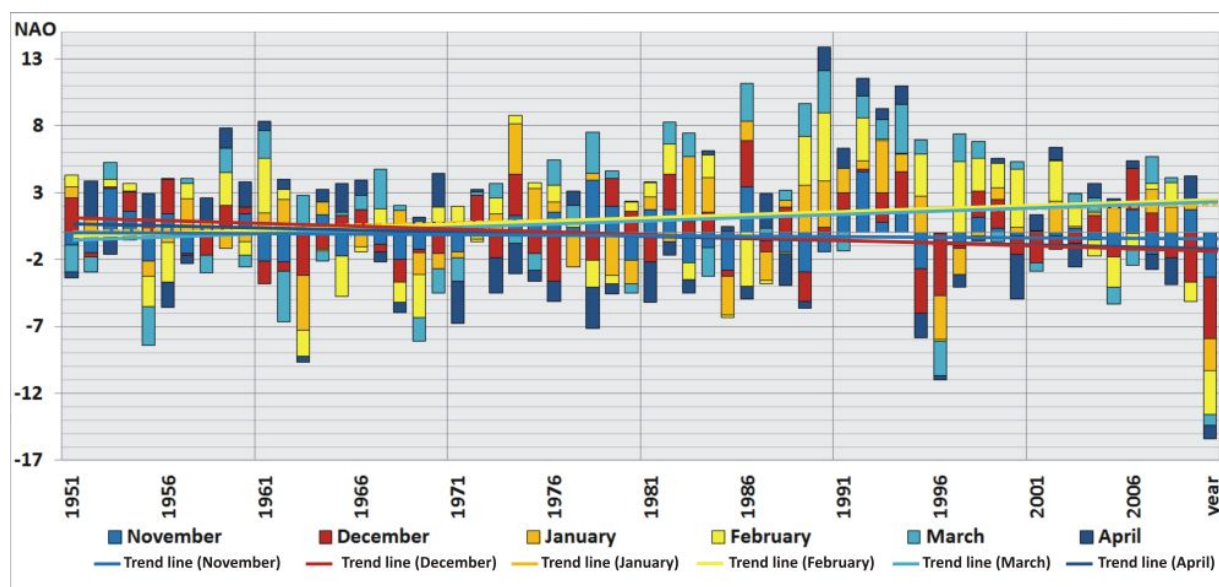


Fig. 6. Progression of positive and negative NAO phases for the winter months of 1951–2010, taking into account the linear trend for individual months.

The predominance of the negative phase over the positive phase (54.0%) was also observed in November, the beginning of the hydrological year, similar to December, whereas in March the positive phase (62.0%) was clearly predominant over the negative phase. A similar tendency was noted in April (51%) – (Figs. 5–6). Based on the results obtained, it was determined that during the last 30 years the frequency of occurrence of the positive phase of the NAO has increased, and this is particularly evident during the winter months.

Research has also shown a clear increase in anomalous winter periods, which exceed the range of calculation values and during which ($T_{mpt.s, multiyear}$) is in the range ($T_{mpt.s, multiyear} - 0.5 SD \leq T_{mat.s, year} \leq +0.5 SD$), and therefore classified as normal seasons. This is particularly evident for the last two observed decades (Fig. 4). Such a situation is brought about by the increase in thermal anomalies in the cool half-year period of the hydrological year, to which the rise in the frequency of occurrence of the positive NAO contributes (Figs. 2, 5–6). The high values of Jones’ index (Fig. 6) point to an increase in cyclonic activity

and its impact on the Baltic coastal zone, in particular for the last twenty observed years, during which the influence of Atlantic oceanic climatic factors grew in significance, resulting in less severe winters. The meteorological stations in Łeba, Ustka and Kołobrzeg (Fig. 1) recorded only two winter seasons that were classified as anomalously cool, which account for no more than 3.3% of all observed seasons. Both seasons occurred in the first half of the researched period, i.e. in the years 1951–1980 (Figs. 2, 4).

Throughout the researched period there were 4 winter seasons that were classified as very warm (class 3), all recorded after 1987, and 7 winter seasons classified as warm (class 4). The first warm winter season was observed in the first observed 30-year period, in the years 1974/1975. The remaining warm winter seasons were recorded only after 1987 (Fig. 4). The largest number of seasons have been classified as normal. Throughout the entire observed period there was not a single extremely cool or extremely warm season. This could have been the result of specific climatic conditions. During the peri-

od from 1951 to 1987, no clear differences were observed in changes in thermal conditions, nor in the course of winter periods between individual meteorological stations, indicating a certainty of stationarity of measurement cycles. This stationarity was also confirmed by KPSS tests performed on measurement series. After 1987, there was a clear increase in the occurrence of periods exceeding the value boundary, where ($T_{mpt, \text{ multiyear}} - 0.5 \text{ SD} \leq T_{mat, \text{ year}} \leq +0.5 \text{ SD}$), resulting in normal classification (Fig. 4) and distorting the stationarity of the entire observed period. Research also allowed us to observe a certain regularity in the characteristics of periods where ($T_{mpt, \text{ multiyear}}$) is within the range below the value boundary ($T_{mpt, \text{ multiyear}} - 0.5 \text{ SD} \leq T_{mat, \text{ year}} \leq +0.5 \text{ SD}$), that is periods classified as normal, i.e. the following periods: slightly cool (class 7), cool (class 8), very cool (class 9) and anomalously cool (class 10). The regularity in the characteristics of these periods manifests itself in a certain regularity of their occurrence. The winter seasons classified in these value ranges occur in 6- or 7-year periods. The observed fact points to the occurrence of a certain phasality of cool winter cycles in the researched period, which is fully dependent on the variability of

atmospheric circulation (Fig. 4). In the last two observed decades there was noted a clear increase in winter seasons classified as slightly warm (class 5), warm (class 4) and very warm (class 3). Their occurrence coincides with that of the positive phase of the NAO. Particularly clear is the increase in seasons in which Jones' index adopted the highest values (Figs. 5–6), while the average annual air temperature in the winter period and the cool half-year period of the hydrological year exceeded the boundary value by approximately 4°C (Figs. 2 and 4). The quantitative analysis of winter seasons shows a clear division occurring between periods classified as cool, which are predominant in the first 30 observed years, and periods classified as warm, predominant in the second 30 observed years.

The results obtained have been confirmed by statistical research into time series, conducted on data series. On the basis of a test of time series autocorrelation, performed using the ARIMA model (seasonal SARIMA), it was determined that the series for average half-year values of individual parameters was not stationary for the majority of stations (Fig. 7). The non-stationarity of measurement cycles or the disruption of this stationarity is impacted by the clear increase in air temperature

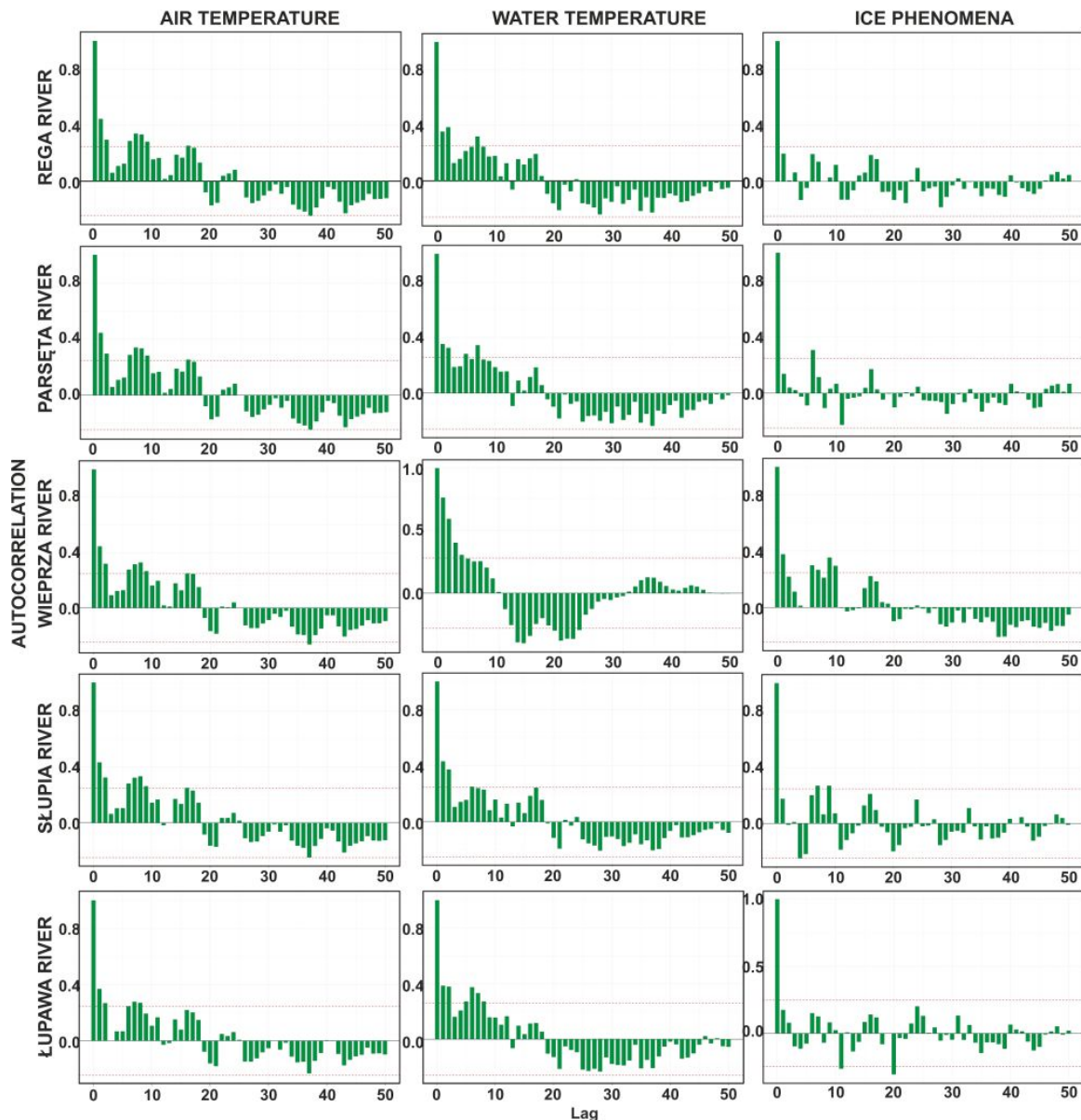


Fig. 7. Results of the autocorrelation test of individual parameters: air and water temperatures and ice phenomena for the years 1951–2010.

and water temperature observed since 1987. The change in the trend has been confirmed by GAM tests. We may therefore assume that the changes in air temperature observed during the last 30 years influenced the periodicity of cool periods and changes in ice phenomena. The number of days with an observed ice phenomenon on rivers is decreasing (Fig. 2), and this is related to the variability of the positive water temperature trend (Fig. 7).

An analysis of the trend using the Yue-Pilon method pointed to the occurrence of a growth trend. Correlation with the monotonic trend was also significantly positive (Fig. 8), meaning that we may talk of a growth trend in data (air and water temperature). A KPSS test performed for the time series associated with the variability in air temperature at meteorological stations and water temperature at water-level indicator points of the IMGW-PIB demonstrated a general non-stationarity of the entire analyzed series for all analyzed stations. At the same time, the KPSS test for the period prior to and including 1980 disclosed a certain stationarity of the data time series, irrespective of ran-

dom fluctuations, around a solidly stable average value.

The results of tests confirmed our assumptions as to the appearance of a positive trend in the 1980s. Until 1981, the average annual water temperatures fluctuated around a certain average value, while in subsequent years they started to experience a gradual linear increase. The test confirmed our assumptions that a change in the trend occurred after 1987. The annual diversity of ice phenomena during the analyzed period, determined as Shannon's entropy for the distribution of phenomena in a given year, also displays a certain irregularity (Fig. 8). Line fitting to non-parametric regression is also somewhat variable, however this does not necessarily signify the occurrence of a clear actual trend. Even though it was determined, based on analysis of raw data, that the number of days with ice on individual sections of rivers in the Przymorze region had decreased over the past 20 years (calculated using the sum and arithmetic means), an analysis performed with the Yue-Pilon method indicated the lack of a clear linear trend. The monotonic correlation (Kendall's) between entropy and time also did not

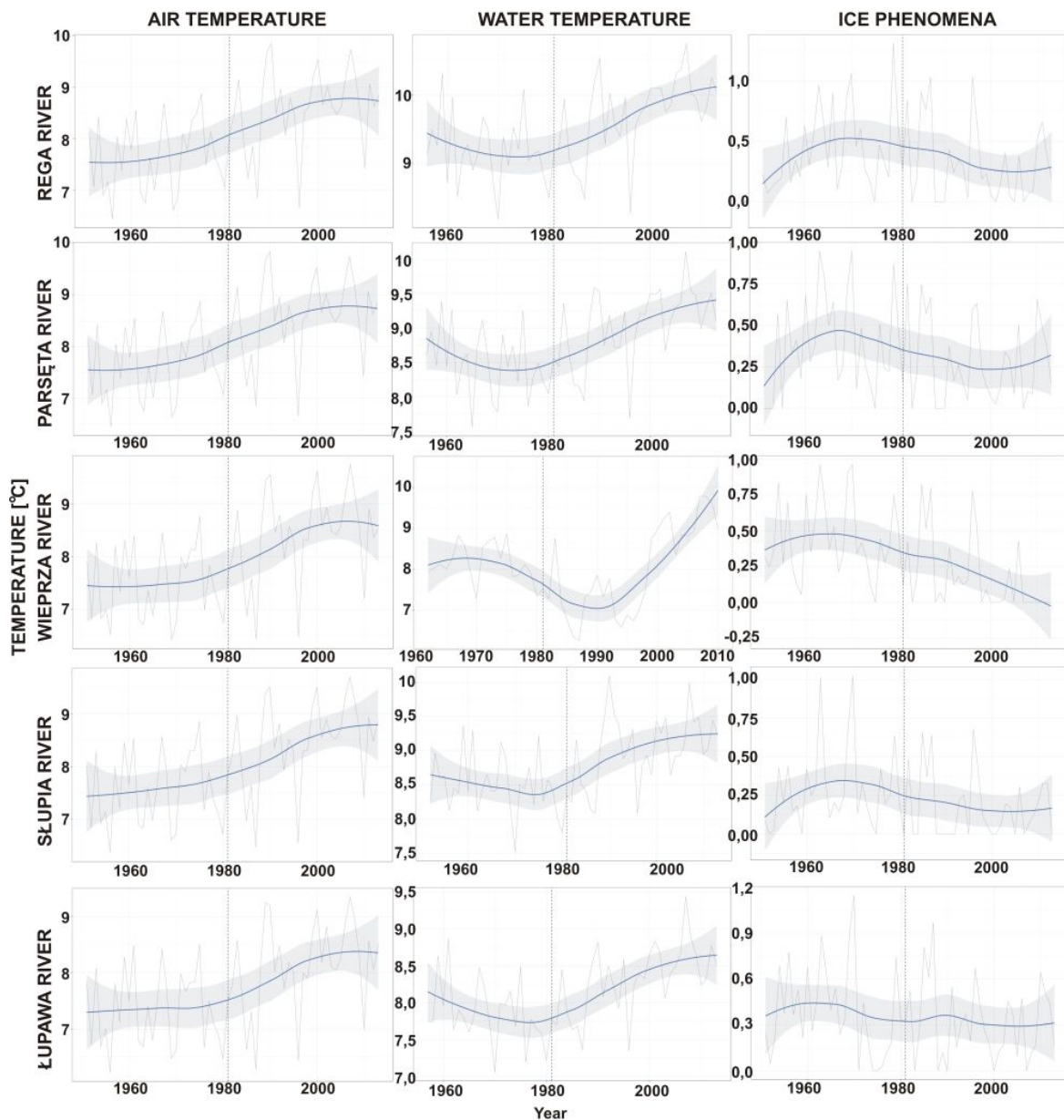


Fig. 8. Analysis results, using the Yue-Pilon method, for air and water temperature trends and ice phenomena for selected sections of Przymorze region rivers during the years 1951–2010.

show any significant trend. This is particularly evident for the rivers located east of Parsęta (Figs. 1, 2, 8), that is rivers characterized by a weakly developed nival regime and those transformed by anthropogenic factors. We may therefore state that the degree of diversity of ice phenomena observed on these rivers has not changed in any systematic way. This was further confirmed by the results of the KPSS test, which displayed a certain stationarity of annual entropy series. This can be the effect of an excessively short series of data. The monotonic trend points to a decrease in the number of ice phenomena,

which would be concordant with the assumption adopted that an increase in water temperature in rivers, brought about by an increase in air temperature, leads to the shortening of the duration of phenomena.

The quantile charts elaborated based upon data concerning air and water temperature have shown that their distribution is basically very well fitted to the normal distribution. This points to the quasi-stable development of temperatures during the researched period, which is confirmed, among others, by the charts drawn up for monthly periods (Fig. 9).

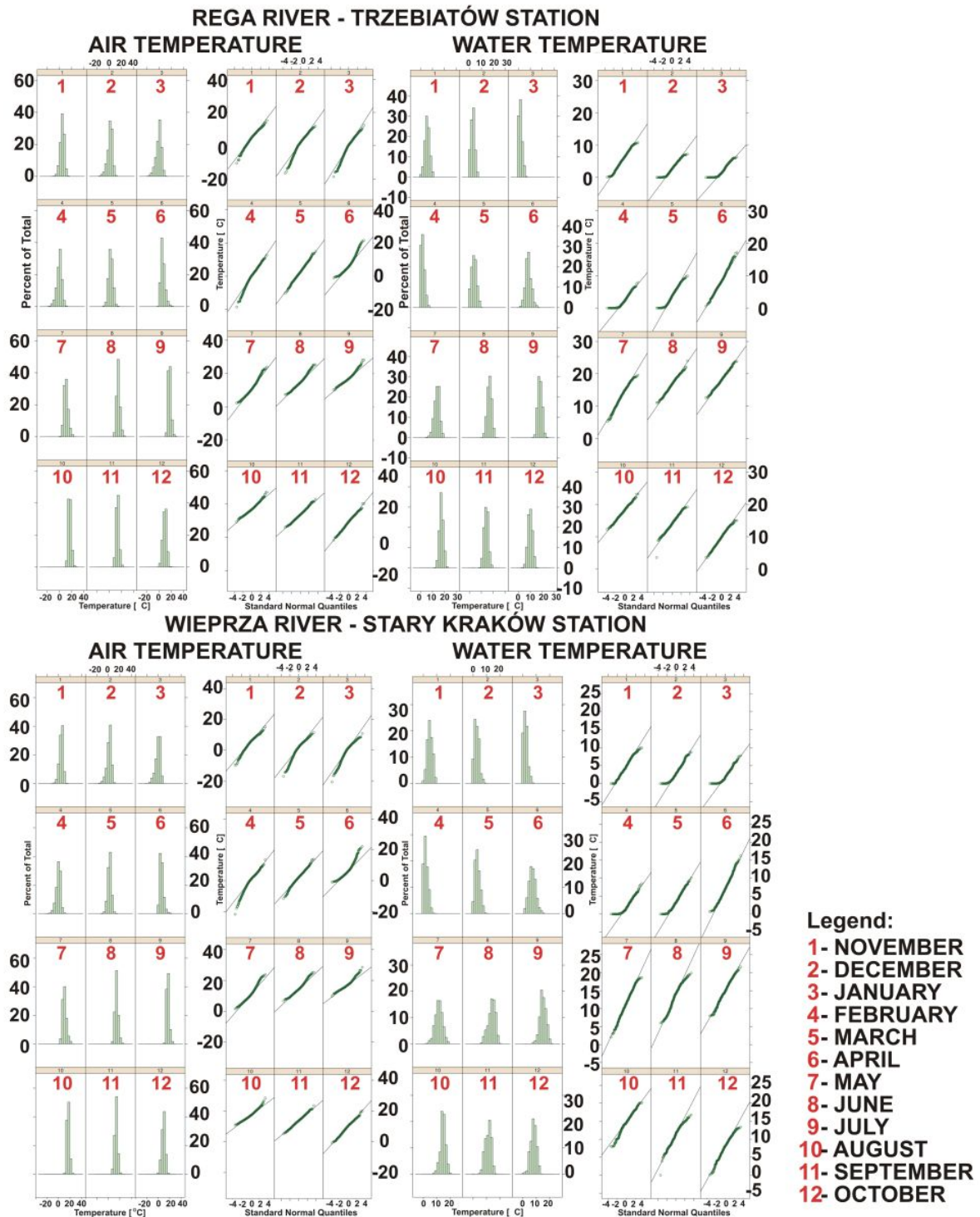


Fig. 9. Histograms and quantile charts of monthly distributions of air and water temperatures for selected sections of rivers in the Przymorze region (1951–2010).

The analyses conducted have proved that the greatest fluctuations caused by the occurrence of low temperatures are in the characteristics of the winter months (the cool half-year period of the hydrological year November – April). A comparative analysis of the frequency of ice phenomena on individual river sections and the types of these phenomena, which takes into consideration the degree of urbanization and the influence of anthropogenic factors, has shown the diversity of their occurrence. This is observed on river sections passing through cities (the station in Słupsk) – (Fig. 1) and on sections with a regulated bed or where the river flow is subject to modification by dumps of water from dammed reservoirs or is regulated by means of dams. This can be observed, for example, on the river section in Słupsk, or in Smółdzino, where there is a lesser diversity in ice phenomena forms (Figs. 2–3). Practically no ice cover – or ice floe, for that matter – have been observed on these sections, whereas on sections with a less transformed bed, or those located outside of urbanized areas, the ice forms observed on rivers are more diversified and the number of days in which they occur is greater, approximately 220 days for the entire researched 60-year period (stations in Trzebiatów, Bardy and Stary Kraków). The results confirm those of research previously conducted on the same aspects of rivers in the Przymorze region (Łukaszewicz, 2016, 2017b).

DISCUSSION AND CONCLUSIONS

The research performed displays a significant variability in the course and frequency of duration of ice phenomena in the rivers of the Przymorze region over the past 60 years. This variability manifests itself in the shortened duration of ice phenomena and a decrease in the diversity of ice forms observed on rivers, and thus in the disruption of the three-phase river icing cycle. Over the past few decades, a clear decrease in the duration of ice forms characteristic of the second and third phases of the icing cycle – such as permanent ice cover, ice jam and ice floe – has been observed. This negative trend is clearly marked after 1987, when the number of days recorded with ice phenomena on rivers fell by nearly one half. In Poland, comparable tendencies have been observed on the Vistula (Gorączko, 2013), the Oder (Kreft, 2013), the River Warta (Graf et al., 2018; Kornaś, 2014), the River Bug (Bączyk and Suchożebrski, 2016), and on rivers in the Przymorze region: Łeba (Łukaszewicz and Jawgiel, 2016), Słupia, Łupawa, Łeba, Reda, Wieprza, Parsęta (Łukaszewicz, 2016, 2017a, b, c; Ptak et al., 2016).

The research conducted has shown that the main cause of this variability was the increase in average annual air temperature observed in the cool half-year period of the hydrological year, which was particularly evident during the last two observed decades. The increase in air temperature was related to an increase in cyclonic activity, caused in part by the percentage growth of the positive phase of the North Atlantic Oscillation (NAO) and the rise in the value of Jones' index. The research has also revealed the significant impact of climatic changes on the variability of the thermal conditions of river waters. A positive trend is now being observed, manifesting itself with an increase in water temperature for all the stations on the Pomorze region rivers and having a statistically significant coefficient for the correlation between the analyzed parameters.

The results obtained pertaining to the increase in air temperature are concordant with research conducted by others authors in the Przymorze region. Kożuchowski (2000) while analysing the course of air temperature in Poland during the years 1959–1968 and 1989–1998, demonstrated that the influence of Atlan-

tic oceanic climatic factors increased, leading to a rise in air temperature and the moderation of winter in the South Baltic Coastal strip. Research performed by Filiipiak (2004) also confirmed that in the second half of the 20th century there occurred a positive air temperature trend in the winter season of the Przymorze region. Similar tendencies may be observed in the work of Kirschenstein and Łukaszewicz (2014). These tendencies have also been observed in the results of research concerning other regions of Poland and Europe (Bednorz and Kosowski, 2004; IPCC, 2007; Russak, 2009; Tylkowski, 2013).

The results of the conducted research have shown significant changes in the ice regime during the period of 1951–2010. This has also been confirmed by the results of research conducted on rivers in various parts of the Baltic region (in the northern and western part of the Baltic region). For 10-year increments over the past 30 years, the shortening of the duration of the ice cover on the rivers of the Baltic republics (and Belarus) has been demonstrated by Klavins et al. (2009) to be about 2–6 days per 10-year increment. The duration of the icing and ice-breaking period varies on rivers by more than one month, depending on the distance from the Baltic Sea and the Gulf of Riga, as well as on the characteristics of the river basin. The ice regime on the rivers of the Baltic region is strongly correlated with the North Atlantic NAO index, which is also highlighted by the results of research relating to the Baltic coastal zone in northern Poland. However, observed trends are not consistent between periods that are associated with the occurrence of mild and cold winters. The periodicity of ice phenomena in the Baltic region should be considered as quasi-periodic processes (Klavins et al. 2009).

Positive NAO phases, associated with strong western winds and increased flow of warm and humid air to Western Europe, result in warmer winters, later beginnings to winters and earlier springs (Chen and Hellström, 1999; Hurrell, 1995; Paeth et al., 1999). Over recent decades, a significant increase in air temperature has been detected in the Baltic region, as evidenced by, for example, meteorological observations in Riga (Latvia) and Uppsala (Sweden) (Klavins et al., 2009). At the Riga-University station, over the last 200 years (1795–2002), the average annual air temperature increased by 1.1°C, with its highest increase being observed in the spring season (an increase of 2.1°C). A significant increase in air temperature in the winter and spring season has been observed since the 1970s (Klavins et al., 2002; Lizuma et al., 2007). It has been observed that NAO affects winter precipitation with varying intensity along the Norwegian coast, in northern Sweden and in southern Finland (Uvo, 2003). It should be noted that close links between large-scale NAO enforcement and climate processes occur in the Baltic region on a regional scale (de Rham et al., 2008; Hagen and Feistel, 2005; Marshall et al., 2001). Yoo and D'Odorico (2002), in studying the climate impact during the end of ice phenomena in the Baltic region, showed that the winter NAO index still has a weak but significant effect on the spring temperature regime in the Baltic region, which explains the most important variables embedded in cryophenological records. In their opinion, other climate threats related to regional and global warming (for example, caused by CO₂) influence the appearance of clear trends in the spring temperature regime at the end of the ice season. This is confirmed by Hagen and Feistel (2005), Morse and Hicks (2005), and other research carried out in other regions. In the Baltic region this influence is revealed by the earlier disappearance of ice phenomena in the last few decades.

Research into the so-called spring ice breakup (IBU), conducted on the Aura River in Turku (southwest Finland) over the

period of 1749–2018, showed the so-called inter-seasonal trends in the disappearance of ice phenomena. The disappearance of the ice on the river in March, which was extremely rare before 1900, became widespread, while the disappearance in May (previously once every decade) has not occurred since 1881. Over the last 100 years in Finland, there was a statistically significant increase in the average annual air temperature. During the first 50 years of this period, the greatest temperature increases were observed in the spring; however, for the next 50 years the greatest temperature increases took place in the winter season. This influenced the delayed dates for the occurrence of fading on rivers and lakes and accelerated the dates for their disappearance (Kuusisto and Elo, 1998). These results are also confirmed with research conducted on rivers in both the European and Asiatic regions of Russia (Agafonova and Frolova, 2007; Frolova and Alekseevskiy, 2010).

A comparative analysis of individual sections of rivers in the Przymorze region has also demonstrated a certain dependence concordant with research performed by other authors. On sections of regulated rivers that have hydrotechnical structures, the number of ice forms observed is considerably smaller than on sections undisturbed by anthropogenic activity or ones that have experienced only a slight degree of such activity. In order to supplement information about local Przymorze region rivers icing determinants at individual sections of the course, it is recommended to identify and continuous monitoring zones of impact of anthropogenic factors, which contribute to increases in the temperature of waters in the winter season, thereby limiting the formation of ice phenomena, and in particular ice cover. The results obtained are of particular significance for identifying the thermal and circulatory factors determining the appearance of ice phenomena on the rivers of the Baltic coastal zone in the Northern Poland. They are also of potential significance for indicating climate change. Additionally, the results are important for maintaining the economic and ecological functions of the river, including the assessment of the risk of occurrence of extreme thermal and river icing conditions.

Acknowledgements. The present paper is the result of research on ice phenomena occurrence and thermal conditions of the river water, carried out as part of the research at the Department of Hydrology and Water Management of the Adam Mickiewicz University in Poznań, Poland.

REFERENCES

- Agafonova, S.A., Florova, N.L., 2007. Features of ice regime of Northern Dvina rivers' basin. *Water Resources J.*, 34, 2, 123–131. (In Russian.)
- Akaike, H., 1969. Fitting autoregressive models for prediction. *Annals of the institute of statistical mathematics*, Tokyo, 21, 243–247.
- Allan, J.D., 1998. *Ecology of Running Water*. Polish Scientific Publishers (PWN), Warsaw. (In Polish.)
- Bączek, A., Suchożębski, J., 2016. Variability of ice phenomena on the Bug River (1903–2012). *Inżynieria Ekologiczna*, 49, 136–142. (In Polish.)
- Bednorz, E., Kossowski, T., 2004. Long-term changes in snow cover depth in eastern Europe. *Climate Research*, 27, 3, 231–236.
- Box, G.E.P., Jenkins, G.M., 1983. *Time Series Analysis: Forecasting and Control*. PWN, Warszawa. (In Polish.)
- Chen, D., Hellström, C., 1999. The influence of the North Atlantic Oscillation on the regional temperature variability in Sweden: spatial and temporal variations. *Tellus*, 51A, 505–516.
- Cleveland, W.S., Devlin, S.J., 1988. Locally-weighted regression: An approach to regression analysis by local fitting. *Journal of the American Statistical Association*, 83, 403, 596–610.
- de Rham, L.P., Prowse, T.D., Bonsal, B.R., 2008. Temporal variations in river-ice break-up over the Mackenzie River Basin, Canada. *J Hydrol*, 349, 441–454.
- EEA Report No. 12/2012. *Climate change, impacts and vulnerability in Europe 2012*. [online]. <http://www.eea.europa.eu/pl/themes>
- Filipiak, J., 2004. *Variability of Air Temperature on the Coast and Pomeranian Lake District in the Second Half of the 20th Century*. IMGW, Warszawa. (In Polish.)
- Frolova, N.L., Alekseevskiy, N.I., 2010. Influence of ice regime on hydroecological safety under climate change: the chase study in the north of European part of Russia. In: Servat, E., Demuth, S., Dezter, A., Daniell, T. (Eds.): *Proc. 6th Word FRIEND Conf. Global Change: Facing Risk and Threats to Water Resources*. IAHS Publ. No. 340. IAHS Press, Wallingford, UK, pp. 40–46.
- Grjajtowicz, J.P., Świątek, M., Olechwir, T., 2002. The relationships of the North Atlantic Oscillation with ice conditions at the Polish Baltic coast. In: Marsz, A., Styszyńska, A. (Eds.): *North Atlantic Oscillation and its Inflow on Variability of Climatic and Hydrologic Conditions of Poland*. Maritime Academy, Gdynia, pp. 191–203. (In Polish.)
- Gorączko, M., 2013. Variability of ice phenomena on the Vistula River in the vicinity of Bydgoszcz. *Prz. Nauk. Inż. Środ.*, 62, 382–388. (In Polish.)
- Graf, R., 2015. Variations of the thermal conditions of the Warta in the profile connecting the Urstromtal and gorge sections of the valley (Nowa Wieś Podgórna – Śrem – Poznań). In: Absalon, D., Matysik, M., Ruman, M. (Eds.): *Nowoczesne metody i rozwiązania w hydrologii i gospodarce wodnej*. Komisja Hydrologiczna PTG, PTG Oddział Katowice, pp. 177–194. (In Polish.)
- Graf, R., 2018. Distribution properties of a measurement series of river water temperature at different time resolution levels (Based on the example of the Lowland River Noteć, Poland). *Water*, 10, 2, 203.
- Graf, R., Tomczyk, A.M., 2018. The impact of cumulative negative air temperature degree-days on the appearance of ice cover on a river in relation to atmospheric circulation. *Atmosphere*, 9, 6, 204.
- Graf, R., Łukaszewicz, J.T., Jawgiel, K., 2018. The analysis of the structure and duration of ice phenomena on the Warta river in relation to thermic conditions in the years 1991–2010. *Woda-Środowisko-Obszary Wiejskie*, 18, 4, 64, 5–28. (In Polish.)
- Hagen, E., Feistel R., 2005. Climatic turning points and regime shifts in the Baltic Sea region: the Baltic winter index (WIBIX) 1659–2002. *Boreal Environ Res.*, 10, 211–224.
- Hester, E.T., Doyle, M.W., 2011. Human impacts to river temperature and their effects of biological process: A quantitative synthesis. *Journal of the American Water Resources Association*, 47, 3, 571–587.
- Hurrell, J.W., 1995. Decadal trends in the North Atlantic oscillation: regional temperatures and precipitation. *Science*, 269, 5224, 676–679.
- IPCC, 2007. *International Panel on Climate Change Fourth Assessment Report: Climate Change 2007*. Cambridge University Press, Cambridge.
- Jurgelėnaitė, A., Kriauciūnienė, J., Šarauskienė, D., 2012. Spatial and temporal variation in the water temperature of Lithuanian rivers. *Baltica*, 25, 1, 65–76.
- Kirschenstein, M.C., Łukaszewicz, J.T., 2014. Ekologiczne problemy osobo ochranjaemich przyrodnich territorii. Charakterystyka temperatury wozducha i atmosferycznych osadkow, a takze anomalii temperatury i osadkow w Koszalinie. In: *Proc. Conf. Aktualnyje nauczno-technicheskie i ekologiczeskie problemy sochranienia sredy obtantija*. [Current scientific technical and ecological problems of the environmental resources protection]. Brest, pp. 119–128. (In Russian.)
- Klavins, M., Briede, A., Rodinov, V., Kokorite, I., Frisk, T., 2002. Long-term changes of the river runoff in Latvia. *Boreal Environ Res.*, 7, 447–456.

- Klavins, M., Briede, A., Rodinov, V., 2009. Long term changes in ice and discharge regime of rivers in the Baltic region in relation to climatic variability. *Climatic Change*, 95, 3–4, 485–498.
- Kondracki, J., 2009. *Regional Geography of Poland*. PWN, Warszawa. (In Polish.)
- Kornaś, M., 2014. Ice phenomena in the Warta River in Poznań in 1961–2010. *Questiones Geographice*, 33, 1, 51–59.
- Koronacki, J., Cwik, J., 2005. *Statistical Learning Systems*. ISBN, Warszawa, pp. 168–179. (In Polish.)
- Kozuchowski, K., (Ed.), 2000. *Seasons in Poland – Seasonal Changes in the Environment versus Long-Term Climatic Tendencies*. IMGW Publisher. (In Polish.)
- Kozuchowski, K., Degirmendžic, J., 2002. Circulation indicators and air temperature in Poland. In: Marsz, A., Styszyńska, A. (Eds.): *North Atlantic Oscillation and its inflow on variability of climatic and hydrologic conditions of Poland*. Akademia Morska w Gdyni, pp. 111–128. (In Polish.)
- Kreft, A., 2013. Ice problems in the Odra section of the Oder. *Gospodarka Wodna*, 6, 1–4. (In Polish.)
- Kuusisto, E., Elo, A.R., 1998. Lake and river ice variables as climate indicators in Northern Europe. In: *Internationale Vereinigung für Theoretische und Angewandte Limnologie: Verhandlungen*, pp. 2761–2764.
- Kwiatkowski, D., Philips, P.C.B., Schmidt, P., Shin, Y., 1992. Testing the null hypothesis of stationary against the alternative of a unit root. *Journal of Econometrics*, 54, 159–178.
- Lizuma, L., Klavins, M., Briede, A., Rodinovs, V., 2007. Long-term changes of air temperature in Latvia. In: Klavins, M. (Ed): *Climate Change in Latvia*. UL Publishing House, Riga, pp. 11–21.
- Lorenc, H., 1998. Evaluation of the degree of implementation of the program "meteorological observations and climate studies in the system of integrated environmental monitoring" and synthesis of obtained results for the period 1994–1997. In: Kostrzewski, A. (Ed.): *Integrated Monitoring of the Natural Environment. Functioning and development trends of Poland's geo-ecosystems*. IX Symposium of the ZMŚP, Biblioteka Monitoringu Środowiska. Warszawa, pp. 113–119. (In Polish.)
- Łukaszewicz, J., 2017a. The frequency and nature of the occurrence of ice phenomena in the lower reaches of the Wieprza River in the aspect of climate change, with particular regard to changes in air temperature. *Nauki Przyrodnicze*. II, 5, 69–74. (In Polish.)
- Łukaszewicz, J.T., 2016. The process of the ice phenomenon on the Słupia River in 1960–2013. *Słupskie Prace Geograficzne*, 12, 5–20. (In Polish.)
- Łukaszewicz, J.T., 2017b. The course and the character of the ice phenomena in selected sections of Przymorze Rivers with a high influence of anthropopressure in relation to the climate changes that occur in the coastal zone of the Baltic Sea. *Acta Architectura*, 16, 1, 93–113. (In Polish.)
- Łukaszewicz, J.T., 2017c. Nature and variability of the ice phenomena in lower reaches of the Rega river in the context of the climate changes. In: Zinoviyev, E.A., Kitaev, A.B. (Eds): *Proc. Int. Conf. Hydrobiology and Ichthyology*. Perm State University, Perm, 3, 3, pp. 123–130. (In Russian.)
- Łukaszewicz, J.T., Jawgiel, K., 2016. The process of the ice phenomenon on the Leba River. *Badania Fizjograficzne, Seria - A - Geografia Fizyczna*, pp. 97–116. (In Polish.)
- Magnuson, J.J., Robertson, D.M., Benson, B.J., Wynne, R.H., Livingstone, D.M., Arai, T., Assel, R.A., Barry, R.G., Card, V., Kuusisto, E., Grain, N.G., Prowse, T.D., Stewart, K.M., Vuglinski, V.S., 2000. Historical trends in lake and rivers ice cover in the Northern Hemisphere. *Science*, 289, 5482, 1743–1746.
- Majewski, W., 2009. Flows in open channel and ice phenomena. *Acta Geophysica*, 55, 1, 11–2. DOI: 10.2478/s11600-006-0041-8.
- Marsz, A., Styszyńska, A., 2001. *The North Atlantic Oscillation and the Air Temperature over Poland*. Wyższa Szkoła Morska, Gdynia. (In Polish.)
- Marshall, J., Kushnir, Y., Battisti D., Chang, P., Czaja, A., Dickson, R., Hurrell, J., McCartney, M., Saravanan, R., Visbeck, M., 2001. North Atlantic climate variability: phenomena, impacts and mechanisms. *Int. Journal of Climatology*, 21, 1863–1898.
- Morse, B., Hicks, F., 2005. Advances in river ice hydrology 1999–2003. *Hydrol. Process.*, 19, 1, 247–263.
- Niedźwiedź, T., 2002. Relations between NAO and circulation indicators over Poland. In: Marsz, A., Styszyńska, A. (Eds.): *North Atlantic Oscillation and its inflow on variability of climatic and hydrologic conditions of Poland*. Wyższa Szkoła Morska, Gdynia, pp. 87–97. (In Polish.)
- Paeth, H., Hense, A., Glowienka-Hense, R., Voss, R., Cubash, U., 1999. The North Atlantic Oscillation as an indicator for greenhouse-gas induced regional climate change. *Clim. Dyn.*, 15, 953–960.
- Prowse, T.D., Beltaos, S., 2002. Climatic control of river-ice hydrology: a review. *Hydrol. Process.*, 16, 805–822, DOI: 10.1002/hyp.369.
- Przybylak, R., Wójcik, G., Marciniak, K., 2003. Influence of the North Atlantic Oscillation and Arctic Oscillation on thermal conditions in the cold season in Poland from the 16th to the 20th centuries. *Przegl. Geofiz.*, 48, 61–74. (In Polish.)
- Ptak, M., Choiński, A., Kirviel, J., 2016. Long-term water temperature fluctuations in coastal rivers (southern Baltic) in Poland. *Bulletin of Geography. Physical Geography Series*, 11, 35–42.
- Russak, V., 2009. Changes in solar radiation and their influence on temperature trend in Estonia (1955–2007). *Journal of Geophysical Research Atmospheres*, 114, 1, 114 (D00D01).
- Shannon, C.E., Weaver, W., 1949. *The Mathematical Theory of Communication*. University of Illinois Press, Urbana.
- Shumway, R.H., Stoffer, D.S., 2010. *Time Series Analysis and its Applications with R Examples*. Springer Science & Business Media.
- Taylor, S., Letham, B., 2017. *Prophet: Automatic Forecasting Procedure*. R package version 0.1.1.
- Tylkowski, J., 2013. Temporal and spatial variability of air temperature and precipitation at the Polish coastal zone of the southern Baltic Sea. *Baltica*, 26, 1, 83–94.
- Uvo, C.B., 2003. Analyses and regionalization of Northern Europe winter precipitation based on its relationship with North Atlantic Oscillations. *Int. J. Climatol.*, 23, 1185–1194.
- Webb, B.W., Nobilis, F., 2007. Long-term changes in river temperature and the influence of climatic and hydrological factors. *Hydrological Sciences Journal*, 52, 1, 74–85.
- Woś, A., 2010. *Climate of Poland in the Second Half of the Twentieth Century*. Wydawnictwo Naukowe UAM, Poznań. (In Polish.)
- Yoo, J., D'Odorico, P., 2002. Trends and fluctuations in the dates of ice break-up of lakes and rivers in Northern Europe: the effect of the North Atlantic. *Journal of Hydrology*, 268, 1–4, 100–112.
- Yue, S., Pilon, P., Phinney, B., Cavadias, G., 2002. The influence of autocorrelation on the ability to detect trend in hydrological series. *Hydrological Processes*, 16, 9, 1807–1829.

Received 22 January 2019

Accepted 5 June 2019

Equations for predicting interrill erosion on steep slopes in the Three Gorges Reservoir, China

Qian Feng^{1, 2, 3*}, Dong Linyao^{1, 3}, Liu Jigen¹, Sun Bei¹, Liu Honghu¹, Huang Jiesheng², Li Hao¹

¹ Department of Soil and Water Conservation, Changjiang River Scientific Research Institute, Wuhan, Hubei 430072, China.

² School of Water Resources and Hydropower Engineering of Wuhan University, Wuhan, Hubei 430010, China.

³ Research Center on Mountain Torrent and Geologic Disaster Prevention, Ministry of Water Resources, Wuhan, Hubei 430010, China.

*Corresponding author. Tel.: +86 02782926992. Fax: +86-02782926357. E-mail: Qianfeng@whu.edu.cn

Abstract: The Three Gorges Reservoir region suffers from severe soil erosion that leads to serious soil degradation and eutrophication. Interrill erosion models are commonly used in developing soil erosion control measures. Laboratory simulation experiments were conducted to investigate the relationship between interrill erosion rate and three commonly hydraulic parameters (flow velocity V , shear stress τ and stream power W). The slope gradients ranged from 17.6% to 36.4%, and the rainfall intensities varied from 0.6 to 2.54 mm·min⁻¹.

The results showed that surface runoff volume and soil loss rates varied greatly with the change of slope and rainfall intensity. Surface runoff accounted for 67.2–85.4% of the precipitation on average. Soil loss rates increased with increases of rainfall intensity and slope gradient. Regression analysis showed that interrill erosion rate could be calculated by a linear function of V and W . Predictions based on V ($R^2 = 0.843$, $ME = 0.843$) and W ($R^2 = 0.862$, $ME = 0.862$) were powerful. τ ($R^2 = 0.721$, $ME = 0.721$) did not seem to be a good predictor for interrill erosion rates. Five ordinarily interrill erosion models were analyzed, the accuracy of the models in predicting soil loss rate was: Model 3 ($ME = 0.977$) > Model 4 ($ME = 0.966$) > Model 5 ($ME = 0.963$) > Model 2 ($ME = 0.923$) > Model 1 ($ME = 0.852$). The interrill erodibility used in the model 3 (WEPP) was calculated as 0.332×10^6 kg·s·m⁻⁴. The results can improve the precision of interrill erosion estimation on purple soil slopes in the Three Gorges Reservoir area.

Keywords: Purple soil; Interrill erosion rate; Rainfall intensity; Slope gradient; Hydraulic parameter.

INTRODUCTION

In recent decades, soil erosion by water is considered to be a great environmental problem in the Three Gorges Reservoir region of China (Peng et al., 2015). Owing to the thin and loose soil layer, numerous rainstorms and unreasonable land use, there have been serious soil degradation and eutrophication in this region. Average soil loss rates in the Three Gorges Reservoir region have reached 2741 t km⁻² year⁻¹, with approximately 3440 km² subjected to a soil erosion rate of over 8000 t km⁻² year⁻¹ (Long et al., 2012).

According to the source of eroded sediments, soil erosion by water is usually divided into two parts: rill and interrill erosion (Meyer and Wischmeier, 1969). Interrill erosion plays an important link between rainfall and concentrated flow (Issa et al., 2006). Hence, it is essential to establish a interrill erosion model to assist in making decisions on soil erosion control. Many physically based erosion models, originally developed for a particular area, are viable for estimating interrill erosion rate, including the ANSWERS model (Beasley and Huggins, 1982), the WEPP model (Water Erosion Prediction Project) (Nearing et al., 1989), the EUROSEM model (European Soil Erosion Model) (Morgan et al., 1998), and LISEM model (the Limburg Soil Erosion model) (De Roo et al., 1994). Process-based models contain more parameters and demand a large amount of data to verify. By contrast, experience models are simple and easy for calibration (Zhang and Wang, 2017). The frequency of rainfall, reflecting the raindrop impact, had been used in predicting interrill erosion rate (Nearing et al., 1989). Kinnell (1993) suggested that factors such as runoff rate and slope could be used for calculating interrill erosion rate. Numerous studies have confirmed this finding. (Qian et al., 2016; Wei et

al., 2009). The exponents of factors varied in different models. Meyer (1981) observed that rainfall intensity exponent decreased with the increase of soil clay content. Zhang (1998) suggested that the exponent of slope gradient was two thirds. This conclusion is in agreement with report of Bulygin et al. (2002).

As soil erosion by water is largely determined by flow hydraulic characteristics, commonly, concepts were derived from river sediment dynamic theory and applied to interrill erosion. The hydraulic parameters often used to predict interrill erosion rate are flow velocity, shear stress and stream power (Hairsine and Rose, 1992; Qian et al., 2016). Interrill erosion rates are also well correlated with the power functions of flow velocity, shear stress and stream power (Ding and Huang, 2017; Fan and Wu, 1999; Wu et al., 2017). Some studies have shown that stream power is superior to shear stress and flow velocity in predicting interrill erosion rate (Wu et al., 2017).

Although many models have been used to predict interrill erosion rate, it was unclear for technicians how to choose an appropriate model for purple soil region. Kinnell and Cummings (1993) observed that the runoff process and the associated erosion response are related to soil properties. There is no existing expression that can handle the entire range of data (Govers, 1992). Purple soil is widely distributed in the Three Gorges Reservoir region. In addition, most of the researches were carried out on relatively low slopes (less than 26.8%), whereas the farmlands on the Three Gorges Reservoir area are distributed almost entirely across steep slope land. Liu et al. (1994) determined that equation could result in a large error when extrapolation exceeds the range of slopes. Hence, we focused on steep slopes, which are characteristic topographies on the Three Gorges Reservoir area, in combination with dif-

ferent rainfall intensities and with purple soil as the test soil. The main objectives of this study are: (i) to quantify the production mechanism of runoff and sediment during the interrill erosion process; (ii) to investigate the relationship between interrill erosion rate and hydraulic parameters; (iii) to compare commonly used interrill erosion models, as well as develop more precise equations for predicting interrill erosion rate of purple soil regions.

MATERIAL AND METHODS

Study area

Soil samples were selected from WangJiaQiao watershed, which is located in the Three Gorges Reservoir (31°5'N to 31°9'N, 110°40'E to 110°43'E). It has a subtropical monsoon climate with an annual mean temperature of 18°C. Mean annual precipitation is 1016 mm, of which more than 70% occur between May and September. Slope gradients within the watershed range from 3.5% to 160.0% with an average of 42.4%. The vegetation mainly consists of secondary coniferous and broadleaved mixed forest. The research area is an agricultural watershed where a large number of disturbed soil slopes are constructed in agricultural, construction and other activities.

Three slope gradients (17.6%, 26.8% and 36.4%) were selected to represent sloping farmland on gentle, mild and steep slope, respectively. Soil samples were taken from 0–40 cm soil layer of sloping cropland. To remove impurities such as stones and grass, the air-dried soil samples were sieved through a 5 mm mesh. The soil has been developed from purple sandy shale. Selected purple soil was classified as Entisols based on US Soil Taxonomy. The physicochemical properties of the selected soil were measured by standard methods (ISSAS, 1978). The particle size distribution was determined using the pipette method, and bulk densities were determined using 250mL cylinders. Aggregate size distribution was measured by dry and wet sieve (Kemper and Rosenau, 1986). The stability of soil aggregate was represented by the mean weight diameter (MWD) (Yan et al., 2008):

$$MWD = \sum_{i=1}^7 x_i w_i \tag{1}$$

where x_i is the average diameter of the i level, w_i is the weight fraction of aggregates at the i level, and i stands for the 7 size levels. The pH value of soil was estimated using pH probe in 1:2.5 soil-water mixture. Soil organic matter (OM) was measured by the $K_2Cr_2O_7$ wet oxidation method. Cation exchange capacity (CEC) was determined by the ammonium acetate method. The physical and chemical properties of the soil are given in Table 1.

Experiment setup

Experiments were conducted in the soil erosion laboratory of the Institute of Changjiang River Scientific Research, Wuhan City, China. A slope adjustable soil flume was used in this study that is: 3 m (length) × 1 m (width) × 0.5 m (depth), with perforated drains at the drain bed. The soil flume was structured with metal sheets and the slope gradient ranges from 0.0% to 46.6% with adjustment step of 8.7%. A “V”- shape trough was inserted at the soil surface and via plastic pipes, into a surface runoff collection container (Figure 1). The soil flumes were packed using the method by Römken et al. (2002). First of all, a 0.02–0.03 m sand layer was filled for adequate drainage. Then the subsequent layer from 0.03–0.15 m was packed carefully with soils of size 0–4 mm. A 0.4 m surface layer was packed into the soil flume in 0.05 m increments. The soil was evenly distributed on the flume, punned with a wood brick and hands, and adjusted to a uniform surface.

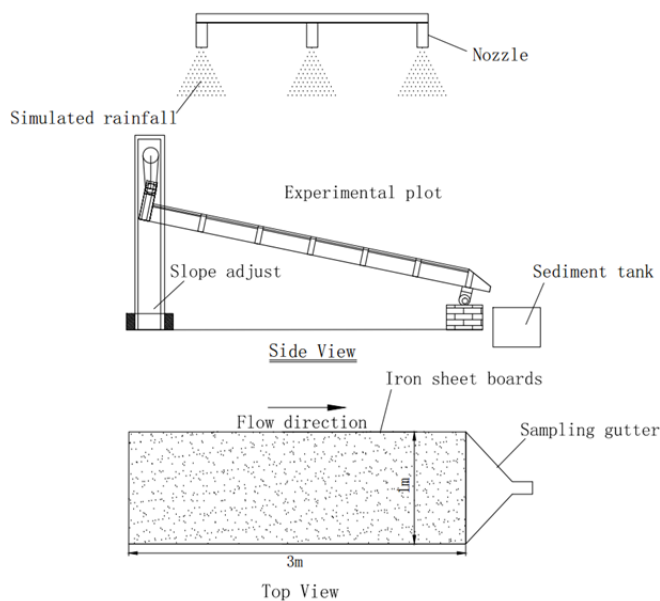


Fig. 1. Rainfall simulation experimental equipment.

The rainfall simulator system, which includes three sets of oscillating TSPT-X type nozzles described by Römken et al. (2002), was used to apply precipitation with different intensities. By adjusting the nozzles aperture and water pressure, this rainfall simulator system can be set at any selected rainfall intensity, ranging from 0.33 to 5.00 mm min⁻¹. The installation height of the nozzles was 3 m. The diameter of raindrops ranged from 0.2 mm to 2 mm, and the median raindrop diameter was 0.8 mm, with uniform rainfall variation (>85% of raindrop diameters were <1.0 mm). The kinetic energy distribution of raindrops was 55.7–137.6 J m⁻² h⁻¹. Since high-intense (>50 mm h⁻¹) and short-duration rainstorms cause the most severe soil erosion, five rainfall simulations (0.6, 1.1, 1.61, 2.12 and 2.54 mm min⁻¹) were conducted in this study. Every test was performed varying rainfall intensity but with a fixed rainfall volume of 50 mm. Rainfall duration was controlled by the intensity. The rainfall duration was 20, 24, 31, 45, and 83 min, and the corresponding rainfall intensity was of 2.54, 2.12, 1.61, 1.1 and 0.6 mm min⁻¹, respectively, following a similar method as Ding and Zhang (2016). The water used for rainfall simulation was deionized water. Before each rain simulation, a known amount of rainfall was sprayed to minimize the differences

rated drains at the drain bed. The soil flume was structured with metal sheets and the slope gradient ranges from 0.0% to 46.6% with adjustment step of 8.7%. A “V”- shape trough was inserted at the soil surface and via plastic pipes, into a surface runoff collection container (Figure 1). The soil flumes were packed using the method by Römken et al. (2002). First of all, a 0.02–0.03 m sand layer was filled for adequate drainage. Then the subsequent layer from 0.03–0.15 m was packed carefully with soils of size 0–4 mm. A 0.4 m surface layer was packed into the soil flume in 0.05 m increments. The soil was evenly distributed on the flume, punned with a wood brick and hands, and adjusted to a uniform surface.

Table 1. Physical-chemical properties of the study soils.

Soils	Parent material	Bulk density (g cm ⁻³)	Particle size distribution (%)			Organic matter (%)	pH (H ₂ O)	MWD (mm)	
			Clay	Silt	Sand			Dry	Wet
Purple soil (PS)	Shale	1.35±0.01	24.43±3.11	30.39±3.25	45.18±8.54	1.23±0.59	6.0±0.15	4.62±0.46	0.89±0.06

MWD is mean weight diameter.

in antecedent soil moisture. Surface runoff was collected in the bucket. Runoff samples were sampled and measured every 3 min. Sediment samples were deposited from the water, and then oven-dried at 105°C for 12 h to calculate sediment concentration. Three replicates were performed on each treatment, and the means values were applied in all analysis.

Determination of hydraulic parameters and interrill erosion rate

Flow depth was measured vertically by a level probe (SX40, Chongqing Hydrological Equipment Factory) with a precision of 0.01 mm. For each test, three measured sections were set: 1.0, 2.0 and 3.0 m, respectively, from the upper edge to the lower edge of the plot. In each position, three flow depths were measured in left, right and center with three replicates. Surface flow velocities (V_s) were measured using the dye method in which three measurement positions were set along the flow direction with 1 m interval. In the dye tracer technique, potassium permanganate solution was used to measure the surface flow velocities. A small amount of dye was injected into the runoff at the top of the flume, and a digital watch was used to measure the travel time of the leading edge of the dye cloud along the 1 m of the flume. In addition, the leading edge of the dye cloud can be visually observed, which leads to some errors in the measurement of travel time (Dunkerley, 2003). The mean flow velocity (V) was calculated by the product of surface flow velocity (V_s) and a reduction coefficient (n). For laminar flow, transition flow and turbulent flow, n is 0.67, 0.70 and 0.80, respectively (Abrahams et al., 1986).

Hydraulic variables such as the Reynolds number, shear stress and stream power were calculated based on the flow rate, measured flow depth and velocity as follows (Hairsine and Rose, 1992):

$$Re = \frac{Vh}{\nu_m} \quad (2)$$

where, Re is the Reynolds number, which is a dimensionless parameter used for describing the flow hydraulic characteristics, the Reynolds number were from 48.98 to 392.92 in this study; V ($\text{m}\cdot\text{s}^{-1}$) is the mean flow velocity; h (m) is the measured mean depth of flow; ν_m ($\text{m}^2\cdot\text{s}^{-1}$) is kinematic viscosity coefficient of silt-laden flow, which was calculated using (Sha, 1965):

$$\nu_m = \nu / \left(1 - \frac{S_v}{2\sqrt{d_{50}}} \right) \quad (3)$$

where, ν ($\text{m}^2\cdot\text{s}^{-1}$) is the kinematic viscosity, which was calculated by the relation of $\nu = 0.01775 / (1 + 0.0337t + 0.000221t^2)$, t is the water temperature; S_v (%) is the volume of sediment

concentration and d_{50} (mm) is the median size of the sediment particle;

$$\tau = \rho ghS \quad (4)$$

where, τ (Pa) is the shear stress, ρ ($\text{kg}\cdot\text{m}^{-3}$) is the mass density of water; g ($\text{m}\cdot\text{s}^{-2}$) is acceleration of gravity; S is slope gradient ($\text{m}\cdot\text{m}^{-1}$); and

$$W = \tau V = \rho ghSV \quad (5)$$

where W ($\text{kg}\cdot\text{m}^{-1}$) is the stream power, which reflects the impact of slope and flow rate on erosion (Huang, 1995).

No rill erosion was initiated during the simulated rainfall experiment. Interrill erosion rate was given by:

$$D_i = \frac{M_s}{LWt} \quad (6)$$

where, D_i ($\text{kg}\cdot\text{s}^{-1}\cdot\text{m}^{-2}$) is the soil loss rate of interrill areas, T (s) is the sampling time, M_s (kg) is the weight of sediments in the sampling time, L (m) is the length of the flume and W (m) is the width of the flume.

Five commonly used interrill erosion models were used to predict interrill erosion rate on purple soil slope. The equation and source of selected models are described in Table 2.

Data analysis

Data analyses included the analysis of variance (ANOVA) and regression analysis. An analysis of variance was utilized to compare the runoff and soil loss rates of different treatments and the least significant difference (LSD) method in the probability of 0.05 was used to distinguish the statistical difference between different treatments. Two-way ANOVA was used to examine rainfall and slope factors related to flow hydraulics and erosion responses. The performance of the proposed models was evaluated by using the coefficient of determination (R^2) and Nash-Sutcliffe model efficiency (ME). The values of R^2 and ME were calculated as follows:

$$R^2 = \frac{\left[\sum_{i=1}^n (O_i - \bar{O})(P_i - \bar{P}) \right]^2}{\sum_{i=1}^n (O_i - \bar{O})^2 \sum_{i=1}^n (P_i - \bar{P})^2} \quad (7)$$

$$ME = 1 - \frac{\sum_{i=1}^{15} (O_i - P_i)^2}{\sum_{i=1}^{15} (O_i - \bar{O})^2} \quad (8)$$

where R^2 is the coefficient of determination, O_i are the

Table 2. Models applied to interrill erosion rate.

	Equation	Slope exponent	Rainfall intensity exponent	Runoff exponent
Model 1	$D_i = K_i I^2$ (Nearing et al., 1989)	–	2	–
Model 2	$D_i = K_i I Q S$ (Kinnell, 1993)	1	1	1
Model 3	$D_i = K_i I Q S_f$ (Flanagan and Nearing, 1995)	–	1	1
Model 4	$D_i = K_i I Q S^{2/3}$ (Bulygin et al., 2002)	2/3	1	1
Model 5	$D_i = K_i I Q^{1/2} S^{2/3}$ (Zhang et al., 1998)	2/3	1	1/2

D_i is the interrill erosion rate ($\text{kg}\cdot\text{m}^{-2}\cdot\text{s}^{-1}$), K_i is the soil erodibility ($\text{kg}\cdot\text{m}^{-4}\cdot\text{s}$), I is the rainfall intensity ($\text{m}\cdot\text{s}^{-1}$), Q is the average runoff rate ($\text{m}\cdot\text{s}^{-1}$), S is slope gradient ($\text{m}\cdot\text{m}^{-1}$), and S_f is a slope adjustment factor given by: $S_f = 1.05 - 0.85e^{-4\sin\theta}$, where θ is the slope gradient of the plot.

measured values, \bar{O} is the average of the measured values, P_i are the predicted values, \bar{P} is the average of the predicted values. ME is the Nash-Sutcliffe model efficiency (Nash and Sutcliffe, 1970), an ME value indicates that the residual variance of relative size compared to the measured values of variance [good ($ME > 0.8$), acceptable ($0.4 < ME < 0.8$) and unacceptable ($ME < 0.4$)] (An et al., 2012).

RESULTS AND DISCUSSION
Runoff and erosion response

Significant differences were found on surface runoff volume and soil loss rates among different treatments (Figure 2). Surface runoff varied from 35.9 to 40.5 mm, 32.7 to 41.0 mm and 36.1 to 41.7 mm as rainfall intensity increased from 0.6 to 2.54 mm·min⁻¹ for slope gradients of 17.6%, 26.8% and 36.4%, respectively. The surface runoff amount and the difference were greater in the experiments with the steep slope gradients (26.8%, 36.4%) compared with the low slope gradient event. Obviously, on a steeper slope, the ponding time was shorter, the flow velocity was higher and the surface infiltration decreased more quickly (Chaplot and Le Bissonnais, 2003; Fang et al., 2015). These are likewise the reasons why Fox et al. (1997) found runoff amount increased with slope gradient on mobile beds.

Under the experimental conditions, soil loss rates ranged from 0.09 to 2.87 g·m⁻²·s⁻¹ (Figure 2). For all slopes, the soil loss rate increased with the increase of rainfall intensity, indicating positive interactions between rainfall intensity and slope.

Higher soil loss rates meant greater erosion potential, which suggested that soil loss could be greater for steep slopes in a short duration, high intensity rainfall if sediment transport capacity was not limited to the runoff transport on steep slopes (Foster and Meyer, 1975). In order to find out the factors affecting hydrological and erosion response, two-way ANOVA was conducted (Table 3). The results showed that soil loss rate, flow velocity and Reynold number were statistically correlated to rainfall intensity and interactions between rainfall intensity and slope. Nevertheless, surface runoff was statistically independent of slope and rainfall intensity.

Modeling interrill erosion rate using hydraulic parameters

Numerous studies have shown that hydraulic parameters can be used to calculate the rate of interrill erosion (Guo et al., 2013; Nearing et al., 1999). In this study, the soil loss rate of interrill areas were plotted with these three hydraulic parameters to establish prediction models (Figures 3, 4, 5). Fig. 3 shows the interrill erosion rate was a positive linear correlation with flow velocity (v), which is expressed as in Eq. (9):

$$D_i = 0.0506V - 0.0027 \quad (9)$$

$$(R^2 = 0.843, ME = 0.843, P < 0.01, n = 15)$$

where, D_i (kg·s⁻¹·m⁻²) is the soil loss rate of interrill areas, V (m s⁻¹) is the mean flow velocity. The determination coefficient of Eq. (9) was 0.843 (good: $R^2 > 0.8$), which implied that D_i was directly related to V and P -value < 0.01 indicated that D_i was

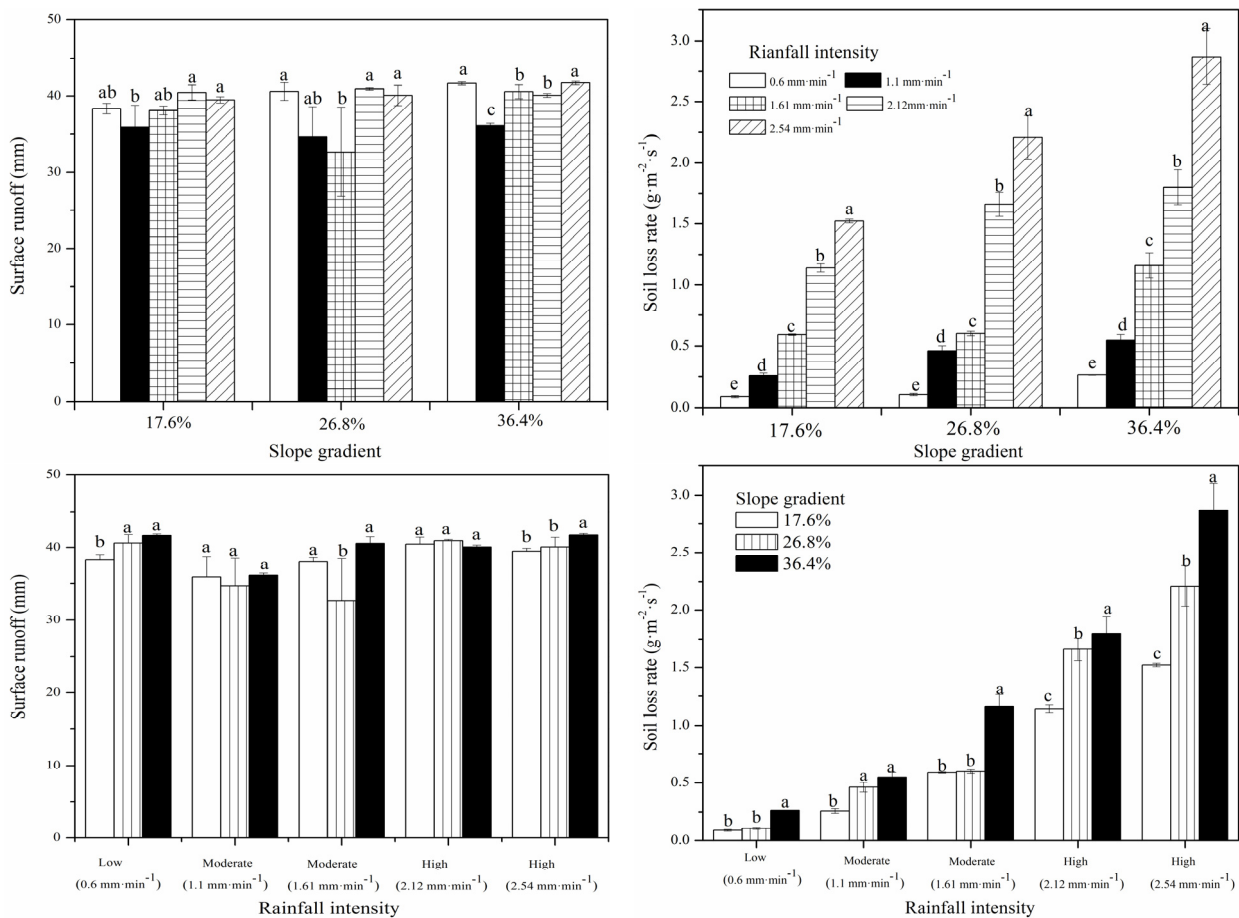
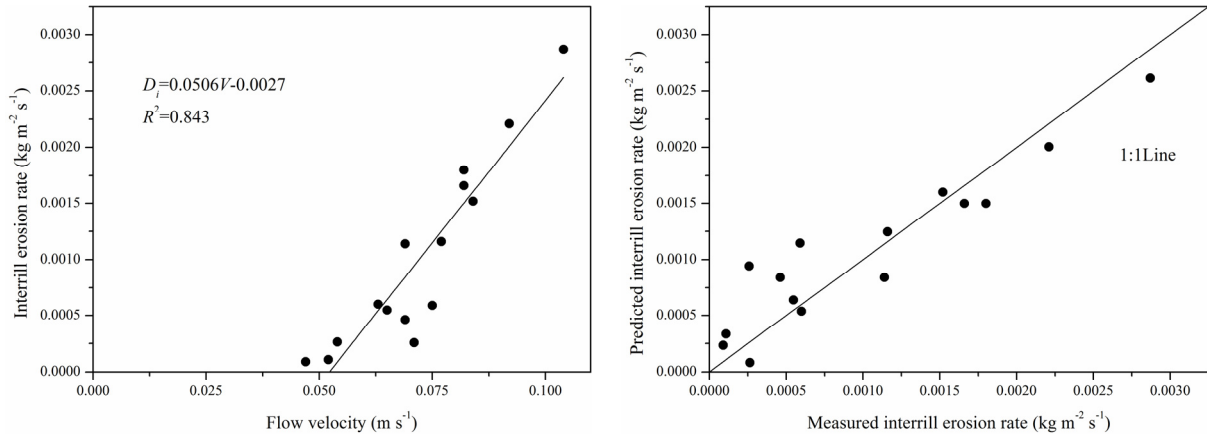
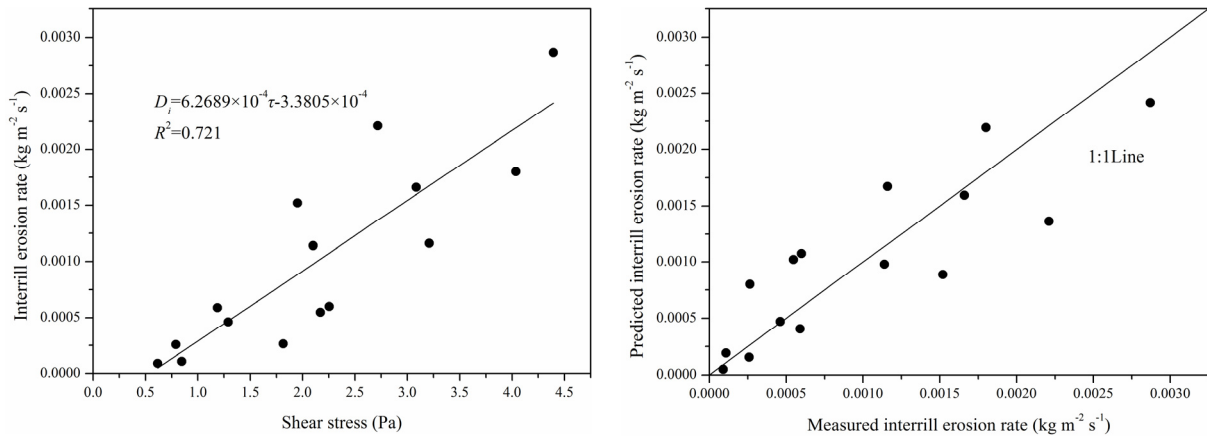
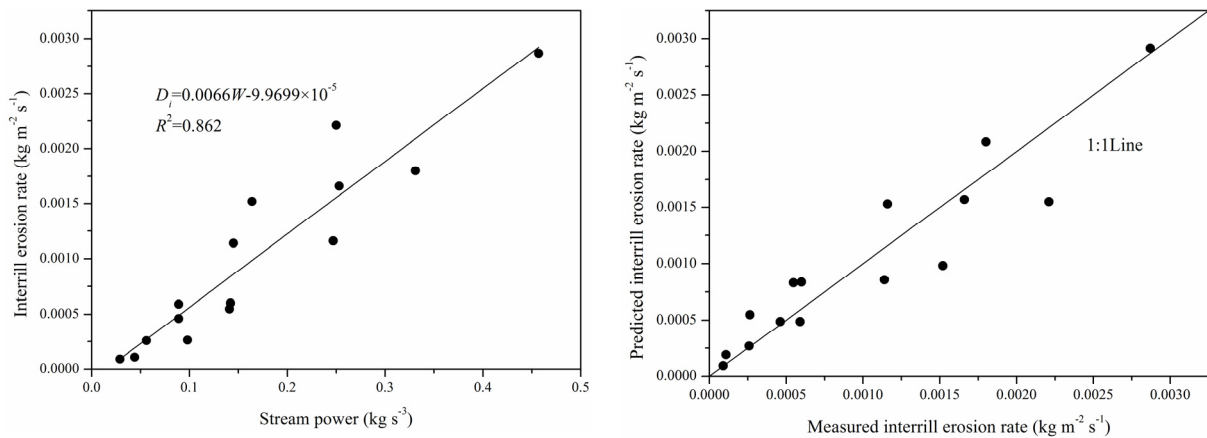


Fig. 2. Surface runoff volumes and soil loss rates for different slope gradients and rainfall intensities. For each treatment, means with the same lower-case letter are not significantly ($p < 0.05$, least significant difference) different.

Table 3. Two-way ANOVA of rainfall intensity and slope gradient for different variables related to hydrological and erosion response.

Variable	Soil detachment rate D_i ($\text{g}\cdot\text{m}^{-2}\cdot\text{s}^{-1}$)	Surface runoff $S\text{-}R$ (mm)	Flow velocity V ($\text{m}\cdot\text{s}^{-1}$)	Reynold number Re
Rainfall intensity I	0.902**	0.284n.s.	0.892**	0.954**
Slope gradient S	0.306n.s.	0.244n.s.	0.198n.s.	0.213n.s.
$I\times S$	0.946**	0.364n.s.	0.878**	0.918**

n.s. not significant, * marked p -values are significant (<0.05), ** marked p -values are significant (<0.01).

**Fig. 3.** Relationship between interrill erosion rates and flow velocity.**Fig. 4.** Relationship between interrill erosion rates and shear stress.**Fig. 5.** Relationship between interrill erosion rates and stream power.

significant correlated to V (significant: $P < 0.05$); The high model efficiency (ME) value in Eq. (9) showed a good agreement between the predicted and measured values (good: $ME > 0.8$). Thus, the linear flow velocity models could be used to predict the interrill erosion rate. Similar results were also point-

ed out by Guo et al. (2013). However, Wu et al. (2017) found that D_i could be calculated as a power function of V . The difference in results may be ascribed to two reasons. (1) Flow velocity was susceptible to the range of slope, the maximum slope gradient in this study were 36.4%, but the slope gradient of Wu

et al. (2017) ranged from 12.23% to 46.63%, thus slope range differences resulted in the difference between D_i and V . (2) Soil surface roughness can influence runoff generation and flow velocity, which are similar to the results of many previous studies (Ding and Huang, 2017; Gomez and Nearing, 2005; Hairsine et al., 1992).

Fig. 4 shows the interrill erosion rate had positive linear relationships with shear stress (τ), which is expressed as in Eq. (10):

$$D_i = 6.2689 \times 10^{-4} \tau - 3.3805 \times 10^{-4} \quad (10)$$

$$(R^2 = 0.721, ME = 0.721, P < 0.01, n = 15)$$

where D_i ($\text{kg} \cdot \text{s}^{-1} \cdot \text{m}^{-2}$) is the soil loss rate of interrill areas, τ (Pa) is the shear stress. The determination coefficient of Eq. (10) was 0.721 and the model efficiency (ME) value was 0.721, which implied that for the selected intensities and slopes, the consistency between predicted and measured values was low. Thus, shear stress did not predict interrill erosion rate well. In the view of definition, that flow shear stress is proportional to the product of the flow depth and slope gradient, showing that D_i must be sensitive to slope and flow depth (Wang et al., 2016). However, soil detachment rate was statistically independent of slope gradient in our study, so shear stress did not seem to be a good predictor for interrill erosion rates.

Fig. 5 shows the interrill erosion rate had positive linear relationships with stream power (W), which is expressed as in Eq. (11):

$$D_i = 0.0066W - 9.9699 \times 10^{-5} \quad (11)$$

$$(R^2 = 0.862, ME = 0.862, P < 0.01, n = 15)$$

where D_i ($\text{kg} \cdot \text{s}^{-1} \cdot \text{m}^{-2}$) is the soil loss rate of interrill areas, W ($\text{kg} \cdot \text{s}^{-3}$) is the stream power. The determination coefficient of Eq. (11) was 0.862 (good: $R^2 > 0.8$), which implied that D_i was directly related to W and P -value < 0.01 indicated that D_i was significant correlated to W (significant: $P < 0.05$). The high model efficiency (ME) value in Eq. (11) showed a good agreement between the predicted and measured values (good: $ME > 0.8$). The result indicated that for the purple soil at the scale of runoff plot, interrill erosion rate could be predicted using the linear stream power models. The result was consistent with Cao et al. (2015) for unpaved roads. Stream power characterizes the influence of topography and runoff in process-based erosion models (Hairsine and Rose, 1992; Huang, 1995; Nearing et al., 1997). The determination coefficient (R^2) and the model efficiency (ME) value of Eq. (11) were higher than the other two hydraulic parameters, which implied that stream power was the best predictor of D_i ($R^2 = 0.862$, $ME = 0.862$), followed by flow velocity ($R^2 = 0.843$, $ME = 0.843$) and shear stress ($R^2 = 0.721$, $ME = 0.721$).

Modeling interrill erosion rate using equations of the multiplication of factor type

Corresponding to equations of the multiplication of factor type adopted in this study, the zero-intercept linear regression analysis was conducted for the five models (Table 4). Regression equations, determination coefficients and model efficiency were shown in Table 4. D_i by rainfall increases as rainfall intensity increases, the relationship is well described by a power function equation (Model 1), which is expressed as:

$$D_i = 1215600I^2 \quad (12)$$

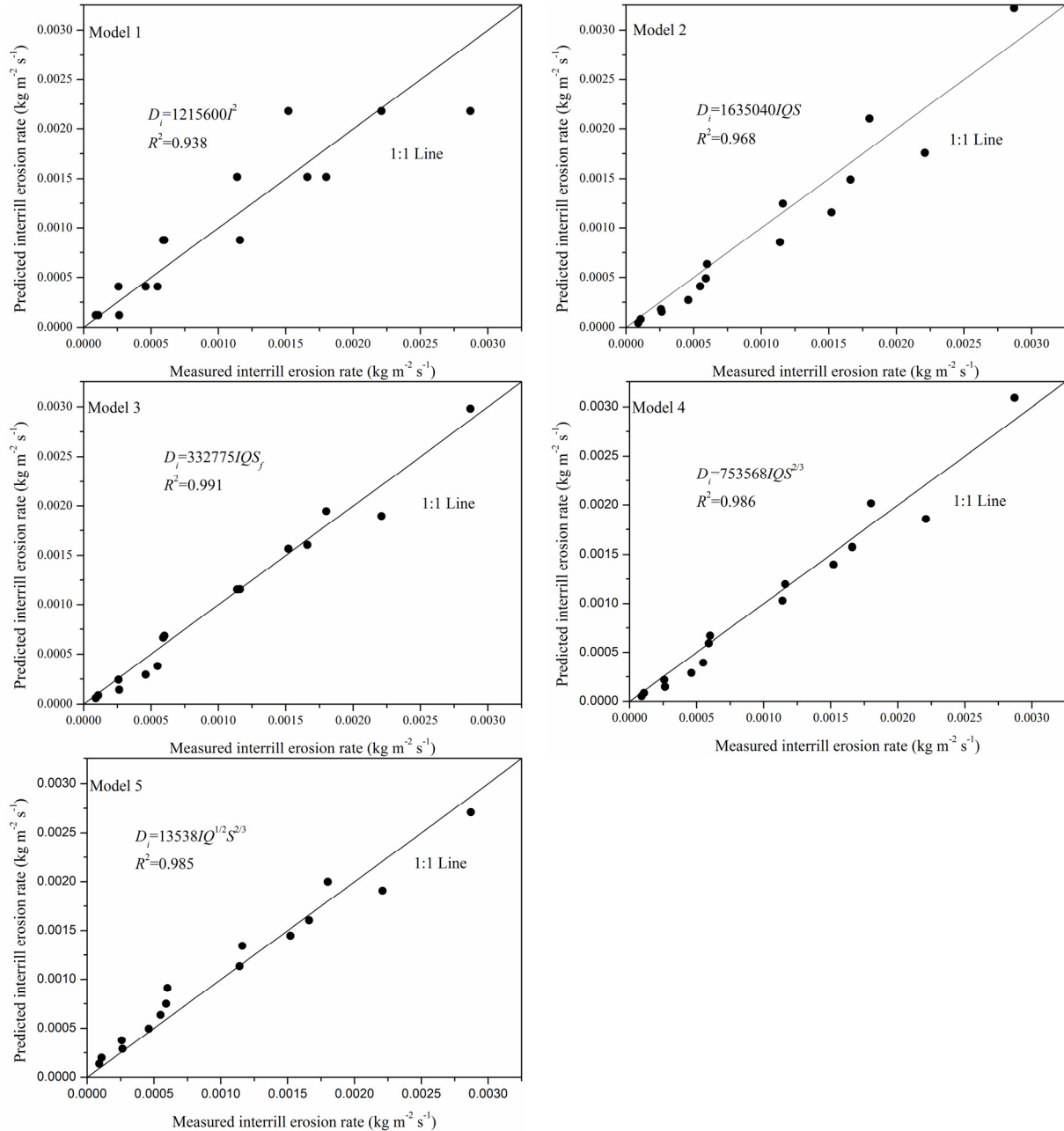
$$(R^2 = 0.938, ME = 0.852, P < 0.01, n = 15)$$

where D_i ($\text{kg} \cdot \text{s}^{-1} \cdot \text{m}^{-2}$) is the soil loss rate of interrill areas and I ($\text{m} \cdot \text{s}^{-1}$) is the simulated rainfall intensity. The comparison of measured and predicted D_i showed a high level of agreement between predicted and measured values (Fig. 6). Generally, rainfall intensity, reflecting the magnitude of rainfall kinetic energy impacts, plays a dual role in interrill erosion process (Flanagan and Nearing, 1995; Zhang and Wang, 2017). In this study, surface runoff accounted for 67.2–85.4% of total rainfall, indicating that the generation of surface runoff was accelerated. With the increase of rainfall intensity and slope, the shear stress and flow velocity induced by rainfall increase, which in turn aggravated soil loss (Assouline and Ben-Hur, 2006; Fang et al., 2015; Zhang and Wang, 2017). Thus, runoff and slope gradient are also the main factors affecting soil loss, which should be expressed in the erosion model. After including the runoff and slope gradient exponents, the equations (Models 2, 3, 4, and 5) show a higher accuracy in predicting the steep slopes of purple soil loss. The further comparison of the selected models (Models 2, 4, and 5) indicated that the slope exponents varied from 0.67 to 1, which were smaller than the convex curvilinear slope factor in Model 3. The performance of model 3 was better than the other three models implied that the slope factor of convex curvilinear was superior to linear and power factors in characterising the role of slope. The exponent of runoff in Models 2, 3 and 4 were 1, which were more than the exponent (0.5) of runoff in Model 5. Models 4 and 5 in Table 2 were basically the same in addition to the different values of runoff factor. The high R^2 values of Models 4 and model 5 indicated that both linear and power factors had enough precision in characterizing the role of runoff.

Among the five selected models, model 3, which was proposed by Flanagan and Nearing (1995), was the most effective in predicting the interrill erosion rate on purple soil slope. Meanwhile, Model 3 was used in the Water Erosion Prediction Project (WEPP) model for soil loss predicting from interrill areas. Soil erodibility in the WEPP model was considered to be constant, while runoff rate varied in response to changes between rainfall intensity and slope gradient. Therefore, in the field application, it was necessary to establish a large number of field observation stations to study the process of runoff generation on purple soil slope. Molina et al. (2007) found that runoff generation was also affected by land cover and soil management. Generally, in practical applications, soil properties, rainfall intensity, topography, vegetation cover, and land use should be considered. According to the formulation of the WEPP model, the coefficient of Model 3 is the interrill erodibility (Flanagan and Nearing, 1995), which was calculated as $0.332 \times 10^6 \text{ kg} \cdot \text{m}^{-4} \cdot \text{s}$ in Table 4. This value was close to the interrill erodibility ($0.4 \times 10^6 \text{ kg} \cdot \text{m}^{-4} \cdot \text{s}$) that was calculated by Cao et al. (2015) in clay loam soil forest. Meanwhile, the interrill erodibility in model 3 was less than that of forest road surface ($1.35 \times 10^6 \text{ kg} \cdot \text{m}^{-4} \cdot \text{s}$) and red soil of masson pine forest ($1.18 \times 10^6 \text{ kg} \cdot \text{m}^{-4} \cdot \text{s}$) (Cao et al., 2015; Foltz et al., 2009). This implies that the purple soil slope surface is harder to erode. However, the risk of soil loss on the steep slopes of purple soil could not be ignored. Purple soil slope could be a considerable source of sediment in the Three Gorges Reservoir region. Furthermore, as reported by Niu et al. (2010), purple soil slope was characterized by overlying thin soil, underlying bedrock, referred to as “binary structure of soil and rock”, and the erosion

Table 4. Efficiency of models selected.

	Equation	R^2	ME
Model 1	$D_i = 1215600I^2$	0.938	0.852
Model 2	$D_i = 1635040IQS$	0.968	0.923
Model 3	$D_i = 332775IQS_f$	0.991	0.977
Model 4	$D_i = 753568IQS^{2/3}$	0.986	0.966
Model 5	$D_i = 13538IQ^{1/2}S^{2/3}$	0.985	0.963

**Fig. 6.** Comparison between measured and predicted interrill erosion rates.

on the steep slope was relatively strong. Therefore, purple soil slope should be evaluated accurately as an important source of soil loss. However, some studies found that with the increase of slope length, sediment delivery increased first (transport-limited) and then decreased (detachment-limited) with distance (Gilley et al., 1985; Zhang and Wang, 2017). Models by using short slope length might overestimate soil loss rate. Future research should be conducted to investigate the limiting process controlling interrill erosion on purple soil slopes.

CONCLUSIONS

Laboratory rainfall simulation experiments on purple soil slopes were conducted under five rainfall intensities (0.6, 1.1, 1.61, 2.12 and 2.54 $\text{mm}\cdot\text{min}^{-1}$) and three slope gradients (17.6%, 26.8% and 36.4%). The results showed that surface runoff varied depending on slope gradient and rainfall intensity. Surface runoff on average occupied 67.2–85.4% of the precipitation, which indicated that the process of surface runoff yield

was the main hydrological process on purple soil slopes. Interrill erosion was the main erosion form on purple soil slopes. In this study, the main hydraulic parameters (flow velocity V , shear stress τ and stream power W) were selected for the interrill erosion rate prediction. Regression analyses indicated that the linear equations of V , τ and W could be used to estimate interrill erosion rate, however, W with $R^2 = 0.862$ and $ME = 0.862$ was the best predictor of interrill erosion rate, followed by V with $R^2 = 0.843$ and $ME = 0.843$ and τ with $R^2 = 0.721$ and $ME = 0.721$.

In addition, five generally used interrill erosion models were analyzed, the fitness of model followed the pattern: Model 3 ($ME = 0.977$) > Model 4 ($ME = 0.966$) > Model 5 ($ME = 0.963$) > Model 2 ($ME = 0.923$) > Model 1 ($ME = 0.852$). The further comparison of the selected models indicated that the convex curvilinear slope factor was superior to linear and power factors in characterising the role of slope. The interrill erodibility used in the Model 3 (WEPP) was calculated as $0.332 \times 10^6 \text{ kg} \cdot \text{s} \cdot \text{m}^{-4}$. The results can improve the accuracy of interrill erosion model for purple soil slopes in the Three Gorges Reservoir area.

Acknowledgements. Funding for this research was provided by the National Key Research and Development Project (No. 2017YFC0505304) and the Basic Research Fund for Central Public Research Institutes (No. CKSF2014026/TB).

REFERENCES

- Abrahams, A.D., Parsons, A.J., Luk, S.H., 1986. Field measurement of the velocity of overland flow using dye tracing. *Earth Surf. Process Landf*, 11, 653–657.
- An, J., Zheng, F., Lu, J., Li, G., 2012. Investigating the role of raindrop impact on hydrodynamic mechanism of soil erosion under simulated rainfall conditions. *Soil Sci*, 177, 8, 517–526.
- Assouline, S., Ben-Hur, M., 2006. Effects of rainfall intensity and slope gradient on the dynamics of interrill erosion during soil surface sealing. *Catena*, 66, 211–220.
- Beasley, D.B., Huggins, L.F., 1982. ANSWERS user's manual. Dep. of Agric. Eng., Purdue Univ., West Lafayette, IN.
- Bulygin, S.Y., Nearing, M.A., Achasov, A.B., 2002. Parameters of interrill erodibility in the WEPP model. *Eurasian Soil Science*, 35, 1237–1242.
- Cao, L.X., Zhang, K.L., Dai, H.L., Liang, Y., 2015. Modeling Interrill erosion on unpaved roads in the Loess Plateau of China. *Land Degrad. Dev.*, 26, 8, 825–832.
- Chaplot, V.A.M., Le Bissonnais, Y.L., 2003. Runoff features for interrill erosion at different rainfall intensities, slope lengths, and gradients in an agricultural loessial hillslope. *Soil Science Society of America Journal*, 67, 3, 844–851.
- De Roo, A.P.J., Wesseling, C.G., Cremers, N.H.D.T., Offermans, R.J.E., Ritsema, C.J., Van Oostindie, K., 1994. LISEM: a new physically-based hydrological and soil erosion model in a GIS-environment, theory and implementation. IAHS Publications – Series of Proceedings and Reports. International Association of Hydrological Sciences, vol. 224, pp. 439–448.
- Ding, W.F., Zhang, X.C., 2016. An evaluation on using soil aggregate stability as the indicator of interrill erodibility. *J. Mt. Sci.*, 13, 5, 831–843.
- Ding, W.F., Huang, C.H., 2017. Effects of soil surface roughness on interrill erosion processes and sediment particle size distribution. *Geomorphology*, 295, 801–810.
- Dunkerley, D., 2003. An optical tachometer for short-path measurement of flow speed in shallow overland flows: improved alternative to dye timing. *Earth Surf. Process. Landforms*, 28, 777–786.
- Fan, J.C., Wu, M.F., 1999. Effects of soil strength, texture, slope steepness and rainfall intensity on interrill erosion of some soils in Taiwan. In: 10th International Soil Conservation Organization meeting, Purdue University, USDA-ARS National Soil Erosion Research Laboratory.
- Fang, H., Sun, L., Tang, Z., 2015. Effects of rainfall and slope on runoff, soil erosion and rill development: an experimental study using two loess soils. *Hydrological Processes*, 29, 11, 2649–2658.
- Flanagan, D.C., Nearing, M.A. (Eds.), 1995. USDA-Water Erosion Prediction Project: Technical Documentation. NSERL Rep. No. 10. Natl. Soil Erosion Res. Lab., West Lafayette, IN.
- Foster, G.R., Meyer, L.D., 1975. Mathematical simulation of upland erosion by fundamental erosion mechanics. Present and prospective technology for predicting sediment yields and sources. ARS-S-40, USDA-ARS, U.S. Gov. Print. Office, Washington, DC.
- Foltz, R.B., Copeland, N.S., Elliot, W.J., 2009. Reopening abandoned forest roads in northern Idaho, USA: quantification of runoff, sediment concentration, infiltration, and interrill erosion parameters. *Journal of Environmental Management*, 90, 2542–2550.
- Fox, D., Bryan, R., Price, A., 1997. The influence of slope angle on final infiltration rate for interrill conditions. *Geoderma*, 80, 1–2, 181–194.
- Gilley, J.E., Woolhiser, D.A., McWhorter, D.B., 1985. Interrill soil erosion – Part I: Development of model equations. *Trans. ASAE*, 28, 147–153, 159.
- Guo, T.L., Wang, Q.J., Li, D.Q., Zhuang, J., Wu, L.S., 2013. Flow hydraulic characteristic effect on sediment and solute transport on slope erosion. *Catena*, 107, 145–153.
- Govers, G., 1992. Evaluation of Transporting Capacity Formulae for Overland Flow. University College London Press, London, pp. 243–273.
- Gomez, J.A., Nearing, M.A., 2005. Runoff and sediment losses from rough and smooth soil surfaces in a laboratory experiment. *Catena*, 59, 3, 253–266.
- Hairsine, P.B., Rose, C.W., 1992. Modeling water erosion due to overland flow using physical principles, 1. Sheet flow. *Water Resour. Res.*, 28, 237–243.
- Hairsine, P.B., Moran, C.J., Rose, C.W., 1992. Recent developments regarding the influence of soil surface characteristics on overland flow and erosion. *Aust. J. Soil Res.*, 30, 3, 249–264.
- Huang, C., 1995. Empirical analysis of slope and runoff for sediment delivery from interrill areas. *Soil Science Society of America Journal*, 59, 4, 982–990.
- ISSAS, 1978. Analysis of Physical and Chemical Properties of Soil. Shanghai Science Press, Shanghai. (In Chinese.)
- Issa, O.M., Le Bissonnais, Y., Planchon, O., Favis-Mortlock, D., Silvera, N., Wainwright, J., 2006. Soil detachment and transport on field-and laboratory-scale interrill areas: erosion processes and the size-selectivity of eroded sediment. *Earth Surf. Process. Landf.*, 31, 929–939.
- Kemper, W.D., Rosenau, R.C., 1986. Aggregate stability and size distribution. In: Klute, A. (Ed.): *Methods of Soil Analysis. Part 1. Physical and Mineralogical Methods*. 2nd ed. SSSA Book Series No. 5. SSSA and ASA, Madison, WI, pp. 425–442.
- Kinnell, P.I.A., 1993. Interrill erodibilities based on the rainfall intensity flow discharge erosivity factor. *Aust. J. Soil Res.*, 31, 3, 319–332.

- Kinnell, P.I.A., Cummings, D., 1993. Soil slope gradient interactions in erosion by rainimpacted flow. *Trans. ASAE*, 36, 381–387.
- Liu, B.Y., Nearing, M.A., Risse, L.M., 1994. Slope gradient effects on soil loss for steep slopes. *Trans. ASAE*, 37, 6, 1835–1840.
- Long, T.Y., Qiao, D., An, Q., Du, K., 2012. Estimating soil erosion in Three Gorges Reservoir area based on GIS and RUSLE. *Journal of Irrigation and Drainage*, 31, 2, 33–37. (In Chinese.)
- Meyer, L.D., Wischmeier, W.H., 1969. Mathematical simulation of the process of soil erosion by water. *Trans. ASAE*, 12, 6, 754–758.
- Meyer, L.D., 1981. How rain intensity affects interrill erosion. *Trans. ASAE*, 24, 1472–1475.
- Morgan, R.P.C., Quinton, J.N., Smith, R.E., Govers, G., Poesen, J.W.A., Auerswald, K., Chisci, G., Torri, D., Styczen, M.E., 1998. The European Soil Erosion Model (EUROSEM): a dynamic approach for predicting sediment transport from fields and small catchments. *Earth Surf. Process. Landf.*, 23, 6, 527–544.
- Molina, A., Govers, G., Vanacker, V., Poesen, J., Zeelmaekers, E., Cisneros, F., 2007. Runoff generation in a degraded Andean ecosystem: Interaction of vegetation cover and land use. *Catena*, 71, 2, 357–370.
- Nash, J., Sutcliffe, J.V., 1970. River flow forecasting through conceptual models part I – A discussion of principles. *J. Hydrol.*, 10, 3, 282–290.
- Nearing, M.A., Foster, G.R., Lane, L.J., Finkner, S.C., 1989. A process-based soil erosion model for USDA-Water Erosion Prediction Project technology. *Trans. ASAE*, 32, 1587–1593.
- Nearing, M.A., Norton, L.D., Bulgakov, D.A., Larionov, G.A., West, L.T., Dontsova, K.M., 1997. Hydraulics and erosion in eroding rills. *Water Resour. Res.*, 33, 865–876.
- Nearing, M.A., Simanton, J.R., Norton, L.D., Bulygin, S.J., Stone, J., 1999. Soil erosion by surface water flow on a stony, semiarid hillslope. *Earth Surf. Proc. Landf.*, 24, 677–686.
- Niu, J., Zhang, P.C., Xing, M.X., 2010. Characteristic of soil and water loss on purple slope farmland and its control in upper reaches of the Yangtze River. *Science of Soil and Water Conservation*, 6, 013. (In Chinese.)
- Peng, W.Y., Zhang, Z.D., Zhang, K.L., 2015. Hydrodynamic characteristics of rill flow on steep slopes. *Hydrol. Process.*, 29, 3677–3686.
- Qian, F., Cheng, D., Ding, W., Huang, J., Liu, J., 2016. Hydraulic characteristics and sediment generation on slope erosion in the Three Gorges Reservoir area, China. *Journal of Hydrology and Hydromechanics*, 64, 3, 237–245.
- Römkens, M.J.M., Helming, K., Prasad, S.N., 2002. Soil erosion under different rainfall intensities, surface roughness, and soil water regimes. *Catena*, 46, 103–123.
- Sha, Y.Q., 1965. *An Introduction to Sediment Kinematic*. China Industry Press, Beijing.
- Wang, D.D., Wang, Z.L., Shen, N., Chen, H., 2016. Modeling soil detachment capacity by rill flow using hydraulic parameters. *Journal of Hydrology*, 535, 473–479.
- Wei, H., Nearing, M.A., Stone, J.J., Guertin, D.P., Spaeth, K.E., Pierson, F.B., Nichols, M.H., Moffet, C.A., 2009. A new splash and sheet erosion equation for rangelands. *Soil Sci. Soc. Am. J.*, 73, 1386–1392.
- Wu, B., Wang, Z.L., Zhang, Q.W., Shen, N., Liu, J.N., 2017. Modelling sheet erosion on steep slopes in the loess region of China. *Journal of Hydrology*, 533, 549–558.
- Yan, F.L., Shi, Z.H., Li, Z.X., Cai, C.F., 2008. Estimating interrill soil erosion from aggregate stability of Ultisols in subtropical China. *Soil Tillage Research*, 100, 34–41.
- Zhang, X.C., Nearing, M.A., Miller, W.P., Norton, L.D., West, L.T., 1998. Modeling interrill sediment delivery. *Soil Sci. Soc. Am. J.*, 62, 438–444.
- Zhang, X.C., Wang, Z.L., 2017. Interrill soil erosion processes on steep slopes. *Journal of Hydrology*, 548, 652–664.

Received 25 June 2018
Accepted 10 March 2019

Collisional transport model for intense bed load

Václav Matoušek*, Štěpán Zrostlík

Czech Technical University in Prague, Department of Civil Engineering, Thákurova 7, 166 29 Prague 6, Czech Republic.

* Corresponding author. E-mail: v.matousek@fsv.cvut.cz

Abstract: In an open channel with a mobile bed, intense transport of bed load is associated with high-concentrated sediment-laden flow over a plane surface of the eroded bed due to high bed shear. Typically, the flow exhibits a layered internal structure in which virtually all sediment grains are transported through a collisional layer above the bed. Our investigation focuses on steady uniform turbulent open-channel flow with a developed collisional transport layer and combines modelling and experiment to relate integral quantities, as the discharge of solids, discharge of mixture, and flow depth with the longitudinal slope of the bed and the internal structure of the flow above the bed.

A transport model is presented which considers flow with the internal structure described by linear vertical distributions of granular velocity and concentration across the collisional layer. The model employs constitutive relations based on the classical kinetic theory of granular flows selected by our previous experimental testing as appropriate for the flow and transport conditions under consideration. For given slope and depth of the flow, the model predicts the total discharge and the discharge of sediment. The model also predicts the layered structure of the flow, giving the thickness of the dense layer, collisional layer, and water layer. Model predictions are compared with results of intense bed-load experiment carried out for lightweight sediment in our laboratory tilting flume.

Keywords: Granular flow; Sheet flow; Sediment transport; Grain collision; Tilting flume experiment; Kinetic theory.

INTRODUCTION

For intense bed load transport in an open channel with a mobile bed, collisional interactions of transported sediment grains are typical and they significantly affect behavior of flow carrying the sediment above a plane mobile bed at high bed shear (the upper-stage bed regime). The flow exhibits a layered structure in which virtually all grains are transported through a collisional transport layer. If the total bed shear stress exerted by the flow is high, a sliding dense layer develops between the collisional layer and the bed. In the dense layer, grains remain in virtually permanent contact and slide over each other rather than collide with each other. Typically, the collisional layer dominates the internal structure of the flow. Appropriate modelling of friction and transport in the layered structure of the flow is crucial for prediction ability of a bed-load transport model. So far, collisional mechanisms are poorly understood and hence modelling approaches are seldom sufficiently accurate.

Most widely used transport formulae are simple and semi-empirical by nature (e.g., Cheng, 2002; Meyer-Peter and Müller, 1948; Rickenmann, 1991; Smart, 1984; Wilson, 1966; Wong and Parker, 2006). They employ only integral quantities of the flow and do not take the internal structure of the flow into account.

One of the appropriate theory-based approaches to modelling of flows dominated by granular collisions seems to be the kinetic theory of granular flows. It offers constitutive relations for local shear-induced collision-based granular quantities – normal stress, shear stress and fluctuation energy – and relate them with distribution of local grain concentration and velocity across the flow depth. Kinetic-theory based models enable a prediction of relevant flow quantities in the layered pattern of the flow. Model predictions include integral flow quantities (discharges of solids and mixture, flow depth) and simplified distributions of solids concentration and velocity.

Typically, a kinetic-theory based model assumes certain conditions at interfaces of the layered flow and quantifies the

interfacial stresses, concentration, and velocity. Additional equations (momentum balances) are employed to use the interfacial values of the granular quantities for the prediction of thicknesses of the relevant layers. The discharges of solids and mixture are obtained through integration of the velocities and concentrations over the flow depth. The existing models differ mainly in assumptions taken for the layered flow and in forms of the constitutive relations selected for the models (e.g., Berzi, 2011; Berzi and Fraccarollo, 2013; Capart and Fraccarollo, 2011; Spinewine and Capart, 2013).

In our previous work (Matoušek and Zrostlík, 2018a), results from a tilting-flume facility including measured velocity distribution and deduced concentration distribution (approximated as linear profiles) were used to calculate distributions of the collision-based quantities by the constitutive relations and hence to test the ability of the selected kinetic-theory constitutive relations to predict conditions observed in these collision-dominated flows.

In this paper, we aim on formulating a simple kinetic-theory-based model using the constitutive relations previously tested for flow conditions observed in our intense-bed-load experiment in a laboratory tilting flume.

TRANSPORT MODEL FOR COLLISIONAL BED LOAD IN OPEN-CHANNEL FLOW OF LAYERED STRUCTURE

A modelling approach is discussed which enables to predict characteristics of steady uniform turbulent open-channel flow carrying a large amount of colliding sediment (intense bed-load). The approach is based on the classical kinetic theory, considers a layered structure of the sediment-laden flow and employs conditions at layer interfaces to evaluate mutual relations among the flow slope, depth, the thickness of the layers and flow rates of both the sediment and sediment-water mixture. In the discussed model, the dense limit condition consider-

ing the local volumetric concentration $c \rightarrow 1$ (see a discussion on this condition in Matoušek and Zrostlík (2018a)) is not assumed at the bottom of the collisional transport layer because our experiments indicate that for the studied flow conditions the local concentration at the bottom of the collisional layer is too low to satisfy the dense limit condition (Matoušek et al., 2016).

Modelled conditions for open-channel flow and sediment transport

- Gravity-driven open-channel flow, steady-state uniform turbulent flow.
- Broad range of bed slopes, flows depths, sediment flow rates, and total flow rates.
- Flow over mobile bed at upper-stage plane bed regime (high bed shear).
- Transported sediment grains supported by mutual contacts, negligible turbulent support.
- Strongly non-uniform distribution of sediment across the flow depth.
- Stratified flow as the result of the sediment distribution.

It is typical of flows with intense bed load transport that local concentrations and velocities of grains span a broad range of values over the thickness of the collisional layer. As mentioned previously, it is also typical that the collisional layer dominates the layered structure of the flow and occupies a considerable part of the flow depth. Figure 1 shows the layered character of flow with intense bed-load identified for flow of mixture of water and lightweight sediment in a laboratory flume (plastic cylinder-shaped grains of the characteristic size of 5.41 mm and the density of 1307 kg/m³). It recognizes the following distinct layers: the bed (stationary deposit with the surface expressed as the 0-boundary in Figure 1), the dense sliding layer (DL, with the top d-boundary), the collisional layer (CL, with the upper c-boundary), and the water layer (WL, with water surface at the top of the plot in Figure 1). Visual observations of the flow and measurements of local velocities u at different vertical positions y above the bed allowed the layer boundaries to be identified. The CL (the layer of colliding grains) exhibits the velocity distribution which can be approximated by a line reaching virtually zero velocity at the bottom of CL and this identifies the position of the d-boundary. Hence, the velocity of grains in the DL (the dense layer of grains slowly sliding over each other and being in permanent contact with each other) is negligible compared to velocities in the CL. Above the top of the CL no grains occur, which identifies the c-boundary.

Two plots of Figure 1 are for two flows of different values of the bed Shields parameter θ_0 , which is the dimensionless total shear stress at the surface of the bed (i.e., at the 0-boundary), $\theta_0 = \frac{\tau_{e,0}}{(\rho_s - \rho_f) \cdot g \cdot d}$ ($\tau_{e,0}$ = the total shear stress at

the surface of the bed, ρ_s = density of grains, ρ_f = density of liquid, g = gravitational acceleration, and d = grain size). The plots show that the thickness of individual layers varies with θ_0 . At low values of θ_0 , the thickness of the dense layer is negligible but can reach a thickness of the multiple of the grain size d at very high θ_0 . Furthermore, an analysis of measured discharges suggested that the local volumetric concentration at the bottom of collisional layer, c_b , was smaller than the bed volumetric concentration, c_0 , and varied with θ_0 until a certain maximum value typical for bed was reached (Matoušek et al., 2016).

The existence of the individual layers, the variation of their thickness and of the conditions at the boundaries must be taken into account in the transport model.

Model principles

The conditions subject to modelling require that the model is based on principles describing the collisional character of sediment transport. Different forms of constitutive relations are available in the literature. As tested in a laboratory (Matoušek and Zrostlík, 2018a), the constitutive relations of the classical kinetic theory (CKT) below are appropriate for our modelled conditions. The testing revealed that for the conditions given by our experiments, the constitutive relations worked well if the local volumetric concentration of sediment did not exceed approximately 0.47. Furthermore, the experimental results showed that the local concentration at the bottom of the collisional transport layer varied with the bed shear stress and reached values smaller than 0.47 in most of flow conditions observed. Therefore, the use of the constitutive relations at this boundary is appropriate, at least in the range of bed shear stresses for which the modelled flow conditions and model assumptions are satisfied. Also, the testing of the constitutive relations showed that the application of the dense limit condition is not appropriate due to these relatively low values of the local concentration even though it meant that more complex forms of the relations have had to be solved at the bottom of the collisional layer.

CKT considers sheared granular bodies, in which grains are supported exclusively by mutual binary collisions. The constitutive relations are formulated for local grain stresses (normal and shear) and for a balance of grain fluctuation energy in the collisional regime.

The local shear-induced granular normal stress, σ_s , is related to the local volumetric concentration of grains, c , the local granular temperature, T (which expresses a measure of local grain velocity fluctuations due to intergranular collisions), and after the theory by Garzo and Dufty (1999) as in Berzi (2011),

$$\sigma_s = 4 \cdot \rho_s \cdot f_\sigma \cdot c \cdot G \cdot T \quad (1)$$

where G, f_σ = concentration-related functions defined as

$$G = c \cdot \frac{2 - c}{2 \cdot (1 - c)^3} \quad (2)$$

$$f_\sigma = \frac{1 + e}{2} + \frac{1}{4 \cdot G} \quad (3)$$

where e = the coefficient of wet restitution (local values of e may vary with position above bed).

The local shear-induced granular shear stress, τ_s , is also related to c and T at any vertical position y above the bed. Moreover, τ_s is related to the local strain rate γ_s , i.e. the distribution of longitudinal velocity of grains u_s ($\gamma_s = du_s/dy$), (Berzi, 2011),

$$\tau_s = \rho_s \cdot f_\tau \cdot c \cdot G \cdot \sqrt{T} \cdot \gamma_s \cdot d \quad (4)$$

with concentration-related function

$$f_\tau = \frac{8}{5 \cdot \sqrt{\pi}} \cdot \left(\frac{1 + e}{2} + \frac{\pi}{32} \cdot \frac{[5 + 2 \cdot (1 + e) \cdot (3 \cdot e - 1) \cdot G] \cdot [5 + 4 \cdot (1 + e) \cdot G]}{[24 - 6 \cdot (1 - e)^2 - 5 \cdot (1 - e^2)] \cdot G^2} \right) \quad (5)$$

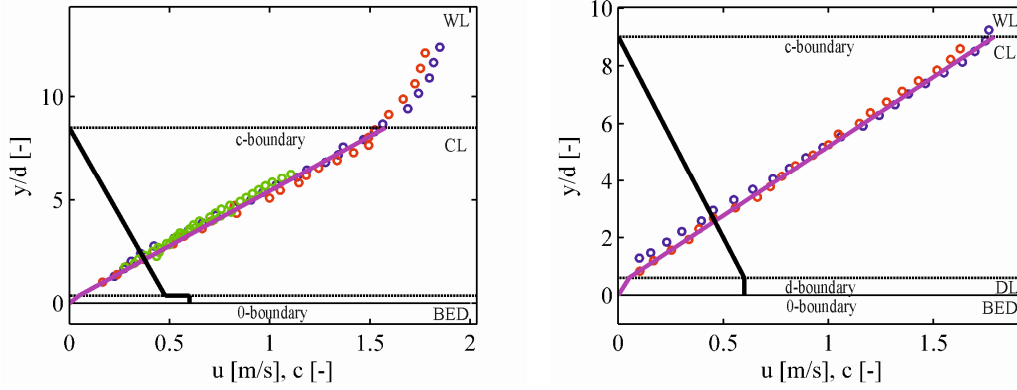


Fig. 1. Positions of boundaries, velocity and concentration profiles in layered-structure flow carrying plastic (TLT50) grains. Legend: circle – measurement of local velocity by different measuring techniques (blue – Pitot tube, red – Ultrasonic Velocity Profiler, green – Acoustic Doppler Velocitometer); horizontal lines – boundaries between layers (bed, DL = dense layer, CL = collisional layer, WL – water layer); thick lines – velocity profile by local velocity approximation and concentration profile deduced from measurement (Matoušek and Zrostlík, 2018b).

Another constitutive relation expresses the balance of the particle collisional fluctuation energy. It requires that the gradient of the vertical component of the flux of particle fluctuation energy balances the net rate of production of fluctuation energy per unit volume of the mixture (Jenkins and Hanes, 1998). The relation is composed of three terms. The first term represents the diffusion of fluctuation energy, the second term the production of energy due to shearing, and the third term represents the rate of collisional dissipation, i.e. the fluctuation energy dissipated by interparticle collisions (Armanini et al., 2005). For our conditions, the diffusion term can be neglected in the lower part of the collisional layer (Matoušek and Zrostlík, 2018a) and the kinetic-energy relation becomes an additional equation relating the granular shear stress with the granular temperature and the strain rate,

$$\tau_s = \frac{24}{\sqrt{\pi}} \cdot \rho_s \cdot c \cdot G \cdot (1-e) \cdot \frac{\sqrt{T^3}}{\gamma_s \cdot d} \quad (6)$$

Alternative equations relating the distribution of the local concentration with the distributions of the granular stresses are based on the principle of momentum balance. In gravity-driven solid-liquid flow with a free surface, the force balance between the driving force and the resisting force assumes that the total shear stress, τ_e (composed of the granular component, τ_s , and the liquid component, τ_f) at each vertical position y balances the longitudinal component of the weight of overlaying burden of liquid and solids,

$$\tau_e = g \cdot \sin \omega \cdot \int_y^H [\rho_s \cdot c + \rho_f \cdot (1-c)] \cdot dy \quad (7)$$

in which ω = angle of longitudinal slope of bed, and H = total flow depth.

The granular normal stress balances the normal component of the submerged weight of grains above y ,

$$\sigma_s = (\rho_s - \rho_f) \cdot g \cdot \cos \omega \cdot \int_y^H c \cdot dy \quad (8)$$

It follows from re-arrangements of Eqs. (7) and (8) that

$$\tau_e = \sigma_s \cdot \tan \omega + \rho_f \cdot g \cdot \sin \omega \cdot (H - y) \quad (9)$$

where the first term on the right-hand side of Eq. (9) is the granular component, τ_s , of the total shear stress and the second term is the liquid component, τ_f .

Model features

Semi-empirical transport formulae for bed load relate the solids discharge with the shear stress at the top of the mobile bed. A kinetic-theory based model can serve the same purpose by relating the granular shear stress at the bottom of the collisional layer with relevant flow quantities responsible for the solids discharge. Furthermore, an incorporation of the momentum balance equations allows to capture the layered structure of the flow and to identify positions of the layer boundaries. For chosen (e.g. experimentally determined) input quantities, the model does not require the classical law of the wall to relate the total discharge with the flow depth.

In the presented model, the constitutive relations of the classical kinetic theory are employed to describe granular flow conditions at the bottom of the CL, where the local concentration is supposed to vary with the boundary shear stress. The constitutive relations also predict the slope of the linear profile of solids velocity in the CL and hence they determine the local velocity u_c at the top of the CL. The momentum balances are combined with the shear-to-normal stress ratios at the relevant boundaries to determine positions of the boundaries in the layered flow structure. The discharges of solids and mixture are obtained through integration of the velocities and concentrations over the flow depth.

Model assumptions

- Distribution of velocity and concentration linear in the CL, concentration distribution uniform and solids velocity negligible in the DL. Local concentration zero at the top of CL (c-boundary). These assumptions are in an agreement with conditions observed in Figure 1.
- Negligible fluid stress at the d-boundary and at the 0-boundary.
- No side-wall effect.
- No local slip between grain and liquid in the CL and DL.
- The diffusive term of the energy-balance relation is negligible at the d-boundary (and 0-boundary).

Set of model governing equations

The model is composed of the following set of equations (constitutive relations, momentum balances, and closures). The situation at the bottom of the collisional layer (the d-boundary) is central to the modelling procedure. The constitutive relations for stresses at this boundary are formulated as follows. The shear induced normal granular stress (based on Eq. (1) with G - and f_σ -functions by Eqs. (2) and (3), respectively) is

$$\sigma_{s,d} = 4 \cdot \rho_s \cdot f_{\sigma,d} \cdot c_d \cdot G_d \cdot T_d \quad (10)$$

the corresponding granular shear stress (based on Eq. (4) with the f_τ -function by Eq. (5)) is

$$\tau_{s,d} = \rho_s \cdot f_{\tau,d} \cdot c_d \cdot G_d \cdot \sqrt{T_d} \cdot \gamma_{s,d} \cdot d \quad (11)$$

and the same shear stress expressed from the energy balance with negligible diffusion term as in Eq. (6) is

$$\tau_{s,d} = \frac{24}{\sqrt{\pi}} \cdot \rho_s \cdot c_d \cdot G_d \cdot (1 - e_d) \cdot \frac{\sqrt{T_d^3}}{\gamma_{s,d} \cdot d} \quad (12)$$

The local coefficient of restitution at the bottom of the CL, e_d , equals (e.g., Berzi and Fraccarollo, 2013)

$$e_d = \varepsilon - 62.1 \cdot \frac{\mu_f \cdot (1 + \varepsilon)}{\rho_s \cdot \sqrt{T_d} \cdot d} \quad (13)$$

in which ε = effective coefficient of dry collisional restitution (a material constant, which is a model input parameter), μ_f = dynamic viscosity of fluid.

At the d-boundary, the granular stresses are mutually related through the friction coefficient

$$\beta_d = \frac{\tau_{s,d}}{\sigma_{s,d}} \quad (14)$$

and its value is determined by Eq. (14) from the obtained values of both stresses in the model.

The momentum balance equations based on Eqs. (8) and (9) relate the local stresses at the d-boundary with the and local concentration c_d , and the positions the d-boundary, y_d , and c-boundary, y_c ,

$$\sigma_{s,d} = (\rho_s - \rho_f) \cdot c_d \cdot g \cdot \cos \omega \cdot (y_c - y_d) / 2 \quad (15)$$

$$\tau_{e,d} = \tau_{e,c} + \sigma_{s,d} \cdot \tan \omega + \rho_f \cdot g \cdot \sin \omega \cdot (y_c - y_d) \quad (16)$$

Similarly, Eqs. (8) and (9) applied to the 0-boundary (the top of the bed, $y_0 = 0$) produce

$$\sigma_{s,0} = \sigma_{s,d} + (\rho_s - \rho_f) \cdot c_0 \cdot g \cdot \cos \omega \cdot y_d \quad (17)$$

$$\tau_{e,0} = \tau_{e,d} + (\sigma_{s,0} - \sigma_{s,d}) \cdot \tan \omega + \rho_f \cdot g \cdot \sin \omega \cdot y_d \quad (18)$$

where the local concentration at the 0-boundary, c_0 , is one of the input constants of the model.

At the bottom of the flow (the 0-boundary), the Coulomb yield criterion requires

$$\beta_0 = \frac{\tau_{s,0}}{\sigma_{s,0}} \quad (19)$$

and its value is another input constant of the model.

At the top of the collisional layer (the c-boundary), the total shear stress is entirely due to fluid shearing (the local solids stress is zero) and hence following Eq. (9),

$$\tau_{e,c} = \rho_f \cdot g \cdot \sin \omega \cdot (H - y_c) \quad (20)$$

The linear distribution across the CL leads to

$$u_{s,c} = u_{s,d} + \gamma_{s,d} \cdot (y_c - y_d) \quad (21)$$

Linear distributions of u_s and c across the CL (with assumed $c_c = 0$, $u_{s,d} = 0$) are combined with the earlier determined positions of the boundaries to give the sediment discharge (Matoušek et al. 2016),

$$q_s = \frac{c_d \cdot u_{s,c} \cdot (y_c - y_d)}{6} \quad (22)$$

If the assumptions of no slip in the CL and of the uniform velocity distribution in the WL are taken, then the total discharge (mixture of sediment and liquid) is

$$q_m = \frac{u_{s,c} \cdot (y_c - y_d)}{2} + u_{s,c} \cdot (H - y_c) \quad (23)$$

The average spatial volumetric concentration of sediment in the flow cross section is

$$C_{vi} = \frac{c_0 \cdot y_d + c_d / 2 \cdot (y_c - y_d)}{H} \quad (24)$$

Summary of model constants, input and output variables

In general, there are 4 mutually related major quantities characterizing the sediment-laden flow: the longitudinal slope of bed, ω , the flow depth, H , the sediment discharge, q_s , and the mixture discharge, q_m . To be able to compare model predictions with experimental results of flume tests (as the test results in Figure 1), we use the measured bed slope and the measured thickness of CL, $y_c - y_d$, as inputs and predict the flow depth and the two discharges. Alternatively, the model can consider the flow depth as an input and to predict the thickness of the CL. Additional model outputs are the position of the top of the DL, y_d , the velocity at the top of the CL, $u_{s,c}$, and the granular-stress ratio at the bottom of the CL, β_d . Additional model inputs are the concentrations c_d and c_0 , the properties of solids (ρ_s , d) and fluid (ρ_f , μ_f), the coefficient of internal friction at the top of bed, β_0 , and the dry restitution coefficient, ε .

DISCUSSION OF TRANSPORT MODEL AND COMPARISON OF MODEL PREDICTIONS WITH EXPERIMENTAL RESULTS

For a comparison of model predictions with experimental data, the model version was used with the thickness of the CL as an input to the model and the flow depth as one of the model outputs. The experimental values of $(y_c - y_d)$ and c_d were used as inputs to initialize model calculations. The model flow chart in Figure 2 visualizes the model calculation procedure further described in the paragraph below.

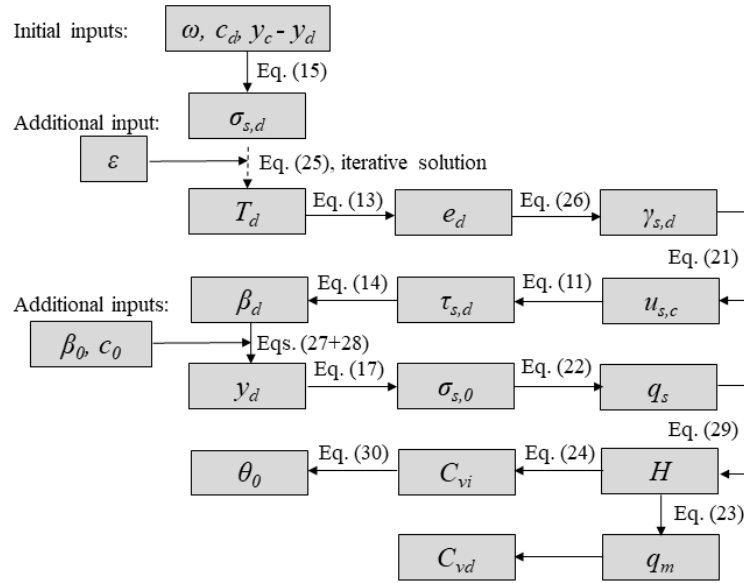


Fig. 2. Model flow chart.

Model calculation for CL-thickness as input and flow depth as output

Eq. (15) calculates the solids normal stress at the d-boundary, $\sigma_{s,d}$. The CKT-based relations (Eqs. (10) and (13)) combined produce an iterative solution for the granular temperature at the d-boundary,

$$T_d = \frac{\sigma_{s,d}}{4 \cdot \rho_s \cdot f_{\sigma,d}(T_d) \cdot c_d \cdot G_d} \quad (25)$$

For the obtained T_d , the two shear-stress constitutive relations (Eqs. (11) and (12)) combined give the velocity gradient at the d-boundary,

$$\gamma_{s,d} = \sqrt{\frac{24 \cdot (1 - e_d) \cdot T_d}{\sqrt{\pi} \cdot f_{\tau,d} \cdot d^2}} \quad (26)$$

The linear distribution of velocity is assumed in the CL above the d-boundary and thus the gradient remains constant across the entire CL. The momentum balance equations for the 0-boundary (Eqs. (17) and (18)) together with the equations for the friction coefficients at the 0-boundary and d-boundary (Eqs. (14) and (19)) and the assumption of zero fluid shear stresses at the two boundaries leads to the relation for the thickness of the dense layer,

$$y_d = \frac{(\beta_0 - \beta_d) \cdot \sigma_{s,d}}{\rho_0 \cdot g \cdot \sin \omega - \beta_0 \cdot (\rho_0 - \rho_f) \cdot g \cdot \cos \omega} \quad (27)$$

in which the local density of mixture at the 0-boundary,

$$\rho_0 = \rho_f + (\rho_s - \rho_f) \cdot c_0 \quad (28)$$

A combination of shear-stress balances at the d-boundary and c-boundary (Eqs. (16) and (20) together with Eq. (14)) leads to the determination of the total flow depth,

$$H = y_d + \frac{\sigma_{s,d} \cdot (\beta_d - \tan \omega)}{\rho_f \cdot g \cdot \sin \omega} \quad (29)$$

Then Eq. (24) calculates C_{vi} using H and both quantities can be further employed to express the bed Shields parameter, i.e. the dimensionless total shear stress at the 0-boundary, as

$$\theta_0 = \left(C_{vi} + \frac{\rho_f}{\rho_s - \rho_f} \right) \cdot \frac{H}{d} \cdot \tan \omega \quad (30).$$

Comparison of model predictions with experimental results

Experimental results for 4 fractions of plastic grains of different sizes and shapes (Table 1) are compared with predictions of the model. The experimental results were collected in our tilting flume and the data, the procedure of their collection and processing and the experimental set-up itself are described elsewhere (e.g., Matoušek et al., 2016).

The properties the sediment fractions produce values of the particle Reynolds number ($Re_p = v_t d / \nu_f$) $Re_p = \rho_f \cdot v_t \cdot d_{eq} / \mu_f$ in the range from 416 to 1149 and the flow conditions correspond with values of the bed Shields parameter from 0.3 to 1.6. The absence of local turbulent support of grains in the collisional layer is checked by determining a distribution of the velocity ratio u_f^*/v_t (u_f^* is the fluid shear velocity, $u_f^* = \sqrt{\tau_f / \rho_f}$) across the CL for each test run (examples are shown in Matoušek and Zrostlík (2019)). Local values were always below unity and typically smaller than 0.8, indicating that the turbulent support can be neglected. This argument is supported by regime maps (Fig. 7 in Berzi and Fraccarollo (2013) and Fig. 6 in Berzi and Fraccarollo (2016)) in which our flows collapsed in the collisional regime. The experimental conditions were similar to those used previously by other authors for testing their bed-load transport models (Armanini et al., 2005; Berzi and Fraccarollo, 2013; Capart and Fraccarollo, 2011).

For all sediment fractions, the model predictions are obtained with the same values of the model constants ($\beta_0 = 0.55$, $c_0 = 0.55$), in an exception of values of the restitution coefficient ε . The ε values are summarized in Table 1 and the table indicates that the required different values are associated with the different shapes of grains of the different fractions. The better agreement is reached between the predictions and the experimental results if cylindrical grains, i.e. the grains of the height comparable with the diameter of the cylinder (TLT50 and FA60) are given a lower value of ε than the lens-shaped grains for which the height is approximately one half of the lens diameter (TLT25 and FA30).

From the total collected dataset, only those experimental data were selected which corresponded with the model assumption that the local concentration at the top of the collisional layer is zero ($c_c = 0$). Some of the flume experiments were carried out for saturated flows in which sediment particles occupied the entire flow depth. Hence, the water layer was non-existent and the local concentration of particles was considerable even at positions just below the water surface. This was the case for flows of the highest values of the Shields parameter θ_0 , and such flows were excluded from the comparison with model predictions.

The velocity and concentration distributions of the experimental test runs were processed using the procedure described in Matoušek et al. (2016) and the positions of the boundaries and local concentrations at the boundaries were produced. Figures 3 and 4 show the experimentally determined values of the concentration c_d (Figure 3) and of the relative thickness of the collisional layer $(y_c - y_d)/d$ (Figure 4). As discussed previously, values of these two parameters are among the model inputs, although the thickness of the CL can be replaced by the flow depth H as a model input. Note, that the experimentally determined values of c_d and y_d are both quite sensitive to θ_0 , as Figures 3 and 4 demonstrate.

The thickness of the dense layer (represented by y_d) is predicted by the model using Eq. (27). Although the dense layer tends to be very thin (typically up to 2 or 3 layers of grains at very high θ_0) and unimportant from the point of view of sediment transport (usually the transport through the layer is negligible), apparently the variation in its thickness indicates the variation in c_d and this variation is important for the overall transport (see e.g., Matoušek and Zrostlík, 2018b).

The parity plots of Figure 5 indicate how successful is the model in a prediction of the local velocity at the top of the collisional layer. The model captures the velocity $u_{s,c}$ (obtained from Eq. (21)) reasonably well over the entire range of the observed flow conditions.

Values of the predicted flow depth H (calculated by Eq.

(29)) prove the model's ability to successfully transform the prediction of the internal structure of the flow into the prediction of integral quantities of the mixture flow and sediment transport as is the depth H in Figure 6 and other important integral quantities shown in Figures 7 and 8. For the predicted depth H , the agreement is again reasonable although less strong than is the agreement with the experiments for the predicted discharge of sediment q_s shown in Figure 7.

The ratio of two flow-depth averaged concentrations is evaluated in Figure 8. The delivered concentration of sediment is defined and determined as $C_{vd} = q_s/q_m$ (using results from Eqs. (22) and (23)). Its value must be smaller than the corresponding value of the spatial volumetric concentration C_{vi} (Eq. (24)) and it is indeed the case for all results in Figure 8. Furthermore, a predicted value of the concentration ratio C_{vd}/C_{vi} is sensitive to predicted values of all other integral quantities (q_s , q_m , H) and to predicted values of the local quantities (velocities and concentrations at all boundaries). Hence, it is an interesting parameter for an overall evaluation of the model performance. The degree of the agreement is very similar for this ratio as for the quantities presented in the previous figures.

In overall, the results of model predictions are satisfactory, although a bigger body of experimental results is required to make the validation more general, particularly including results for natural solids like sand and gravel. Moreover, additional work is required to further sophisticate the model, e.g., by finding out whether the observed variation of c_d with the transport conditions could be captured by the model instead of taking it as model input information.

To finalize, the proposed way of modelling of the steady-state uniform open-channel sediment-laden (bed-load) flow is compared with the traditional way. It considers only integral parameters and requires two equations to predict 2 of the 4 mutually related major quantities (ω , H , q_s , q_m). Those equations are the momentum equation for mixture flow and the transport formula for the sediment transport. The momentum equation (typically Chezy equation) includes a solution for the boundary friction (the law-of-the-wall formula for bed friction coefficient). The Meyer-Peter and Müller transport formula is often used for bed load transport. Usually, the slope ω and the flow depth H are the inputs and the sediment discharge q_s is obtained from the transport formula and the mixture discharge q_m from the momentum equation. In principle, the here proposed model serves the same purpose (predicts 2 major quantities using the other 2 as inputs) and besides the properties of solids and liquid requires just a few additional constants (ε , β_0 , c_0). There is one another input parameter, c_{ds} which cannot be considered constant and its value must be estimated or obtained by experiment.

Table 1. Properties of model sediment fractions of lightweight (PVC plastic) grains.

<i>Experimentally determined values</i>	TLT50	TLT25	FA60	FA30
Density ρ_s (kg/m ³)	1307	1381	1411	1368
Shape of grains	cylinder	thick lens	cylinder	thick lens
Height of cylinder or lens (mm)	5.0	2.2	5.0	2.2
Diameter of cylinder or lens (mm)	4.8	4.8	6.1	4.0
Equivalent mass-median diameter d_{eq} (mm)	5.41	4.23	6.42	3.65
Terminal settling velocity of grain v_t (m/s)	0.149	0.106	0.179	0.114
<i>Estimated values of model constant</i>	TLT50	TLT25	FA60	FA30
Restitution coefficient ε (–)	0.70	0.85	0.60	0.85

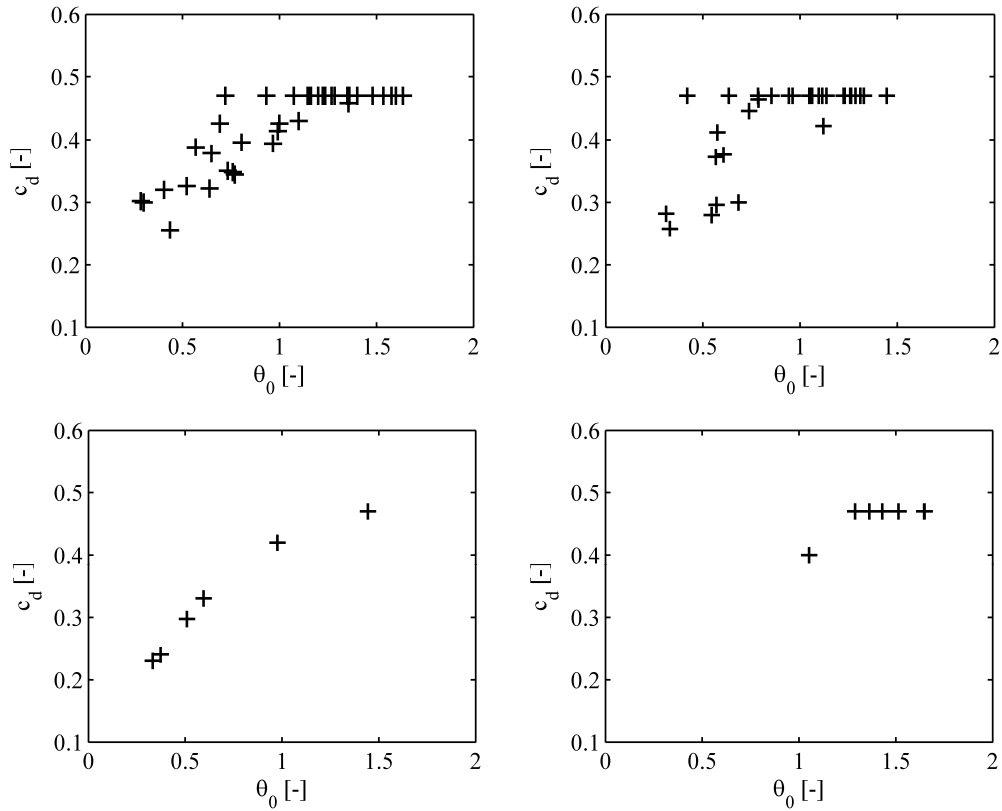


Fig. 3. Experimentally determined local concentration at bottom of collisional layer for flows of different bed Shields parameter (upper-left panel: TLT50, upper-right panel: TLT25, lower-left panel: FA60, lower-right panel: FA30).

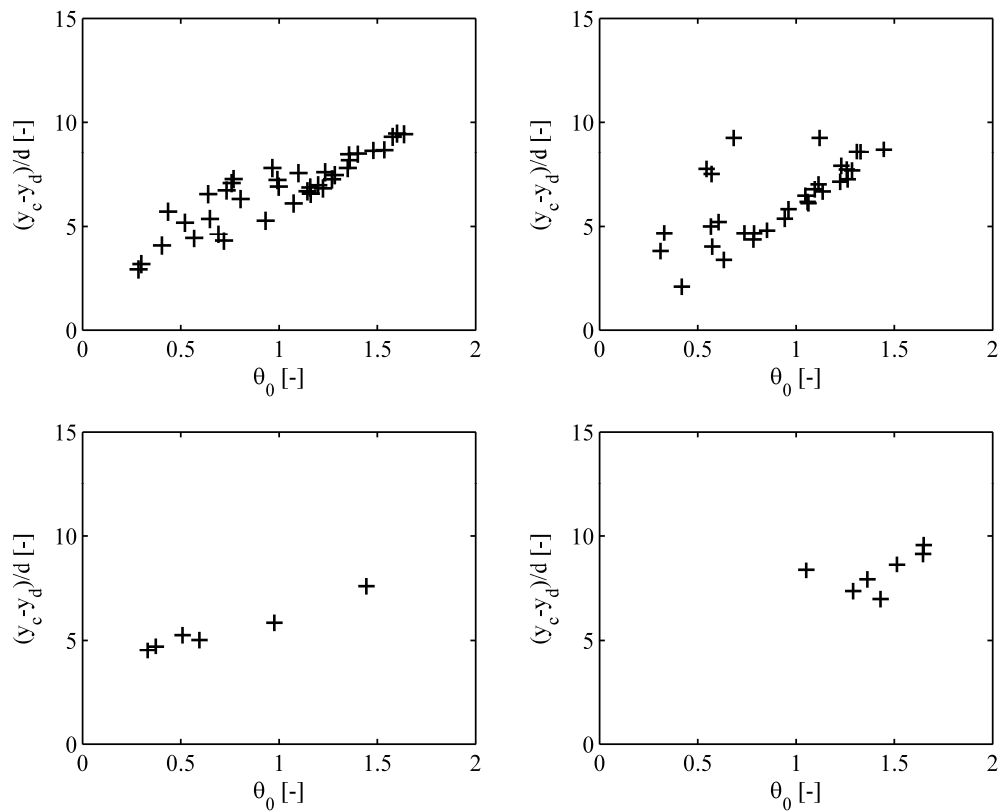


Fig. 4. Experimentally determined relative thickness of collisional layer (layer thickness divided by grain size) for flows of different bed Shields parameter (upper-left panel: TLT50, upper-right panel: TLT25, lower-left panel: FA60, lower-right panel: FA30).

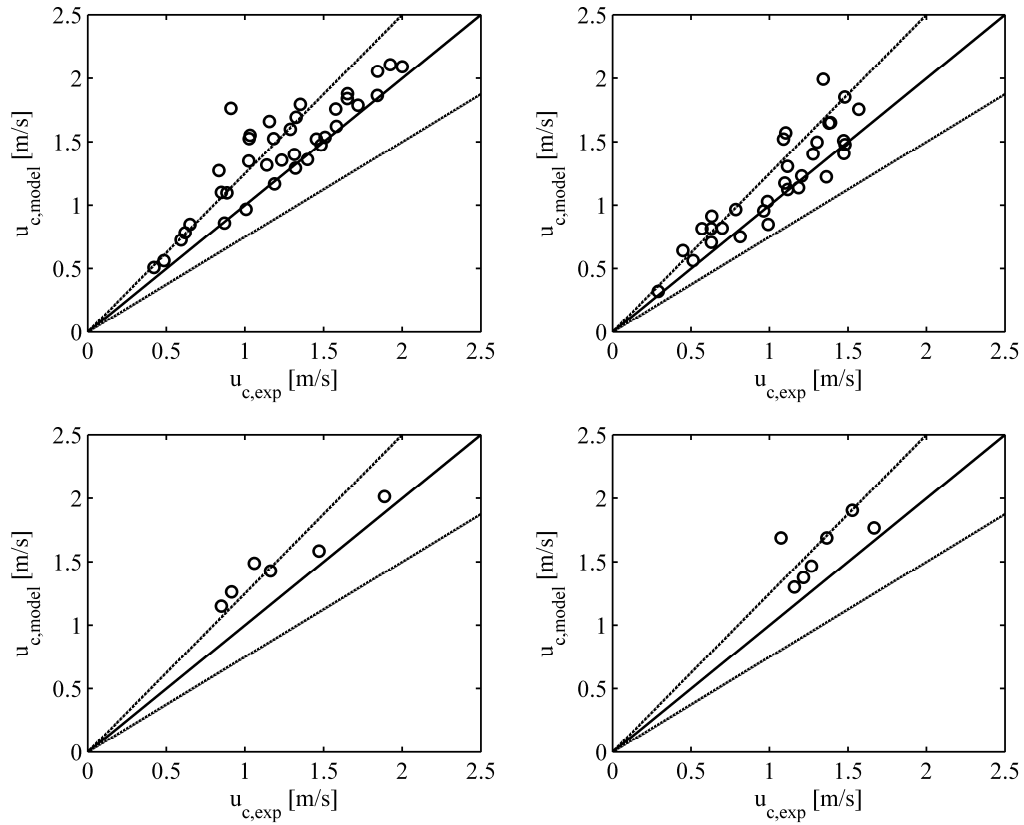


Fig. 5. Parity plot for experimental and predicted velocity at top of collisional layer. Legend: lines of perfect fit and of ± 25 per cent deviation. (upper-left panel: TLT50, upper-right panel: TLT25, lower-left panel: FA60, lower-right panel: FA30).

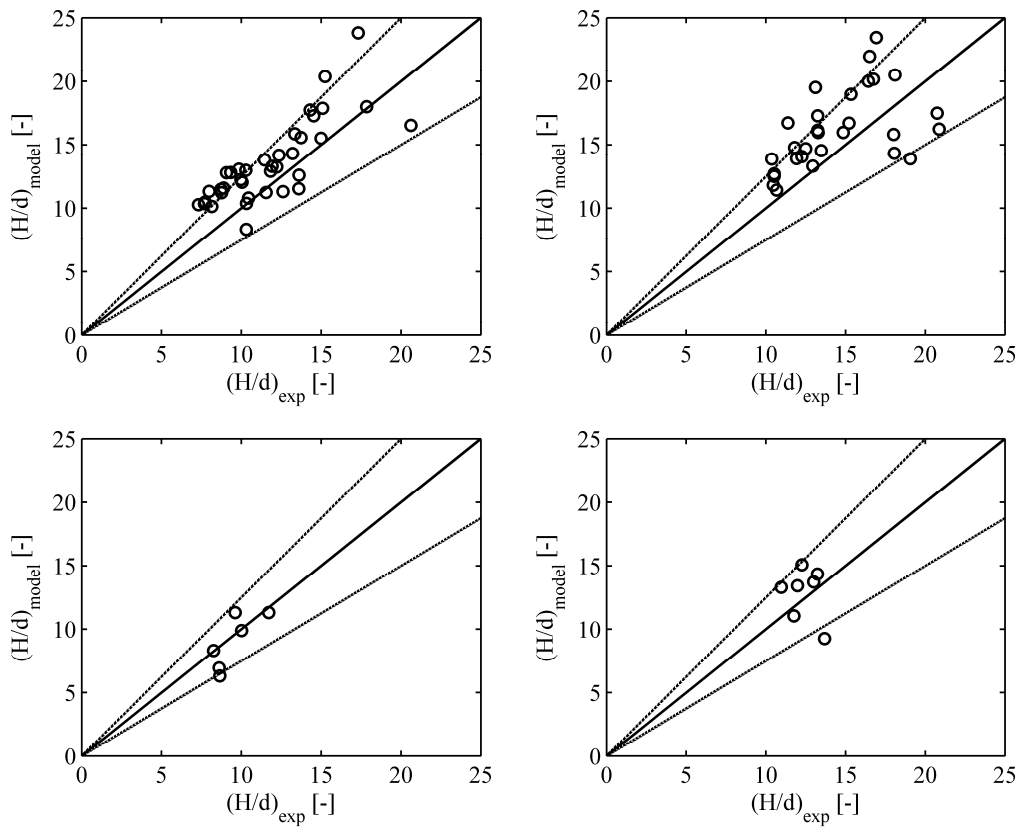


Fig. 6. Parity plot for experimental and predicted relative depth of flow (flow depth divided by grain size). Legend: lines of perfect fit and of ± 25 per cent deviation. (upper-left panel: TLT50, upper-right panel: TLT25, lower-left panel: FA60, lower-right panel: FA30).

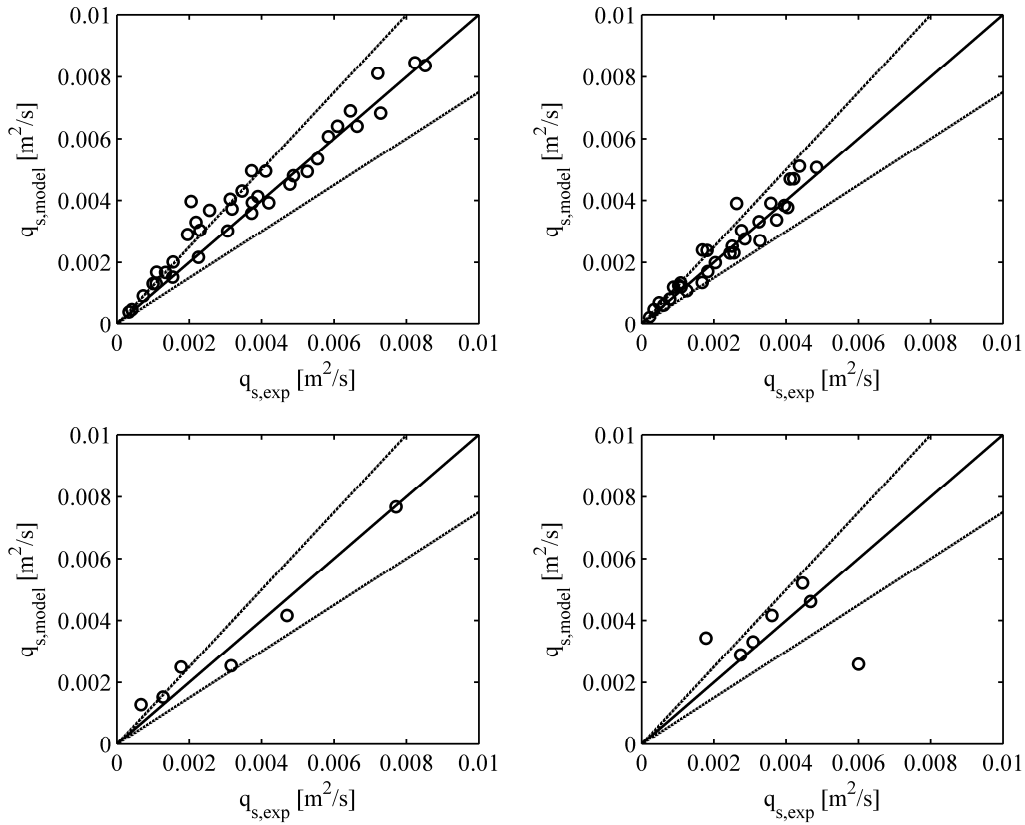


Fig. 7. Parity plot for experimental and predicted discharge of sediment (upper-left panel: TLT50, upper-right panel: TLT25, lower-left panel: FA60, lower-right panel: FA30). Legend: lines of perfect fit and of ± 25 per cent deviation.

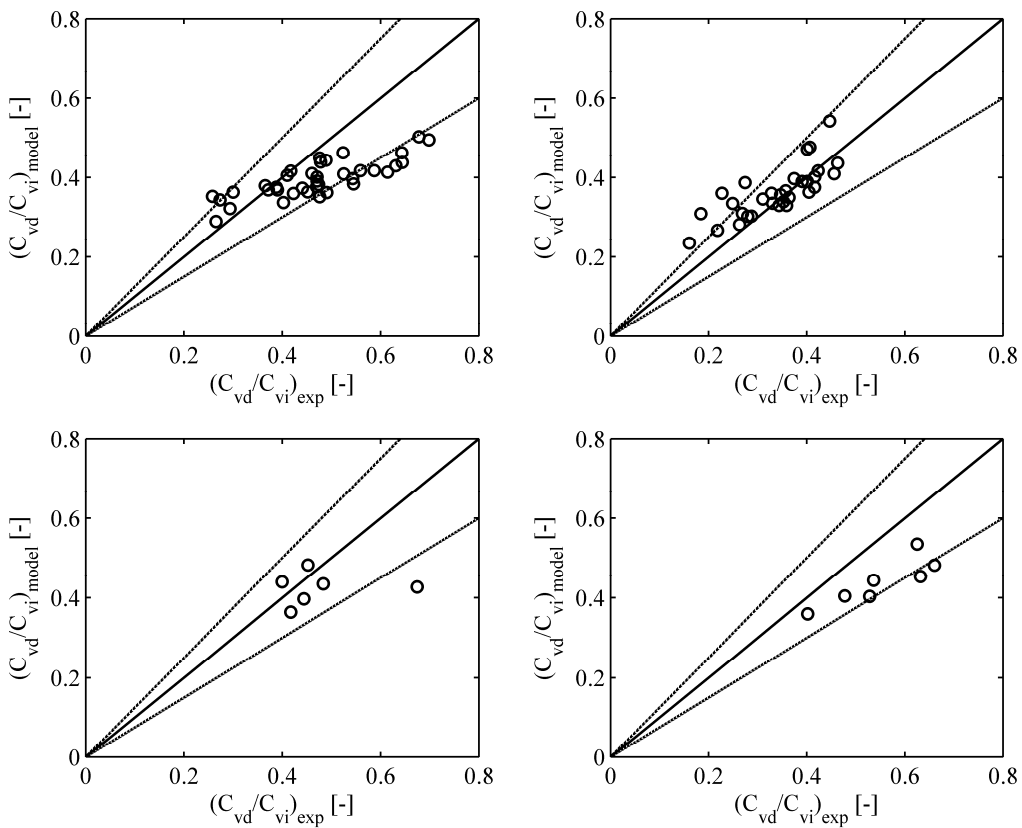


Fig. 8. Parity plot for experimental and predicted ratio of delivered concentration and spatial concentration of transported sediment (upper-left panel: TLT50, upper-right panel: TLT25, lower-left panel: FA60, lower-right panel: FA30). Legend: lines of perfect fit and of ± 25 per cent deviation.

CONCLUSIONS

A predictive model is presented for collisional bed load transport at high bed shear in an open channel. It employs constitutive relations of the classical kinetic theory previously selected as appropriate for transport and flow conditions under consideration on a basis of our laboratory testing. The model allows a prediction of the discharges of sediment and mixture for flows of given depth and longitudinal slope. Furthermore, it predicts the layered structure of the flow transporting bed load particles, giving the thickness of the collisional layer and the thickness of the sliding dense layer in the flow with intense bed load.

A comparison with experimental results for four fractions of lightweight model sediment suggests that the model reasonably predicts flow rates of both sediment and mixture at flow conditions observed in the laboratory tilting-flume experiment. Also, the predictions of the relation between the flow depth and the thickness of the collisional layer are satisfactory. The observed variation of the local concentration at the bottom of the collisional layer is considered in the model calculations.

Acknowledgement. The research has been supported by the Czech Science Foundation through the grant project No. 16-21421S. An assistance of J. Krupička and T. Pícek with the experimental part of the research is highly acknowledged.

REFERENCES

- Armanini, A., Capart, H., Fraccarollo, L., Larcher, M., 2005. Rheological stratification in experimental free-surface flows of granular-liquid mixtures. *Journal of Fluid Mechanics*, 532, 269–319.
- Berzi, D., 2011. Analytical solution of collisional sheet flows. *ASCE Journal of Hydraulic Engineering*, 137, 10, 1200–1207.
- Berzi, D., Fraccarollo, L., 2013. Inclined, collisional sediment transport. *Physics of Fluids*, 25, 106601.
- Berzi, D., Fraccarollo, L., 2016. Intense sediment transport: Collisional to turbulent suspension. *Physics of Fluids*, 28, 023302.
- Capart, H., Fraccarollo, L., 2011. Transport layer structure in intense bed-load. *Geophysical Research Letters*, 38, L20402.
- Cheng, N.S., 2002. Exponential formula for bedload transport. *ASCE Journal of Hydraulic Engineering*, 128, 10, 942–946.
- Garzo, V., Dufty, J.W., 1999. Dense fluid transport for inelastic hard spheres. *Physical Review E* 59, 5895–5911.
- Jenkins, J.T., Hanes, D.M., 1998. Collisional sheet flows of sediment driven by a turbulent fluid. *Journal of Fluid Mechanics*, 370, 29–52.
- Matoušek, V., Bareš, V., Krupička, J., Pícek, T., Zrostlík, Š., 2016. Structure of flow with intense bed load layer. In: Proc. Int. Conf. River Flow 2016, Saint Louis, USA.
- Matoušek, V., Zrostlík, Š., 2018a. Laboratory testing of granular kinetic theory for intense bed load transport. *Journal of Hydrology and Hydromechanics*, 66, 3, 330–336.
- Matoušek, V., Zrostlík, Š., 2018b. Bed load transport modelling using kinetic theory. In: Proc. Int. Conf. River Flow 2018, Lyon, France.
- Matoušek, V., Zrostlík, Š., 2019. Evaluation of local turbulent support of particles in intense transport of contact load. In: Proc. 19th Int. Conf. Transport & Sedimentation of Solid Particles, Cape Town, RSA.
- Meyer-Peter, P., Müller, R., 1948. Formulas for bed-load transport. In: Report of 2nd Meeting of IAHSR, Stockholm, Sweden, pp. 39–64.
- Rickenmann, D., 1991. Hyperconcentrated flow and sediment transport at steep slopes. *ASCE Journal of Hydraulic Engineering*, 117, 11, 1419–1439.
- Smart, G.M., 1984. Sediment transport formula for steep channels. *ASCE Journal of Hydraulic Engineering*, 110, 3, 267–276.
- Spinewine, B., Capart, H., 2013. Intense bed-load due to a sudden dam-break. *Journal of Fluid Mechanics*, 731, 579–614.
- Wilson, K.C., 1966. Bed-load transport at high shear stress. *Journal of Hydraulic Division ASCE*, 92, 6, 49–59.
- Wong, M., Parker, G., 2006. Reanalysis and correlation of bed-load relation of Meyer-Peter and Müller using their own database. *ASCE Journal of Hydraulic Engineering*, 132, 11, 1159–1168.

NOMENCLATURE

- c_c – local volumetric concentration at top of collisional layer
 c_d – local volumetric concentration at bottom of collisional layer
 c_0 – local volumetric concentration at top of bed
 d – particle diameter
 e – coefficient of wet restitution
 e_d – coefficient of wet restitution at bottom of collisional layer
 f_s – concentration-related function
 f_σ – concentration-related function
 g – gravitational acceleration
 q_m – total volumetric discharge of mixture
 q_s – volumetric discharge of sediment
 u – local velocities at different vertical positions
 u_s – local velocity of solids
 $u_{s,c}$ – velocity of solids at top of collisional layer
 $u_{s,d}$ – velocity of solids at bottom of collisional layer
 u_f – local liquid shear velocity
 v_t – terminal settling velocity of grain
 y – vertical position above top of bed
 y_c – vertical position of top of collisional layer
 y_d – vertical position of top of dense layer
 C_{vd} – delivered concentration of sediment
 C_{vi} – average spatial volumetric concentration of sediment in flow cross section
 G – concentration-related function
 H – total flow depth
 T – local granular temperature
 T_d – granular temperature at bottom of collisional layer
 β_d – friction coefficient at bottom of collisional layer
 β_0 – friction coefficient at top of bed
 γ_s – local gradient of solids velocity
 $\gamma_{s,d}$ – solids velocity gradient at bottom of collisional layer
 ε – dry restitution coefficient
 θ_0 – Shield parameter at top of bed
 ρ_f – density of liquid
 ρ_s – density of grains
 μ_f – dynamic viscosity of liquid
 ω – angle of longitudinal slope of bed
 σ_s – local solids normal stress
 $\sigma_{s,d}$ – solids normal stress at top of dense layer
 $\sigma_{s,0}$ – solids normal stress at top of bed
 τ_e – local total shear stress
 $\tau_{e,d}$ – total shear stress at top of dense layer
 τ_f – local liquid shear stress
 τ_s – local solids shear stress
 $\tau_{s,d}$ – solids shear stress at top of dense layer

Received 2 September 2019

Accepted 9 December 2019

Velocity profiles and turbulence intensities around side-by-side bridge piers under ice-covered flow condition

Mohammad Reza Namaee, Jueyi Sui*

Environmental Engineering Program, University of Northern British Columbia, 3333 University Way, Prince George, BC, Canada.

*Corresponding author. E-mail: jueyi.sui@unbc.ca

Abstract: Recent studies have shown that the presence of ice cover leads to an intensified local scour pattern in the vicinity of bridge piers. To investigate the local scour pattern in the vicinity of bridge pier under ice-covered flow condition comparing to that under open channel flow condition, it is essential to examine flow field around bridge piers under different flow conditions. In order to do so, after creation of smooth and rough ice covers, three-dimensional time-averaged velocity components around four pairs of bridge piers were measured using an Acoustic Doppler velocimetry (ADV). The ADV measured velocity profiles describe the difference between the velocity distributions in the vicinity of bridge piers under different covered conditions. Experimental results show that the vertical velocity distribution which represents the strength of downfall velocity is the greatest under rough covered condition which leads to a greater scour depth. Besides, results show that the turbulent intensity increases with pier size regardless of flow cover, which implies that larger scour depth occurs around piers with larger diameter.

Keywords: Bridge pier; Ice cover; Local scour; Acoustic Doppler velocimetry (ADV); Horseshoe vortex.

INTRODUCTION

Bridges constructed with elements within the boundaries of rivers are potentially exposed to scour around their foundations. If the depth of scour exceeds a critical value, instability and vulnerability caused by the scour will threaten the bridge foundation, which might possibly lead to critical issues such as bridge collapse, significant transport disruption and, in an extreme case, human casualty. Melville and Coleman (2000) studied 31 cases of bridge failures due to scour in New Zealand and concluded that, on average, one major bridge failure each year can be attributed to scour occurring around the bridge foundations. Wardhana and Hadipriono (2003) studied 500 cases of bridge structure failures in the United States between 1989 and 2000 and stated that the most common causes of bridge failure were either floods or scour. Sutherland (1986), in conjunction with National Roads Board of New Zealand, determined that of the 108 bridge failures recorded between 1960 and 1984, 29 could be attributed to abutment scour. Note that abutment scour is the removal of sediment around bridge abutments. Local scour around bridge foundations has been the focal point of many studies (Ahmed and Rajaratnam, 1998; Dey and Raikar, 2007; Ettema et al., 2011; Graf and Istiarto, 2002; Melville and Sutherland, 1988; Melville and Chiew, 1999; Sheppard et al., 2013; Williams et al., 2018; Williams et al., 2017; Wu and Balachandar, 2016; Wu et al., 2014, 2015a, b, c). Namaee and Sui (2019a) investigated the impact of armour layer on the scour depth around side-by-side bridge piers under ice-covered flow condition. Their study showed that the impact of armour layer is dependent on sediment type in which the piers are placed, and it increases as the sediment gets coarser regardless of pier size and pier shape.

Figure 1 illustrates mechanism of local scour around a submerged vertical cylinder adapted from Zhao et al. (2010). According to Williams et al. (2018), the scour commences in the region of the highest velocity in the vicinity of the separating streamline. The horseshoe vortex which forms at the pier face

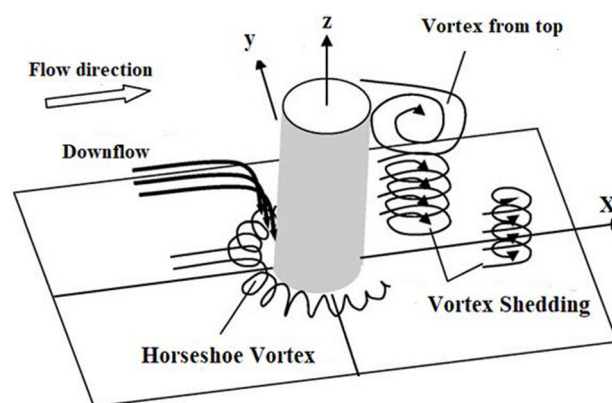


Fig. 1. Flow pattern around a submerged vertical cylinder (adapted from Zhao et al., 2010).

shifts the maximum downflow velocity closer to the pier in the scour hole. The downflow acts as a vertical jet to erode a groove in front of the pier. The eroded sand particles are carried around the pier by the combined action of accelerating flow and the spiral motion of the horseshoe vortex (Hafez, 2016). Melville and Coleman (2000) report a wake-vortex system which occurs behind the pier, acts like a vacuum cleaner sucking up bed material and carries the sediment moved by the horseshoe vortex system and by the downward flow to downstream of the pier (Vortex shedding in Fig. 1). However, wake-vortices are not normally as strong as the horseshoe vortex and therefore, are not able to carry the same sediment load as the horseshoe vortex does. Note that although a wider bridge pier results in a more accumulated armour layer around the bridge pier which ultimately decreases the scour depth, it results in a stronger horseshoe vortex at the pier face. Horseshoe vortex is the main driver in creation of local scour, and its impact is much stronger

than the impact of armour layer. According to Mohammed et al. (2007), a reduction of 15% in local scour depth can be obtained by using a pier having a streamlined shape instead of a squared-nose pier. This finding clearly shows that the pier shape factor has more impact on scour depth than that of the armour layer around bridge piers. Vijayasree et al. (2019) also stated that the scour process and the location of the maximum scour depth around the pier depended on shape of bridge pier. They claimed that a sharp nose with curved body is ideal for a bridge pier because of less scour around the pier. Gautam et al. (2019) investigated the variations in the turbulent flow field generated in the vicinity of a complex pier due to the presence of the pile-cap, and the results were compared with that of a simple pier without any pile-cap. It was concluded that the magnitude of the mean velocities, turbulence intensities and Reynolds shear stresses around a complex pier were less than those of the simple pier, indicating simpler fluid flow around the complex pier. Regarding scour at pile groups, Galan et al. (2019) revealed that depending on the submergence ratio as well as the angle of the piles with the approaching flow (skew-angle) and pile arrangements, the location of the maximum scour depths differs and it does not always occur at the first upstream pile. The experimental results of Zhao et al. (2010) which focuses on the local scour around a submerged pier showed that a decrease in pier height weakened the horseshoe vortex and vortex shedding which resulted in lower scour depths.

The velocity distribution in the vicinity of bridge piers is very important for the scouring process around bridge piers. Up to date, many researches regarding velocity distribution around bridge piers have been reported, such as Graf and Istiarto (2002); Unger and Hager (2007); Beheshti and Ataie-Ashtiani; (2009). Graf and Istiarto (2002) performed an experimental study of the flow pattern in the upstream and downstream plane of a cylinder positioned vertically in a scour hole. Detailed measurements were obtained by using an acoustic-Doppler velocity profiler (ADVP) in and around the scour hole. The results indicated that in the upstream reach of the cylinder, a strong vortex system was detected (horseshoe vortex) at the foot of the cylinder. In the downstream reach of the cylinder, a flow reversal existed towards the water surface. In their study, the results indicated the turbulent kinetic energy was very strong at the foot of the cylinder on the upstream side and in the wake behind the cylinder. Unger and Hager (2007) investigated the temporal evolution of the vertical deflected flow at the pier front and the horseshoe vortex inside the scour hole as it formed. Their work provided novel insight into the complex two-phase flow around circular bridge piers placed in loose sediment. A three-dimensional turbulent flow field around a complex bridge pier placed on a rough fixed bed was experimentally investigated by Beheshti and Ataie-Ashtiani (2009). Comparison of flow patterns with the observed scour map revealed that the scour patterns at the upstream and sides of the pier correlate well with the contracted flow below the pile cap. A flow field analysis around side-by-side piers with and without a scour hole was carried out by Ataie-Ashtiani and Aslani-Kordkandi (2012). They found that the streamwise velocity increased between the two piers. As a result, the maximum depth of the scour hole was approximately 15% greater than in the single-pier case. Kumar and Kothiyari (2011) studied flow patterns and turbulence characteristics within a developing (transient stage) scour hole around both circular uniform and compound piers using an Acoustic Dropper Velocimeter (ADV). Their results for velocity, turbulence intensity and Reynolds shear stress around each of the piers along different vertical planes exhibited similar profiles with respect to flow

depth. However, at certain locations close to the pier, significant changes occurred in the vertical profile of the flow parameters. While the observations made in the upstream planes revealed that within the scoured region, the bed shear stress was much smaller compared with the bed shear stress of the approach flow. Due to the difficulty in making velocity measurements under ice-covered conditions, nearly all the studies regarding velocity distribution around bridge piers have been carried out using open channel flow conditions. The number of studies on the flow field around both bridge abutments and bridge pier under ice-covered conditions is limited. Wu et al. (2015a) studied the effect of relative bed coarseness, flow shallowness, and pier Froude number on local scour around a bridge pier and reported the scour depth under covered conditions is larger compared to open channel flow conditions. It has been found that the presence of an ice cover alters the hydraulics of the channel by imposing an extra boundary to the water surface (Sui et al., 2010). Under ice-covered flow conditions, the velocity drops to zero at each boundary (ice-covered water surface and the bed) due to the no-slip boundary condition, resulting in a parabolic-shaped flow profile (Ettema, et al., 2000; Zabilansky et al., 2006). The maximum velocity occurs between the bed and the bottom of the ice cover and is dependent on the relative roughness of the two boundaries (Wang et al., 2008). Sui et al. (2010) showed that the upper flow is mainly influenced by the ice cover resistance while the lower flow is primarily impacted by the channel bed resistance. Wang et al. (2008) stated that the location of maximum velocity depends on the relative magnitudes of the ice and bed resistance coefficients. According to Wang et al. (2008), as the ice resistance increases, the maximum flow velocity will move closer to the channel bed. In terms of local scour depth, the severity of the local scour in the vicinity of a bridge's foundation intensifies during the freezing period when the water surface is covered with ice. The presence of ice has been found to increase local clear-water scour depth at bridge piers by 10%–35% (Hains and Zabilansky, 2004). In terms of transverse flow distributions and velocities of secondary currents, ice cover can impact flows in an existing thalweg, altering the position of the thalweg and changing the morphology of the stream which, in an extreme case, will lead to bank and bed erosion (Beltaos et al., 2007). Zabilansky et al. (2006) performed a series of flume experiments under smooth and rough ice cover conditions and found the maximum velocity for rough ice cover was 20 percent greater than for smooth ice cover. This statement was confirmed by Muste et al. (2000) who found the measured maximum velocity under smooth cover is located roughly at $0.8y_0$, while maximum velocity under rough cover is approximately located at $0.6y_0$, where y_0 represents the approaching flow depth. Overall, the rougher the ice cover, the closer the locale of maximum flow velocity to the bed. As a consequence, the bed shear stress increases which ultimately leads to increase in scour depths. In this study, a series of large-scale flume experiments were conducted to examine scour hole patterns along with scour hole velocity profile measurements around four side-by-side bridge piers under ice-covered and open channel flow conditions. The objective of this paper is mainly composed of two sections. In this section, it is explained how the existence of an ice cover changes the flow field in the vicinity of bridge piers. In the second section, it explains different scouring process resulted from different flow covers (open channel flow, smooth and rough ice-covered flows) by examining the 3D flow field velocity components especially down-flow velocity which is proportional to the strength of horseshoe vortex.

METHODOLOGY

Experiments were carried out in a large-scale flume at the Quesnel River Research Centre of the University of Northern British Columbia, Canada. The flume was 38.2 m long, 2 m wide and 1.3 m deep. Fig. 2 shows a plan view and a side view of the experiment flume. The longitudinal slope of the flume was 0.2 percent. A holding tank with a volume of 90 m³ was located at the upstream end of the flume to maintain a constant discharge during the experimental runs. To create different velocities, three input valves were connected to control the inlet volume discharge. Water level in the flume was controlled by the downstream tailgate. Two types of tailgate configurations (one-tailgate and two-tailgate configurations) were incorporated to produce a wide range of main channel approaching velocities. The range of flow depth was from 0.09 m to 0.137 m for the one-tailgate configuration and from 0.165 m to 0.28 m for the two-tailgate configuration. For the case of two-tailgate configuration, two pumps were employed for the lowest flow discharge while three pumps were employed to create the highest flow discharge. At the end of the holding tank and upstream of the main flume, water overflowed from a rectangular weir into the flume. Two sand boxes were constructed in the flume. Both had a depth of 0.3 m and were 10.2 m apart. The length of

the sand boxes were 5.6 m and 5.8 m, respectively. Side-by-side cylindrical bridge piers with diameters of 60 mm, 90 mm, 110 mm and 170 mm were used. In terms of selection of sediment grain size, the mason, concrete and bedding mix sand types with median grain size $D_{50} = 0.47$ mm, 0.58 mm, 0.50 mm were selected. According to Hirshfield (2015), this selection was based upon the fact that the mason, concrete and bedding sands were the three most common sands mined from the surrounding quarries. Thus, our experiments have been conducted using these three sands in order to have the opportunity to meticulously compare our results of side-by-side bridge piers to those results of singular bridge pier of Hirshfield (2015) which is shown in Fig. 4.

The piers were spaced from each 0.50 m from center to center. Fig. 3 shows the piers and the space ratio (G/D) in which G is the distance between the piers and D is the pier diameter. The geometric channel aspect ratio (channel width/flow depth) in these series of experiments ranged from 7.14 to 22.2. The bridge pier spacing ratio G/D ranged from 1.94 to 7.33 (Fig. 3). In front of the first sand box, a 2D Flow Meter (Sontek, 2001) was installed to measure flow velocities and water depth. A staff gauge was also installed in the middle of each sand box to manually verify water depth. Styrofoam panels were used as ice cover across the entire surface of flume. Both smooth and rough

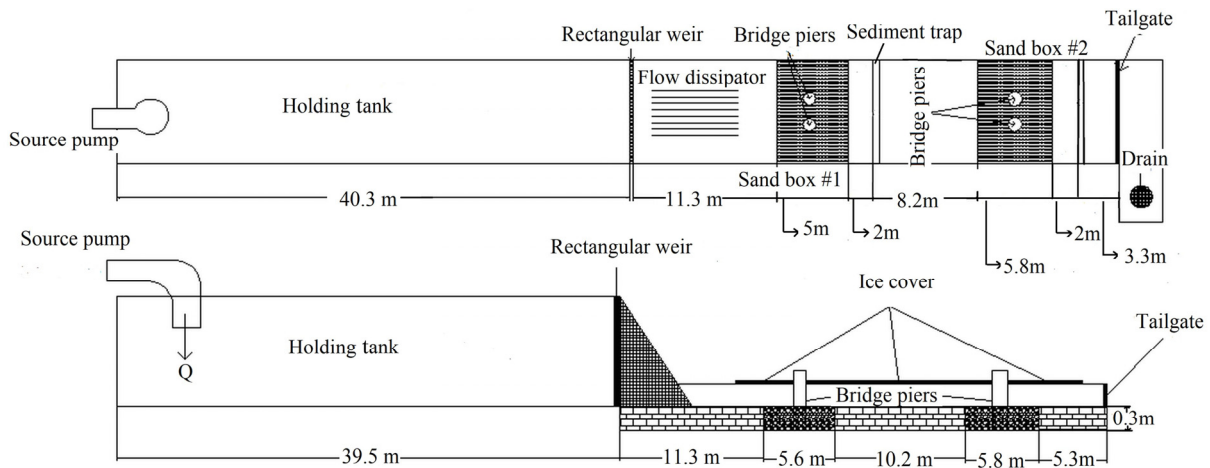


Fig. 2. Plan view and vertical view of experiment flume (Dimensions in m) (Namaee et al., 2019a).

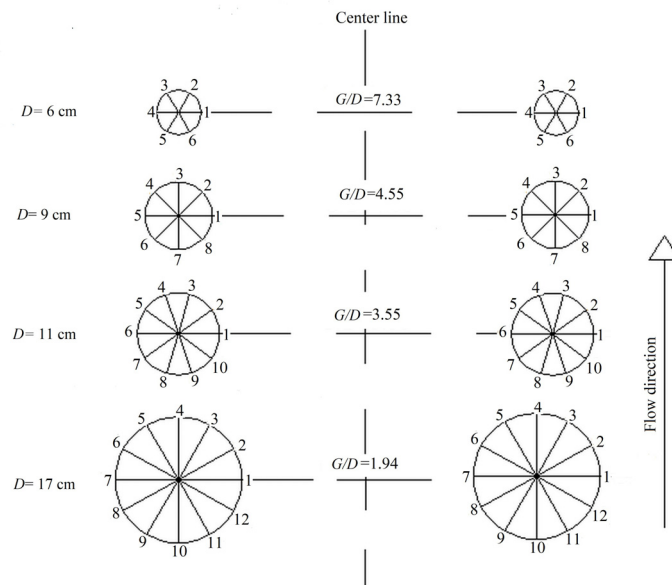


Fig. 3. The spacing ratio and measuring points around the circular bridge piers (Namaee et al., 2019a).

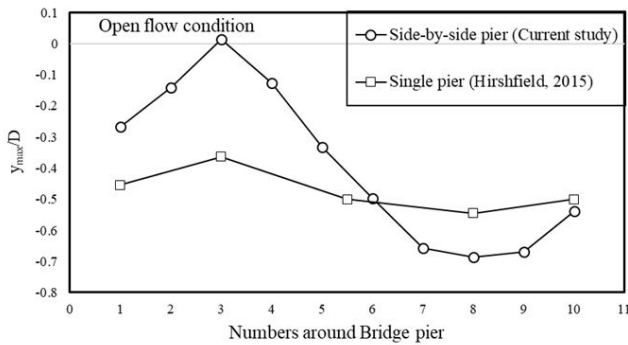


Fig. 4a. Scour depth around the 110-mm bridge pier for $D_{50} = 0.47$ mm type sediment under open flow.

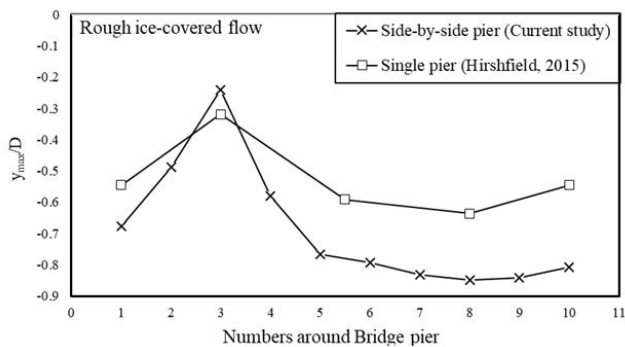


Fig. 4b. Scour depth around the 110-mm bridge pier for $D_{50} = 0.47$ mm type sediment under rough covered flow conditions using the highest flow discharge.

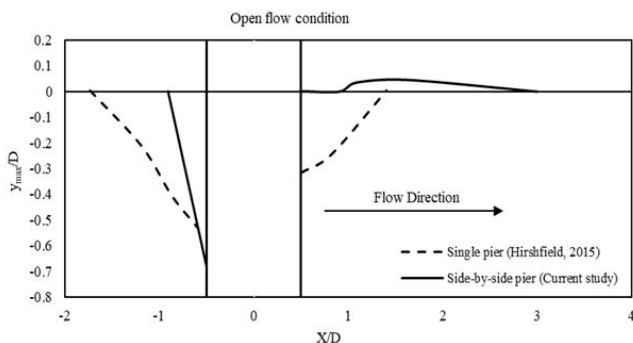


Fig. 4c. Cross-section of scour and depositional pattern at the upstream and downstream of the 110-mm bridge pier under open flow condition.

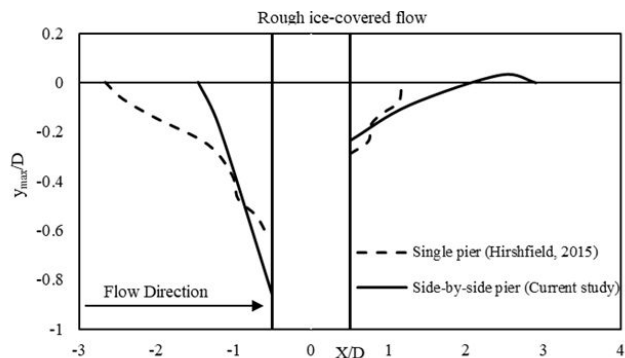


Fig. 4d. Cross-section of scour and depositional pattern at the upstream and downstream of the 110-mm bridge pier under rough covered flow conditions for $D_{50} = 0.47$ mm.

ice covers were simulated. The smooth cover was the smooth surface of the original Styrofoam panels while the rough cover was made by attaching small Styrofoam cubes to the bottom of the smooth cover. The dimensions of Styrofoam cubes were 25 mm \times 25 mm \times 25 mm and they were spaced 35 mm apart. The velocity field in the scour holes was measured using a 10-MHz acoustic Doppler velocimeter (ADV). The sampling volume of the 10-MHz ADV is 100 mm from the sensor head. In a standard configuration, the sampling volume is approximately a cylinder of water with a diameter of 6 mm and a height of 9 mm. The ADV functions on the principle of a Doppler shift, measuring the phase change when the acoustic signal reflects off particles in the flow (Sontek, 1997).

In this study, the ADV measured the scour hole velocity profiles at approaching flow depths within 0.18–0.28 m range for four sets of bridge piers (60 mm, 90 mm 110 mm and 170 mm) when using the two-tailgate flume configurations for the highest and lowest levels of discharge. The positive direction of three-dimensional velocity components is shown in the coordinate system of Fig. 1. Scour hole velocity measurements for shallow flow depths (one-tailgate flume configuration) were inaccessible due to the limitations of the ADV in measuring shallow flow depths. Note that the difference between the water temperature measured by IQ with the water temperature measured by ADV was within 0.25 degrees Celsius. Velocity measurements were performed at one hour before the end of the experimental run (total test time = 24 hours) at which point the scour hole was fully developed and stabilized. For the purposes of these experiments, the streamwise velocity component is denoted as U_x , is the component in the direction of the flow, the span-wise velocity component is denoted as U_y is the component in the lateral direction and the vertical velocity component is denoted as U_z . Of note, a negative value of U_z means the velocity vector is directed downwards. To develop the three-dimensional velocity profiles, measurements were obtained at each point for 120 seconds. Of note, for velocity values very close to the channel bed, the presence of sediment affected the ADV velocity measurement, therefore, the velocity values are representative of sediment and water velocity as previous noted by Muste et al. (2000). The scour hole flow field was measured at 20 mm increments from the bottom of scour hole in front of the bridge pier up to free surface for each experimental run. In the ice-covered experiments, a part of the Styrofoam was cut to allow for the ADV to be positioned inside the flow for flow field measurements. Further, since the ADV measuring volume is located 100 mm from the probe head, the velocity profile for each channel condition does not continue up to the water surface. After the experiments were completed, collected data were analyzed to filter out for velocity spikes. Signal strengths and correlations are used principally to judge the quality and accuracy of the velocity data (Fugate and Friedrichs, 2002). In this study, data quality was defined based on signal-to-noise ratio amplitudes ($\text{SNR} \geq 15$) and correlation coefficient scores (≥ 70). In terms of uncertainty in velocity measurements, at a sampling rate of 25Hz and an SNR above 15, uncertainty due to Doppler noise can be estimated as 1% of the maximum velocity range (Sontek, 1997). Once ADV data is filtered for correlation, signal to noise ratios and data spikes, the velocity measurements were assumed to be accurate within 0.25 cm/s (Sontek, 1997). In total, 108 experiments (36 experiments for each sediment type) were conducted under open channel, smooth covered, and rough covered conditions. In terms of different boundary conditions (open channel, smooth, and rough covered flows), for each sediment type and each boundary condition, 12 experiments were carried out. In the preliminary stage of the

experiments, local scour around bridge piers was carefully observed for any changes in the scour depths. It was observed that after approximately a period of 6 hours, no significant change in scour depth was observed and scour hole equilibrium depth was achieved. The experiment was continued for 24 hours and again no obvious change in scour depth was observed. For the 110-mm bridge pier under open channel and ice-covered flow condition for the highest discharge, the experimental time was extended to 38 hours and there was not any significant change in scour depth between 24 hr. and 38 hr. experiments. Further, this agrees with a series of experiments by Wu et al. (2014), regarding local scour around a semicircular bridge abutment which determined the time for development of equilibrium scour depth as 24 hrs. After 24 hours, the flume was gradually drained, and the scour and deposition pattern around the piers was measured. Duration of experimental runs is one of important factors that affects the maximum scour depth. To explain it in more details, it is noteworthy to mention that one of the main criteria related to the bridge pier design is to predict the maximum scour depth where the bridge is constructed and subsequently to optimize the design of the foundation depth based. Clearly, the deeper the foundation placement,

the higher cost for construction. However, the local scour process around bridge piers is a complex phenomenon which is dependent on many factors and is not easy to predict. For instance, the scour depth is dependent on the soil type that the piers are placed in (whether it is low-erodible or high-erodible), pier shape, pier spacing distance (our experiments showed that the closer the piers to each other, the larger the scour depth) and the existence of ice cover, to mention only a few. Most importantly, in most of the experiments including ours, the approaching velocity is kept as constant in order to simply the analysis of the experiments. However, in natural rivers, flow velocity is constantly changing, and thus the scouring process is a dynamic process. This means the prediction for local scour is even more difficult. On the other side, the scour process is much faster at the beginning and then slows down as the scour depth gets closer to the equilibrium scour depth. In our experiments, the majority of scouring process took place within the first 6 hours of the experiments. In the laboratory experiments of Vijayasree et al. (2019), it was observed that about 80% of the maximum scour depth occurred in the first 2 hours. Overall, local scour process is a very complex phenomenon and depends on many factors. That is the reason for attracting many

Table 1. Summary of experimental running conditions.

Run #	Cover	d (mm)	$^{\circ}\text{C}$ (degrees)	y_0 (mm)	y_{max} (mm)	U (m/s)	U^* (m/s)	U/U^* –	Q (m^3/s)
1B	Open flow	60	11.83	250	22	0.11	0.20	0.56	0.056
2B	Open flow	60	11.62	110	35	0.18	0.14	1.30	0.040
3B	Open flow	60	11.45	280	25	0.17	0.21	0.81	0.094
4B	Open flow	90	11.83	200	35	0.13	0.18	0.74	0.054
5B	Open flow	90	11.62	90	60	0.25	0.13	1.96	0.045
6B	Open flow	90	11.45	230	68	0.20	0.19	1.05	0.093
7B	Open flow	110	11.50	242	25	0.12	0.19	0.60	0.058
8B	Open flow	110	11.83	100	71	0.28	0.13	2.09	0.056
9B	Open flow	110	11.72	253	75	0.20	0.20	1.05	0.101
10B	Open flow	170	11.50	250	24	0.12	0.20	0.59	0.059
11B	Open flow	170	11.83	100	45	0.18	0.13	1.35	0.036
12B	Open flow	170	11.72	270	48	0.16	0.20	0.77	0.084
13B	Smooth	60	11.62	250	29	0.12	0.15	0.82	0.061
14B	Smooth	60	11.59	110	35	0.17	0.10	1.68	0.037
15B	Smooth	60	11.55	260	42	0.17	0.15	1.16	0.090
16B	Smooth	90	11.62	200	31.2	0.15	0.13	1.13	0.060
17B	Smooth	90	11.59	100	64	0.23	0.10	2.40	0.046
18B	Smooth	90	11.55	240	68	0.20	0.14	1.38	0.096
19B	Smooth	110	11.59	243	42	0.10	0.14	0.68	0.048
20B	Smooth	110	11.10	90	78	0.21	0.09	2.29	0.038
21B	Smooth	110	11.57	255	80	0.20	0.15	1.44	0.102
22B	Smooth	170	11.59	260	29	0.09	0.15	0.63	0.049
23B	Smooth	170	11.10	105	48	0.15	0.10	1.55	0.032
24B	Smooth	170	11.54	250	49	0.18	0.15	1.20	0.089
25B	Rough	60	11.48	220	47	0.16	0.14	1.18	0.072
26B	Rough	60	11.45	100	55	0.17	0.10	1.76	0.034
27B	Rough	60	11.59	250	57	0.22	0.15	1.48	0.109
28B	Rough	90	11.48	220	67	0.14	0.14	0.99	0.061
29B	Rough	90	11.45	100	73	0.23	0.10	2.38	0.046
30B	Rough	90	11.59	230	85	0.20	0.14	1.37	0.090
31B	Rough	110	11.58	240	80	0.12	0.14	0.86	0.058
32B	Rough	110	11.61	90	92	0.20	0.09	2.22	0.037
33B	Rough	110	11.62	220	93	0.19	0.14	1.39	0.085
34B	Rough	170	11.58	220	49	0.12	0.14	0.86	0.053
35B	Rough	170	11.61	110	58	0.16	0.10	1.61	0.036
36B	Rough	170	11.62	280	61	0.17	0.16	1.08	0.093

researchers to do research work regarding the maximum scour depth around pier foundation.

To accurately read the scour depth at different locations and to draw scour hole contours, the outside perimeter of each bridge pier was divided between 6 and 12 labeled segments based on the diameter of the cylinder (Fig. 3). The measurement of scour hole was subject to an error of ± 0.3 mm. Table 1 tabulates the complete measured experimental data for $D_{50} = 0.47$ mm. In Table 1, y_{\max} is the maximum scour depth, y_0 is the approach flow depth, U is the approaching flow velocity which is averaged over the flow depth, U^* is shear velocity also called friction velocity which is equal to $(gRS)^{0.5}$ (Namaee et al., 2017; Rickenmann and Recking, 2011), d is the diameter of the bridge piers, D_{50} is the medium grain size, Q is the volumetric flow discharge and θ is the flow (liquid) temperature. Of note, the maximum scour depth between left hand side and the right-hand side bridge piers were more or less identical. Note that this study is a part of a broad project in which impact of different parameters such as densimetric Froude number, armor layer, pier spacing and flow cover on the local scour in the vicinity of bridge piers has been painstakingly investigated (Namaee and Sui, 2019a; Namaee and Sui, 2019b and Namaee et al., 2019). Therefore, Fig. 2 and Fig. 3 are already refereed in those studies.

RESULTS AND DISCUSSIONS

Local Scour pattern around bridge piers

Fig. 4(a–b) shows scour depth around the 110 mm bridge pier and Figs. 4(c–d) compares the scour and depositional pattern upstream and downstream of the pier for $D_{50} = 0.47$ mm under open and rough flow conditions for the highest flow discharge, respectively. Fig. 4(a–d) also compares the scour depth of the present study with that of Hirshfield (2015) in which local scour around 110-mm single bridge pier under open and rough ice-covered flow conditions for $D_{50} = 0.47$ mm. Result of comparison reveals interesting information regarding how the local scour pattern around side-by-side bridge piers differs from that around singular bridge pier. As indicated in Fig. 4(a–b), regardless of the flow condition (either open flow or ice-covered flow conditions) and the number of piers, the maximum scour depth occurred at the upstream apex point of the pier face (point 8) where the horseshoe vortex and down-flow velocity coexist and are the strongest. The least amount of scour occurred near point 3 which is diametrically opposed to point 8 and behind the pier. Further, Fig. 4 shows that the scour depth around the side-by-side pier configuration is deeper than that around the singular bridge pier in the study of Hirshfield (2015). According to Fig. 4b, sediment ridges have been developed downstream of the side-by-side bridge pier under all the flow cover conditions. However, for the single bridge pier, sediment ridges downstream of the pier were not reported by Hirshfield (2015). The reason is due to the confining effects of the side-by-side bridge pier when compared to the singular bridge pier which has resulted in greater scour depth and more developed sediment ridge at the downstream side of the bridge pier. This is in good agreement with result of Hodi (2009) that states, as the blockage ratio increases, larger amount of discrepancies will be developed in both scour depth and bed geometry. In the present study, regardless of flume cover, the maximum scour depths were always located at the upstream face of the pier. Since horseshoe vortex is stronger than the wake vortex, according to the description of Fig. 1, sediment deposition is likely to occur downstream of the pier in the form of a sediment ridge which is clearly shown in Fig. 4b. The scour pattern

around the 110-mm bridge pier under highest flow discharge viewed from the top for $D_{50} = 0.47$ mm was mapped into Surfer 13 plotting software (Golden Software, 1999) as shown in Figs. 5(a–c) for open, smooth, and rough flow cover, respectively. Note that Namaee et al. (2019) already investigated the scour morphology around the 110-mm bridge pier under highest flow discharge for $D_{50} = 0.47$ mm. The reason why the same scour morphology is shown here is firstly because the aforementioned scour morphology is the most critical one in which the highest maximum scour depth was reached and secondly many more scour depths were collected for this scour morphology after the experiment to show a higher resolution scour morphology. According to Fig. 5, the deepest location of scour depth around the pier is clearly at the face of bridge pier and the location of deposition ridge is downstream of the pier which is densest and most widely spread for the rough ice-covered flow condition. The same pattern was observed for the other bridge piers regardless of sediment type and bridge pier diameter. It was experimentally noted by Qadar (1981) that the maximum value of scour depth should certainly be a function of the initial vortex strength. Therefore, the deepest scour depth, which is the result of a stronger vortex, should occur under the highest approaching velocity and roughest ice cover as observed in these experiments which clearly shows that the ice coverage increases the scour depth, and the rougher the ice cover, the greater the scour depth. Other factor which significantly impacts the local scour around side-by-side bridge piers compared to the singular bridge pier is the bridge spacing. Namaee and Sui (2019b) stated that the pier Reynolds number (Re_b) declines with increase in the pier spacing indicating that the strength of the horseshoe vortices reduces as the spacing distance between the side-by-side piers rises. Moreover, it was concluded that regardless of flow cover, the impact of ice cover on pier Reynolds number diminishes as the pier spacing distance increases. Note that the pier Reynolds number is defined as:

$$Re_b = \frac{Ud}{\nu} \quad (1)$$

where, U is the average velocity of the approaching flow; d is the diameter of the bridge pier, and ν is the kinematic viscosity.

Flow velocity profiles

Scour hole velocity profiles for the streamwise (U_x) and vertical (U_z) velocity components under open, smooth and rough ice cover for all the piers size separately and under $D_{50} = 0.47$ mm for the lowest discharge is presented in Fig. 6. Fig. 7 shows scour hole velocity profiles for the streamwise (U_x) and vertical (U_z) velocity components distinguished by flow cover for all the pier sizes under $D_{50} = 0.47$ mm for the lowest discharge. Fig. 8 shows the vertical velocity distribution for the lowest discharge for the 90-mm bridge pier under rough ice-covered condition for the three D_{50} s. In order to be able to generalize the velocity profiles and to compare different velocity profiles under different flow cover, the depth of flow on the vertical axis has been non-dimensionalized by taking the ratio of vertical distance from bed (z) to approach flow depth (y_0). The streamwise scour hole velocity component (U_x) and the vertical scour hole velocity component (U_z) are also non-dimensionalized by the approaching flow velocity (U). Of note, the ADV location for the velocity measurement of all the experiments was set at 10 mm upstream of the pier face where the maximum scour depth occurred. The following outcome can be concluded from Figs. (6–8):

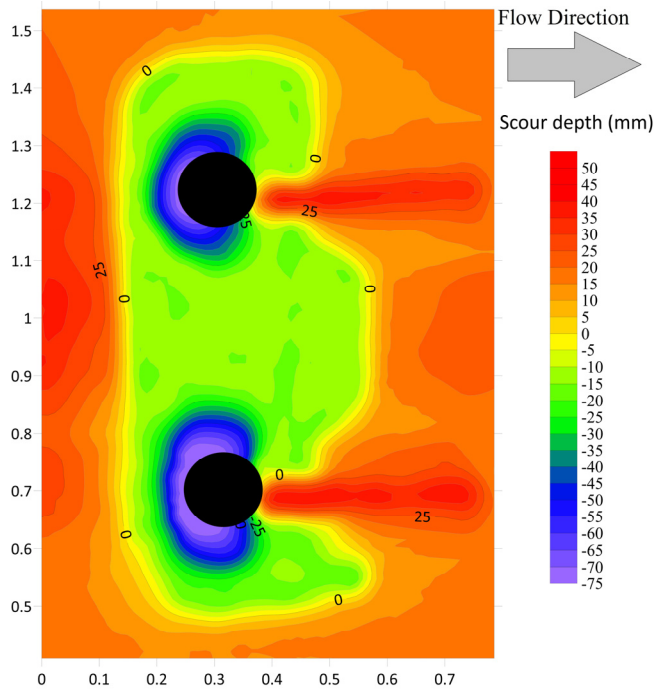


Fig. 5a. Scour pattern around the 110-mm bridge pier for $D_{50} = 0.47$ mm type under open for the highest flow discharge (Namaee et al., 2019).

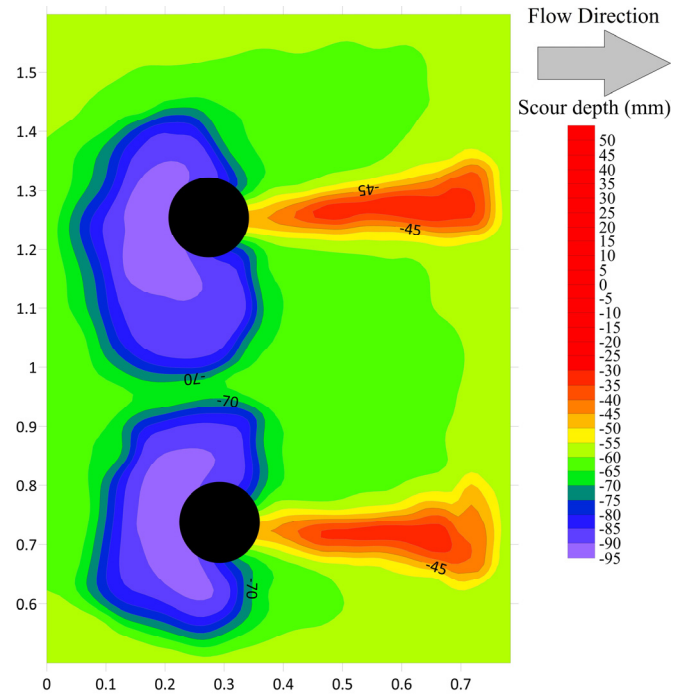


Fig. 5c. scour patterns around the 110-mm bridge pier for $D_{50} = 0.47$ mm type under rough for the highest flow discharge (Namaee et al., 2019).

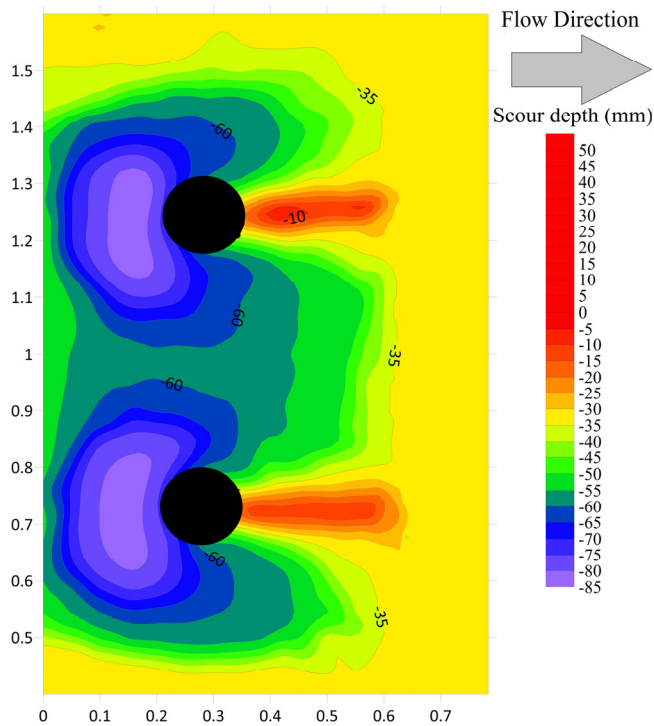


Fig. 5b. Scour pattern around the 110-mm bridge pier for $D_{50} = 0.47$ mm type under smooth for the highest flow discharge (Namaee et al., 2019).

1) The streamwise velocity distribution has a reversed C-shaped profile which begins from the scour hole up to the water surface. The same pattern was also reported by Hirshfield (2015) and Kumar and Kothiyari (2011). In terms of velocity magnitude, the streamwise velocity for rough cover is generally greater than the scour hole velocity for smooth and open channel conditions. As expected, the magnitude of velocity is smallest in the scour hole and is the highest at the water surface. Furthermore, regardless of flow cover, pier size and

sediment type, the values of the velocity component are mostly negative within the scour hole which is an indication of reversal flow happening due to the presence of horseshoe vortex which is strongest at the pier face. Moreover, for the 90-mm and 110-mm bridge piers, which were placed in the first sand box and were exposed to nearly the same flow depth and approaching flow velocity, the average value of U_x is higher for the 110-mm pier under all flow cover conditions. Similarly, for the 60 mm and 170 mm bridge piers which were placed in the second sand box and were exposed to nearly the same flow depth and approaching flow velocity, the average value of U_x is higher for the 170-mm pier under all flow cover conditions. In other words, these results indicate that the strength and intensity of the horseshoe vortex increased with pier size. Note that since the 90-mm and 110-mm bridge piers were placed in the first sand box and the 60 mm and 170 mm bridge piers were placed in the second sand box, the ADV measurements were done in both of the sandboxes.

2) Within the scour hole upstream of the pier, the most significant feature is the appearance of down-flow velocities in the vertical direction due to obstruction of the flow by the pier. It is represented by negative and values and is highly significant in terms of scour hole development. In terms of flow cover, it is obvious the value of U_z is the largest under rough ice cover. The downward velocity originates from the horizontal curvature of the streamline in front of the pier and the reduction of velocity near the bed by friction. Downward velocity intensifies the horseshoe vortex at the pier face and can effectively speed up the process of scour hole development, which in an extreme case, leads to bridge failure. Generally, considering the absolute value of U_z , the value of U_z diminishes from the channel bed toward the scour hole. From the channel bed toward the free surface, U_z values tend to move toward zero or the positive direction which implies that downflow velocity vectors are changing their direction and diminishing as they get closer to free surface which causes the velocity profile to have a parabolic shaped profile.

3) Under the same flow cover and flow condition, the larger pier yielded the larger values of the streamwise and vertical velocity values. However, these values are larger under rough ice-covered flow conditions. The larger scour hole velocity under rough ice cover justifies the findings of greater pier scour depth.

4) The vertical velocity distribution exhibits the same pattern for the three sands as seen in Fig. 8. According to the figure, the finest sediment ($D_{50} = 0.47$ mm), has a greater velocity magnitude and, consequently, a deeper scour depth. In addition, the location of maximum velocity under the finest sediment is closer to the bed which has resulted in stronger horseshoe vortices.

Table 2 represents the location of maximum velocity based on z/y_0 for different flow cover. Of note, the velocity profiles were measured before the cylinder inside the scour hole in the upstream region. According to Table 2, the location of maximum velocity under rough ice cover is closer to the bed which is in good agreement with the findings of Zabilansky et al. (2006) and Muste et al. (2000).

Fig. 9 shows scour hole velocity profiles for the lateral velocity component (U_y) distinguished by flow cover for all the pier size ($D_{50} = 0.47$ mm). As indicated by Fig. 9, there is not any meaningful pattern in the lateral velocity components due to high turbulence of flow in this direction.

Fig. 10a shows the vertical velocity component (U_z) for the 60- and 170-mm bridge piers (bridges in the second sand box) from the scour hole up to the maximum velocity point under open, smooth and rough-covered flow covers, while Fig. 10b shows U_z of the 90- and 110-mm bridge piers (bridges in the first sand box) from the scour hole up to the maximum velocity point under open, smooth and rough-covered flow covers.

Table 2. Location of maximum velocity based on (z/y_0) values according to flow cover.

Flow cover	Stage of maximum velocity (z/y_0)
Open channel	0.25
Smooth cover	0.15
Rough cover	0.10

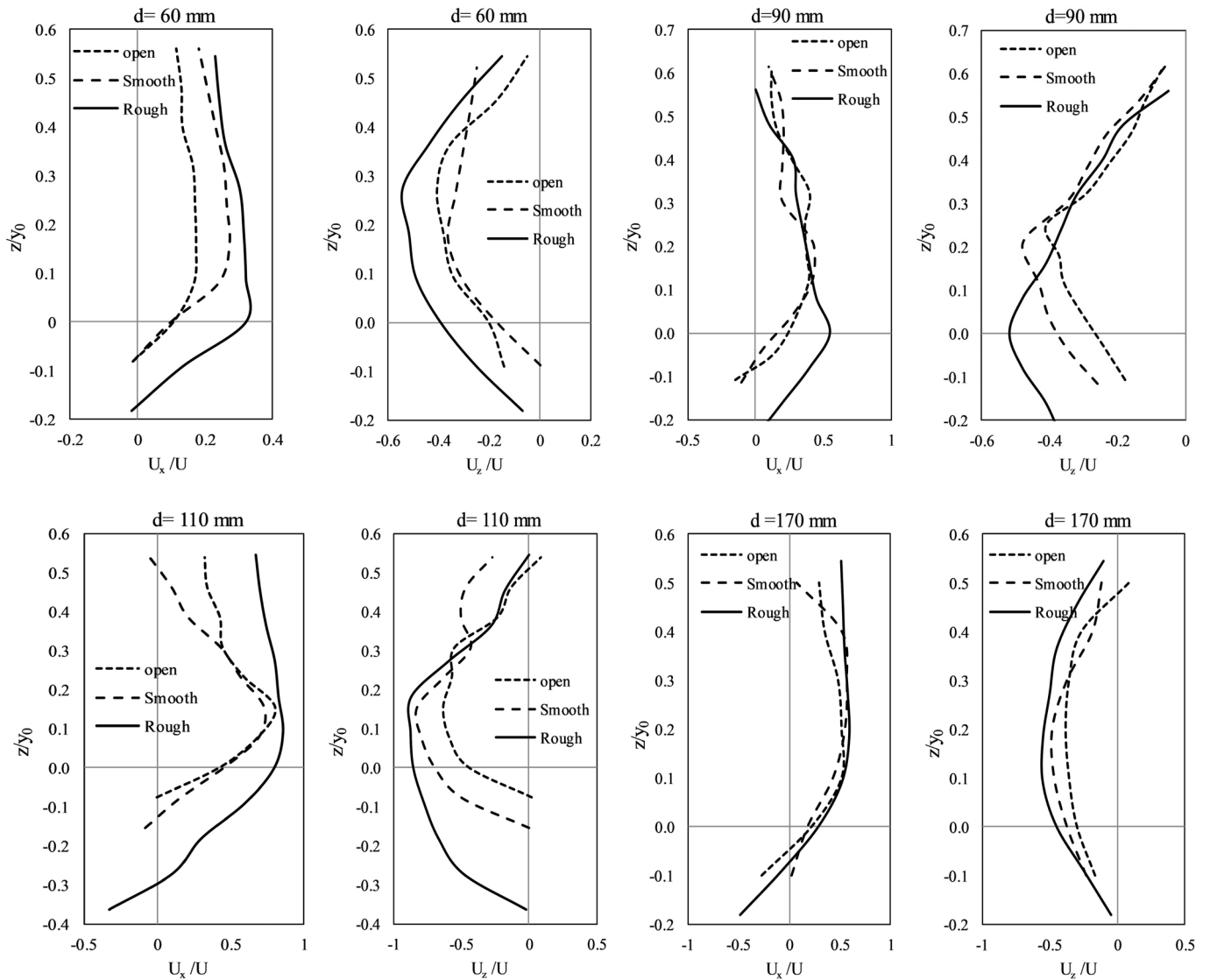


Fig. 6. Scour hole velocity profiles for the streamwise (U_x) and vertical (U_z) velocity components under open, smooth and rough ice-cover distinguished by the pier size and under $D_{50} = 0.47$ mm for the lowest discharge.

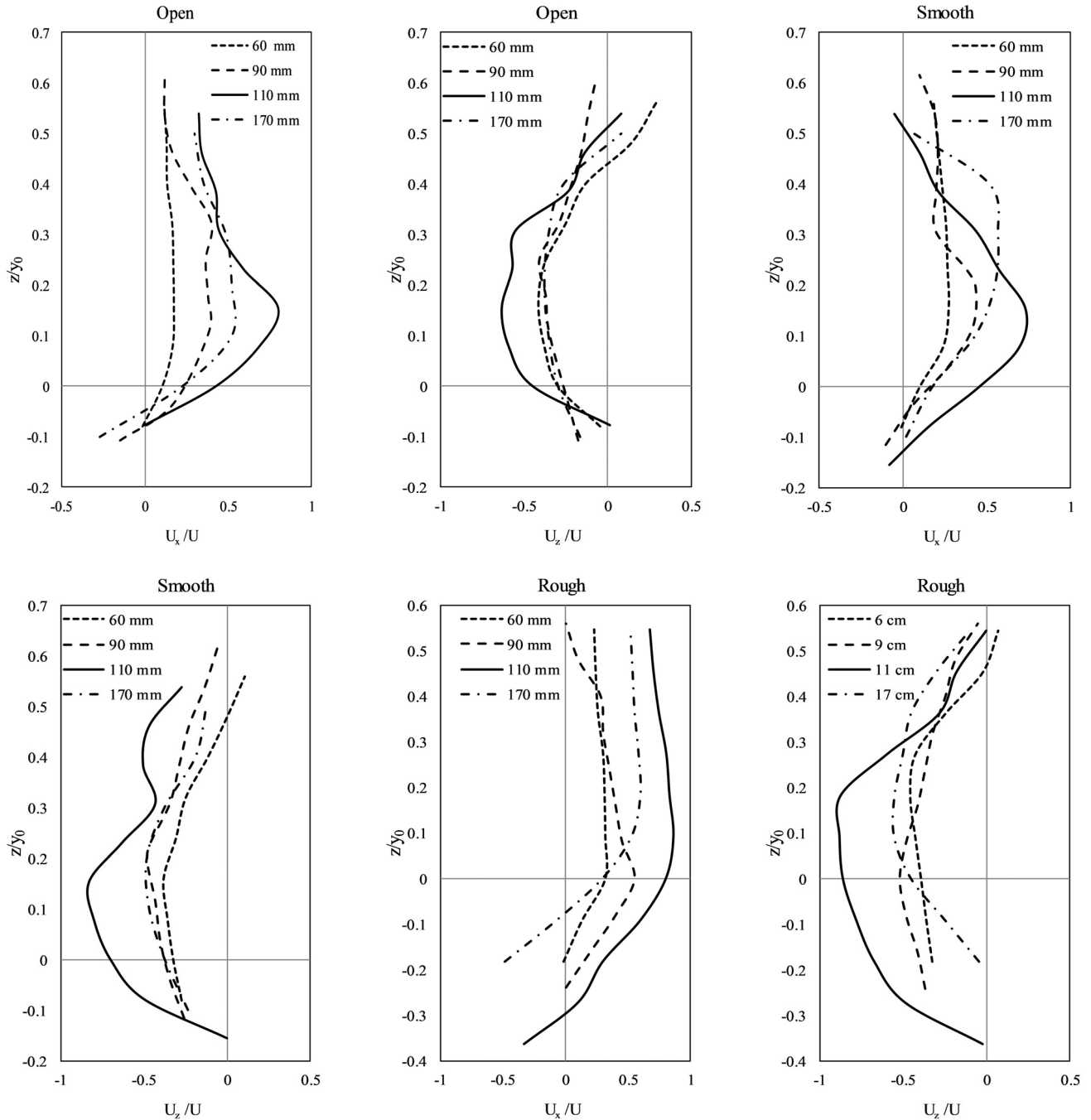


Fig. 7. Scour hole velocity profiles for the streamwise (U_x) and vertical (U_z) velocity components distinguished by flow cover for all the pier size and under $D_{50} = 0.47$ mm for the lowest discharge.

As mentioned before, the location of maximum velocity depends on the relative magnitudes of the ice and bed resistance coefficients and the rougher the ice cover, the closer the location of the maximum velocity to the channel bed. Therefore, the magnitude of vertical velocity is generally higher near the channel bed under rough flow cover compared to open channel flow cover. According to Figs. 10(a–b), location of the maximum velocity is closer to the bed under ice-covered condition which is in good agreement with previous findings. Since there was not any significant change from the maximum location of the vertical component of velocity (U_z) up to the free surface, a general linear relationship is developed for all the bridge piers under open channel and ice-covered flow conditions in Fig. 10c which reads as follows:

$$\frac{z}{y_0} = 0.5816 \left(\frac{U_z}{U} \right) + 0.5503 \quad (2)$$

Of note, due to the limitations of ADV in measuring the full vertical velocity profile, there is no data in the upper portions of the depth. Since the measurement of flow velocity is located at 10 cm beneath the measuring head of the 10 MHz ADV, the Sontek's 16 MHz micro ADV is recommended since the measuring head of the Sontek's 16 MHz micro ADV is smaller in size which also has less impact on the flow field around the scour depths. The velocity magnitude is calculated for the lowest discharge of $D_{50} = 0.47$ mm and are presented in Fig. 11.

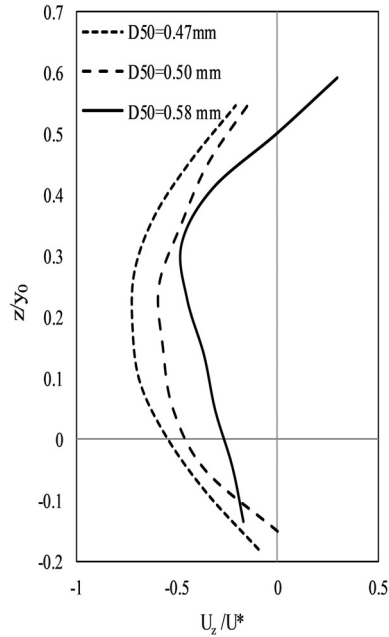


Fig. 8. The vertical velocity distribution for the lowest discharge for the 90-mm bridge pier under rough ice-covered condition for the three values of D_{50} .

The results indicate regardless of flow discharge and pier size, the velocity magnitude is highest for rough cover. For the 90-mm pier and 110-mm pier which were placed in the first sand box and were under nearly the same flow conditions, the larger pier has resulted in larger values of the velocity magnitude which implies that the strength and intensity of horseshoe vortex increases with pier size. The stronger horse vortex has also resulted in deeper scour depth for 110-mm bridge pier. The same trend can be seen for the 60-mm piers and 170-mm piers which were placed in the second sand box.

Turbulence intensities and turbulent kinetic energy (TKE)

In terms of ice-covered flow condition, the formation of a stable ice cover almost doubles the wetted perimeter compared to open channel conditions. This alters the hydraulics compared to an open channel by imposing an extra boundary to the flow, causing the velocity profile to be shifted towards the smoother boundary (channel bed) and adding to the flow resistance. Since the near-bed velocity is higher under ice-covered conditions, a higher shear stress is exerted on the riverbed (Sui et al., 2010; Wang et al., 2008). As the near bed velocity increases, the kinetic energy exerted on the bed increases correspondingly. An increase in kinetic energy affects the capacity of flow in terms of sediment transport rate. To determine turbulence intensities along with turbulent kinetic energy, the root-mean-square of the turbulent velocity fluctuations about the mean velocity are calculated. The root mean squares of the stream-wise, cross-stream, and vertical velocities for each time series were used to estimate TKE. The same unstructured turbulent intensities pattern was also observed by other studies such as Muste et al. (2000) and Robert and Tran (2012). Fig. 12 shows TKE values for all the piers for $D_{50} = 47$ mm for the lowest discharge. Note that since the profiles of turbulent intensities showed a rather similar pattern to TKE, only the result of TKE are shown. The following observations can be obtained:

- 1) Regardless of flow cover, the vertical turbulent intensity is highest just over the channel bed and diminishes towards the flow surface. According to Muste et al. (2000), observing the highest value of turbulent intensity near the bed is due to the highest rate of sediment movement near the bed. Muste et al. (2000) also concluded the turbulent intensities are relevant to sediment transport as the strength of the turbulence will affect sediment suspension.
- 2) The vertical turbulent intensity for the rough flow conditions is greater than those for open channel and smooth ice-covered flow conditions. As the turbulent intensity in the vertical direction is higher under the rough ice-covered flow

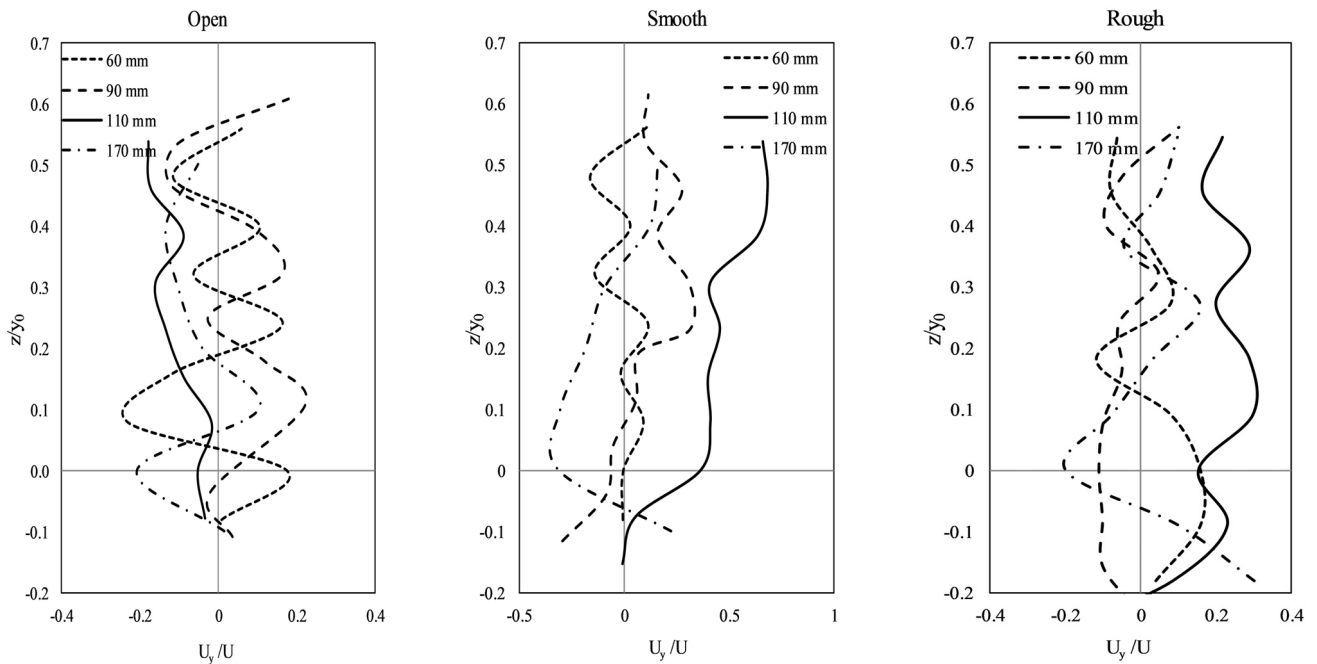


Fig. 9. Scour hole velocity profiles for the lateral (U_y) velocity component distinguished by flow cover for all the pier size and under $D_{50} = 0.47$ mm for the lowest discharge.

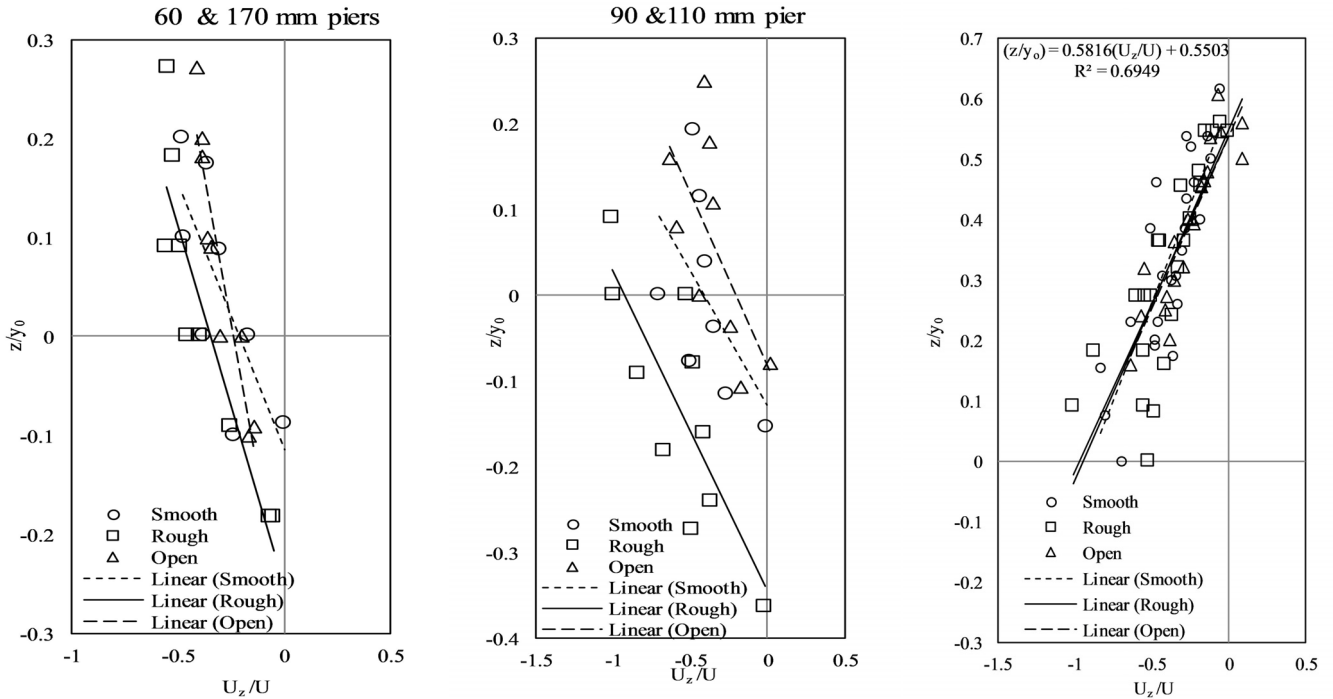


Fig. 10. a) Vertical velocity component (U_z) of the 60- and 170-mm bridge piers from the scour hole up to the maximum velocity locale under open, smooth and rough-covered flow covers; b) Vertical velocity component (U_z) of the 90- and 110-mm bridge piers from the scour hole up to the maximum velocity locale under open, smooth and rough-covered flow covers; c) Vertical velocity component (U_z) of all the bridge piers from the maximum velocity locale toward the free surface under open, smooth and rough-covered flow covers.

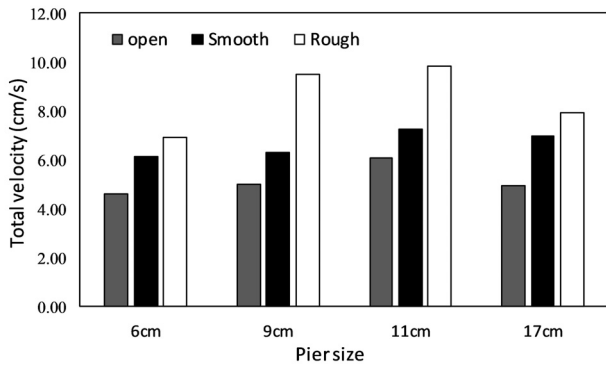


Fig. 11. Scour hole velocity profiles for velocity magnitude under open, smooth and rough ice cover for $D_{50} = 0.47$ mm for the lowest discharge.

conditions, there is more potential for sediment transport due to the higher kinetic energy than in the open channel and smooth ice-covered flow conditions.

3) Similar to the observations made for the velocity profile, for the 90 mm and 110 mm bridge piers in the first sand box, exposed to nearly the same flow depth and approaching flow velocity, the vertical turbulent intensities is higher for 110 mm than 90 mm pier under all forms of flow cover. Similar results were obtained for the 60 mm and 170 mm bridge piers in the second sand box with the 170 mm pier having higher values than the 60 mm pier under all flow cover conditions. The results show the turbulent intensity increases with pier size. The above statement can also be generalized for TKE. Therefore, it can also be concluded that, under nearly the same flow condition, the maximum value of turbulence kinetic energy occurs at a larger diameter pier.

CONCLUSIONS

In this paper, three-dimensional velocity components along with scour hole development patterns were measured around four pairs of bridge piers in channel bed with three non-uniform bed materials under open channel, smooth ice-covered, and rough ice-covered flow conditions. Following milestones of the experimental results are drawn from this study:

1) Experimental results showed that the local scour around side-by-side bridge piers was greater than that around a singular bridge pier. However, regardless of the flow condition (either open flow or ice-covered flow conditions) and the number of piers (either singular or side-by-side piers), the maximum scour depth occurred at the upstream front face of the bridge pier in which the horseshoe vortex and down-flow velocity coexist and were the strongest. On the other hand, the least amount of scour occurred behind the pier for both types of bridge arrangements regardless of flow cover. In terms of the impact of ice cover, the maximum scour depth was clearly the greatest under rough covered flow condition. Results also indicated that more sediment deposited at the downstream side of side-by-side bridge piers comparing to that of singular bridge pier.

2) The streamwise velocity component (U_x) was the lowest inside the scour hole and increased toward the free surface which gave a reversed C-shaped profile pattern. The negative values of U_x within the scour hole was an indication of reversal flow happening due to the presence of horseshoe vortex. In terms of velocity magnitude, the streamwise velocity under rough covered condition was generally greater than those under smooth covered and open channel conditions.

3) The vertical velocity distribution (U_z), which is a representative of the strength of downfall velocity, was the greatest under rough covered condition. Generally, The U_z values were negative inside the scour hole which indicated that U_z is down-

ward inside the scour hole. Under rough covered condition, the values of downward velocity component were higher which caused greater downfall velocities and ultimately greater scour depths. From the bed level before scouring process started, U_z tended to change its direction upward as it moved towards the water surface.

4) In terms of the lateral velocity component (U_y), there was not any meaningful pattern. Besides, there was no significant difference in velocity field if the channel bed material is different.

5) The experimental results showed that the locale of maximum velocity is closer to the bed under rough ice-covered flow conditions which was in a good agreement with the previous studies.

6) Regardless of flow cover, the vertical turbulent intensity was highest exactly over the channel bed and diminished towards the flow surface which implies that the shear stress is strongest on the channel bed causing sediment to be transported at a higher rate. Besides, under the same flow conditions, the value of turbulence kinetic energy increased with pier size.

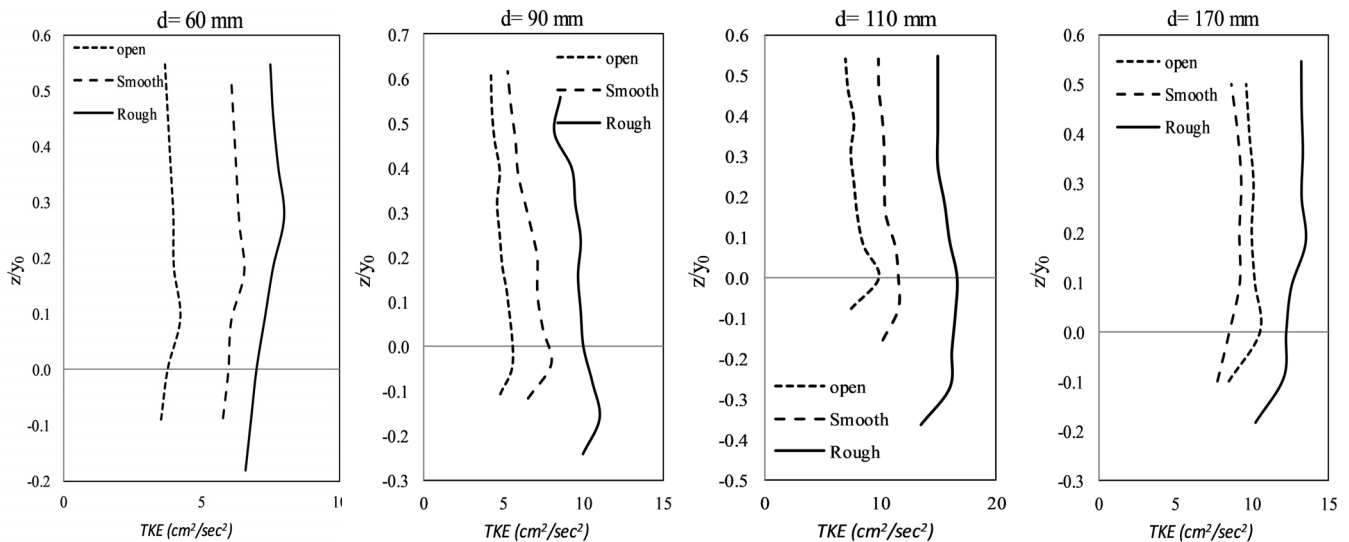


Fig. 12. Distributions of the turbulent kinetic energy at the upstream of the piers.

REFERENCES

- Ahmed, F., Rajaratnam, N., 1998. Flow around bridge piers. *Journal of Hydraulic Engineering*, 124, 3, 288–300.
- Ataie-Ashtiani, B., Aslani-Kordkandi, A., 2012. Flow field around side-by-side piers with and without a scour hole. *European Journal of Mechanics-B/Fluids*, 36, 152–166.
- Beheshti, A.A., Ataie-Ashtiani, B., 2009. Experimental study of three-dimensional flow field around a complex bridge pier. *Journal of Engineering Mechanics*, 136, 2, 143–154.
- Beltaos, S., 2007. River ice breakup processes: recent advances and future directions. *Canadian Journal of Civil Engineering*, 34, 6, 703–716.
- Dey, S., Raikar, R., 2007. Clear-water scour at piers in sand beds with an armour layer of gravels. *Journal of Hydraulic Engineering*, 133, 703–711.
- Ettema, R., Braileanu, F., Muste, M., 2000. Method for estimating sediment transport in ice-covered channels. *Journal of Cold Regions Engineering*, 14, 3, 130–144.
- Ettema, R., Melville, B.W., Constantinescu, G., 2011. Evaluation of bridge scour research: Pier scour processes and predictions. *Transportation Research Board of the National Academies*, Washington, DC.
- Fugate, D.C., Friedrichs, C.T., 2002. Determining concentration and fall velocity of estuarine particle populations using ADV, OBS and LISST. *Continental Shelf Research*, 22, 11–13, 1867–1886.
- Golden Software, 1999. *Surfer User's Guide: Contouring and 3D Surface Mapping for Scientists and Engineers*. Golden Software, Inc., 809, 14th Street, Golden, CO 80401-1866.
- Graf, W., Istiarto, W., 2002. Flow pattern in the scour hole around a cylinder. *Journal of Hydraulic Research*, 40, 1, 13–20.
- Galan, A., Simarro, G., Fael, C., Cardoso, A.H., 2019. Clear water scour at submerged pile groups. *International Journal of River Basin Management*, 17, 1, 101–108.
- Gautam, P., Eldho, T.I., Mazumder, B.S., Behera, M.R., 2019. Experimental study of flow and turbulence characteristics around simple and complex piers using PIV. *Experimental Thermal and Fluid Science*, 100, 193–206.
- Hafez, Y.I., 2016. Mathematical modeling of local scour at slender and wide bridge piers. *Journal of Fluids*, Article ID 4835253. <http://dx.doi.org/10.1155/2016/4835253>.
- Hains, D.B., Zabilansky L., 2004. Laboratory test of scour under ice: data and preliminary results. *Cold Regions Research and Engineering Laboratory, ERDC/CRREL TR-04-09*, Hanover, NH, USA.
- Hirshfield, F., 2015. The impact of ice conditions on local scour around bridge piers. PhD Thesis. University of Northern British Columbia, **Prince George**.
- Hodi, B., 2009. Effect of blockage and densimetric froude number on circular bridge pier scour. M.A.Sc. Thesis. Department of Civil and Environmental Engineering, Faculty of Engineering, University of Windsor, Windsor, Ont.
- Kumar, A., Kothiyari, U.C., 2011. Three-dimensional flow characteristics within the scour hole around circular uniform and compound piers. *Journal of Hydraulic Engineering*, 138, 5, 420–429.
- Melville, B.W., Sutherland, A.J., 1988. Design method for local scour at bridge piers. *Journal of Hydraulic Engineering*, 114, 10, 1210–1226.
- Melville, B.W., Chiew, Y.M., 1999. Time scale for local scour at bridge piers. *Journal of Hydraulic Engineering*, 125, 1, 59–65.

- Melville, B.W., Coleman, S.E., 2000. Bridge Scour. Water Resources Publication.
- Muste, M., Braileanu, F., Ettema, R., 2000. Flow and sediment transport measurements in a simulated ice-covered channel. *Water Resources Research*, 36, 9, 2711–2720.
- Namaee, M.R., Sui, J., Whitcombe, T., 2017. A revisit of different models for flow resistance in gravel-bed rivers and hydraulic flumes. *International Journal of River Basin Management*, 15, 3, 277–286.
- Namaee, M.R., Sui, J., 2019a. Impact of armour layer on the depth of scour hole around side-by-side bridge piers under ice-covered flow condition. *Journal of Hydrology and Hydropower*, 67, 3, 240–251.
- Namaee, M.R., Sui, J., 2019b. Local scour around two side-by-side cylindrical bridge piers under ice-covered conditions. *International Journal of Sediment Research*, 34, 4, 355–367.
- Namaee, M.R., Sui, J., Wu, P., 2019. Experimental Study of Local Scour around Side-by-Side Bridge Piers under Ice-Covered Flow Conditions. In: *Fluvial Processes and Forms-Dynamics, Delineation and Conservation*. IntechOpen. <http://dx.doi.org/10.5772/intechopen.86369>.
- Mohammed, T.A., Noor, M.J.M.M., Ghazali, A.H., Yusuf, B., Saed, K., 2007. Physical modeling of local scouring around bridge piers in erodible bed. *Journal of King Saud University-Engineering Sciences*, 19, 2, 195–206.
- Qadar, A., 1981. The vortex scour mechanism at bridge piers. Part 2. *Proceedings of the Institution of Civil Engineers*, 71, 3, 739–757.
- Rickenmann, D., Recking, A., 2011. Evaluation of flow resistance in gravel bed rivers through a large field data set. *Water Resources Research*, 47, 7, Article Number W07538.
- Robert, A. Tran, T., 2012. Mean and turbulent flow fields in a simulated ice-covered channel with a gravel bed: some laboratory observations. *Earth Surface Processes and Landforms*, 37, 951–956.
- Sontek, A.D.V., 1997. Operation manual, firmware version 4.0. Sontek, San Diego.
- Sontek, 2001. ADV operation manual. 1st Ed. Sontek Inc., San Diego.
- Sheppard, D.M., Melville, B., Demir, H., 2013. Evaluation of existing equations for local scour at bridge piers. *Journal of Hydraulic Engineering*, 140, 1, 14–23.
- Sutherland, A.J., 1986. Reports on bridge failure. RRU Occasional Paper. National Roads Board, Wellington, New Zealand.
- Sui, J., Wang, J., He, Y., Krol, F., 2010. Velocity profiles and incipient motion of frazil particles under ice cover. *International Journal of Sediment Research*, 25, 1, 39–51.
- Unger, J., Hager, W.H., 2007. Down-flow and horseshoe vortex characteristics of sediment embedded bridge piers. *Experiments in Fluids*, 42, 1, 1–19.
- Vijayasree, B.A., Eldho, T.I., Mazumder, B.S., Ahmad, N., 2019. Influence of bridge pier shape on flow field and scour geometry. *International Journal of River Basin Management*, 17, 1, 109–129.
- Wardhana, K., Hadipriono, F.C., 2003. Analysis of recent bridge failures in the United States. *Journal of Performance of Constructed Facilities*, 17, 3, 144–150.
- Wang, J., Sui, J., Karney, B., 2008. Incipient motion of non-cohesive sediment under ice cover – an experimental study. *Journal of Hydrodynamics*, 20, 1, 117–124.
- Williams, P., Bolisetti, T., Balachandar, R., 2017. Evaluation of governing parameters on pier scour geometry. *Canadian Journal of Civil Engineering*, NRC Research Press, 44, 1, 48–58. DOI: 10.1139/cjce-2016-0133.
- Williams, P., Balachandar, R., Bolisetti, T., 2018. Blockage corrections for pier scour experiments. *Canadian Journal of Civil Engineering*. <http://doi.org/10.1139/cjce-2017-0563>.
- Wu, P., Hirshfield, F., Sui, J., 2014. Further studies of incipient motion and shear stress on local scour around bridge abutments under ice cover. *Canadian Journal of Civil Engineering*, 41, 892–899.
- Wu, P., Balachandar, R., Sui, J., 2015a. Local scour around bridge piers under ice-covered conditions. *J. of Hydraulic Engineering*, 142, 1, Art. No. 04015038, 10.1061/(ASCE)HY.1943-7900.0001063.
- Wu, P., Hirshfield, F., Sui, J., 2015b. Armour layer analysis of local scour around bridge abutment under ice covered condition. *River Research and Applications*, 31, 6, 736–746. DOI: 10.1002/rra.2771.
- Wu, P., Hirshfield, F., Sui, J., 2015c. Local scour around bridge abutments under ice covered condition- an experimental study. *International Journal of Sediment Research*, 30, 39–47.
- Wu, P., Balachandar, R., 2016. Local scour around bridge abutments including effects of relative bed coarseness and blockage ratio. *Canadian Journal of Civil Engineering*, 43, 1, 51–59.
- Zabilansky, L.J., Hains, D.B., Remus, J.I., 2006. Increased bed erosion due to ice. In: *13th International Conference on Cold Regions Engineering*, pp. 1–12. DOI: 10.1061/40836(210)16
- Zhao, M., Cheng, L., Zang, Z.P., 2010. Experimental and numerical investigation of local scour around a submerged vertical circular cylinder in steady currents. *Coastal Engineering*, 57, 8, 709–721.

NOMENCLATURE

- d : Pier diameter (mm)
 D_{50} : 50th percentile particle diameter (mm)
 G : Bridge spacing (m)
 Fr : Upstream Froude number
 Q : Volumetric flow discharge (m³/s)
 R : Hydraulic radius (m)
 Re_b : Pier Reynold number
 S : Longitudinal slope of the channel
 TKE : Turbulent kinetic energy (J/kg)
 U_z : Vertical velocity component (m/s)
 U_x : Streamwise velocity component (m/s)
 U_y : Span-wise velocity component (m/s)
 U : Average approach velocity (m/s)
 U^* : Shear velocity (m/s)
 U_R : Velocity magnitude (m/s)
 X : Longitudinal distance in the channel (m)
 y_0 : Approach flow depth (mm)
 y_{max} : Maximum scour depth (mm)
 z : Vertical distance from bed (m)
 θ : Flow temperature (°C)
 ν : Kinematic viscosity (m²/s)

Received 15 July 2019
 Accepted 17 December 2019

Concentration distribution and deposition limit of medium-coarse sand-water slurry in inclined pipe

Pavel Vlasák*, Václav Matoušek, Zdeněk Chára, Jan Krupička, Jiří Konfršt, Mikoláš Kesely

Institute of Hydrodynamics of the Czech Academy of Sciences, v. v. i., Pod Patankou 30/5, 160 00, Prague 6, Czech Republic.

*Corresponding author. Tel.: +420 233109092. E-mail: vlasak@ih.cas.cz

Abstract: Sand-water slurry was investigated on an experimental pipe loop of inner diameter $D = 100$ mm with the horizontal, inclined, and vertical smooth pipe sections. A narrow particle size distribution silica sand of mean diameter 0.87 mm was used. The experimental investigation focused on the effects of pipe inclination, overall slurry concentration, and mean velocity on concentration distribution and deposition limit velocity. The measured concentration profiles showed different degrees of stratification for the positive and negative pipe inclinations. The degree of stratification depended on the pipe inclination and on overall slurry concentration and velocity. The ascending flow was less stratified than the corresponding descending flow, the difference increasing from horizontal flow up to an inclination angle of about $+30^\circ$. The deposition limit velocity was sensitive to the pipe inclination, reaching higher values in the ascending than in the horizontal pipe. The maximum deposition limit value was reached for an inclination angle of about $+25^\circ$, and the limit remained practically constant in value, about 1.25 times higher than that in the horizontal pipe. Conversely, in the descending pipe, the deposition limit decreased significantly with the negative slopes and tended to be zero for an inclination angle of about -30° , where no stationary bed was observed.

Keywords: Sand-water slurry; Pipe inclination; Concentration distribution; Deposition limit; Gamma-ray radiometry.

INTRODUCTION

Hydraulic transport is well-known as a technically feasible and economically attractive method of transporting large volume commodities; it is commonly used in the dredging, building, energy and mining industries, and tailings disposal operations, and in different industrial applications for the transport of bulk materials. Transport pipelines often contain inclined sections, as they have to overcome different terrain irregularities. Despite the fact that published pipeline design guidelines recommend maximum upward inclinations of 25° , it is not always possible for designers to follow these guidelines (Spelay et al., 2016).

Lack of information concerning slurry flow in inclined pipe sections has caused engineers to design them with extreme caution and practice transportation with uncertainty. Extra safety factors have been thrown into the system design to avoid possible problems during operation, start-up, and shutdown. This is reflected by efforts to use gentle slopes in the pipeline designs. This will mean greater construction costs and capital expanses for freight pipeline systems over relatively rugged terrain in mountainous or urbanized and industrial areas (Kao and Hwang, 1979).

For settling slurry, pipe inclination considerably affects behavior, flow structure, and energy consumption. Settling slurries tend to stratify; the degree of stratification is sensitive to the pipe inclination and affects the pressure drops and deposition limit velocity. The deposition limit velocity is the minimum operational velocity at which the pipe should safely operate without danger of blockage. It is defined as the flow velocity at which the conveyed particles fall out of the mixture and stop moving and at which a stationary deposit, called the bed, starts to form at a pipe invert. The deposition limit velocity is affected by the solid concentration, mean flow velocity, and the physical properties of the solids, liquids, and pipe (Parzonka et al., 1981; Sobota and Plewa, 2000; Wilson et al., 2006).

Compared to the horizontal flow, the inclined flow produces an additional force (a component of the submerged weight of grains) that acts either against the direction of the flow (an ascending pipe) or in the same direction (a descending pipe) (Matousek et al., 2018b).

Flow of heterogeneous slurry in inclined pipelines should receive broader attention and stimulate interest in research to obtain design criteria for the transportation of solid particles and accuracy of energy loss correlation equations. Considerable work has been done on test systems composed of horizontal pipes, as well as on vertical pipes for hydraulic hoisting of solids. However, comparatively little work has been conducted on slurry systems involving sloping pipes. The effect of pipe inclination on flow conditions of settling slurries has not received adequate attention up to now (Kao and Hwang, 1979).

Slurry flow behavior, concentration distribution, slip velocity, and pressure drops in ascending and descending pipe sections are distinctly different. Because of the changing solid concentration and the solid and liquid phases' velocity distributions and due to the effect of gravitational force acting on the solid particles, the critical operational conditions in inclined pipes are different from that observed in horizontal pipes.

The pipe inclination induces change in the internal slurry structure, primarily the variation in the solid's distribution in a pipe cross section, and effects the Coulombic (sliding bed) friction and, consequently, the frictional pressure drops, the behavior of the pipeline during unsteady flows (shutdown or start-up), the deposition limit velocities, and the degrees of stratification (Doron et al., 1997; Matousek et al., 2018a; Spelay et al., 2016; Wilson et al., 2006). The internal structure of an ascending slurry flow differs from that of a descending one, the difference being greater for coarse particles than for fine particles because of the greater submerged weight of the bed at the bottom of the pipe (Matousek, 1996).

The effect of inclination on frictional pressure drops can be explained using the layered models. Layered models are based

on principles formulated originally by Wilson (1976) and are expressed as force balances applied to layers of stratified flow. The layered models exist in different versions for fully or partially stratified flows and some have been adapted to inclined flows (Doron, et al. 1997; Matousek, 1996; Matousek et al., 2018a; Messa et al., 2018; Shook and Roco, 1991; Wilson et al., 2006). Wilson used his early version of the two-layer model for horizontal fully stratified flow to calculate the deposition velocity from the force balance on the bed at the slip point (i.e. at the condition where the bed stops sliding). Later, Wilson and Tse (1984) applied the Durand parameter

$$F = V_D / [2g D (\rho_s - \rho_w) / \rho_w]^{1/2} \quad (1)$$

to express the effect of pipe inclination α on deposition limit V_D as

$$\Delta F = F_\alpha - F_0, \quad (2)$$

where F_α and F_0 is Durand parameter for the inclined and horizontal pipe section, respectively. In the Durand parameter, V_D is the deposition limit velocity; g is the gravitational acceleration; ρ_s and ρ_w is the density of solids and carrying liquid, respectively; and D is the pipe diameter. Durand presented an empirical nomogram of dependence of parameter F on slurry concentration C_v and medium grain size d_{50} (Durand and Condolios, 1952).

To obtain experimental data suitable for verification of a newly introduced computational model of partially stratified slurry flow with an interfacial shear layer in inclined pipes (Matousek et al., 2018a) the sand-water slurry was investigated in a test loop of internal diameter $D = 100$ mm with inclinable measuring sections.

In the paper, we discuss results of experimental investigation of the effect of pipe inclination on the solid particles' distribution at slurry velocities close to the deposition limit velocity V_D . The bed slides along the pipe wall at velocities above the deposition limit and forms a stationary deposit below the deposition limit velocity. The bed is an important contributor to the frictional pressure drops in settling slurry flow. Matousek and Zrostlik (2018) dealt with the effect of the longitudinal component of the solids' weights in the bed layer and distinguished between contributions of contact solids, suspended solids, and those carrying liquid to the pressure drops in a partially stratified flow. Friction losses of the settling slurries' flows are strongly dependent on the concentration distribution; unfortunately, experimental data containing measured solid distributions, especially in vertical and inclined pipes, are extremely scarce in the literature (Matousek et al., 2019a; Vlasak et al., 2017, 2019a).

EXPERIMENTAL EQUIPMENT AND MATERIAL

The experimental investigation was carried out on an experimental pipe loop of inner diameter $D = 100$ mm with the horizontal (A), inclinable (B), and short vertical (C) pipe sections in the Institute of Hydrodynamics of the CAS in Prague (Vlasak et al., 2017, 2019a). The loop was made from smooth, stainless steel pipes; its total length was 93 m, see Fig. 1. The investigation was focused on the effect of the pipe inclination, overall concentration, and average slurry velocity on the local concentration distribution and deposition limit velocity. Slurry flow was measured simultaneously in the ascending and descending branches of the inclinable U-tube at slopes α , varying from -45° to $+45^\circ$. Measured slurry was prepared in a mixing tank (1) and pumped by a centrifugal slurry pump GIW LCC-M 80-

300 (2) with a variable speed drive Siemens 1LG4283-2AB60-Z A11 (3).

The inclinable U-tube in a vertical position was used to determine the volumetric transport concentration C_d , using a method proposed by Clift and Clift (1981). Local in situ concentration distribution was studied with the application of gamma-ray densitometers controlled by a computer. The slurry flow behavior and deposition limit velocity V_D were investigated in transparent viewing pipe sections (7).

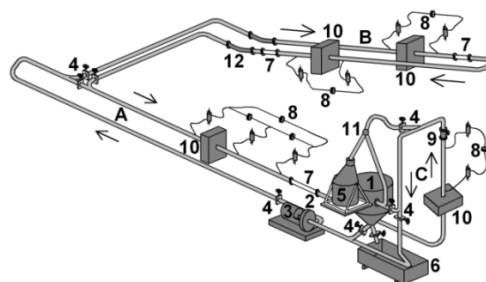


Fig. 1. Experimental test loop $D = 100$ mm (Institute of Hydrodynamics CAS, Prague).

The pressure drops were measured by Rosemount 1151DP differential pressure transducers (8), and slurry velocities were measured by a Krohne OPTIFLUX 5000 magnetic flow meter (9) mounted in the short vertical section (C). The flow divider (11) and the sampling tank (5) allow for measuring of the flow rate and delivered concentration. For easier operation, the loop is also equipped with slide valves (4) and a slurry output tank (6). Measurements were taken simultaneously in the ascending and descending branches of the loop from maximum values, $V_{max} \approx 3.0$ m/s, to values $V_{min} \approx 1$ m/s.

Based on the law of the gamma radiation absorption, a time-averaged slurry density was determined along a set of horizontal chords, and a density (or concentration) profile along the vertical axis of the pipe was determined. This method was introduced by Michalik (1973) and Przewlocki et al. (1979). The loop was equipped with two gamma-ray density meters (10) placed on a special support and controlled by a computer. The support served as the vertical linear positioning of both the source and the detector to measure the chord-averaged vertical concentration profiles. They consisted of a γ -ray source caesium ^{137}Cs (activity 740 MBq) and of a detector – a scintillating crystal of NaI(Tl). A multi-channel digital analyzer enabled the evaluation of the energy spectrum of the detected signal. The measuring time period of 16 seconds was used to sense the local concentration at each position (Krupicka and Matousek, 2014; Vlasak et al., 2014).

The studied slurry consisted of narrow-graded silica sand SP0612 (mean particle diameter $d_{50} = 0.87$ mm, density $\rho_s = 2620$ kg/m³) and water. Values of the Archimedes number

$$Ar = 4g\rho_w \cdot (\rho_s - \rho_w) \cdot d_{50}^3 / (3\mu_w^2) \quad (3)$$

were determined from 13,000 to 18,000, and the turbulent suspension efficiency parameter

$$\text{TSP} = (w / u_{*w,D}) \cdot \exp(d_{50}/D) \quad (4)$$

varied between 1.15 and 1.45, thus completing an area of upward slope data covered by Spelay et al. (2016). Here, μ_w is the dynamic viscosity of the carrier liquid, w is particle terminal settling velocity, and $u_{*w,D}$ is the friction velocity of the carrier

liquid at the deposition limit velocity V_D . The experiments were carried out for three overall volumetric concentrations C_v (11%, 25%, and 35%).

CONCENTRATION DISTRIBUTION

The effect of the mean concentration, slurry velocity, and angle of pipe inclination on the local concentration distribution c_v was studied. The measured chord-averaged concentration profiles for the different overall volumetric concentrations C_v revealed the stratified flow pattern of the measured slurry in horizontal and inclined pipe sections. The solids' distribution varied considerably with the pipe inclination. The shapes of the chord-averaged concentration profiles $c_v = c_v(y)$ indicated the stratified flow with different degrees of stratification for the positive and negative pipe inclinations. The differences between ascending and descending flows are illustrated in Fig. 2 for the constant positive and negative inclination angles α for overall concentrations $C_v = 0.25$ and different flow velocities V close to V_D .

The local concentration in the ascending pipe section was always higher than that in the descending pipe section due to the effect of the axial component of the gravity force. It is also valid for vertical upward and downward flow, where the difference between the concentration values corresponds to the particle slip velocity. For the vertical pipe, a nearly constant concentration distribution was observed (see Fig. 3).

In very steep flows ($\alpha \approx \pm 45^\circ$, see Fig. 2, bottom right panel), no bed was present in both the ascending and descending pipe sections. For the less inclined pipe sections and slurry velocities close to the deposition limit, the measured slurry flow was fully stratified at negative slopes $\alpha = -35^\circ$ and -25° and became less stratified for the pipe inclination ranging from $\alpha = -15^\circ$ to $+35^\circ$ (Vlasak et al., 2019b).

For a low pipe inclination $\alpha = \pm 15^\circ$ and a velocity close to the deposition limit $V \approx V_D$, a bed layer was observed in both the ascending and descending pipe sections. The local

concentration c_v and the deposit height h in a bed layer of the descending flow reached lower values than those in the ascending pipe ($c_v \approx 0.50$ instead 0.60, see top left panel). The local concentration c_v in a bed layer slightly decreased with increasing pipe inclination. In the direction to the pipe top, the local concentration in the central portion of the pipe gradually decreased. For velocity $V > V_D$, a sliding bed was observed in both the ascending and descending pipe sections. No deposit was observed for inclination angles $\alpha > +25^\circ$ in the ascending pipe. It was confirmed that the effect of pipe inclination on concentration distribution for low values of the inclination angle α was not significant, as it is similarly valid for pressure drops (Spelay et al., 2016; Vlasak et al., 2014, 2016, 2017).

The effect of the pipe inclination was verified for two other concentrations, $C_v = 0.11$ and 0.35 (see Fig. 4 and Fig. 5) for slurry velocity V below and above the deposition limit V_D , respectively. A similar effect of the pipe inclination was found as for the slurry concentration $C_v = 0.25$. The measured profiles document an increase of slurry stratification with a decreasing slurry concentration C_v and pipe slope α .

The shape of the concentration profiles was highly dependent on the slurry velocity; for gentle pipe slope ($\alpha = \pm 15^\circ$) and the slurry velocity $V > V_D$, a bed layer with a local concentration around $c_v \approx 0.55$ was observed for higher values of overall concentrations $C_v = 0.35$ and only $c_v \approx 0.40$ – 0.50 for lower concentrations $C_v = 0.11$. The local concentration in the bed layer decreased for both ascending and descending branches for velocity values $V < V_D$. For the ascending branch, the slurry stratification was smaller than that for the descending branch, and this trend decreases with the increasing slurry concentration. For higher pipe slopes ($\alpha > \pm 35^\circ$), the bed layer originated in the descending branch only.

For slurry concentration $C_v = 0.11$ and the descending pipe section at flow velocities under the deposition limit V_D , the difference between the shape of the concentration profiles was relatively small; stratification increased with increasing negative

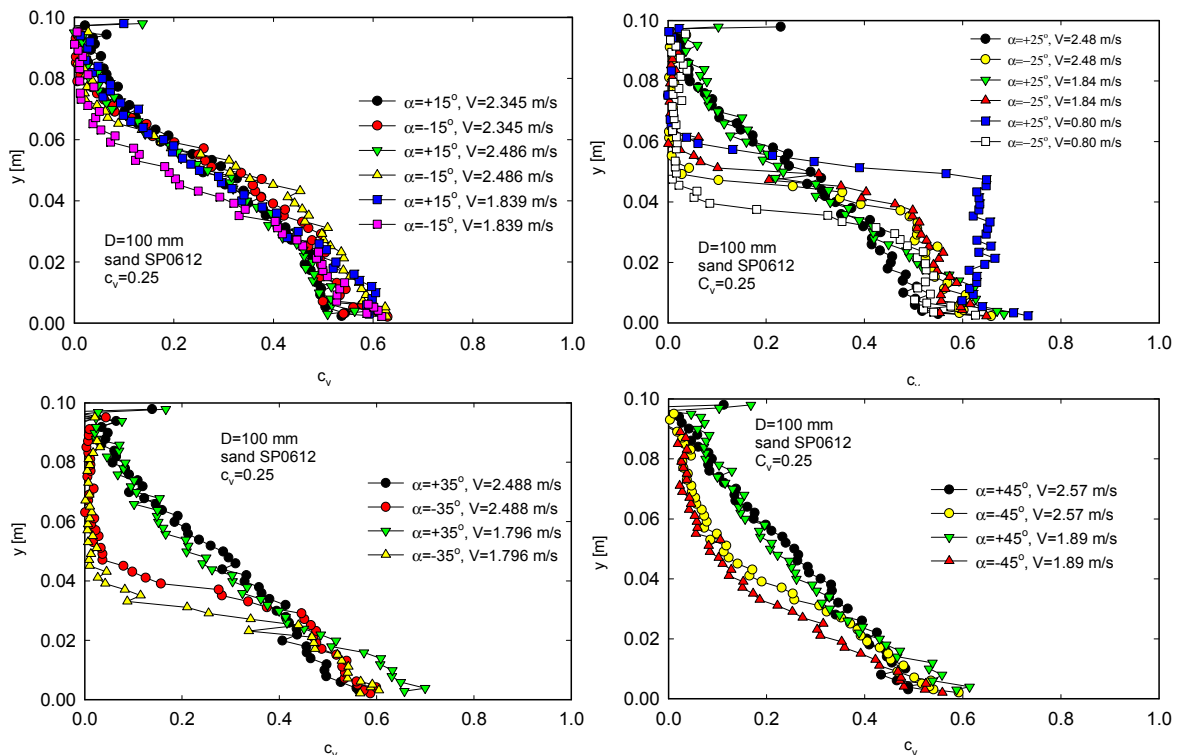


Fig. 2. Effect of the pipe inclination α and slurry velocity V on local concentration profiles, $C_v = 0.25$.

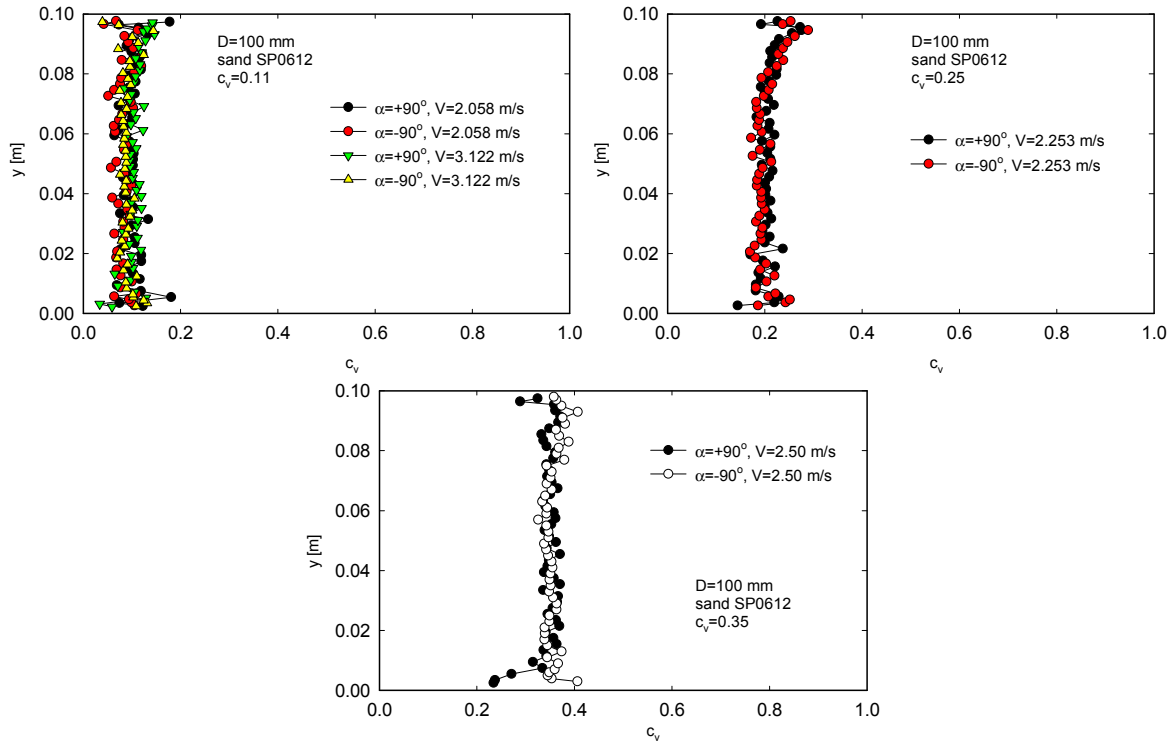


Fig. 3. Local concentration profiles in vertical pipe section.

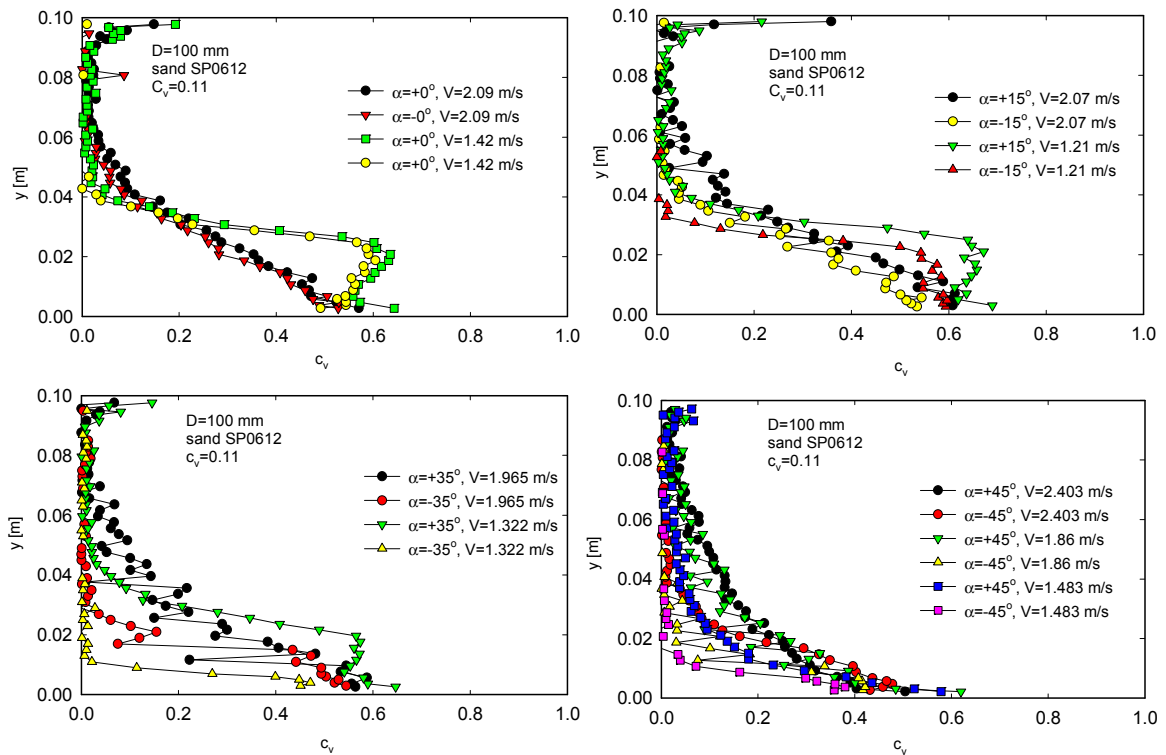


Fig. 4. Effect of mean slurry velocity V on local concentration profiles for given inclination α and $C_v = 0.11$.

inclination. For the descending pipe, the solid particles concentrated in the layer near the pipe bottom and moved more quickly due to the joint effects of the carrier liquid flow and an axial component of the gravitational force. For the slope $\alpha \geq -35^\circ$, the concentration profiles were probably already influenced by the sedimentation of sand particles in the horizontal and ascending pipe sections, and due to the reduction of the transport concentration, no stationary bed was observed (Vlasak et al., 2019c).

In Figs. 6–8, the chord-averaged concentration profiles, $c_v(y)$, are illustrated for different pipe inclinations α and slurry velocities V close to deposition limit V_D . The concentration profiles showed different degrees of stratification for the positive and negative pipe inclination (Krupicka and Matousek, 2014; Vlasak et al., 2016, 2017, 2018a). The degree of stratification varied with the pipe inclination, decreasing with increasing pipe inclination and slurry velocity for both the ascending and descending pipe sections. For the less inclined flow and

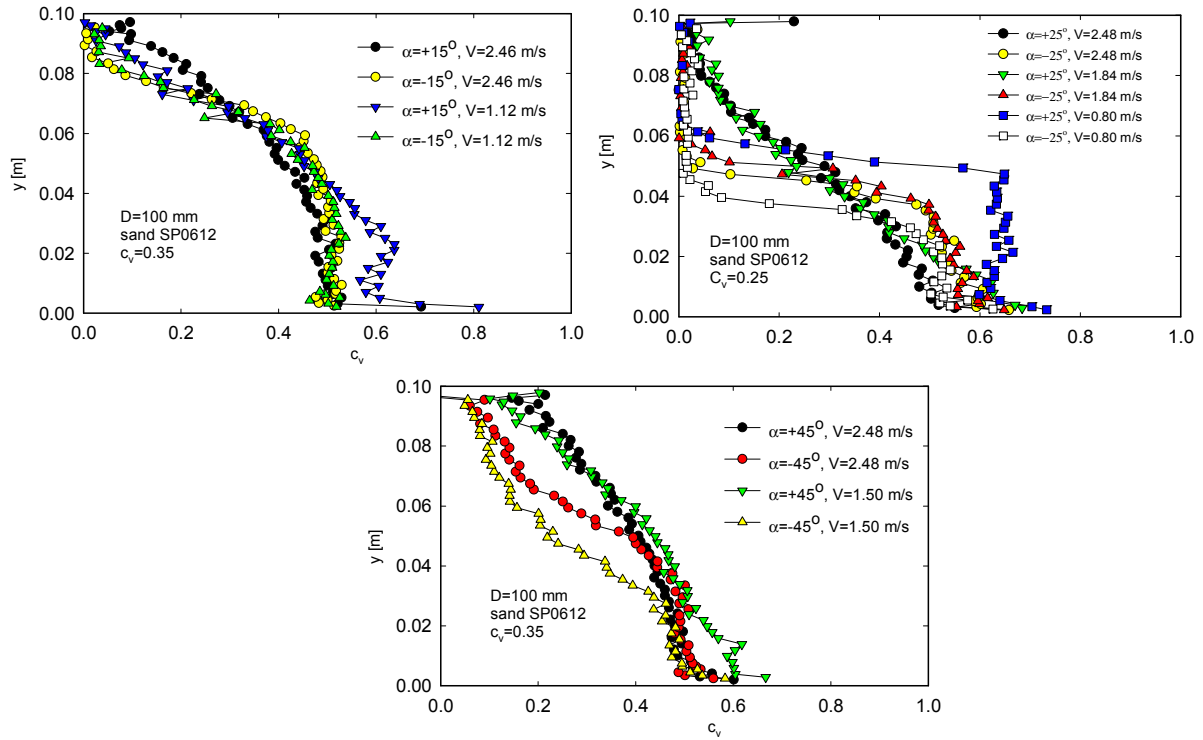


Fig. 5. Effect of mean slurry velocity V on local concentration profiles for given inclination α and $C_v = 0.35$.

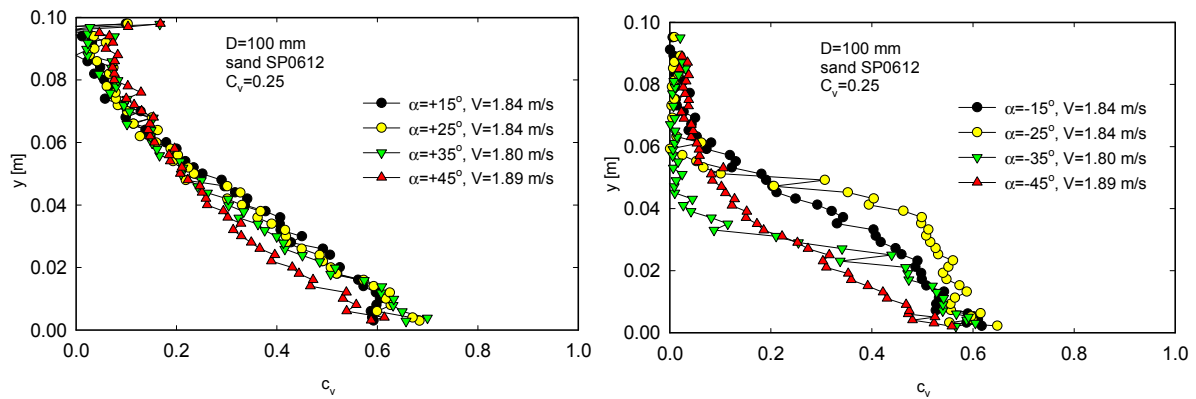


Fig. 6. Effect of the pipe inclination α on local concentration profiles for given V , $C_v = 0.25$.

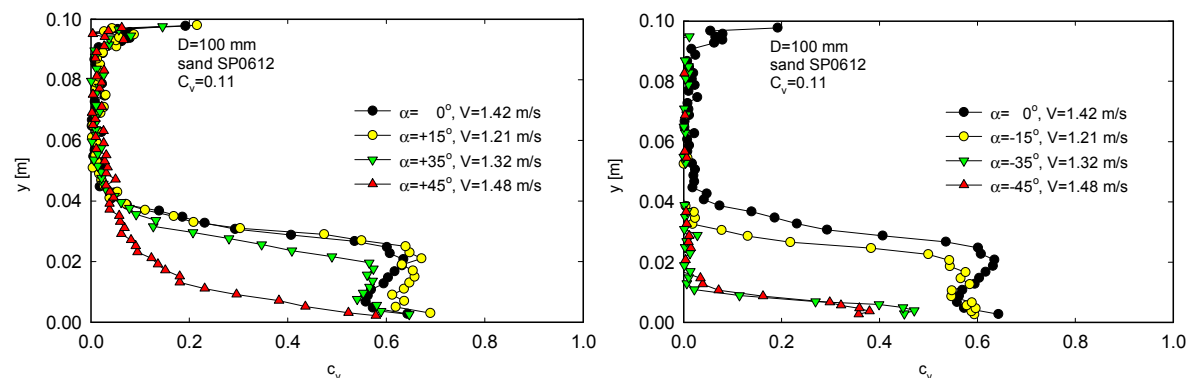


Fig. 7. Effect of the pipe inclination α on local concentration profiles for given V , $C_v = 0.11$.

slurry velocity close to the deposition limit, the slurry was fully stratified at negative slopes $\alpha = -35^\circ$ and -25° and became less stratified for the pipe inclination ranging from $\alpha = -15^\circ$ to $+45^\circ$. For slurry velocity $V > V_D$, the thickness of the bed layer decreased with increasing slurry velocity V .

For the steeper negative slopes, the flow did not exhibit any bed, and slurry stratification was strongly decreased due to the

increasing axial component of the gravity force acting on the sand particles. For pipe inclination $\alpha \approx \pm 45^\circ$, no bed was observed in both the ascending and descending pipe sections. The local concentration c_v in the upper part of the pipe increased, this effect is more pronounced in the ascending than in the descending flow.

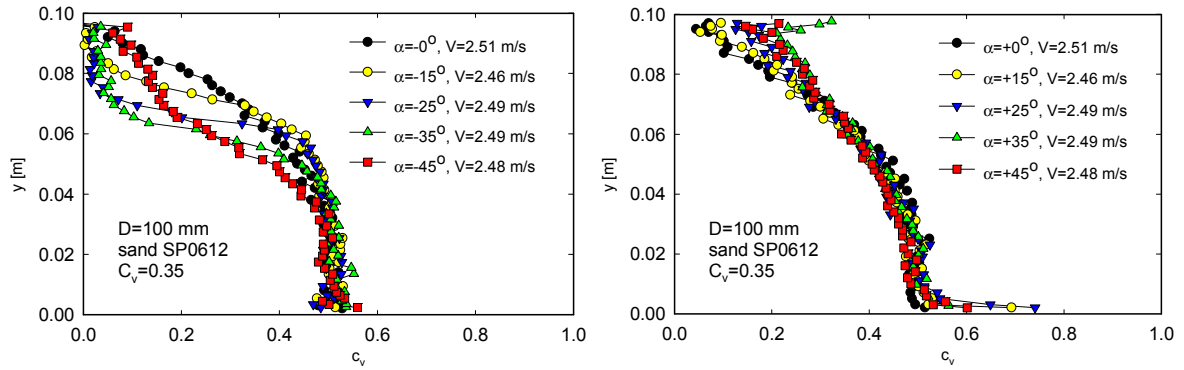


Fig. 8. Effect of the pipe inclination α on local concentration profiles, $C_v = 0.35$.

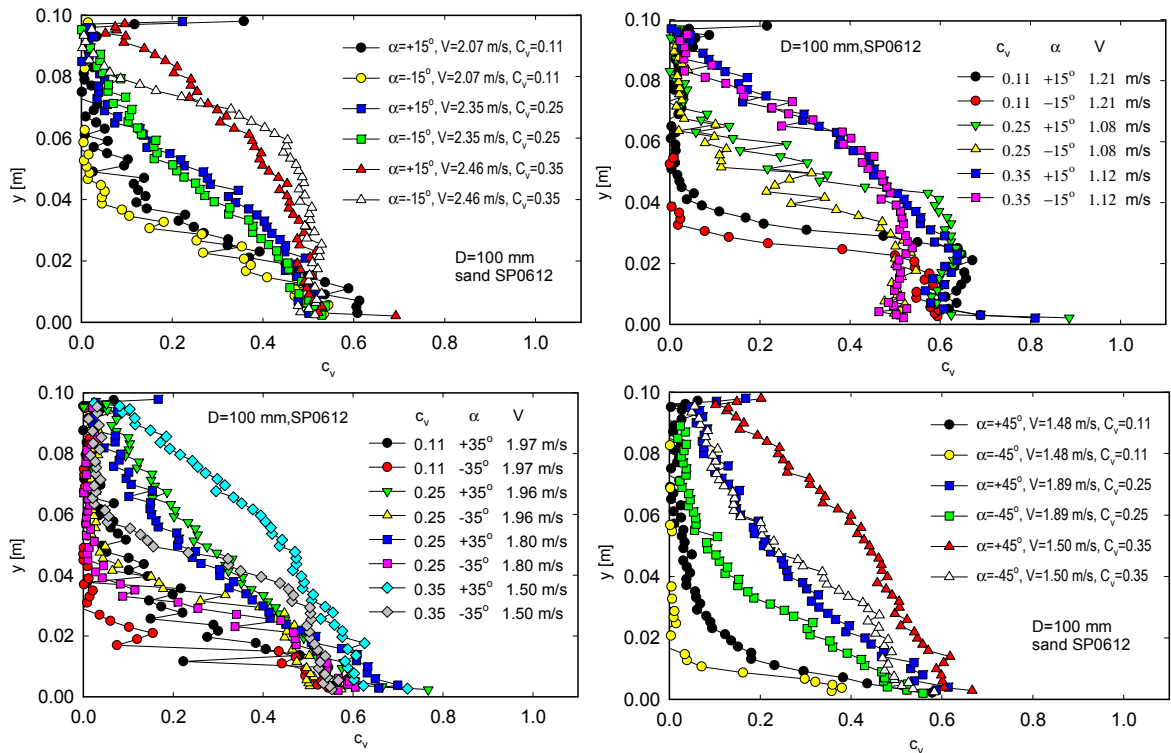


Fig. 9. Effect of the mean slurry volumetric concentration C_v on local concentration profiles.

Near and above the deposition limit, the ascending flow was less stratified than the corresponding descending flow. For velocities below the deposition limit, the stationary bed was observed in the ascending pipe for an inclination angle $\alpha < 30^\circ$. For descending flow, the thickness of the bed layer was significantly less, and the bed disappeared for pipe slope $\alpha < -15^\circ$ (Vlasak et al., 2018a). Analogous behavior was observed for lower and higher transport concentrations, $C_v = 0.11$ and 0.35 (see Figs. 7 and 8).

The effect of the mean slurry concentration C_v on the chord-averaged concentration profiles is illustrated in Fig. 9 for different pipe inclinations α and slurry flow velocities V above and below deposition limit V_D . The velocity profiles document a decrease of the degree of stratification with increasing slurry concentration C_v and pipe slope α .

The shape of the concentration profiles was highly dependent on the slurry velocity; for a gentle pipe slope ($\alpha = \pm 15^\circ$) and the slurry velocity $V > V_D$, a bed layer was observed with local concentration around $c_v \approx 0.55$ for mean slurry concentrations $C_v = 0.35$, and $c_v \approx 0.40-0.50$ for lower mean concentrations. For velocities below the deposition limit V_D , the local concentration in the bed layer decreases for both branches.

For higher pipe slopes ($\alpha > \pm 35^\circ$), a bed layer originated in the descending branch. For the ascending branch, slurry stratification was smaller than for the descending branch, and it decreased with increasing slurry concentration (Vlasak et al., 2019c).

For slurry velocity V above the deposition limit V_D , the ascending flow was less stratified than the corresponding descending flow. This fact is in contradiction with the assumption of the Worster-Denny (1955) formula, which from this reason overestimates the frictional pressure gradient in an ascending pipe section (Vlasak et al., 2019b).

In comparison, this sand slurry with fine-material slurry (glass ballot B134, $d_{50} = 0.180$ mm – Vlasak et al., 2018b, 2019a) stratification was more pronounced. For velocities close to V_D , stratification was significant for the low values of pipe inclination ($\alpha < 25^\circ$). For higher inclination and ascending flow, the shape of the concentration profile was less stratified with an increasing pipe slope, while for descending flow the conveyed solids were concentrated in the lower part of the pipe even for high pipe inclinations ($\alpha = -35^\circ$). At low concentration values, stratification was more pronounced for both upward and downward flows.

DEPOSITION LIMIT VELOCITY

The conducted experiments confirmed that the solids distribution in stratified slurry flow considerably varies with the pipe inclination, flow velocity, and slurry concentration. Determination of the deposition limit velocity V_D in stratified and partially stratified slurry flow is rather difficult and complicated work because of a usually unstable flow pattern near the deposition limit. The most often used method of an experimental determination of the deposition limit velocity V_D is a visual observation of a deposit formation in a section of viewing pipe. With increasing content of fine particles, the visual observation becomes difficult and not very accurate, and it was necessary to use another method, for example, radiometric measurement (Gillies et al., 2000). To determine the slurry velocity at which stationary deposit starts to be formed, we applied a camera system aimed on the pipe invert. Unfortunately, when the slurry velocity V approached a region close to the value of the deposition limit velocity V_D , the slurry flow became significantly unstable, especially for higher concentrations, and concentration waves were even observed. The velocity range for which a stationary bed was developed, such as velocity values for which the first particles stopped moving and velocity values when a real stationary bed (steady state deposit) were developed, was rather broad, sometimes even about 1 m/s. Into this velocity range, the bed deposit was repeatedly interrupted and started sliding - we call this behavior a “caterpillar behavior” of the sliding bed. The value of deposition limit V_D was determined to a ratio roughly equal to 1 to 5 of periods of sliding bed to stationary bed.

To increase the accuracy of V_D determination and reduce uncertainty, we combined visual observations and changes of the pressure gradient versus the velocity diagram with radiometric measurements of local concentration, c_{v10} , in the layer at a height of $y = 10$ mm above the pipe invert to identify the velocity value at which a bed forms at the pipe. A typical result of a c_{v10} test run is shown in Fig. 10 for slurry volumetric concentrations $C_v = 0.11$ and 0.25 .

The measurement started at the flow velocity V higher enough than the deposition limit V_D , and then slurry velocity V was gradually decreased during the test run. The local concentration c_{v10} in this chord was then measured as a function of the slurry velocity. As the slurry velocity decreased, the value of c_{v10} , at first slowly and then rapidly, increased until the flow velocity V decreased to a value close to the deposition limit V_D . Near the deposition limit, the local concentration c_{v10} suddenly increased and reached a value typical for the sliding or stationary bed (approximately $c_{v10} \approx 0.55-0.60$), when a stable deposit was formed at velocities below V_D (Matousek et al., 2019a; Vlasak et al., 2019a). The results of the radiometric method agree rather well with the visual observations; if the flow is steady and stable, the difference was less than 10%. The variation of the local concentration c_{v10} illustrated concentration waves in the flow regime with a slurry velocity above the deposition limit.

From the experimental data (see Table 1 and Fig. 11) it was obvious that the deposition limit velocity V_D was sensitive to the pipe inclination; in the ascending pipe, V_D was higher than in the horizontal pipe. The deposition limit V_D in the ascending pipe section increased with an inclination angle α in range of the inclination angle $\alpha = 0^\circ$ and $+25^\circ$; for higher pipe inclinations, it remained practically constant on value about 1.25 times higher than that in the horizontal pipe.

This is fully consistent with Wilson and Tse’s (1984) results, which indicated that the deposition limit V_D can increase up to 50% for coarse materials (sand and gravel with a mean diameter d_{50} from 1.1 to 5.8 mm). De Hoog et al. (2017) verified a usefulness of the Wilson-Tse nomogram for three gravel fractions (d_{50} from 4.6 to 12 mm) and found the maximum V_D at the pipe inclination of about 30° . On the contrary, in the descending pipe, the deposition limit values decreased significantly with the increasing negative slope and tended to zero for inclination angles exceeding a value $\alpha \approx -30^\circ$, where no stationary bed was observed. For such negatively steep sloped flows, a sliding bed was observed, where particles were driven downward predominantly by the downward component of the gravity force.

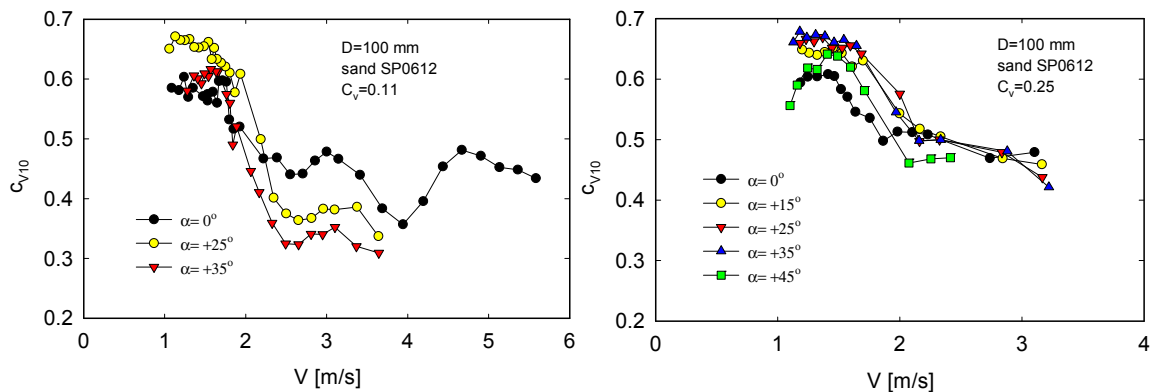


Fig. 10. Effect of the flow velocity V on local in situ concentration c_{v10} .

Table 1. Deposition limit velocity V_D , SP0612.

Deposition limit velocity V_D [m/s]						
measurement	inclination α [°]	0	15	25	35	45
gamma-ray	concentration $C_v = 0.11$	1.65	1.80	2.00	1.92	1.92
gamma-ray	concentration $C_v = 0.25$	1.58	1.92	1.98	1.90	1.75
visual	concentration $C_v = 0.25$	1.56	1.79	1.82	1.84	1.81
visual	concentration $C_v = 0.35$	1.28	1.68	1.77	1.80	1.65

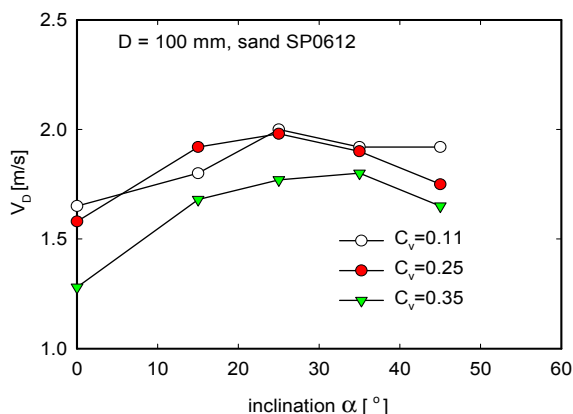


Fig. 11. Effect of the pipe inclination α and volumetric concentration C_v on deposition limit velocity V_D .

CONCLUSIONS

The effect of pipe inclination, slurry concentration, and mean velocity on flow behavior of medium-coarse sand-water slurry was studied in an experimental pipe loop of inner diameter $D = 100$ mm with inclinable pipe sections. The experimental investigation was focused on the effect of pipe inclination, overall slurry concentration, and mean velocity on flow behavior, concentration distribution, and deposition limit velocity.

It was revealed that a layered structure is a typical flow pattern for a settling slurry flow in horizontal and inclined pipe sections. The solids distribution in the tested slurry flow was very sensitive to the pipe inclination. The measured chord-averaged concentration profiles showed different degrees of stratification for the positive and negative pipe inclinations.

For slurry velocity above the deposition limit, the ascending flow was less stratified than the corresponding descending flow. The degree of stratification was sensitive to pipe inclination and depended on the mean slurry concentration and the slurry velocity. This fact is in contradiction with the assumption of the Worster-Denny (1955) formula, which overestimates the frictional pressure gradient in an ascending pipe section.

The difference between the ascending and descending flows increased from the horizontal flow up to an inclination angle of about $+30^\circ$. The mean in situ concentration for the descending flow was always lower than that for the ascending flow. The local concentration in the bed layer decreased with the increasing mean slurry velocity and the decreasing pipe inclination angle.

The deposition limit velocity was sensitive to the pipe inclination; it reached higher values in the ascending pipes than in the horizontal pipe. The maximum deposition limit value was reached for an inclination angle of about $+25^\circ$, while for the higher pipe inclination the deposition limit remained practically constant on value at about 1.25 times higher than that in the horizontal pipe.

On the contrary, in the descending pipe, where particles were driven by the downward component of the force of gravity, the deposition limit decreased significantly with the increasing negative slope and tended to be zero for inclination angles about -30° , where no stationary bed was observed.

Acknowledgement. Supports under the project 17-14271S of the Grant Agency of the Czech Republic, and RVO: 67985874 of the Czech Academy of Sciences are gratefully acknowledged.

REFERENCES

- Clift, R., Clift, D.H.M., 1981. Continuous measurement of the density of flowing slurries. *International Journal of Multiphase Flow*, 7, 5, 555–561.
- Doron, M., Simkhis, M., Barnea, D., 1997. Flow of solid-liquid mixtures in inclined pipes. *International Journal of Multiphase Flow*, 23, 313–323.
- Durand, R., Condolios, E., 1952. Étude expérimentale du refoulement des matériaux en conduite. 2èmes Journées de l'Hydraulique, SHF, Grenoble.
- Gillies, R.G., Schaan, J., Summer, R.J., Mc Kibben, M.J., Shook, C.A., 2000. Deposition velocities for Newtonian Slurries in Turbulent Flow. *Can. J. Chemical Engineering*, 78, 704–708.
- De Hoog, E., in't Veld, M., Van Wijk, J., Talmon, A., 2017. An experimental study into flow assurance of coarse inclined slurries. In: *Proceedings of 18th Transport and Sedimentation of Solids Particles*, Prague, Czech Republic, pp. 113–120.
- Kao, D.T.Y., Hwang, L.Y., 1979. Critical slope for slurry pipeline transporting coal and other solid particles. In: *Proc. HYDROTRANSPORT*, Canterbury, UK, Pap A5, pp. 57–74.
- Krupicka, J., Matousek, V., 2014. Gamma-ray-based measurement of concentration distribution in pipe flow of settling slurry: vertical profiles and tomographic maps. *Journal of Hydrology and Hydromechanics*, 62, 2, 126–132.
- Matousek, V., 1996. Internal structure of slurry flow in inclined pipe. Experiments and mechanistic modelling. In: *Proc. HYDROTRANSPORT 13*, BHRG, Cranfield, UK, pp. 187–210.
- Matousek, V., Krupicka, J., Kesely, M., 2018a. A layered model for inclined pipe flow of settling slurry. *Powder Technology*, 333, 317–326.
- Matousek, V., Kesely, M., Chara, Z., 2019a. Effect of pipe inclination on internal structure of settling slurry flow at and close to deposition limit. *Powder Technology*, 343, 533–541.
- Matousek, V., Kesely, M., Konfrst, J., Vlasak, P., 2018b. Effect of pipe inclination on settling slurry flow near deposition velocity. In: *Proc. ASME 2018 5th Joint US-European Fluids Engineering Summer Conference*, Montreal, Canada, paper FEDSM2018-83423.
- Matousek, V., Zrostlik, S., 2018. Laboratory testing of granular kinetic theory for intense bed load transport. *Journal of Hydrology and Hydromechanics*, 66, 3, 330–336.
- Messa, G.V., De Lima Branco, R., Filho, J.G.D., Malavasi, S., 2018. A combined CFD-experimental method for abrasive erosion testing of concrete. *Journal of Hydrology and Hydromechanics*, 66, 1, 121–128.
- Michalik, A., 1973. Density patterns of the inhomogeneous liquids in the industrial pipe-lines measured by means of radiometric scanning. *La Houille Blanche*, 1, 53–57.
- Parzonka, W., Kenchinton, J.M., Charles, M.E., 1981. Hydrotransport of solids in horizontal pipes: Effects of solids concentration and particle size on deposit velocity. *The Canadian Journal of Chemical Engineering*, 59, 3, 291–296.
- Przewlocki, K., Michalik, A., Korbel, K., Wolski, K., Parzonka, W., Sobota, J., Pac-Pomarnacka, M., 1979. A radiometric device for the determination of solids concentration distribution in a pipeline. In: *Proc. HYDROTRANSPORT 6*, Pap B3, pp. 105–112.
- Shook, C.A., Roco, M.C., 1991. *Slurry Flow. Principles and Practice*. Butterworth-Heinemann, Stoneham, USA.
- Sobota, J., Plewa, F., 2000. Global and local characteristics of ash mixture flows. *Electronic Journal of Polish Agricultural Universities*, 3, 2, #01.

- Spelay, R.B., Gillies, R.G., Hashemi, S.A., Sanders, R.S., 2016. Effect of pipe inclination on the deposition velocity of settling slurries. *The Canadian Journal of Chemical Engineering*, 94, 1032–1039.
- Vlasak, P., Chara, Z., Konfrst, J., 2017. Flow behaviour and local concentration of coarse particles-water mixture in inclined pipes. *Journal of Hydrology and Hydromechanics*, 65, 2, 183–191.
- Vlasak, P., Chara, Z., Krupicka, J., Konfrst, J., 2014. Experimental investigation of coarse particles-water mixture flow in horizontal and inclined pipes. *Journal of Hydrology and Hydromechanics*, 62, 3, 241–247.
- Vlasak, P., Chara, Z., Konfrst, J., Krupicka, J., 2016. Distribution of concentration of coarse particle-water mixture in horizontal smooth pipe. *Canadian Journal of Chemical Engineering*, 94, 1040–1047.
- Vlasak, P., Chara, Z., Matousek, V., Kesely, M., Konfrst, J., 2018a. Experimental investigation of settling slurry flow in inclined pipe sections. In: *Proc. 24th Int. Conf. Eng. Mech.*, Svatka, Czech Republic, Pap. #64, pp. 909–912.
- Vlasak, P., Chara, Z., Matousek, V., Konfrst, J., Kesely, M., 2018b. Effect of pipe inclination on flow behaviour of fine-grained settling slurry. In: *Proc. Experimental fluid mechanics 2018*, , Prague, Czech Republic, pp. 664–670.
- Vlasak, P., Chara, Z., Matousek, V., Konfrst, J., Kesely, M., 2019a. Experimental investigation of fine-grained settling slurry flow behaviour in inclined pipe sections. *Journal of Hydrology and Hydromechanics*, 67, 2, 113–120.
- Vlasak, P., Chara, Z., Matousek, V., Kesely, M., Konfrst, J., Mildner, M., 2019b. Effect of pipe inclination on local concentration and flow behaviour of settling slurry. In: *Proc. 25th Int. Conf. Eng. Mech.*, Svatka, Czech Republic, pp. 391–394.
- Vlasak, P., Chara, Z., Matousek, V., Kesely, M., Krupicka, J., Konfrst, J., 2019c. Local concentration distribution of settling slurry flow in inclined pipe sections. In: *Proc. 19th Int. Conf. on Transport and Sedimentation of Solid Particles*, Cape Town, S. Africa, pp. 229–236.
- Wilson, K.C., 1976. A unified physically based analysis of solid-liquid pipeline flow. In: Stephens, H.S., Streat, M., Clark, J., Coles, N.G. (eds.): *Proc. HYDROTRANSPORT 4* B.H.R.A., Cranfield, UK, Pap. A1, pp. 1–16.
- Wilson, K.C. Tse, J.K.P., 1984. Deposition limit for coarse-particle transport in inclined pipes. In: *Proc. HYDROTRANSPORT 9*, BHRA Fluid Engineering, Cranfield, UK, pp. 149–161.
- Wilson, K.C., Addie, G.R., Sellgren, A., Clift, R., 2006. *Slurry Transport Using Centrifugal Pumps*. Springer, US.
- Worster, R.C., Denny, D.F., 1955. Hydraulic transport of solid materials in pipelines. *P. I. Mech. Eng.*, 169, 563–586.

Received 2 September 2019

Accepted 25 October 2019

Vertical sorting in collisional layer of bimodal sediment transport

Štěpán Zrostlík*, Václav Matoušek

Czech Technical University in Prague, Department of Civil Engineering, Thákurova 7, 166 29 Prague 6, Czech Republic.

* Corresponding author. E-mail: stepan.zrostlik@fsv.cvut.cz

Abstract: Intense collisional transport of bimodal sediment mixture in open-channel turbulent flow with water as carrying liquid is studied. The study focusses on steep inclined flows transporting solids of spherical shape and differing in either size or mass. A process of vertical sorting (segregation) of the two different solids fractions during the transport is analyzed and modelled. A segregation model is presented which is based on the kinetic theory of granular flows and builds on the Larcher-Jenkins segregation model for dry bimodal mixtures. Main modifications of the original model are the carrying medium (water instead of air) and a presence of a non-uniform distribution of sediment across the flow depth. Testing of the modified model reveals that the model is applicable to flow inclination slopes from 20 to 30 degrees approximately, making it appropriate for debris flow conditions. Changing the slope outside the specified range leads to numerical instability of the solution. A use of the bimodal mixture model is restricted to the grain size ratio 1.4 and no restriction is found for the grain mass ratio in a realistic range applicable to natural conditions. The model reveals trends in the vertical sorting under variable conditions showing that the sorting is more intense if flow is steeper and/or the difference in size or mass is bigger between the two sediment fractions in a bimodal mixture.

Keywords: Grain segregation; Bimodal mixture; Granular flow; Sheet flow; Sediment transport.

INTRODUCTION

Transport of sediment in environmental conditions has been subject to frequent investigations. Current climate developments with more frequent occurrences of extreme weather conditions leading to flash floods and landslides focus research attention to geomorphic flows with intense sediment transport. Typically for such flows, sediment grains of different properties are transported by water current in an open channel.

Grains of different sizes and/or densities are transported in flow of mixture composed of fluid and different fractions of grains. During the transport, grains of the different fractions can segregate forming regions a preferential presence of grains of the particular fractions across the flow depth. This phenomenon is observed in many natural processes (also some industrial processes) involving transport of solid grains. The segregation is affected by various conditions associated with the granular flow. If coarse solids fractions are transported in dense granular flows, then intergranular collisions have a major impact of the segregation. This type of segregation is known as kinetic sieving, intergranular percolation or gravity driven segregation (Frey et al., 2019) and a typical example of its occurrence is the dry gravity-driven flow recognized as snow- or rock avalanches on steep hillsides of mountains. One of the major forces, besides the gravitational force, acting on grains transported in avalanches or debris flows, is the force generated by intergranular collisions. The segregation itself affects properties of the flow and those mutual interactions must be considered in modelling of the segregation process in dense granular flows. Basically, there are two approaches to modelling of the segregation of colliding grains. One approach is the discrete element modelling (DEM) and it follows a movement of each individual grain in flow subjected to vertical sorting of grains, e.g. (van der Vaart et al., 2018; Zhao et al., 2019). The other approach considers a moving body of colliding grains as a continuum, while the flow is described using (time- and space-) averaged characteristics expressing the motion of individual grains.

Kinetic-theory (KT) based studies of solid-liquid flows dominated by intergranular collisions follow principles of the second of the two approaches and they have been conducted by several authors, Jenkins and Hanes (1998), Armanini et al. (2005), Berzi and Fraccarollo (2013) among others. A majority of the studies have been focused on collisions of mono-size grains. Just recently, more attention has started to be paid to collisional transport involving vertical sorting of grains of different properties. Naturally, it was methodologically correct that first studies focused on dry bimodal flows. Larcher and Jenkins (2013) proposed a segregation model for a prediction of the final stage of segregation in dry inclined flows of two types of spheres with same value of a restitution coefficient, following works of Silbert et al. (2001), Arnarson and Jenkins (2004), and others. The segregation model was further elaborated (Larcher and Jenkins, 2015) into two versions, again for dry inclined flows of binary mixtures of spheres, one predicting the time- (unsteady) evolution of the segregation process and the other describing the steady spatial (longitudinal) evolution of the segregation in the gravity-driven flow.

It is of practical importance to include the condition of a presence of water as carrying fluid in dense granular flow dominated by collisions (the condition is typical for instance for intense transport of bed load during flash floods on mountain streams). The presence of water complicates the modelling as the role of fluid viscosity and buoyancy must be considered. Recently, Larcher and Jenkins (2019) published a model to predict the final stage of segregation in flow of water and bimodal granular mixture.

In our previous works, we have been looking at conditions and mechanisms of intense bed load in steady turbulent open-channel flow of water carrying grains above the eroded plane bed. Results of our laboratory-experiment based investigations for mono-size model sediments (fractions of plastic grains) have been published in a number of papers, starting with (Matoušek et al., 2015). Our investigations have further extended to bimodal granular mixtures composed of fractions of the

model lightweight sediments (Zrostlík and Matoušek, 2016). The fractions differed primarily in size (and color, which made observations of vertical sorting easy). The laboratory experiments with bimodal mixtures revealed a development of the interfacial layer between the granular bed and the collisional transport layer. This layer, in which grains slid over each other, was almost exclusively occupied by grains of the finer of the two fractions transported as bed load in the observed flow. We analyzed the flow at steady state after grain segregation was finished. The overall flow structure consisted of clear water as the upper layer, middle collision layers and lower deposit. The segregation of grains takes place only in the middle part.

Our modelling efforts in the field of dense gravity-driven aqueous bimodal mixtures started with works on a modification of the model by Larcher and Jenkins (2015) for the time evolution of segregation in a bimodal mixture. The modification introduces water as carrying liquid for the dense granular flow subjected to vertical sorting of grains (Zrostlík and Matoušek, 2017). The aim of this work is to present a complete modification of the Larcher-Jenkins model and to discuss the range of conditions to which it can be applied.

Before the modified model is introduced, it is useful to summarize principles and equations of the original model for dry bimodal flow.

SORTING MODEL FOR COLLISIONAL DRY FLOW OF BIMODAL MIXTURE

The Larcher-Jenkins model (2015) considers dry flow of a mixture of two size spherical grains A and B with radii r_A and r_B , mass densities ρ_A and ρ_B , masses m_A and m_B , and number densities $n_A = \rho_A/m_A$ and $n_B = \rho_B/m_B$. The local density number of mixture $n = n_A + n_B$ at each position within the transport layer. The density number is related to the local volumetric concentration of the A-fraction through $c_A = 4\pi n_A r_A^3/3$. A parameter called the measure of segregation X is defined as $X \equiv (n_A - n_B)/2n$ in the model.

Model equations

The equations below are from Larcher and Jenkins (2015). For uniform time-dependent segregation in bimodal mixture, the following mass balance equation solves sorting in the mixture with respect to time t and position above the flow bottom y ,

$$\rho \frac{\partial X}{\partial t} + \frac{\partial}{\partial y} \left[\frac{m_A n}{4} (1 - 4X^2) (v_A - v_B) \right] = 0 \quad (1)$$

In Eq. (1), the y -axis is normal to the main flow direction. This balance equation in its entirety considers sorting in time and also in space $\rho = \rho_A + \rho_B$.

The following relations are based on the kinetic theory and express quantities D_{AB} and $(v_A - v_B)$ for the condition of dry collisions. A relation for the difference in the vector diffusion velocities $(v_A - v_B)$ was derived originally by Arnarson and Jenkins (2004) and modified by Larcher and Jenkins to the form

$$(v_A - v_B) = -D_{AB} \left[\begin{array}{l} (\Gamma_1 \delta m + R_1 \delta r) \frac{\nabla T}{T} - \\ (\Gamma_2 \delta m + R_2 \delta r) \frac{m_{AB} \cos \phi}{2T} + \\ \frac{\nabla X}{0.25 - X^2} \end{array} \right]. \quad (2)$$

The measure of size difference δr is determined from $\delta r \equiv (r_A/r_B) - 1$ and the measure of mass ratio $\delta m \equiv (m_A - m_B)/m_{AB}$. The quantity m_{AB} is the sum of mass of the two fractions and r_{AB} is the sum of radii. The diffusivity coefficient D_{AB} ,

$$D_{AB} = \frac{\pi^{1/2} r_{AB}}{16 G} \left(\frac{2T}{m_{AB}} \right)^{1/2}, \quad (3)$$

and additional coefficients for Eq. (2) also originate in the kinetic theory,

$$\Gamma_1 = \frac{179}{29} G + \frac{105}{116} \doteq 6.17G, \quad (4)$$

$$R_1 = \frac{5}{58} \left[2 + \frac{c(3-c)}{2-c} - \frac{12}{5} G \right] + \quad (5)$$

$$2G \left[3 + \frac{c(3-c)}{2-c} \right] - \frac{12cH(1+4G)}{1+4G+4cH} \doteq -4.35G,$$

$$\Gamma_2 = 2, \quad R_2 = -\frac{12cH}{1+4G+4cH} \doteq -3, \quad (6a, b)$$

$$c = \frac{c_M G}{G + 5.69(c_M - 0.49)}. \quad (7)$$

The individual coefficients are simplified as in the original model. The simplification is justified as its effect on values of the coefficients is small. The granular temperature T for Eqs. (2) and (3) is expressed using the following relation which considers a mixture with a uniform concentration distribution across the flow depth (Silbert et al., 2001) and it is derived by a mathematical simulation of 3D motions and collisions of grains,

$$T = \frac{m_{AB}(h-y)}{4(1+e)G} g \cos \phi (1 + 2X \delta m) \quad (8)$$

For Eq. (8), the parameter G is determined by an expression based on the same mathematical simulation,

$$G = \left\{ \frac{4J}{5\pi^{1/2}} \frac{1}{1+e} \left[\frac{15(1-e^2)}{J\alpha} \right]^{1/3} \frac{1}{\tan \phi} \right\}^9 [1 + 3X(\delta r + \delta m)] \quad (9)$$

in which e is the coefficient of restitution and ϕ is the angle of inclination. The function H is related to radia distribution function of the mixture and it can be expressed as $H = \partial G / \partial c$. The coefficient J for very dissipative spheres reads

$$J = \frac{(1+e)}{2} + \frac{\pi}{4} \frac{(3e-1)(1+e)^2}{[24 - (1-e)(11-e)]} \quad (10)$$

From Eqs. (1) to (10), the final equation for the vertical sorting reads

$$\frac{\partial X}{\partial t} = \frac{r_{AB}(\pi g \cos \phi)^{1/2}}{128G^{2/3}} \left(\frac{2}{1+e} \right)^{1/2} \frac{\partial}{\partial y} \left[(h-y)^{1/2} \left\{ \left[(2(1+e)G\Gamma_2 - \Gamma_1)\delta m + (2(1+e)GR_2 - R_1)\delta r \right] \frac{1-4X^2}{h-y} + 4 \frac{\partial X}{\partial y} \right\} \right] \quad (11)$$

The sorting formula (Eq. (11)) is converted to the dimensionless form by normalizing the depth and time using $z \equiv y/h$, $\tau \equiv t/(r_{AB}/g)^{1/2}$. The sorting parameter X transforms to ζ which ensures a conservation of the total number of grains over the height of flow, $\frac{2cX}{(\hat{c}_A + \hat{c}_B)} = \zeta$ in

which $\hat{c}_A \equiv \frac{\bar{n}}{\bar{n}_A} \bar{c}_A$. Hence, the final relation for vertical sorting

is reached in the form of the parabolic-elliptic partial differential equation,

$$\begin{aligned} \frac{\delta \zeta}{\delta \tau} &= \left(\frac{r_A + r_B}{h} \right)^{3/2} \frac{(\pi \cos \phi)^{1/2}}{128G^{3/2}} \left(\frac{2}{1+e} \right)^{1/2} \frac{2c}{(\hat{c}_A + \hat{c}_B)} \times \\ &\times \frac{\delta}{\delta z} \left\{ \frac{\left[(2(1+e)G\Gamma_2 - \Gamma_1)\delta m + (2(1+e)GR_2 - R_1)\delta r \right]}{(1-z)^{1/2}} \right. \\ &\times \left. \left[1 - \frac{(\hat{c}_A - \hat{c}_B)}{c^2} \zeta^2 \right] + 2(1-z)^{1/2} \frac{(\hat{c}_A - \hat{c}_B)}{c} \frac{\delta \zeta}{\delta z} \right\}. \end{aligned} \quad (12)$$

A prediction of vertical sorting by the Larcher-Jenkins model requires to find a solution for Eq. (12).

Modelled conditions

The original conditions considered by Larcher and Jenkins model of dry flow are:

- Dry gravity-driven flow on inclined plane,
- grains of spherical shape,
- mixture of two fractions with not much different size and mass (the max relative size 1.3 was tested by Larcher and Jenkins 2015),
 - uniform distribution of grains across flow depth, i.e. constant concentration profile (see Figure 1),
 - velocity profile using Eq. (12) from Larcher and Jenkins (2013), see Figure 1,

$$\begin{aligned} u &= u_0 + \frac{5\pi^{1/2}}{6J} \frac{1}{r_{AB}} \left(\frac{1+e}{2G} g \cos \phi \right)^{1/2} \\ &\left[h^{3/2} - (h-y)^{3/2} \right] \tan \phi (1 - X \delta r) \end{aligned} \quad (13)$$

Figure 1 shows the model assumptions for vertical segregation conditions in bimodal mixture.

MODEL MODIFICATION FOR WET SORTING (WATER AS CARRIER)

In aqueous flow transporting in bed load, a concentration profile can be considered as approximately linear across the collisional transport layer through which grains are transported in the upper plane bed regime, e.g. (Capart and Fraccarollo, 2011; Matoušek et al., 2015). For modelling of the segregation

process in bimodal bed load, we focus on the collisional transport layer in which the segregation takes place.

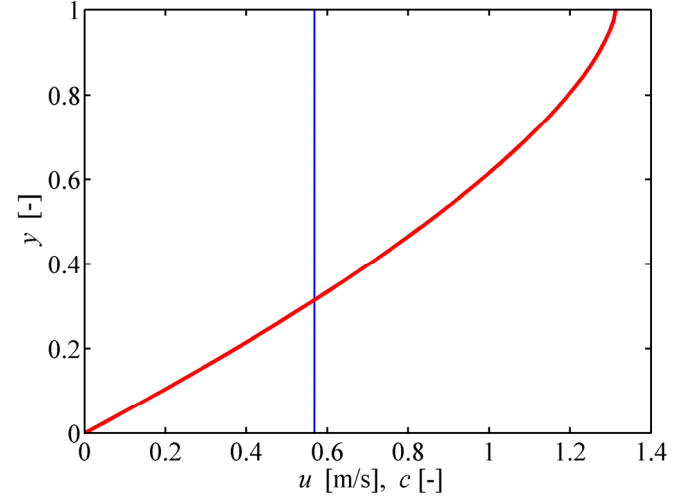


Fig. 1. Velocity profile (using Eq. (13)) and total concentration profile for $e = 0.65$, $c_M = 0.586$, $r_B = 1.1r_A$, $\phi = 25^\circ$. Legend: red line - velocity profile, blue line - total concentration profile for mixture of two fractions.

Modifications in model equations

We assume a linear concentration profile with zero at the top of the collisional layer and the maximum local concentration at the bottom of the collisional layer. It is determined by Eq. (7).

A modification is required in Eq. (12) to accommodate the presence of the linear concentration profile (the local concentration varies with the vertical position). In principle, the variable local concentration affects other c -related parameters, which become sensitive to a vertical position in the flow. Unfortunately, modifications for the other parameters made the model computationally unstable and had to be abandoned. Therefore, the height variation was introduced only for the local concentration c . The other c -related parameters of the segregation model (Γ_1 , Γ_2 , R_1 , R_2 , G) use a value of the flow-depth averaged concentration at the initial condition instead of c .

Further mathematical complications were associated with values of local concentration at the boundaries of the collisional layer, leading to dividing by zero in the model equations. Therefore, computations were carried out only in the range of the dimensionless vertical positions between 0.1 and 0.9. The boundary conditions were set so that the granular fluxes were zero at the top and at the bottom of the collisional layer. The initial conditions for each calculation included the constant ratio of volumes of both fractions at every height position and the perfect mixing of fractions at the initiation of the segregation process. The following paragraph and Figure 2 summarize the conditions.

Modelled conditions

Conditions of use for modified model according to water suspension with bimodal mixture of particles:

- wet gravity-driven flow on inclined plane,
- fully developed turbulent flow,
- grains of spherical shape,
- mixture of two fractions with not much different size and mass (quantification will follow),
- linear distribution of grains across transport layer (see Figure 2),
- velocity profile using Eq. (13), see Figure 2.

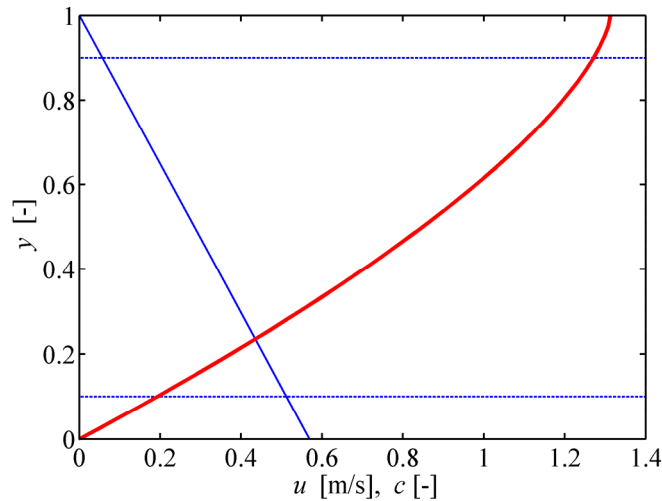


Fig. 2. Initial profiles of velocity and total concentration. Legend: red line – velocity profile, inclined blue line – concentration profile, horizontal blue lines – range of computation.

RESULTS OF MODIFIED MODEL AND THEIR DISCUSSION

The model solves Eq. (12) in time steps using the Matlab solver called pdepe. The solver is constructed for boundary value problem for initial boundary condition. The boundary value of ζ is 1 at the top of normalize transport layer, i.e. at $z = 1$. At the bottom of flow ($z = 0$), $\zeta = -1$.

A model simulation produces a prediction of a distribution of the sorting parameter X , representing the effort of sorting of the individual grains. In order to interpret a simulation result in the form of concentration profiles of the individual fractions, the following equations are used,

$$c_A = \frac{(2X+1)c}{(2X+1)-(2X-1)(r_B/r_A)^3} \quad (14a)$$

$$c_B = \frac{(2X-1)c}{(2X-1)-(2X+1)(r_A/r_B)^3} \quad (14b)$$

Profiles of these concentrations are presented for the final state of vertical sorting in figures below. Also plotted as model results are graphs showing the speed of sorting, i.e. time required to reach the final state of sorting. Effects of different grain size ratio, different mass ratio and slope of flow are discussed as well. Furthermore, possible ranges of values of

individual parameters are determined applicable in the model solved with the mathematical solver pdepe.

Effect of flow slope on vertical sorting

An influence of the flow longitudinal slope, ϕ , on the granular sorting was tested first. In various simulations with variable ϕ , the grain size and mass were kept constant to isolate the slope effect. The range of slopes to which the model can be applied is found to be limited by values of 20 and 30 degrees. It turned out that there were two conditions restricting the use of the model for smaller slopes. The first restriction was caused by a structure of the computational solver, resulting in values sweeping in the area with sudden change of values. A possible solution for this restriction could be to use a computing network with more grid points. The second restriction is more significant. Sorting at smaller slopes is much slower and it is necessary to choose a much finer step in time discretization, which leads to a requirement of too high computational power for a common use.

Figure 3 plots final concentration profiles for fractions A and B in dimensionless time 6000 at three different slopes, 20, 26 and 30 degrees. The simulations show that a steeper slope produces a more intense sorting, even in the lower part of the collision layer. At the same time, a shallower slope creates a sharper interface between the sorted fractions.

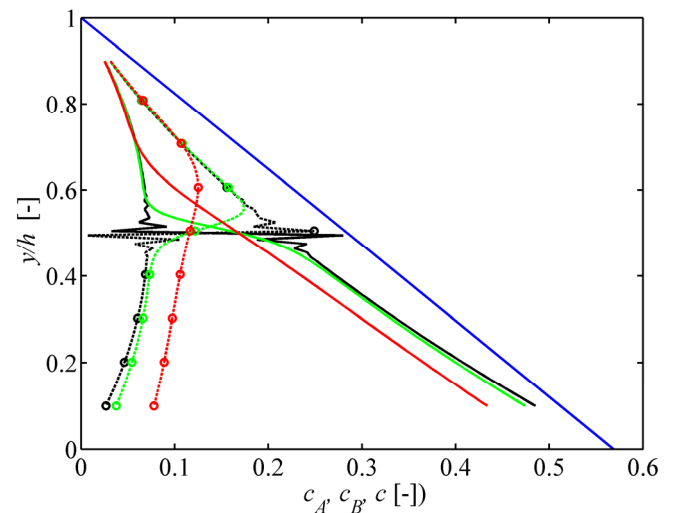


Fig. 3. Final concentration profiles of c_A and c_B , for $r_A = r_B$, $m_A = m_B$, at dimensionless time 6000 for 3 different flow slopes. Legend: inclined blue line – total concentration, lines with symbols – spheres A, lines without symbols – spheres B (black - $\phi = 20^\circ$, green - $\phi = 26^\circ$, red - $\phi = 30^\circ$).

Figure 4 shows the time evolution of sorting for the three cases plotted in Figure 3. Each curve in Figure 4 represents the time development in the centre of gravity of a concentration profile of an individual fraction. Apparently, the speed of sorting increases with the flow slope.

Sorting by grain size

An effect of the relative size of grains of fractions A and B, r_A/r_B (i.e. the ratio of grain sizes of the two fractions), on the vertical sorting was tested by setting values of the relative size as the only variable in the model simulations. The results presented below are for the slope $\phi = 25$ degree. The range of

relative sizes was set from 1 to 1.4. It made no sense to test values smaller than 1 (they do not exist) and the sizes bigger than 1.4 resulted in a reverse sorting tendency at the upper border of the simulated layer. The value of 1.4 also corresponded with suggestions for the relative size in the original model. Furthermore, no experimental data are available to verify sorting for high relative size mixtures.

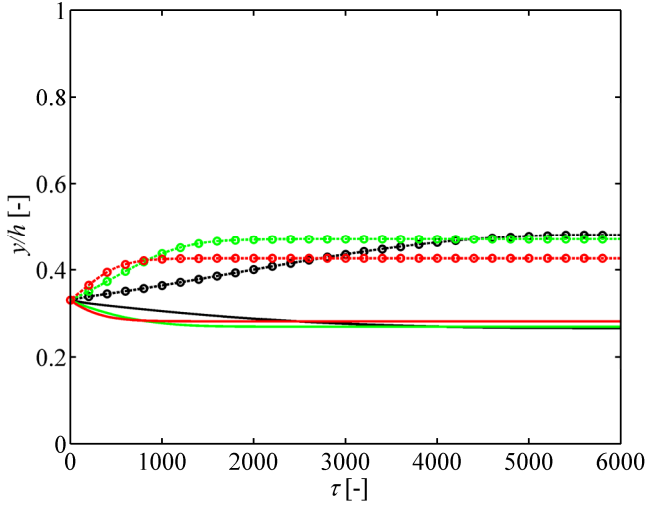


Fig. 4. Time evolution of gravity centroids of concentration profile of c_A and c_B , for $r_A = r_B$, $m_A = m_B$, for 3 different flow slopes as in Figure 3. Legend: increasing curves with symbols = fraction B, decreasing curves = fraction A (black - $\phi = 20^\circ$, green - $\phi = 26^\circ$, red - $\phi = 30^\circ$).

Figure 5 shows the effect of the relative grain size on the vertical sorting in the form of the final concentration profiles for both fractions and of the time evolution of the center of gravity of the profiles. A special case is the condition of the relative size being unity. This exhibits the evolution of sorting only on the basis of the flow itself. If the relative size increases (to 1.1 and 1.4), then the sorting becomes more intense (the right-hand side panel of Figure 5). At the same time, the relative size has a limited effect on the speed of sorting as the right-hand side panel of Figure 5 shows.

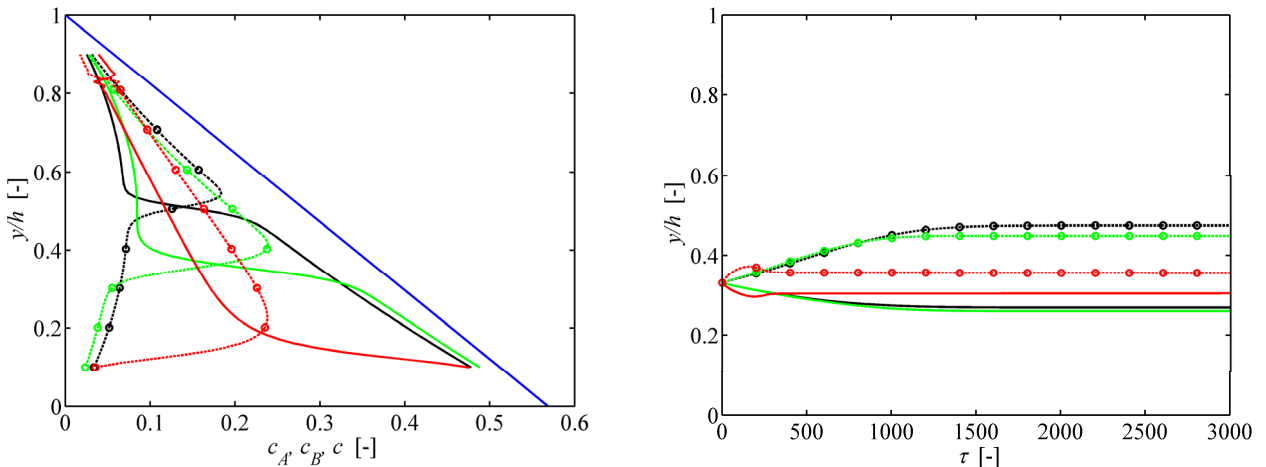


Fig. 5. Left panel: final concentration profiles for different relative grain sizes r_A/r_B , for $\phi = 25^\circ$, $m_A = m_B$. Legend: lines –spheres A, lines with symbols - spheres B (black - $r_A/r_B = 1$, green - $r_A/r_B = 1.1$, red - $r_A/r_B = 1.4$). Right panel: time evolution of gravity centre of concentration profile, for $\phi = 25^\circ$, $m_A = m_B$. Legend: increasing curves with symbols = fraction B, decreasing curve = fraction A (black - $r_A/r_B = 1$, green - $r_A/r_B = 1.1$, red - $r_A/r_B = 1.4$).

Sorting by grain mass

The last tested parameter was the mass ratio, m_A/m_B . Its effect on the vertical sorting was tested by setting values of the mass ratio as the only variable in the model simulations. The results presented below are for the slope $\phi = 25$ degree and the grain size ratio $r_A/r_B = 1$. The range of mass ratios was set from 1 to 5, which was considered to cover the range expected in engineering applications. Figure 6 demonstrates that the larger m_A/m_B the stronger the vertical sorting throughout the collisional transport layer. The effect of m_A/m_B on the time evolution of the separation is relatively weak although considerably stronger than the effect of the size ratio.

CONCLUSIONS

The Larcher-Jenkins segregation model for dry bimodal granular flow is modified to predict vertical sorting in collisional transport layer of bimodal mixture flow with water as a carrying fluid and for a condition of a linear distribution of grains instead of the uniform distribution considered in the original model. The modifications were motivated by experimental observations in our laboratory flume. A testing of the ranges of applicability of the wet sorting model showed that the modified model could be used in the range of slopes from 20 to 30 degree, making it suitable for debris flow conditions. An extension of the model applicability to flatter slopes was restricted by the applied mathematical solution using the Matlab solver called pdepe. A further restriction is the relative size of two granular fractions in bimodal mixture, the testing confirmed that the size ratio should not be bigger than 1.4. No restriction was found for the mass ratio as the model worked also for the maximum set value of 5, which covers all conditions of real-world applications.

The model results suggested that the larger the ratios of mass and size the stronger is the vertical sorting in the lower part of the collisional transport layer in the aqueous mixture flow.

Furthermore, a numerical testing of time evolution of concentration profiles showed that the longitudinal slope of the flow had a considerably greater effect on the vertical sorting than the grain size ratio and the grain mass ratio of the particular fractions.

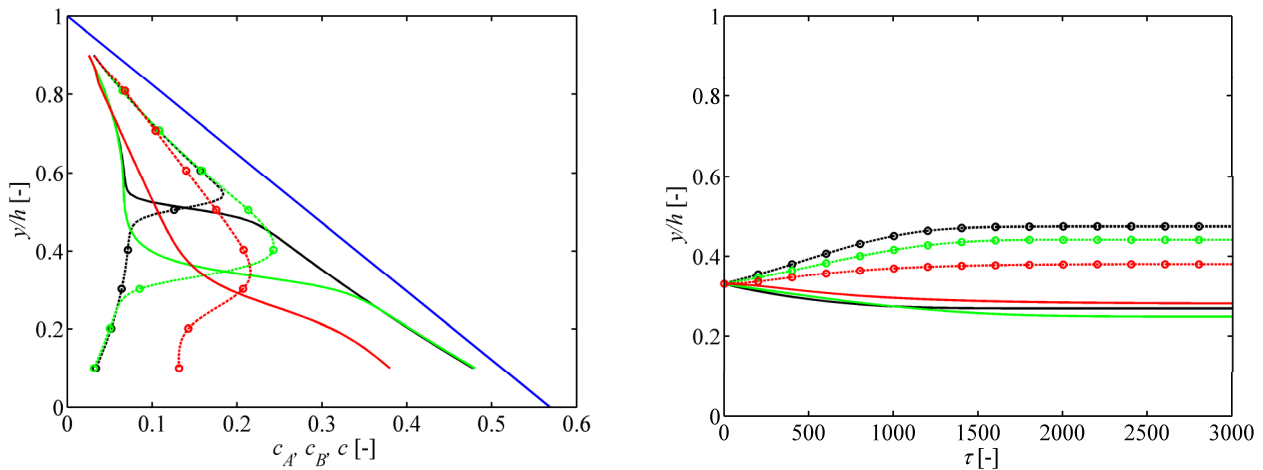


Fig. 6. Left panel: final concentration profile for different mass ratios m_A/m_B , for $\phi = 25^\circ$, $r_A/r_B = 1$. Legend: lines with symbols –spheres A, lines - spheres B (black – $m_A/r_B = 1$, green $m_A/m_B = 1.5$, red – $m_A/m_B = 5$).

Right panel: time evolution of gravity centre of concentration profiles, for $\phi = 25^\circ$, $r_A/r_B = 1$. Legend: increasing curves with symbols = fraction A, decreasing curves = fraction B (black - $m_A/m_B = 1$ green line - $m_A/m_B = 1.5$, red - $m_A/m_B = 5$).

Acknowledgement. The research has been supported by the Czech Science Foundation through the grant project No. 19-18411S.

REFERENCES

- Armanini, A., Capart, H., Fraccarollo, L., Larcher, M., 2005. Rheological stratification in experimental free-surface flows of granular-liquid mixtures. *Journal of Fluid Mechanics*, 532, 269–319.
- Arnarson, B.Ö., Jenkins, J.T., 2004. Binary mixtures of inelastic spheres: simplified constitutive theory. *Phys. Fluids*, 16, 4543–4550.
- Berzi, D., Fraccarollo, L., 2013. Inclined, collisional sediment transport. *Physics of Fluids*, 25, 1–11.
- Capart, H., Fraccarollo, L., 2011. Transport layer structure in intense bed-load. *Geophysical Research Letters*, 38, 1–6.
- Frey, P., Lafaye de Micheaux, H., Bel, C., Maurin, R., Rorsman, K., Martin, T., Ducottet, C., 2019. Experiments on grain size segregation in bedload transport on a steep slope. *Advances in Water Resources*, 135, 1–12.
- Jenkins, J.T., Hanes, D.M., 1998. Collisional sheet flows of sediment driven by a turbulent fluid. *Journal of Fluid Mechanics*, 370, 29–52.
- Larcher, M., Jenkins, J.T., 2013. Segregation and mixture profiles in dense, inclined flows of two types of spheres. *Physics of Fluids*, 25, 1–16.
- Larcher, M., Jenkins, J.T., 2015. The evolution of segregation in dense inclined flows of binary mixtures of spheres. *Journal of Fluid Mechanics*, 782, 405–429.
- Larcher, M., Jenkins, J.T., 2019. The influence of granular segregation on gravity driven particle-fluid flow. *Advances in Water Resources*, 129, 365–372.
- Matoušek, V., Bareš, V., Krupička, J., Pícek, T., Zrostlík, Š., 2015. Experimental investigation of internal structure of open-flow with intense transport of sediment. *Journal of Hydrology and Hydromechanics*, 63, 318–326.
- Silbert, L.E., Ertas, D., Grest, G.S., Halsey, T.C., Levine, D., Plimpton, S.J., 2001. Granular flow down an inclined plane. Bagnold scaling and rheology. *Physical Reviews*, E 64, 1–14.
- van der Vaart, K., van Schroyen Lantman, M.P., Weinhart, T., Luding, S., Ancey, C., Thornton, A.R., 2018. Segregation of large particles in dense granular flows: A granular Saffman effect? *Physical Review Fluids*, 3, 1–9.
- Zhao, L.L., Li, Y., W., Yang, X.-D., Jiao, Y., Hou, Q.-F., 2019. DEM study of size segregation of wet particles under vertical vibration. *Advanced Powder Technology*, 30, 1386–1399.
- Zrostlík, Š., Matoušek, V., 2016. On the effect of segregation on intense bimodal bed load, *EPJ Web of Conferences*, 143, 2017 (EFM16 – Experimental Fluid Mechanics 2016), 1–7.
- Zrostlík, Š., Matoušek, V., 2017. Kinetic theory based approach to modelling of segregation in intense bimodal bed load transport. In: *Proc. 18th Int. Conf. on Transport and Sedimentation of Solid Particles*, Prague, pp. 409–416.

NOMENCLATURE

Remark: symbols with over-line are depth-averaged variables and symbol with roof are variables normalized by depth-averaged variables

- A, B – index for fractions of spheres
 c [-] – total volumetric concentration
 c_M [-] – maximum mixture concentration
 D_{AB} [-] – diffusivity coefficient
 e [-] – coefficient of restitution
 G [-] – concentration-related function
 g [m/s^2] – gravitational acceleration
 H [-] – concentration-related function
 h [m] – depth of flow
 J [-] – coefficient for mixture shear stress
 m [kg] – mass of grain
 m_{AB} [m] – count of mass of grains A and B
 n [m^{-3}] – number density
 $R_{1,2}$ [-] – function of mixture concentration
 r [m] – radius of grain
 r_{AB} [m] – count of radii of grains A and B

T [m^2/s^2] – granular temperature

t [s] – time

u [m/s] – local velocity in longitudinal direction of flow

u_0 [m/s] – slip velocity

X [–] – measure of segregation

y [m] – vertical position

z [–] – dimensionless vertical position

α [–] – dimensionless coefficient of order unity

Γ [–] – rate of collisional dissipation as function of concentration

δr [–] – measure of size difference

δm [–] – measure of mass difference

ϕ [°] – flow slope (angle of longitudinal inclination)

τ [–] – dimensionless time

ρ [kg/m^3] – density of grain

v [m/s] – vertical diffusivity velocity

ζ [–] – dimensionless measure of segregation

Received 9 December 2019

Accepted 15 January 2020